Reconstructie van profielen van zachte X-stralen en wolfraamconcentraties in tokamaks door middel van tomografie met gaussiaanse processen

Reconstruction of soft X-ray and tungsten concentration profiles in Tokamaks using Bayesian method

Tianbo Wang

Promoter: prof. dr. Geert Verdoolaege
Research Unit Nuclear Fusion - Department of Applied Physics
Ghent University

Ph.D. adviser: HDR. dr. Didier Mazon
Institute for Magnetic Fusion Research
CEA cadarache

Co-promoter: prof. dr. Xavier Leoncini
Centre de Physique Théorique
Aix-Marseille University

UNIVERSITE D'AIX-MARSEILLE
UNIVERSITE de Gand

ECOLE DOCTORALE 352 : Physiques et Science de la Matière

Institut de Recherche sur la Fusion par confinement Magnétique

CEA – cadarache

Thèse présentée pour obtenir le grade universitaire de docteur

Spécialité : Energie, Rayonnement, Plasma

Tianbo WANG

Titre de la thèse : **Reconstruction de l'émissivité X-mou et du profil de concentration tungstène dans les plasmas de Tokamak par méthode Bayésienne**

Thesis title: **Reconstruction of soft X-ray and tungsten concentration profiles in Tokamaks using Bayesian method**

Soutenue le 08/07/2019 devant le jury :

Prof. Geert VERDOOLAEGE	Université de Gand	Directeur de thèse
HDR. Didier MAZON	IRFM - CEA cadarache	Responsable de thèse
Prof. Xavier LEONCINI	Aix - Marseille Université	Co-Directeur de thèse
Prof. Marek SCHOLZ	IFJ - PAN	Rapporteur
Prof. Chijie XIAO	Université de Pékin	Rapporteur
Dr. Jakob SVENSSON	IPP - Greifswald	Examinateur
Prof. Conrad BECKER	Aix - Marseille Université	Examinateur
Dr. Sehila GONZALEZ DE VICENTE	IAEA	Examinateur
Prof. Luc TAERWE	Université de Gand	Invitée
Prof. Aleksandra PIZURICA	Université de Gand	Invitée

Acknowledgement

First, I want to express my sincere gratitude to all the examination committee members, Prof. Conrad Becker, Prof. Luc TAERWE, Prof. Marek SCHOLZ, Prof. Chijie XIAO, Prof. Aleksandra PIZURICA, Dr. Jakob SVENSSON, Dr. Sehila GONZALEZ DE VICENTE, thank you very much for attending my Ph.D. examination and help me to improve the quality of this thesis.

At same time, I would like to express my grateful acknowledgement to my supervisors Prof. Geert VERDOOLAEGE and HDR. Didier MAZON, thank you so much for giving me this opportunity to complete my Ph.D. in Ghent University and CEA. I love this topic, which offers me the chance to stay in my favorite researching area, nuclear fusion for energy purpose. For myself, this is one of the most respectful work in the world, when I was in high school and saw first time a tokamak picture in our text book, I've never though that I can also contribute my own value to this great topic of human beings. During my Ph.D. study, Geert and Didier led me to the field of fusion diagnostics and Bayesian theory. Their great patience and serious scientific attitude always strongly inspire me to make progress on my work. I will remember it all my life.

Secondly, I would like to thank Dr. Jakob SVENSSON, whom generously provided his guidance to me on the Gaussian process tomography and Bayesian concepts during my visit to IPP Greifswald. He is one of the most enthusiastic and infective scientists I have met in fusion community. His passion on science shows me that the scientific researching could be so interesting and motivated, I appreciate all the insights he shared with me.

My special thanks to Dr. Xiao-Lan ZOU, who is the most important person because he led me into the fusion career. I have known Dr. ZOU from my master internship in CEA, he has a similar life trajectory as I do, started from a Chinese student studied science of fusion in France. He is my dear friend and my teacher who generously shared his experiences with me, not only on research but also on the life. Without him, I was still a confusing kid who is thinking about the future.

Additionally, I would like to thank Dr. Dong LI, Dr. Axel JARDIN, Dr. Didier VEZINET, this Ph.D. thesis was started from their previous efforts. Without standing on the land which was pioneered by them, I couldn't make a progress on the study of tungsten monitoring method. Especially Dr. Dong LI who's also my close friend and colleague in SWIP, generously gave me a lot of helps during this work.

I want to thank my co-promoter Prof. Xavier LEONCINI, thank you so much for your warm welcome during my visit to AMU. Nevertheless, I want to thank our dear secretaries from UGent and AMU, Madame. Muriel VERVAEKE, Madame. Michele FRANCIA, many thanks for taking care of my administration dossiers.

I thank all the colleagues, friends met at UGent and CEA, for their supports and warm accompany, Dr. Gregoire HORNUNG, Dr. Aqsa SHABBIR, Frank JANSSENS, Kathleen VAN OOST, Eveline INDEMANS, Yan SUN, Xiao SONG, Guoliang XIAO, Rui MAO, Lei XUE, Xinze LI, Long ZHANG, Xinyi LI, Jing MA, Zhaoxi Chen, Dr. Bin ZHANG & Yingkun XI, Dr. Qiang LI, Xiuda YANG, Jinyu XIE, Dr. Andrzej WOJENSKI, Dr. Charles

EHRLACHER, Dr. Alexandre LOUZGUITI. And of course I want to thank the colleagues from UGent low temperature plasma group, Lei WANG, Monica THUKKARAM, Ke Vin CHEN, Silvia GRANDE, Tim EGGHE, Niels WARDENIER, Dr. Patrick DEL REASE, Lu CHENG, Chuanlong MA, Yiwei JIANG. Nevertheless, I also want to thank my Chinese friends from ITER organization for many enjoyable moments in MBA, Dr. Lilong QIU, Dr. Jinchao LI, Shihai ZHAO, Huiyue WU and all the others.

I also want to express my sincere appreciation to China Scholarship Council (CSC) for providing me the necessary life expenses during my study, and as well as my home institute SWIP, for their important supports on my research career.

In the end, my deepest appreciation to my dearest wife Zijin Cecélia ZHOU, to my parents and to all my dear families, their love encourages me at every difficult night, without them I cannot finish this Ph.D.

Summary

Aiming at the development of a sustainable and safe energy source, nuclear fusion research is presently largely concentrated around the construction and operation of the international fusion device ITER. One of the primary issues threatening safe and efficient operation of this type of magnetic confinement fusion devices, called tokamaks, is the accumulation of so-called impurities in the plasma core, causing fuel dilution and radiative power loss. The interaction of the hot hydrogenic plasma with the wall components is one of the most important sources of impurity. In ITER, tungsten (W) has been selected as divertor material due to its low tritium retention and ability to handle large heat fluxes. However, tungsten may also pose an important risk, as highly charged impurities like tungsten radiate energy very efficiently, strongly contributing to radiative power loss. In reactor-relevant plasmas, thermonuclear burn will be possible only if tungsten concentrations remain below 10^{-4}. Therefore, in order to avoid a harmful termination of the plasma that may damage the machine (disruption), a detailed understanding of core impurity transport in tokamaks, including its interplay with magnetohydrodynamic (MHD) activity, is crucial. This requires reliable local information about impurity distributions, at a time resolution that is adapted to MHD time scales. Soft X-ray (SXR) spectroscopy is a diagnostic technique that has the potential to deliver valuable information in this respect. Since SXR spectroscopy can be operated at high temporal resolution (repetition rates up to MHz) and has a high spatial resolution (in order of centimeters), this opens up the very attractive possibility of localized real-time control of impurity concentrations, provided efficient actuators for the spatial impurity distribution can be established. However, the data analysis is challenging because the local two-dimensional SXR emissivity field in a poloidal cross-section has to be reconstructed from line-integrated measurements by tomographic methods. This is an ill-posed inverse problem, because the number of unknowns is far higher than the number of measurements. In addition, the measurement is a superposition of contributions from various impurity species, so disentangling contributions from each individual species can become difficult.

From the above considerations, it is clear that real-time reconstruction of SXR emissivity profiles, with sufficient resolution and accuracy, requires specialized methods that take into account the various uncertainties entering the reconstruction process. Currently used methods, such as minimum Fisher information, often rely on a time-consuming optimization algorithm, which cannot be deployed for real-time applications. In this work, a modern probabilistic approach has been adopted, using Bayesian inference. In the Bayesian framework, every piece of information can be assigned a probability, which is updated through Bayes' rule as new data become available. The framework is therefore ideally suited to provide probability distributions for quantities that have to be calculated from raw measured data that are affected by uncertainties. In addition, Bayes' rule naturally solves inverse problems, such as tomographic reconstruction, by relying on the line-integrated data, without actually performing an error-prone inversion process.

In this doctoral work, a new method called Gaussian process tomography (GPT) has been adopted, validated and extended for the reconstruction of SXR emissivity distributions and tungsten concentration distributions by means of Bayesian probability theory and Gaussian processes. The approach is targeted at studies of impurity transport and MHD activity, as well as real-time impurity control in WEST (Tungsten Environment in Steady-state Tokamak). WEST is an upgrade of the former Tore Supra tokamak from a limiter to a divertor configuration. In GPT, the SXR emissivity field is modeled by a Gaussian process (GP), which is the extension of a multivariate Gaussian distribution to a function space. In practice, the SXR emissivity distribution is described by a multivariate normal distribution over a set of pixels. The covariance matrix takes care of the regularization of the problem, ensuring a single solution with the appropriate level of smoothness. Given measurements of the line-integrated SXR emissivity, the method provides the posterior distribution of the emissivity field, from which point estimates and error bars of the reconstructed emissivity field can be derived. Provided the forward model is linear, like the basic tomography model, the GP prior guarantees a GP posterior, so its moments are available in closed form. The attractive non-iterative and nonparametric features of GPT thus enable high-resolution reconstruction of SXR emissivity fields at limited computational cost.

In this PhD thesis, the GPT technique has been studied and tested on synthetic data in the context of the new WEST SXR diagnostic system, which employs gas electron multiplier (GEM) cameras. Using synthetic emissivity fields of various shapes, the technique was seen to compare favorably with the present standard technique based on minimum Fisher information (MFI). The good quality of the reconstructions was confirmed by maps of the posterior variance. Next, information about the geometry of the magnetic surfaces was incorporated by introducing anisotropy in the length scales determining correlations in the GP covariance matrix. Comparison with MFI revealed a considerably better performance by GPT. For further validation using real data, the method was also applied successfully to bolometry and SXR spectroscopy at the EAST and HL-2A tokamaks, delivering useful information for ongoing physics studies.

The next goal was Bayesian inference of tungsten concentration distributions from line-integrated SXR data, in addition to extra diagnostic information about the electron temperature and density radial profiles from electron cyclotron emission and Thomson scattering, respectively. This required calculation of the tungsten cooling factor which renders the forward model nonlinear, hence a full Bayesian calculation was required, involving posterior sampling by means of Markov Chain Monte Carlo techniques. In a test using synthetic data, tungsten density profiles were successfully reconstructed, although the computational load was significant. Therefore, perspectives were presented towards a solution involving surrogate modeling of the inference process, based on a large database of reconstructions. Preliminary tests on SXR data using various designs of convolutional neural networks suggest a good potential towards real-time reconstruction of impurity density profiles with a view to an impurity monitoring system that could provide feedback for the plasma control system in future devices. The approach could also contribute to the understanding of impurity transport in tokamaks, by providing information on the transport coefficients.

Samenvatting

Het onderzoek naar kernfusie is, met het oog op de ontwikkeling van een duurzame en veilige energiebron, momenteel voor een groot deel gericht op de constructie en operatie van de internationale fusiemachine ITER. Eén van de belangrijkste kwesties die de veilige en efficiënte operatie bedreigen van dit type van fusiemachines doormiddel van magnetische opsluiting, tokamaks genoemd, is de accumulatie van zogenaamde onzuiverheden in de plasmakern, wat voor verdunning zorgt van de brandstof en vermogensverlies door straling. Deze interactie van het hete waterstofplasma met de wandcomponenten is één van de belangrijkste bronnen van onzuiverheid. In ITER is wolfram (W) geselecteerd als divertormateriaal vanwege zijn lage tritiumretentie en vermogen om grote hittebelasting te weerstaan. Wolfram kan evenwel ook een belangrijk risico vormen, omdat sterk geladen onzuiverheden zoals wolfram zeer efficiënt energie wegstralen, waardoor ze sterk bijdragen tot vermogensverlies door straling. In reactor-relevante plasma's zal thermonucleaire verbranding slechts mogelijk zijn mits de concentraties aan wolfram beneden 10^{-4} blijven. Om een gevaarlijke beëindiging van het plasma (disruptie) te vermijden, die de machine zou kunnen beschadigen, is een gedetailleerd begrip van het transport van onzuiverheden in de kern van tokamakplasma's dus cruciaal, inclusief de wisselwerking met magnetohydrodynamische (MHD) activiteit. Dit vereist betrouwbare lokale informatie over onzuiverheidsdistributies, met een tijdsresolutie die aangepast is aan de tijdsschaal van MHD. Spectroscopie doormiddel van zachte X-stralen (SXR) is een diagnostische techniek met het potentieel om hierover waardevolle informatie te leveren. Vermits SXR-spectroscopie kan opereren met hoge tijdsresolutie (herhalingsfrequenties tot in de MHz) en hoge spatiale resolutie (orde centimeters), opent dit de aantrekkelijke mogelijkheid tot gelokaliseerde real-time controle van onzuiverheidsconcentraties, op voorwaarde dat efficiënte actuatoren voor de spatiale onzuiverheidsdistributie gevonden kunnen worden. De data-analyse is echter uitdagend, omdat de lokale tweedimensionale SXR-emissiviteit in een poloïdale doorsnede gereconstrueerd moet worden uit lijn-geïntegreerde metingen door tomografische methodes. Dit is een slecht-gesteld invers probleem, vermits het aantal onbekenden veel groter is dan het aantal metingen. Bovendien is de meting een superpositie van bijdragen van verschillende soorten onzuiverheden, zodat het ontrafelen van de bijdragen van de individuele soorten moeilijk kan worden.

Om de hierboven aangehaalde redenen is het duidelijk dat voor de reconstructie van SXR-emissiviteitsprofielen in reële tijd, met voldoende resolutie en nauwkeurigheid, gespecialiseerde methodes vereist zijn die de verschillende onzekerheden, die hun intrede doen in het reconstructieproces, in rekening brengen. De huidige gebruikte methodes, zoals minimum Fisherinformatie, steunen vaak op een tijdrovend optimalisatiealgoritme, dat niet ingezet kan worden voor real-time toepassingen. In dit werk wordt een moderne probabilistische methode gebruikt, gebaseerd op Bayesiaanse inferentie. In het Bayesiaanse raamwerk kan aan elk stukje informatie een probabiliteit toegekend worden, die ge-updatet wordt zodra nieuwe data beschikbaar wordt. Dit raamwerk is daarom uitstekend geschikt om probabiliteitsdistributies te verschaffen voor grootheden die berekend moeten worden uit ruwe metingen die beïnvloed worden door onzekerheden. Bovendien lost de regel van Bayes op een natuurlijke manier inverse problemen op, zoals de tomografische reconstructie, uitgaande van lijn-geïntegreerde data, zonder een eigenlijk inversieproces uit te voeren dat sterk onderhevig is aan fouten.

In dit doctoraatswerk wordt een nieuwe methode, tomografie door Gaussiaanse processen (GPT), ingezet, gevalideerd en uitgebreid voor de reconstructie van SXR-emissiviteitsprofielen en concentratiedistributies van wolfram door middel van Bayesiaanse probabiliteitstheorie en Gaussiaanse processes. Deze aanpak is gericht op studies van onzuiverheidstransport en MHD-activiteit, en real-time controle van onzuiverheden in WEST (Tungsten Environment in Steady-state Tokamak). WEST is een upgrade van de eerdere tokamak Tore Supra, van een limiter- naar een divertorconfiguratie. In GPT wordt de SXR-emissiviteit gemodelleerd door een Gaussiaans proces (GP), wat een uitbreiding is van een multivariate Gaussiaanse distributie naar een functieruimte. In de praktijk wordt het SXR-emissiviteitsprofiel beschreven door een multivariate normale distributie over een set pixels. De covariantiematrix zorgt voor de regularisatie van het probleem, zodat er één enkele oplossing overblijft met het juiste niveau van gladheid. Gegeven metingen van de lijn-geïntegreerde SXR-emissiviteit, verschaft de methode de a posteriori-distributie van het emissiviteitsveld, waaruit puntschattingen en foutenmarges van het gereconstrueerde emissiviteitsveld afgeleid kunnen worden. Gesteld dat het voorwaartse model lineair is, zoals het eenvoudigste tomografiemodel, dan garandeert de GP-a priori-distributie een GP-a posteriori-distributie, met momenten die in gesloten vorm beschikbaar zijn. De aantrekkelijke niet-iteratieve en niet-parametrische kwaliteiten van GPT maken dus een reconstructie van SXR-emissiviteitsvelden mogelijk met hoge resolutie en met bepekte computationele middelen.

In deze doctoraatsthesis werd de GPT-techniek bestudeerd en getest op synthetische data in de context van de nieuwe SXR-diagnostiek op WEST, die gebruik maakt van camera's op basis van gas-elektronmultiplicatoren (GEM). Gebruik makend van synthetische emissiviteitsvelden van verschillende vormen werd gevonden dat de techniek de vergelijking met de standaardtechniek gebaseerd op minimum Fisherinformatie (MFI) goed doorstaat. De goede kwaliteit van de reconstructies werd bevestigd door kaarten van de a posteriori-variantie. Vervolgens werd informatie over de ligging van de magnetische oppervlakken in rekening gebracht door anisotropie te introduceren in de lengteschalen die de correlaties bepalen in de GP-covariantiematrix. Na vergelijking met MFI bleek GPT aanzienlijk beter te presteren. Voor bijkomende validatie met reële data werd de methode ook met succes toegepast op bolometrie en SXR-spectroscopie op de tokamaks EAST en HL-2A, waarbij nuttige informatie geleverd werd voor aan de gang zijnde fysische studies.

De volgende doelstelling betrof Bayesiaanse inferentie van concentratieprofielen van wolfram uit lijn-geïntegreerde SXR-data, samen met extra diagnostische informatie over radiale profielen van de elektrontemperatuur en –dichtheid uit elektron-cyclotronemissie, respectievelijk Thomsonverstrooiing. Hiervoor was het nodig de koelingsfactor voor wolfram te bereken. Daardoor wordt het voorwaartse model niet-lineair, en een volledige Bayesiaanse berekening was dus vereist, gebruik makend van a posteriori-sampling doormiddel van Markovketen-Monte Carlo-technieken. In een test met synthetische data werden profielen van de wolframdichtheid met succes gereconstrueerd, niettemin met significante computationele vereisten. Daarom werden perspectieven voorgesteld op een oplossing gebruik maken van surrogaatmodellering van het inferentieproces, gebaseerd op een grote databank van reconstructies. Enkele eerste tests op SXR-data gebruik makend van neurale convolutienetwerken met variërende designs, wijzen op een goed potentieel voor de reconstructie van dichtheidsprofielen van onzuiverheden in reële tijd, met het oog op een systeem voor monitoring van onzuiverheden dat feedback zou kunnen leveren aan het systeem voor plasmacontrole in toekomstige machines. Deze aanpak zou ook kunnen bijdragen aan het begrip van onzuiverheidstransport in tokamaks, door informatie te leveren over de transportcoëfficiënten.

List of Acronyms

ADAS : Atomic Database and Analysis Structure

AUG : ASDEX-Upgrade

AXUV : absolute extreme ultraviolet

CFC : carbon fiber composite

CNN : convolutional neural network

CR : collisional radiative

D : deutrium

EAST : Experimental Advanced Superconducting Tokamak

ECCD : electron-cyclotron current drive

ECE : electron cyclotron emission

ELM : edge localized mode

FCNN : fully connected neural network

GAM : geodesic acoustic mode

GEM : gas electron multiplier

GP : Gaussian process

GPT : Gaussian process tomography

ICF : inertial confinement fusion

ILW : ITER-like wall

ITER : international thermonuclear experimental reactor

JET : Joint European Torus

LCFS : last-closed flux surface

LHCD : low-hybrid current driven

LIB : local ionization balance

LOS : lines-of-sight

LVIC : low voltage ionization chamber

MAP : maximum a posterior

MCF : magnetic confinement fusion

MCMC : Markov chain Monte Carlo

MFI : minimum Fisher information

MHD : Magnetohydrodynamic

NTM : neoclassical tearing mode

PDF : probability density function

PF : poloidal field

PFC : plasma-facing components

PTR : Phillips-Tikhonov Regularization

SOL : scrape-off layer

SVD : singular value decomposition

SXR : soft X-ray

T : tritium

TF : toroidal field

TS : Thomson scattering

UV : Ultraviolet

VUV : visible-ultraviolet

W : tungsten

WEST : Tungsten Environment in Steady-state Tokamak

CONTENTS

Chapter 1 Introduction 1

1.1. Energetic challenges and nuclear fusion 1

1.1.1 Energy consumption, resources and environmental constraints 1

1.1.2 Magnetic confinement fusion (MCF) and inertial confinement fusion (ICF) 7

1.2. MCF concepts 9

1.2.1 Tokamaks 9

1.2.2 Stellarator 9

1.2.3 Roadmap of MCF power plants in Europe 10

1.3. Purpose of this thesis 11

Chapter 2 Tokamak Physics 12

2.1. MHD equilibrium and major instabilities 13

2.1.1 Magnetic flux surfaces 14

2.1.2 Sawtooth mode, Kink modes, Neoclassical Tearing modes and mode analysis 19

2.2. Power balance and radiation losses 26

2.2.1 Tokamak power balance 26

2.2.2 Plasma-surface interaction 28

2.2.3 Effects of plasma impurities 30

Chapter 3 Soft X-ray diagnostic on WEST 34

3.1. Soft X-ray emission 34

3.1.1. Line radiation, recombination radiation and Bremsstrahlung radiation 35

3.1.2. Ionization equilibrium 41

3.1.3. Cooling factor 45

3.2. SXR diagnostic on Tokamak 47

3.2.1. SXR detectors 47

3.2.2. Detector calibrations 55

3.3. Gas Electron Multiplier (GEM) on WEST 56

Chapter 4 Tomography and Bayesian inference 60

4.1. Tomography of line-integrated measurements 61

4.1.1. Modeling of SXR tomography 61

4.1.2. Standard regularization approaches 62

4.1.3. Singular-value decomposition 65

4.2. A conceptual introduction of Bayesian probability theory 66

4.2.1. Inverse problems in the Bayesian approach 67

4.2.2. Bayes' theorem 67

4.2.3. Marginalization 70

4.2.4. An example of Bayesian Gaussian process regression 71

4.3. Gaussian Process Tomography (GPT) 73

4.3.1. Bayesian Formalization 74

4.3.2. Bayesian Ockham's Razor 77

4.3.3. Phantom test with WEST SXR radiation field reconstruction case 78

4.3.4. Real-time calculation 82

4.3.5. GPT reconstruction uncertainty and Line-of-sight distribution 84

4.4. Incorporating magnetic equilibrium information in GPT 85

4.4.1. Length scale following magnetic flux surfaces 85

4.4.2. Equi-GPT on WEST 86

4.5. Benchmark with GPT and MFI on WEST synthetic data 88

Chapter 5 Implementation of Equi-GPT on experimental data 91

5.1. Equi-GPT for bolometer in HL-2A H-mode plasmas 91

5.1.1 ELM-induced divertor strike point shifting 93

5.1.2. Deformation of local magnetic flux surfaces with evidence from bolometer tomography 94

5.2. Equi-GPT on EAST 96

5.2.1. Observation of a sawtooth triggered kink mode by using SXR tomography 97

5.2.2. Observation of low frequency oscillations using AXUV bolometer tomography during I-mode on EAST 101

Chapter 6 Reconstruction of tungsten concentration profiles 106

6.1. Effect of transport on tungsten impurity radiation 107

6.2. Direct tungsten density calculation from SXR tomographic reconstructions 109

6.3. Bayesian inference of tungsten density profiles 111

6.3.1 Influence of transport neglected 111

6.3.2. With the consideration of transport 116

6.4. Conclusion 120

Chapter 7 Conclusion 121
Appendix A: Learn deeper 123
Bibliography 133

Chapter 1 Introduction

1.1. Energetic challenges and nuclear fusion

1.1.1 Energy consumption, resources and environmental constraints

Energy is the cornerstone of human civilization, energy keeps us warm during the winter, sends us wind during the summer; energy gives us a message from the other side of the world, brings us to the moon… Energy is about everything.

Energy access is the 'golden thread' that weaves together economic growth, human development and environmental sustainability. Energy has long been recognized as essential for humanity to develop and thrive, but the adoption in 2015 by 193 countries of a goal to ensure access to affordable, reliable, sustainable and modern energy for all by 2030, as part of the new United Nations Sustainable Development Goals (SDGs), marked a new level of political recognition. Energy is also at the heart of many of the other SDGs, including those related to gender equality, poverty reduction, improvements in health and climate change. [WEO 2017]

Concern about a dependable future for energy is only natural, since energy provides 'essential services' for human life - heat for warmth, cooking, and manufacturing, or power for transport and mechanical work. At present, the energy to provide these services comes from fuels - oil, gas, coal, nuclear, wood, and other primary sources (solar, wind, or water power) - that are all useless until they are converted into the energy services needed, by machines or other kinds of end-use equipment, such as stoves, turbines, or motors. In many countries worldwide, a lot of primary energy is wasted because of inefficient design or operation of the equipment used to convert it into the services required. However, there is an encouraging growth in awareness of energy conservation and efficiency.

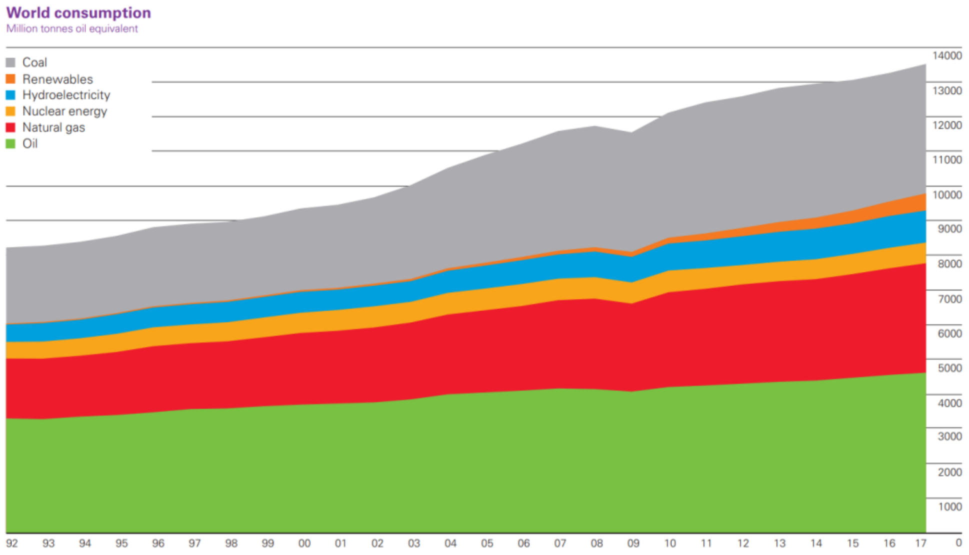

Figure 1.1. World primary energy consumption from 1991 to 2017 in million tons oil equivalent (Mtoe). Source: [BP 2018].

The global energy consumption and needs have increased dramatically in the last century with a characteristic doubling time of about 30 - 40 years. According to the BP Statistical Review of World Energy [BP 2018] primary energy consumption growth averaged to 2.2% in 2017, while consumption of the three primary fossil fuels (oil, coal, natural gas) increased continuously, with a slight slowdown thanks to renewable energy development. The extent to which the current mix of resources used for energy provision is going to change in the 21st century will depend on progress in the development of alternative energy sources.

To give an indicative estimate of how long we still could feasibly consume fossil fuels, we have plotted the reserves-to-production (R/P) ratio for coal, oil and gas in **Figure. 1.2**. The R/P ratio divides the quantity of known fuel reserves by the current rate of production, to estimate how long we could continue if this level of production remained constant. Based on BP's Statistical Review of World Energy 2018, we would have about 134 years of coal production, and roughly 50 years of both oil and natural gas remaining.

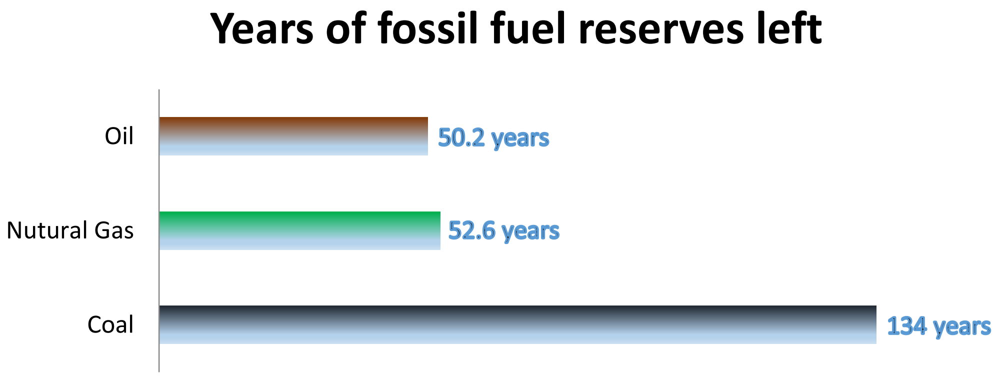

Figure 1.2. Years of fossil fuel reserves left, reported as reserves-to-product ratio, which measures the number of years of production left based on known reserves and production levels in 2017. Data Source: [BP 2018].

However, while depleting reserves could become a pressing issue 50-100 years from now, there is another important limit to fossil fuel production: climate change. Carbon dioxide emissions remain trapped in the atmosphere for long periods of time, building up an atmospheric stock that leads to temperatures rise. Key risks of eventual temperature rise have been reported by the Fifth Assessment Report of the Intergovernmental Panel on Climate Change (IPCC), as follows:

1. Risk of severe ill-health and disrupted livelihoods resulting from storm surges, sea level rise and coastal flooding; inland flooding in some urban regions; and periods of extreme heat.
2. Systemic risks due to extreme weather events leading to breakdown of infrastructure networks and critical services.
3. Risk of food and water insecurity and loss of rural livelihoods and income, particularly for poorer populations.
4. Risk of loss of ecosystems, biodiversity and ecosystem goods, functions and services.

To keep average global temperature increase below two degrees Celsius (as has been agreed in the UN Paris Agreement), we can thus calculate the cumulative amount of carbon dioxide we can emit while maintaining a probability of remaining below this target temperature. This is what we define as a 'carbon budget'. In the latest Intergovernmental Panel on Climate Change (IPCC) report, the budget for having a 50 percent chance of keeping average warming below two degrees Celsius was estimated to be approximately 275 billion tons of carbon (as shown in the chart in Figure. 1.3). Note that with each year that passes, the remaining carbon budget continues to decline—by the end of 2017, this figure will have further decreased from the IPCC's estimates.

The crucial factor is then the following: if the world burned all of its currently known reserves (without the use of carbon capture and storage technology), we would emit a total of nearly 764 billion tons of carbon. This means that we have to leave between 65-80 percent of current known fossil fuels reserves untouched in the ground if we want to meet our global climate targets.

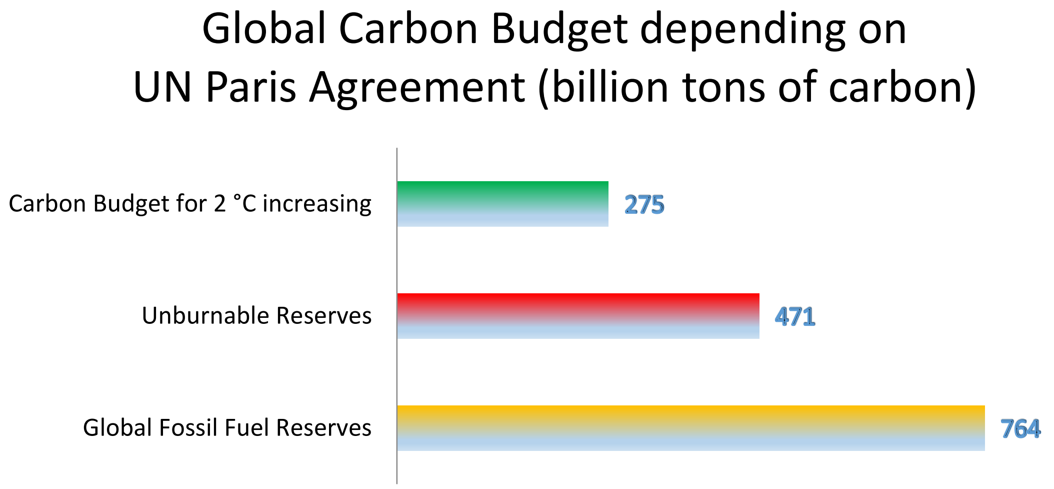

Figure 1.3. The Carbon budget and the amount of carbon that will be released depending on present fossil fuel reserves.

The various arguments mentioned until now point toward a new low-carbon future, by reducing CO_2 emission and by developing alternative energy sources. Indeed, renewable energies (including hydroelectricity, solar power, wind power and biomass) are great candidates that will, by definition, remain available on the long term, and do not (or negligibly) contribute to global warming. However, they do come with their own drawbacks.

The hydroelectricity has been explored to a large extent already. In fact, most of the potential hydropower has already been installed in Europe and North America. Additional contribution for future energy demand is limited with respect to the world energy needs.

Wind and solar power are presently not sufficiently mature for large-scale and stable energy production. A fundamental issue is that their production peaks usually do not coincide with demand peaks and depend on weather patterns. Moreover, expenses for constructing wind and solar farms, as well as reliable energy storage and transport, are considerable. Finally, centralized production and transport of solar and wind energy in suitable regions might create vulnerabilities to geopolitical instabilities.

Biomass energy is a very good candidate, which has greenhouse gas production much more favorable than fossil fuels (growing bio-crops for fuel is a carbon absorption process). However, on the other hand, biomass energy requires at industrial level a large land use, possibly conflicting with food production. This drawback strongly constrains its economic future.

In summary, the current renewable energy mix may not be a fully suitable alternative to fossil fuels. Rather, it would complement existing energy sources.

Table 1.1 Investments needed to produce 1 GW of electricity for several types of renewable energies [Ongena 2001]. Surfaces can be compared to the total surface of Belgium: 32 545 km^2.

Method	**Required surface**
Photovoltaic	About 100 km^2 in Middle Europe (10% efficiency assumed)
Wind power	6660 mills of 150 kW (20 rotor blades and for the average wind speed at the North Sea coast)
Biogas	60 million pigs or 800 million chickens
Bio-alcohol	6200 km^2 of sugar beet, or 7400 km^2 of potatoes, or 16 100 km^2 of corn, or 27 200 km^2 of wheat
Bio-oil	24 000 km^2 of rapeseed
Biomass	30 000 km^2 of wood

Next to traditional renewable energy sources, there are still other candidates to fossil fuels, i.e. nuclear energy. Since December 2, 1942, precisely at 3:25 p.m., a world first nuclear energy pile has been turned on by a scientific group led by Enrico Fermi, the Nobel Prize winner. Starting from this point, humankind obtained a new power source and entered a new energy age.

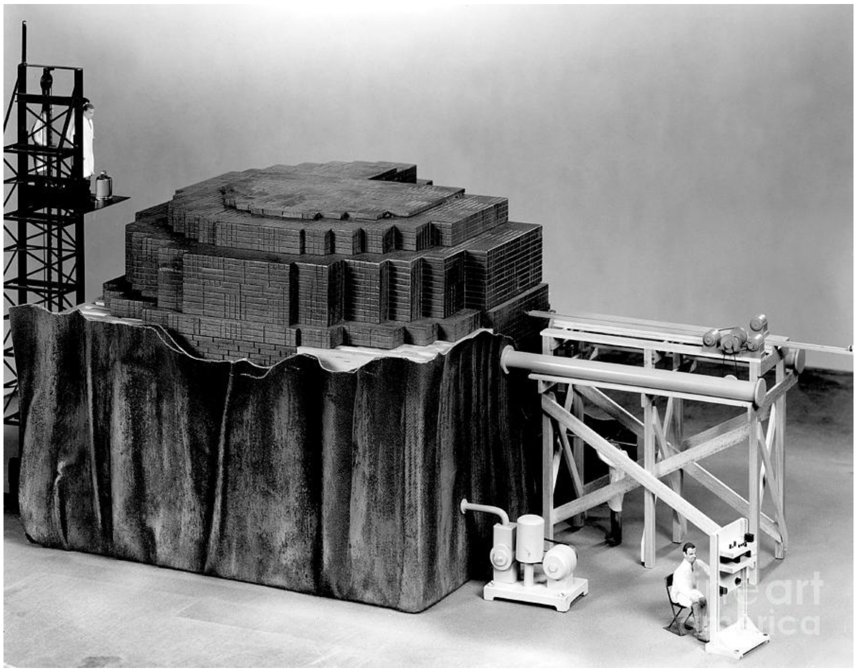
fineart america

Figure 1.4. The world first nuclear pile built in Chicago, US.

[Photo of Chicago Pile -1 scale model from fineartamerica.com]

Nuclear energy employs the binding energy of atomic nuclei to generate heat during exothermic nuclear reaction processes. This heat can then be converted into electricity by heating water to steam and activating turbines. There are two ways to achieve the nuclear reaction and release the energy: fusion and fission. The nuclear fission reaction is a process wherein an atom is split into smaller atoms, accompanied by the release of energy; the nuclear fusion occurs when two light nuclei collide at sufficiently high energy required to overcome the repulsive Coulomb forces and become subject to the strong interaction forces at short distances (10^{-15} m). The resulting nuclei have a lower total mass than the sum of the original nuclei and the mass deficit Δm is converted into energy through $E = \Delta mc^2$.

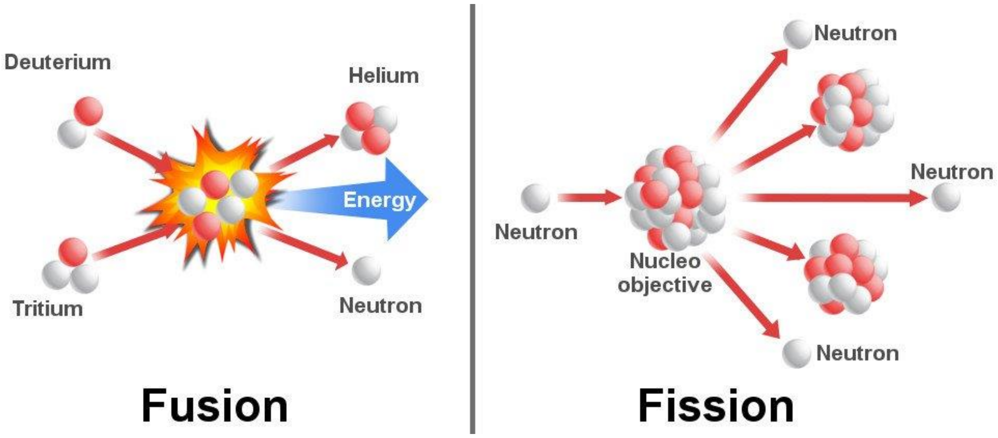
Deuterium
Helium
Energy
Tritium
Neutron
Fusion
Neutron
Neutron
Neutron
Nucleo objective
Neutron
Fission

Figure 1.5. Left: the nuclear fusion reaction between deuterium and tritirum. Right: the principle of a nuclear fission reaction.

Nuclear fission, which is widely adopted as the basic technology of current nuclear power plants, has many advantages: the fuel has a very high energy density and no greenhouse gas is produced from the fission reaction. The production of electricity is manageable, non-intermittent, and can be centralized. Furthermore, with the potential of fuel breeding technology, the uranium reserves could sustain up to 2500 years with the present consumption rate. We can imagine that if the fuel breeding technology succeeds and nuclear fission energy became a principle energy source, e.g. from 5% nowadays to 50% in the future, the uranium reserves could still satisfy the global energy need for 200 years.

However, this is not the end of our story, as the drawbacks of nuclear fission energy are as obvious as its advantages. Among the constraints that fission nuclear must deal with, the fission reaction produces radioactive wastes that require long-term storage solutions and adequate risk management. The reactor has to be designed in order to control the chain reaction process with many safety procedures to prevent the risks of leakage or loss-of-coolant accident. In recent years, especially after the 2011 Fukushima Daiichi disaster, nuclear fission development has reached a difficult period, and increasingly more countries are considering to reduce or eliminate the nuclear fission energy from their primary energy mix.

The second option offered by nuclear energy is nuclear fusion. It is the least developed of the current energy sources but it holds the promise of being a safe, inexhaustible and clean energy production method. As such, it could become the best compromise between nature and the energy needs of mankind. We will come back to this point in the next section.

1.1.2 Magnetic confinement fusion (MCF) and inertial confinement fusion (ICF)

Bring the power of the sun to earth.

Nuclear fusion is the energy source that powers the stars and the sun. Nuclear fusion reactions do not produce greenhouse gases, nor long-term radioactive waste products. There are several types of fusion reactions, e.g. D-T reaction, D-D reaction, D-^{3}He reaction etc. The most accessible way to achieve fusion on earth is the D-T reaction, a reaction between the isotopes of hydrogen, which has the highest reaction cross-section at a lower energy level.

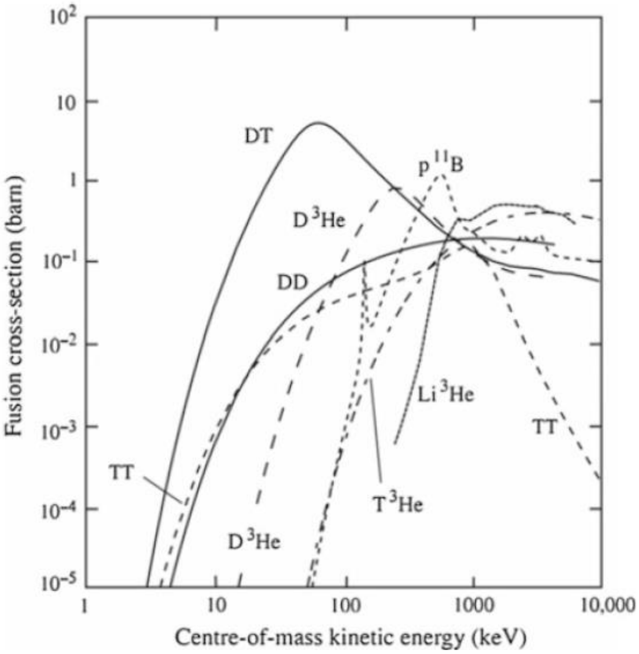

Figure 1.6. The cross-section for different nuclear fusion reactions.

From **Figure. 1.6**, we can clearly see that the D-T reaction cross-section peak is reached around a center-of-mass kinetic energy of 100 keV, corresponding to a temperature of about one billion Kelvin, where 1 eV corresponds to 11600 K. Fortunately, due to the presence of a significant fraction of particles in the Maxwellian tail of the velocity distribution and quantum tunneling effects, the resulting temperature at which D-T reaction can be achieved is about 10keV. At such high temperatures, the reactants are fully ionized and form a plasma state. Plasma is one of the four states of matter, constituting most of the visible matter in the universe, including Aurora Borealis and fluorescent lights on earth.

The D-T fusion reaction can be described as:

$$^{2}_{1}D + ^{3}_{1}T \rightarrow ^{4}_{2}He\ (3.5\ MeV) + ^{1}_{0}n\ (14.1\ MeV)$$

The energy released in the reaction is distributed between the kinetic energy of the α-particle $^{4}_{2}He$ (3.5MeV) and the neutron $^{1}_{0}n$ (14.1MeV). The most obvious advantage of fusion is the virtual inexhaustibility of the fuels, which are cheap and widely accessible. The deuterium reserves in sea water can be extracted in large quantities at low price. At present production levels, natural deuterium reserves would be sufficient for billions of years of electricity production. Tritium is a short-lived radioactive isotope of hydrogen, the half-life time of tritium is 12.3 years. It can be produced via the reaction of lithium and neutrons as:

$$ {}^{6}_{3}Li + {}^{1}_{0}n \rightarrow {}^{3}_{1}T\ (2.75\ MeV) + {}^{4}_{2}He\ (2.05\ MeV) $$

$$ {}^{7}_{3}Li + {}^{1}_{0}n \rightarrow {}^{3}_{1}T\ + {}^{4}_{2}He + {}^{1}_{0}n - 2.47\ MeV $$

The amount of lithium reserves in seawater could satisfy the energy needs for 60 million years.

The strategy of nuclear fusion power production seems clear now. This energy source is a very promising candidate which does not release any greenhouse gas and long-term radioactive waste products. At the same time, the fusion fuels in earth are available in large quantities, which could be considered as infinity on the human civilization time scale. On the other hand, fusion reactions only occur under a critical condition: the temperature needs to achieve levels of 10 keV (10^8K), which is one hundred times higher than the temperature at the sun's center. A question comes to our mind: how should we contain this plasma which is 100 times hotter than the sun?

As is well known, no solid material can withstand the level of temperature we have mentioned above. Thus, a method of confinement is needed to prevent the plasma from losing too much of its energy, degrading its performances or damaging its containment chamber. With these concerns, two confinement methods have been proposed.

- Inertial confinement fusion (ICF): in this method, a D-T solid target can be inertially confined using tens of pulsed lasers which compress the target in a few nanoseconds, at densities high enough for fusion reactions to happen. This method is mainly used today to study the physics of nuclear weapons but is also studied for civil applications. The two main ICF research centers in the world are the National Ignition Facility (NIF) in USA, and the Laser MégaJoule in France.
- Magnetic confinement fusion (MCF): since plasma particles are electrically charged, they are sensitive to electromagnetic fields and can be confined by strong magnetic fields. The main candidates for MCF today are tokamaks. Major experiments include the Joint European Torus (JET) in Oxfordshire (UK), WEST (upgraded from Tore Supra) in Cadarache (France), ASDEX-Upgrade (AUG) in Garching (Germany), TCV in Lausanne (Switzerland), DIII-D in San Diego, CA (USA), JT-60SA in Naka (Japan), EAST and HL-2A in China, and ITER, presently under construction in Cadarache (France). Another good candidate MCF concept is the stellarator, like W7-X in Greifswald (Germany). Other magnetic configurations like magnetic mirrors, Z-pinch, etc. have also been investigated but currently do not enjoy the same favorable prospects for fusion energy production. The tokamak and stellarator concepts are discussed in more detail below.

1.2. MCF concepts

In this thesis, we focus on the tokamak as one of the most advanced magnetic confinement concepts, but we also discuss the stellarator. Both of them utilize the electromagnetic properties of charged plasma particles to trap them and keep them away from material walls in a specifically designed magnetic field configuration.

1.2.1 Tokamaks

In a tokamak, the plasma is formed in the shape of a torus or a doughnut, through a specially designed magnetic field configuration. Such a configuration can be formed by arranging a set of field coils in the form of a torus, thus forming a toroidal magnetic field. However, a purely toroidal magnetic field cannot confine the plasma particles, as the curvature of the field lines produces opposite particle drifts for the ions and the electrons, leading to charge separation. Hence, a poloidal magnetic field is added by passing a toroidal current through the plasma itself. The resultants of the toroidal and poloidal magnetic field lines spiral around the torus along nested toroidal surfaces, forming globally closed magnetic flux surfaces. The combination of the toroidal and poloidal magnetic fields leads to the concept of toroidal magnetic bottles in which one can confine the hot plasma away from material walls in a stable way for long durations.

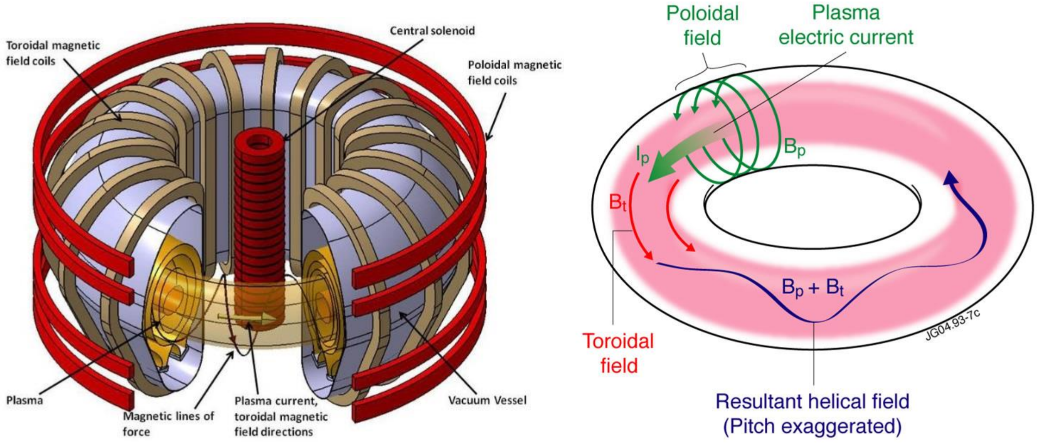
Toroidal magnetic field coils
Central solenoid
Poloidal magnetic field coils
Plasma
Magnetic lines of force
Plasma current, toroidal magnetic field directions
Vacuum Vessel
Poloidal field
Plasma electric current
I_p
B_p
B_t
$B_p + B_t$
JG04.93-7c
Toroidal field
Resultant helical field (Pitch exaggerated)

Figure 1.7. Left: schematic of a tokamak. Right: combination of the toroidal and poloidal magnetic fields to form a helical field along the torus. [Kikuchi 2012]

1.2.2 Stellarator

In stellarators, the poloidal magnetic field is produced by careful profiling of the magnetic field topology. Complex, non-axisymmetric (helical) and closed toroidal magnetic surfaces are formed in three dimensions by fields entirely produced by externally wound coils. Thus, there is no need to drive plasma current in stellarators, eliminating the issue of disruptive instabilities occurring in tokamaks, rendering them very attractive for reactor concepts. The stellarator is capable of steady-state operation, in contrast to the inherently pulsed nature of a tokamak. However, the 3D nature of the stellarator inevitably increases the complexity of its design and analysis of the measurements, leading to higher cost and more demanding engineering. Moreover, the stellarator currently exhibits poorer particle confinement properties than the tokamak, due to large deviations of particle orbits from the 3D flux surfaces. In addition, the level of neoclassical transport of the plasma and alpha particles is relatively high, while knowledge of turbulent heat and particle transport in stellarators is still relatively limited.

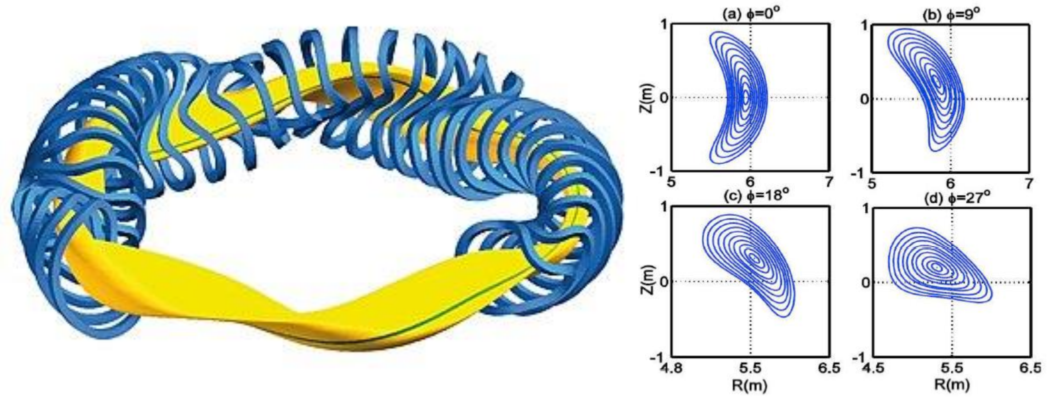

Figure 1.8. Left: schematic of the magnetic coils and the 3D plasma shape in the stellarator W7-X. Right: poloidal cross-section of typical magnetic flux surfaces at different toroidal angles in a stellarator[Li 2014].

1.2.3 Roadmap of MCF power plants in Europe

Since the definition of the Fast Track approach to fusion energy in 2001, the European fusion roadmap has been based on three elements:

- The ITER project as the 'essential step towards energy production in a fast track';
- A single step (DEMO) between ITER and commercial fusion power plants designed 'as a credible prototype for a power-producing fusion reactor, although in itself not fully technically or economically optimized';
- The International Fusion Materials Irradiation Facility (IFMIF), for material qualification under intense neutron irradiation, in parallel with ITER.

The roadmap addresses three separate periods with distinct main objectives.

- Horizon 2020 (2014-2020) with five overarching objectives:
  - Construct ITER within scope, schedule and cost;
  - Secure the success of future ITER operation;
  - Prepare the ITER generation of scientists, engineers and operators;
  - Lay the foundation of the fusion power plant;
  - Promote innovation and EU industry competitiveness.
- Second period (2021-2030):
  - Exploit ITER up to its maximum performance and prepare DEMO construction.
- Third period (2031-2050):
  - Complete ITER exploitation; construct and operate DEMO.

Horizon 2020 milestones and resources have been defined in detail, while a global evaluation is given for the second period and the third period is only outlined.

1.3. Purpose of this thesis

Aiming at the development of a sustainable and safe energy source, nuclear fusion research is presently largely concentrated around the construction and operation of the international fusion device ITER. To achieve this goal, investigation efforts are put on the baseline of fusion confinement problems, one of the primary issues threatening safe and efficient operation of tokamaks like ITER, is the accumulation of so-called impurities in the plasma core, causing unmanageable radiative power loss and plasma performance loss. The interaction of the hot hydrogenic plasma with the wall components is the most important source of impurity. Especially in ITER, tungsten (W) has been selected as divertor material due to its low tritium retention and ability to handle large heat flux load. But tungsten may also pose an important risk, the highly charged impurities like tungsten can radiate energy violently which strongly increase the radiative power loss. In reactor-relevant plasmas, thermonuclear burn will be possible only if tungsten concentrations remain below 10^{-4}. Reliable tools are thus required to monitor the local impurity density, study tungsten transport in the plasma core and identify actuators to avoid W central accumulation.

Soft X-ray (SXR) spectroscopy which is a promising diagnostic can be operated in high temporal resolution (sampling rate up to MHz) and has a high spatial resolution (in order of centimeter). This opens up the very attractive possibility of localized real-time control of impurity concentrations, provided efficient actuators for the spatial impurity distribution can be established. However, the data analysis on this direction is challenging because the local two-dimensional SXR emissivity field in a poloidal cross-section has to be reconstructed from line-integrated measurements by tomographic methods. This is an ill-posed inverse problem, while the high spatial resolution demanding has to always meet the limited measurement access. Thus, there exists a variety of possible reconstructions can give the same measurement. In addition, from the emissivity point of view, the measurement is a superposition which composes all the emissivity from various impurities and ionization stages. The decomposition to distinguish each emissivity contributions from different species, propose considerable difficulties to deal with.

The main purpose of this Phd is composed with two main trajectories:

- To investigate a real-time (refers to the transport time scale $\sim 10\mathrm{ms}$ on WEST) tomography algorithm for the new developed SXR system on WEST in order to provide sufficient access of the MHD and impurity real-time control.
- To develop the most threatening high-Z impurity, tungsten, local distribution monitoring method.

Chapter 2 Tokamak Physics

In this chapter, some basic background regarding the physics of tokamak plasmas is introduced.

As mentioned in previous introduction chapter, a tokamak is a magnetic confinement device in which the poloidal component of the magnetic field is generated mainly by toroidal currents flowing in the plasma (see Figure 1.7). The word tokamak is a Russian acronym for ***to**roidalnaya **ka**mera and **ma**gnitnaya **k**atushka*, meaning 'toroidal chamber and magnetic coil'. The relative simplicity of the tokamak design has led to an initial headway of this design with respect to other prospective designs for a fusion reactor, and the top performance among current fusion experiments has been achieved in tokamaks. As shown in Figure 1.7, the vacuum magnetic field is the toroidal field B_t, generated by a set of toroidal field (TF) coils. Due to the guiding center motion [Kikuchi 2012] of the charged particles in a magnetic field, the plasma particles gyrate around the field lines, and are thus confined in the direction perpendicular to the magnetic field. However, if there were only a toroidal field component, plasma particles would drift toward the vertical direction, preventing confinement, as shown in Figure 2.1.

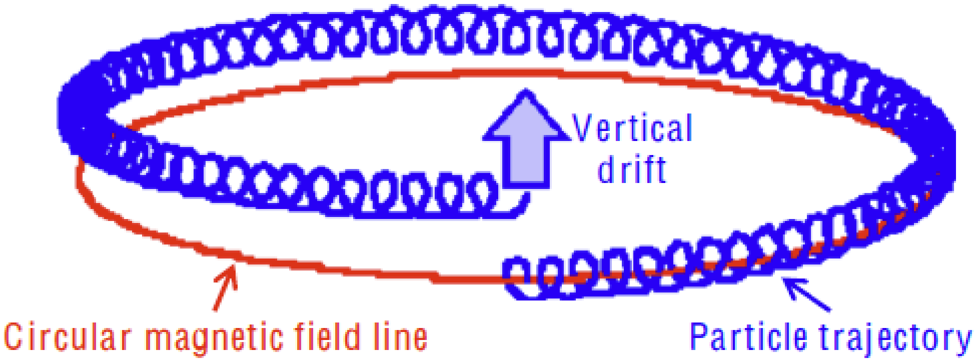

Figure 2.1. Illustration of the vertical drift underwent by charged particles confined by a purely toroidal magnetic geometry. Photo from CEA website.

Therefore, a poloidal magnetic field component B_p is added to the total magnetic field. This component is created by generating an electrical current in plasma (of the order of hundreds kA to MA). The sum of the toroidal magnetic field, and the in comparison small poloidal component, is a helical magnetic field. The plasma current is generated inductively by a central solenoid (CS) coil, which is also sketched in Figure 1.7. In the presence of plasma, an outward force will work on the plasma, similar to that tending to expand the diameter of a rubber tube filled with air. These expanding "hoop" forces can be balanced by the Lorentz force between the toroidal plasma current and an applied field in the vertical direction. The poloidal field (PF) coils set produce this field, and additionally shapes the cross-section of the plasma in the poloidal plane.

2.1. MHD equilibrium and major instabilities

Magnetohydrodynamic (MHD) theory describes the interactions between plasma and electromagnetic fields from a fluid point of view. MHD theory is able to describe many plasma phenomena relevant to magnetic confinement fusion. Ideal MHD is the most basic plasma model, described by the following set of equations:

$$\frac{d\rho}{dt} = -\rho \nabla \cdot \bar{v} \qquad (2.1)$$

$$\rho\left(\frac{d\bar{v}}{dt}\right) = \bar{j} \times \bar{B} - \nabla p \qquad (2.2)$$

$$\frac{dp}{dt} = -\gamma\, p \nabla \cdot \bar{v} \qquad (2.3)$$

$$\bar{E} + \bar{v} \times \bar{B} = 0 \qquad (2.4)$$

$$\nabla \times \bar{E} = -\frac{\partial \bar{B}}{\partial t} \qquad (2.5)$$

$$\nabla \times \bar{B} = \mu\mu_0\, \bar{j} \qquad (2.6)$$

$$\nabla \cdot \bar{B} = 0 \qquad (2.7)$$

Where $d\ \cdot/dt = \partial\ \cdot/\partial t + \bar{v} \cdot\ \nabla$;

$\gamma, \rho, p, \bar{v}$ are the adiabatic index, fluid mass density, pressure and velocity;

$\bar{j}, \bar{E}, \bar{B}$ are the electric current density, electric field and magnetic field strength, respectively.

In plasma physics it is customary to describe all magnetization effects explicitly in terms of the associated currents, therefore μ will always be assumed to be 1. Linearizing the above equations around a homogenous, static equilibrium, one finds that it contains two characteristic wave speeds, Alfven speed v_A and normal sound speed of unmagnified gas c_s:

$$v_A = \sqrt{\frac{B^2}{\mu_0 \rho}} \qquad (2.8)$$

$$c_s = \sqrt{\frac{\gamma p}{\rho}} \qquad (2.9)$$

If our experiment is of a characteristic dimension L_0, which we can identify, for example with either the circumference of the plasma torus in toroidal direction ($2\pi R_0$) or poloidal direction ($2\pi a$), these velocities define characteristic MHD timescales:

$$\tau_A = \frac{L_0}{v_A} \qquad (2.10)$$

$$\tau_s = \frac{L_0}{c_s} \qquad (2.11)$$

Any state persisting significantly longer than these timescales has to satisfy the stationary equilibrium condition:

$$\rho \bar{v} \cdot \nabla \bar{v} = \bar{j} \times \bar{B} - \nabla p \qquad (2.12)$$

Typically, the steady state flow velocities in tokamaks have a Mach number $|\bar{v}|/c_s \ll 1$, so that inertial forces (Coriolis and centrifugal forces) can be neglected compared to pressure forces. Then on the MHD timescales, the following force balance can be assumed:

$$\bar{j} \times \bar{B} = \nabla p \qquad (2.13)$$

During a plasma campaign discharge, the plasma parameters change in time, for example due to changes in externally applied heating power or loop voltage. The plasma profiles adjust to these imposed variations on diffusive timescales, defined by the transport of energy or diffusion of magnetic fields across the plasma column. These timescales — the “energy confinement time” and the “current diffusion time” — are much longer than MHD timescales τ_A and τ_s. As a consequence, during these slow variation, the plasma can be assumed to pass through sequences of static MHD equilibrium states.

2.1.1 Magnetic flux surfaces

In a tokamak the plasma is confined into a torus shape, thus the ideal tokamak equilibrium is described by axisymmetric solutions of the equations set: Eq. (2.6), Eq. (2.7), Eq. (2.13). Usually, it is convenient to split the vector fields of current density and magnetic field into poloidal and toroidal parts: $\bar{j} = \bar{j}_{pol} + \bar{j}_{tor}$, $\bar{B} = \bar{B}_{pol} + \bar{B}_{tor}$, and to express the poloidal components in a poloidal current flux function $F(R, z)$ and a poloidal magnetic flux function $\psi(R, z)$:

$$\bar{j}_{pol} = \frac{1}{2\pi R} \vec{e}_\phi \times \nabla F \qquad (2.14)$$

$$\bar{B}_{pol} = -\frac{1}{2\pi R} \vec{e}_\phi \times \nabla \psi \qquad (2.15)$$

The radian unit $\frac{1}{2\pi}$ is sometimes ignored in these definitions. In addition,

$$F = \int \bar{j}_{pol} \, d\,\bar{S} \qquad (2.16)$$

$$\psi = -\int \bar{B}_{pol} \, d\,\bar{S} \qquad (2.17)$$

The cylindrical coordinate system often used in tokamaks has been illustrated in **Figure 2.2**.

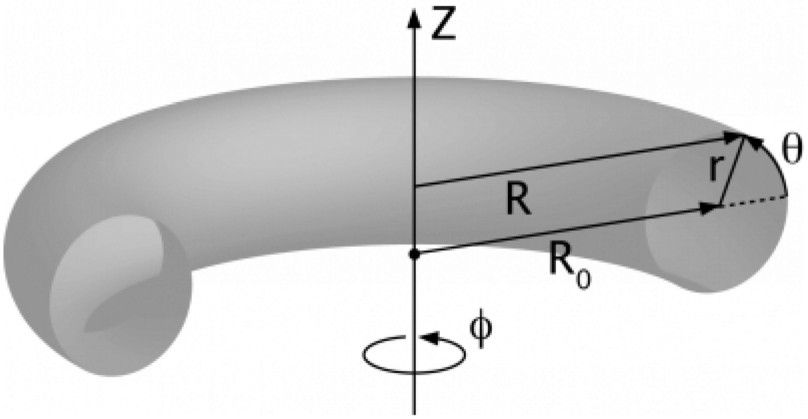

Figure 2.2. Illustration of coordinate system used in tokamaks: cylindrical (R, ϕ, z) – coordinates. [Kikuchi 2012]

Eq. (2.14) implies through Ampere's law:

$$\overline{B}_{pol} = -\mu_0 \frac{F}{R} \cdot \vec{e}_{\phi} \qquad (2.17)$$

Eq. (2.15) ensures that $\overline{B}_{pol} = 0$ when $\nabla \psi = 0$, and the magnetic field lines stay on surfaces $\psi(R, z) =$ constant. In addition, from Eq. (2.13), it follows:

$$\overline{B} \cdot \nabla p = 0 \qquad (2.18)$$

and shows that plasma pressure has to be constant along magnetic field lines. Hence we can write the pressure as a function $p(\psi)$.

From axisymmetry, and by taking inner product of Eq. (2.13) with $\vec{e}_{\phi}$, it follows that:

$$\overline{j}_{pol} \times \overline{B}_{pol} = 0 = \nabla F \times \nabla \psi \qquad (2.19)$$

Therefore, the poloidal current flux function F can be also written as $F(\psi)$, where the poloidal currents will not cross flux surfaces $\psi(R, z) =$ constant.

The inner product of Eq. (2.15) with $\nabla \psi$ yields the non-trivial part of the force balance, and inserting it into the toroidal component of Ampere's Law, gives finally the famous Grad-Shafranov equation as:

$$\frac{\partial^2 \psi}{\partial R^2} - \frac{1}{R}\frac{\partial \psi}{\partial R} + \frac{\partial^2 \psi}{\partial z^2} = -\mu_0 R \overline{j}_{\phi} = -\mu_0 R\, p'(\psi) - \frac{{\mu_0}^2}{2}(F(\psi)^2)' \qquad (2.20)$$

The Grad-Shafranov equation, which has been independently derived in the 1960s by several authors, determines the relation between plasma pressure p, poloidal magnetic flux ψ and toroidal current density

$\bar{j}_\phi$ in the ideal MHD situation. In particular, since the transport across the magnetic field is much slower than the transport along the field, the plasma properties (i.e. electron temperature T_e, electron density n_e, ion temperature T_i, ion density n_i, etc) can as a good approximation be taken as constant on a flux surface. Hence, the equilibrium magnetic flux surface position becomes a very piece of important information for further plasma physics analysis.

Typically, the flux surfaces are labeled by integers m and n, or by safety factor q, defined as:

$$q = \frac{\mathrm{d}\Psi_t}{\mathrm{d}\Psi_p} = \frac{r \cdot B_t}{R \cdot B_p} = \frac{m}{n} \qquad (2.21)$$

The number n corresponds to the number of toroidal rotations necessary for one poloidal rotation on a magnetic flux surface. Because the field pitch varies across different flux surfaces, q is often expressed as a function of the minor radius, $q(r)$.

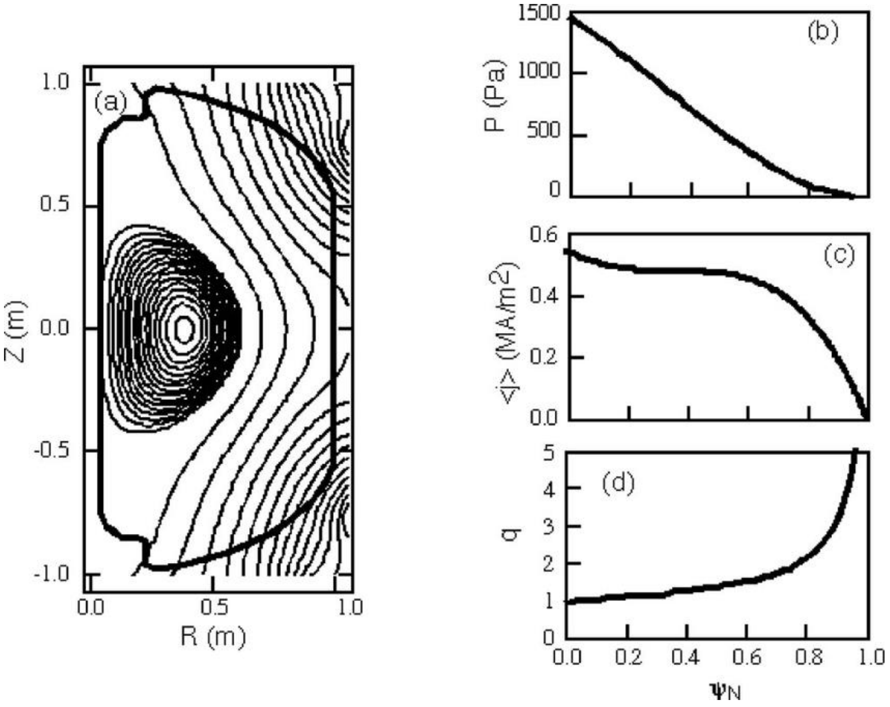

Figure 2.3. (a) Example of a set of equilibrium magnetic flux surfaces (poloidal cross-section) and profile plots of (b) plasma pressure p, (c) surface-averaged current density j and (d) safety factor q. Figure source: [Garstka 2003].

Solving the Grad-Shafranov equation is a non-linear free-boundary problem. Numerical solutions are usually obtained through magnetic equilibrium codes, such as EFIT [Lao 1985] or EQUINOX [Mazon 2012a]. In addition, there is a specific horizontal displacement $\Delta(r)$ between plasma magnetic flux surfaces and vacuum magnetic flux surfaces. In the large aspect ratio approach applied in a circular poloidal cross-section:

$$\frac{\mathrm{d}\Delta(r)}{dr} = -\frac{a}{R}(\beta_p + \frac{l_i}{2}) \qquad (2.22)$$

Here, β_p and β_t are the poloidal, resp. toroidal beta, defined as:

$$\beta_p = \frac{4\mu_0 \int_0^a rpdr}{r^2 B_p^2(r)} \qquad (2.23)$$

$$\frac{1}{\beta} = \frac{1}{\beta_p} + \frac{1}{\beta_t} \qquad (2.24)$$

Here, β is the ratio of the plasma pressure to the magnetic pressure, often used as one of the performance measures for plasma confinement:

$$\beta = \frac{p}{B^2/4\mu_0} \qquad (2.31)$$

l_i is the internal induction parameter which quantifies the magnetic flux storage ability, and is defined as:

$$l_i = \frac{2\int_0^a rB_p^2 dr}{r^2 B_p^2(r)} \qquad (2.25)$$

With boundary conditions $\Delta(a) = 0$ and $\Delta'(0) = 0$, the upper equation can be solved as:

$$\Delta(r) = \frac{R_0}{2}\left(\varepsilon^2 - \frac{r^2}{{R_0}^2}\right)\left(\beta_p + \frac{l_i}{2}\right), \qquad (2.26)$$

With the inverse aspect ratio $\varepsilon = a/R_0$. The displacement of the magnetic axis with respect to the geometric center of the last-closed flux surface (LCFS), is called the Shafranov shift $\Delta_{sh} = \Delta(0)$ [Shafranov 1962]:

$$\Delta_{sh} = \Delta(0) = \frac{R_0\varepsilon^2}{2}(\beta_p + \frac{l_i}{2}) \qquad (2.27)$$

In particular, for the stellarator equilibrium plasma, the current $\bar{j}$ is governed by the force balance condition Eq. (2.13), and can be divided into two components following the parallel and perpendicular direction of magnetic field $\bar{B}$, as $\bar{j}_\parallel$ and $\bar{j}_\perp$. The $\bar{j}_\perp$ contributes to balance the outward pressure force, which from Ampere's law is seen to be given by

$$\bar{j}_\perp = \frac{\bar{B}}{B^2} \times \nabla p \qquad (2.28)$$

With Maxwell's equation $\nabla \cdot \bar{j} = 0$ applied, this gives:

$$\nabla \cdot \bar{j}_\parallel = -\nabla \cdot \bar{j}_\perp = -\nabla \cdot \left(\frac{\bar{B}}{B^2} \times \nabla p\right) = 2\,\nabla p \cdot \frac{\nabla B \times \bar{B}}{B^3} \qquad (2.29)$$

The parallel current density $\bar{j}_\parallel$ is named Pfirsch-Schlüter current [Pfirsch 1962], arising from the pressure gradient. The Pfirsch-Schlüter current $\bar{j}_\parallel$ has a vertical component which can lead to a horizontal displacement $\Delta(r)$ between plasma magnetic flux surfaces and vacuum magnetic flux surfaces. The Shafranov shift of a stellarator is approximately given by [Hirsch 2008]:

$$\Delta_{sh} \approx \frac{\beta R_{0_0}}{2\iota^2} \qquad (2.30)$$

Here, ι is the rotational transform (or field line pitch), where $\iota/2\pi$ is defined as the number of poloidal transits per toroidal transit of a field line on a toroidal flux surface. The maximum allowable displacement of the plasma center $\Delta_{max} = a/2$ limits the maximum achievable performance:

$$\beta_{0,max} \approx \frac{\iota^2 a}{R_0} \qquad (2.32)$$

2.1.2 Sawtooth mode, Kink modes, Neoclassical Tearing modes and mode analysis

MHD equilibrium cannot always hold, and as a consequence there is a variety of MHD instabilities which can affect plasma performance significantly. The plasma has an infinite number of degrees of freedom, hence it is not possible to list every instability in detail. In discussing plasma instabilities, we always start from a quasi-equilibrium situation with small perturbations, to see if this perturbation grows or is damped. A growing perturbation mode refers to an instable mode. In this section, we introduce several major instabilities which are very relevant to our topic.

Sawtooth mode

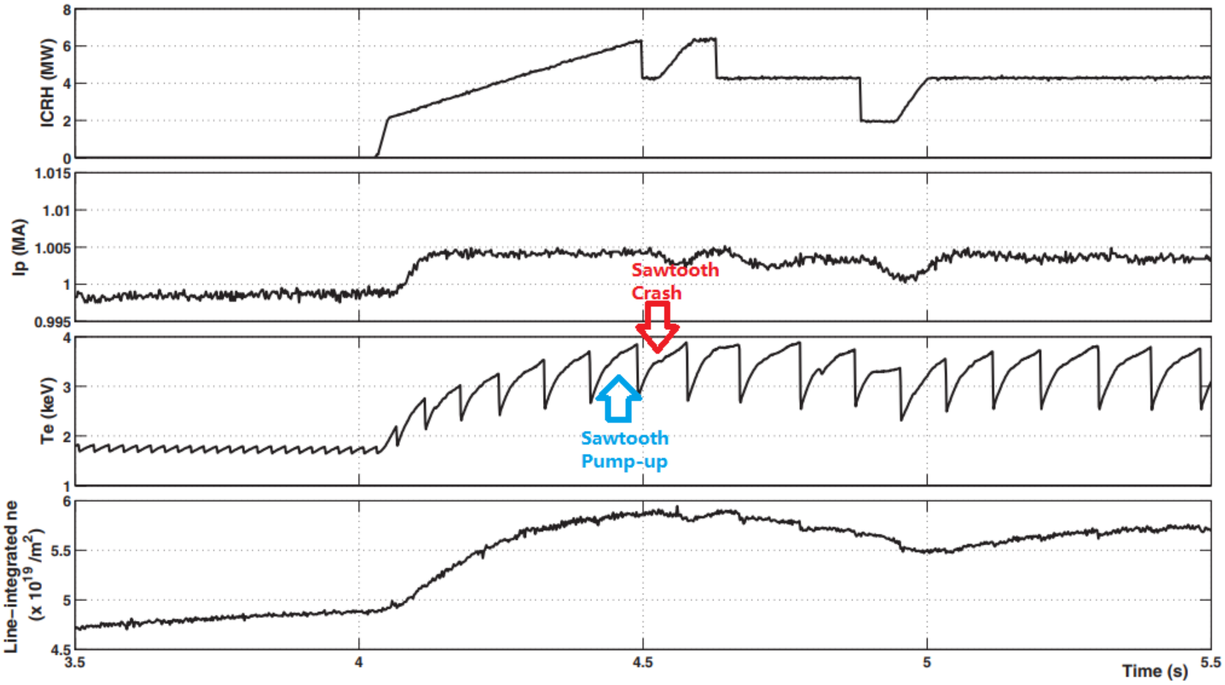

Figure 2.4 Time traces of the main parameters for Tore Supra pulse # 41830. Electron temperature is measured by a central line of sight of the Tore Supra electron cyclotron emission (ECE) diagnostic. The line-integrated electron density is taken from the central line of sight of the Tore Supra interferometry diagnostic. Figure source: [Mazon 2012b]

The sawtooth oscillation (also referred to by the term internal disruption) is one of the most observed phenomena in tokamak plasmas. It is a kind of periodic relaxation in the plasma core area. Sawteeth are named after the sawtooth-like time traces of electron temperature from the plasma core. Sawtooth oscillations are a quasi-periodic process, involving a slow temperature rise at the plasma center, then the build-up of the helical mode $m/n = 1/1$, followed by an abrupt drop in temperature within some region $r < r_s$. Outside this region, i.e. at $r > r_s$, the temperature momentarily increases . The radius r_s is called the inversion radius. The sawtooth oscillation mechanism has not been fully understood yet, but the first theoretical explanation has been provided by Kadomtsev in the frame of MHD analysis [Kadomtsev 1987].

Experimentally, sawtooth crashes are observed as spatial redistributions of electron temperature (T_e) and electron density (n_e). After the build-up phase, during which the T_e and n_e profiles becomes more and more peaked, a very sudden redistribution occurs and both profiles flatten as the electron population has been expulsed out of the core area (inside the inversion radius). The central value of T_e can decrease during the crash by 10% up to 50% compared to the value before the crash, while the value of n_e can decrease during the crash by 1-2%. In contrast to other common MHD instabilities, such as interchange modes, ballooning modes, internal or external kink modes, tearing modes etc., the sawtooth does not destroy the plasma confinement, with a lower corresponding risk to trigger a disruption. Furthermore, its amplitude and time period can be modified significantly by certain heating methods [Lauret 2012].

A magnetic field line reconnection model to explain the sawtooth mode has been suggested by [Kadomtsev 1987]. Let us assume that the safety factor at the plasma centre, $\mathrm{q}(0)$, is less than 1, so that the development of an internal helical mode or resistive tearing mode $m/n = 1/1$ is possible in the region where q < 1. With respect to such a perturbation, the transverse component of the magnetic field has different signs on either side of the radius $r = r_s$, where q = 1. Field line reconnection is then possible in the vicinity of $r = r_s$, as shown in **Figure 2.5**. We should emphasize that the radius r_s in this model is related to the position where $\mathrm{q}(r_s) = 1$. Assuming a parabolic initial current density profile near the magnetic axis, one can find the radius of the reconnection zone, at the X-point in **Figure 2.5**, from the flux conservation condition. The picture of a quiet, laminar, complete reconnection is naturally an over-simplified one. Firstly, the ejection of plasma from the X-point can be a source of strong perturbations in the plasma inside the island. MHD turbulence can be excited there. Moreover, the region near the separatrix can become stochastic because of toroidicity. As a result, the island at the position of the O-point (**Figure 2.5**) can be completely stochastized. The force pushing the central plasma column to the periphery then disappears, and the reconnection stops. Thus, field line reconnection is the most natural mechanism for sawtooth oscillations. The reconnection cannot occur when the newly born moon-like island becomes turbulent. Sawtooth oscillations play an important role in shaping the current profile in a tokamak.

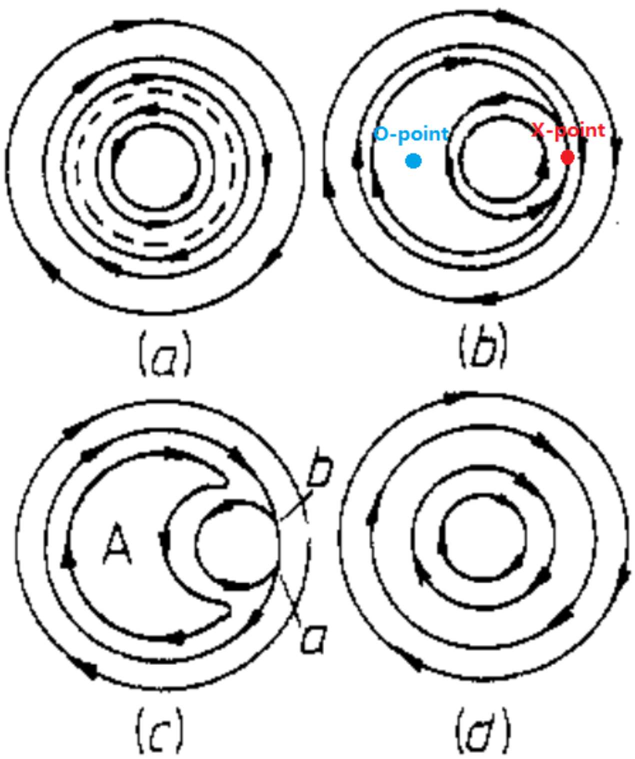

Figure 2.5. A demonstration of sawtooth instability development with magnetic reconnection model [Kadomtsev 1987].

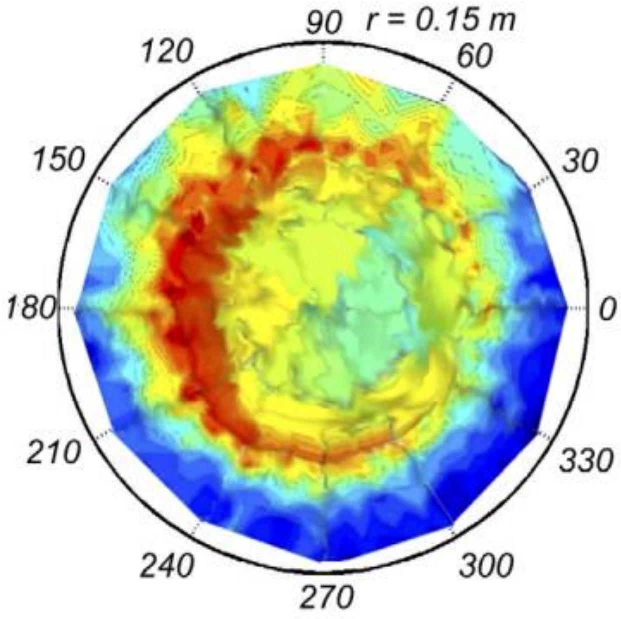

Figure 2.6. Poloidal reconstruction of T_e using the ECE-imaging system on TEXTOR during a sawtooth crash. The hot central plasma has been pushed out, leading to a banana-shaped island surrounding the cold central bubble. [Udintsev 2005]

Kink mode

The ideal MHD instability with potentially the strongest impact on plasma confinement is the kink mode. It is so named because it leads to a kinking movement of the magnetic surfaces and the plasma boundary. The driving force comes basically from the radial gradient of the toroidal current. For a circular, large-aspect ratio tokamak with low β, the potential energy of a perturbation having a radial displacement $\xi(r)e^{i(m\theta-n\varphi)}$ is:

$$\delta W=\frac{\pi^2 B_\varphi^2}{\mu_0 R_0}\left\{\int_0^a\left[\left(r\frac{d\xi}{dr}\right)^2+(m^2-1)\xi^2\right]\left(\frac{n}{m}-\frac{1}{q}\right)^2 r dr\right.$$
$$\left.+\left[\frac{2}{q_a}\left(\frac{n}{m}-\frac{1}{q_a}\right)+(1+m\lambda)(\frac{n}{m}-\frac{1}{q_a})^2\right]a^2\xi_a^2\right\} \qquad (2.33)$$

where

$$\lambda=\frac{(1+(\frac{a}{b})^{2m})}{(1-(\frac{a}{b})^{2m})} \qquad (2.34)$$

a is the minor radius of the plasma, b the radius of a perfectly conducting wall, q the safety factor, q_a the safety factor at position $r=a$ and ξ_a the radial displacement at position $r=a$.

If there is a conducting wall surrounding the plasma, and with boundary condition $\xi_a=0$, it is seen from $Eq.(2.33)$ that in this case $\delta W>0$ and the plasma is stable. For any position of the conducting wall, including $b\to\infty$, δW is positive for all modes having $m/n<q_a$. If q is an increasing function of r, modes having a resonant surface within the plasma will have $m/n<q_a$ and will therefore be stable.

Since outside the plasma $q\propto r^2$, modes with resonant surfaces outside the plasma have $m/n>q_a$. Such modes can therefore be unstable. A straightforward way to determine stability for a particular case is to solve the eigenmode equation:

$$\frac{d}{dr}\left[(\rho\omega^2-F^2)r\frac{d}{dr}(r\xi)\right]-\left[m^2(\rho\omega^2-F^2)-r\frac{dF^2}{dr}\right]\xi=0, \qquad (2.35)$$

where ρ is the plasma density, $F=(m-nq)\mathrm{B}_\theta/\mathrm{r}{\mu_0}^{1/2}$, and the mode has a time-dependence $\mathrm{e}^{-\mathrm{i}\omega\mathrm{t}}$. The boundary condition to be applied at the origin is $\xi\propto r^{m-1}$ and that at the plasma surface is:

$$\frac{d}{dr}(r\xi)=\frac{m(m-nq_a)^2}{(\mu_0\rho\omega^2a^2/B_\theta^2)-(m-nq_a)^2}\left(\lambda-\frac{2}{m-nq_a}\right)\xi \qquad (2.36)$$

This condition represents the requirements of pressure balance and the condition that the plasma boundary remains a flux surface.

The mode $m=1$ is a special case, in particular the one that has a toroidal mode number $n=1$. The resonant surface for this internal kink instability is $q=1$. Thus the instability only occurs if there is a $q=1$ surface in the plasma. In the past, this has been confused with the sawtooth mode which we discussed above. However, in recent studies [Delgado 2015], the (1,1) internal-kink (IK) mode is distinct from the sawtooth instability.

Neoclassical tearing mode

Neoclassical tearing mode (NTM) is one of the most important main limitations to achieve high normalized plasma pressure, β_N, which is an important operational confinement indicator in scenarios such as ELMy H-mode in tokamaks today. β_N is defined from β as

$$\beta_N = \beta \frac{aB_T}{I_p}, \qquad (2.37)$$

where B_T is the toroidal magnetic field in T, a is the minor radius in m, and I_p is the plasma current in MA. Originally identified on TFTR [Chang 1995], NTMs take the form of low poloidal and toroidal mode number ('m/n') island structures on rational q surfaces within the plasma. They are driven by helical holes in the bootstrap current in plasma, arising as a result of pressure profile flattening in the region of an island. At small island sizes other effects act to oppose this drive, leading to the requirement of a critical island size or 'seed' perturbation (e.g., from some other MHD event, such as a sawtooth instability) in order to obtain neoclassical growth.

NTMs act to significantly confinement performance reduction (and sometimes cause disruptions) [Gates 1997, Zohm 1995] at levels of normalized β_N in present devices, $\beta_N \sim 2$ or higher, comparable to those envisaged for baseline scenarios in next-step devices such as ITER. The modes are often marked with the magnetic flux surface's number where they appear, like $m/n = 2/1, 3/2, 4/3, 5/4$, etc. At intermediate β, a 3/2 mode is often observed that degrades confinement. This is typically observed on various devices, where a drop of confinement~10–20% is common for the 3/2 NTM in conventional shear scenarios.

Usually, at higher β_N, the much more catastrophic 2/1 NTM is observed, which often causes disruptions. An example is shown for ASDEX Upgrade in **Figure 2.7**, where following a step-up in neutral beam power, a sawtooth occurs, exciting a 3/2 NTM. The β_N remains high (and local collisionality falls), and a second sawtooth triggers a 2/1 mode, growing over ~10 ms. This leads to a sharp drop in β_N, further enhanced by a transition from H to L mode as the mode locks (note the disappearance of ELMs in the Hα signals).

The evolution of the radial island width w is described by the generalized Rutherford equation [Sauter 1997]:

$$\frac{\tau_R dw}{\rho_s^2 dt} = \Delta'(w) + \beta_p \left(\left(a_{bs} - a_{GGJ}\right) \frac{w}{w^2 + w_d^2} - a_{pol} \frac{1}{w^3} \right) \qquad (2.38)$$

where τ_R is the resistive time on the resonant flux surface with radius ρ_s. The first term on the right-hand-side of $\mathrm{Eq.}\,(2.38)$ describes the conventional driving mechanism for tearing modes via the tearing parameter $\Delta'(w)$, which itself depends on w. The destabilizing effect of the perturbed bootstrap current is proportional to parameter a_{bs} and the Glasser-Green-Johnson effect to parameter a_{GGJ}. The threshold island width w_d is due to an incomplete flattening of the pressure profile caused by the finite heat conductivity across field lines. The term a_{pol} describes the neoclassical polarization current, which arises from the perturbed bootstrap current inertial response to a rotating perturbation. The effect of perpendicular heat transport and polarization currents is only important for small islands. For large islands and sufficiently negative Δ' the main stabilizing effect arises from the magnetic energy needed for the island formation. Usually $\Delta' < 0$, and then the modes must overcome the natural tearing stability of the plasma. This is most easily achieved for low m modes, where Δ' values are lower (higher m modes require more field line bending, and are thus more stable). The width of the saturated island is then given by:

$$w_{sat} = \beta_p \cdot \frac{a_{bs} - a_{GGJ}}{-\rho_s \Delta'(w_{sat})} \qquad (2.39)$$

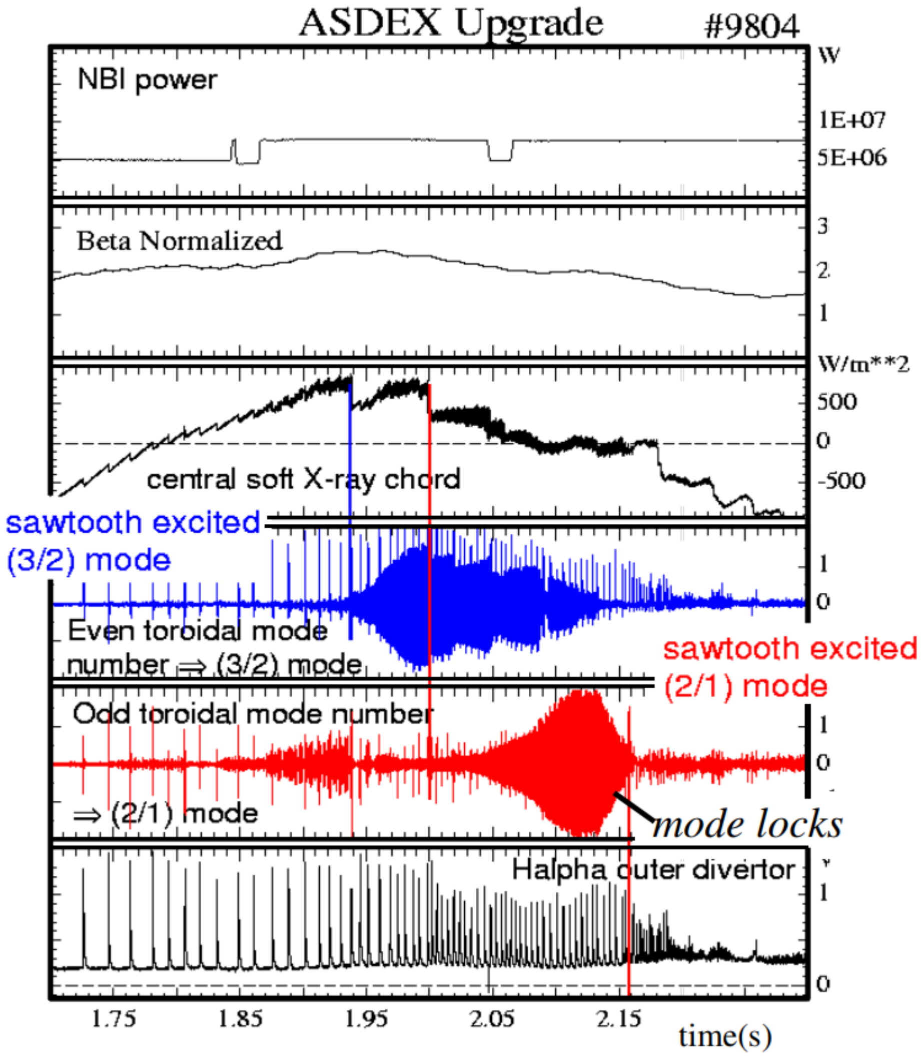

Figure 2.7. Strong heating on ASDEX Upgrade leads to a 2/1 NTM, triggering a sharp drop in β_N and transition to L-mode [Buttery 2000].

As shown in **Figure 2.8**, SXR tomography can be used to identify mode location and mode numbers on Tokamaks as JET [Huysmans 1999]. Singular-value decomposition (SVD) has been implemented to reveal this structure, which will be discussed in *Chapter 4*. As mentioned before, NTM growth requires a large enough seed island to be already present in the plasma. This must come from some other form of MHD activity (most commonly a sawtooth) and so depends on further physical mechanisms governing the size of that MHD perturbation, coupling to the NTM resonant surface, and shielding effects. An example of this seed can be seen in **Figure 2.7**, where sawteeth trigger the NTMs. Detailed studies of onset behavior have been made [Buttery 1999]. These reveal the NTM being seeded by harmonics of sawtooth or fishbone events. On JET, the NTM is observed to correlate well with sawtooth events, and is speculated to be driven by toroidal coupling to n = 2 harmonics of the sawtooth precursor.

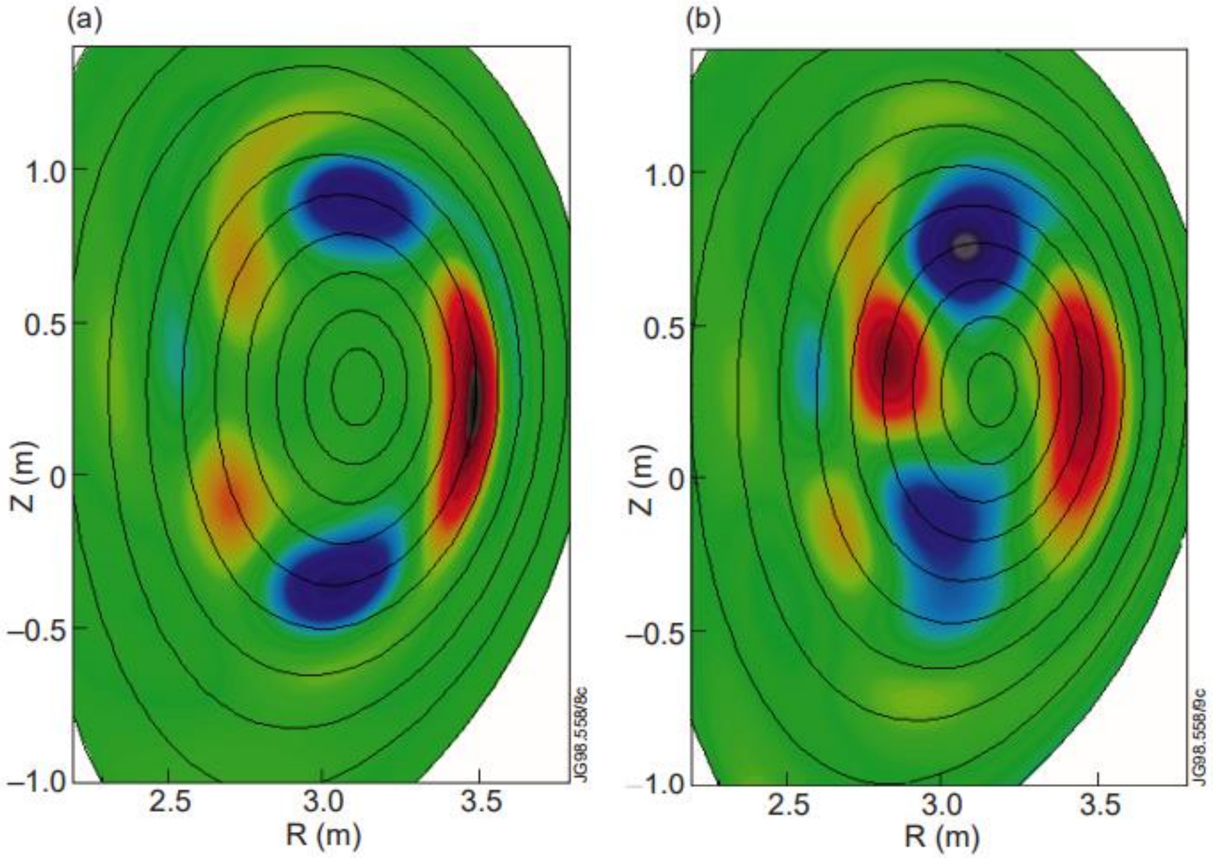

Figure 2.8 Tomographic reconstruction of the perturbation in the SXR emission on JET in the poloidal plane due to an n = 2 NTM for two cases: (a) m = 3 at medium β ($\beta_N = 2.4$) in discharge 40563; (b) m = 2 at high β ($\beta_N = 3.4$) in discharge #40564 [Huysmans 1999].

In order to avoid confinement degradation or even disruption caused by NTMs, means for their avoidance or stabilization have been developed. One obvious method is to prevent the creation of seed islands by background MHD, in particular by sawteeth which might reach large amplitudes in reactors due to the stabilizing effect of the fast α particles. As discussed above, this can be done by controlling sawteeth via the magnetic shear at the q=1 surface. As, however, NTMs are expected to be metastable already at low β values, any accidental MHD event can trigger mode onset. Therefore, one needs to be able to remove an already existing magnetic island as well. This can be done by replacing the helical perturbation of the bootstrap current caused by the island with externally driven current. Particularly suited for this goal is electron-cyclotron current drive (ECCD), which allows for localized current drive in the island region. This method has been proved to be successful, and is foreseen as a tool for NTM control in ITER.

2.2. Power balance and radiation losses

In this section, we will discuss operational aspects of fusion devices that are important with a view to power plants. In particular, we discuss the power balance in tokamaks, as well as consequences of impurity radiation and dust, which can pollute the plasma and decrease significantly the energy confinement by radiation, sometimes even leading to disruptions.

2.2.1 Tokamak power balance

Since there would be a continuous loss of energy from the plasma of the thermonuclear power of the reactor should be sufficiently large to replace these losses. The Lawson criterion is a statement of the condition for this to be achieved by auxiliary heating from a source outside the plasma.

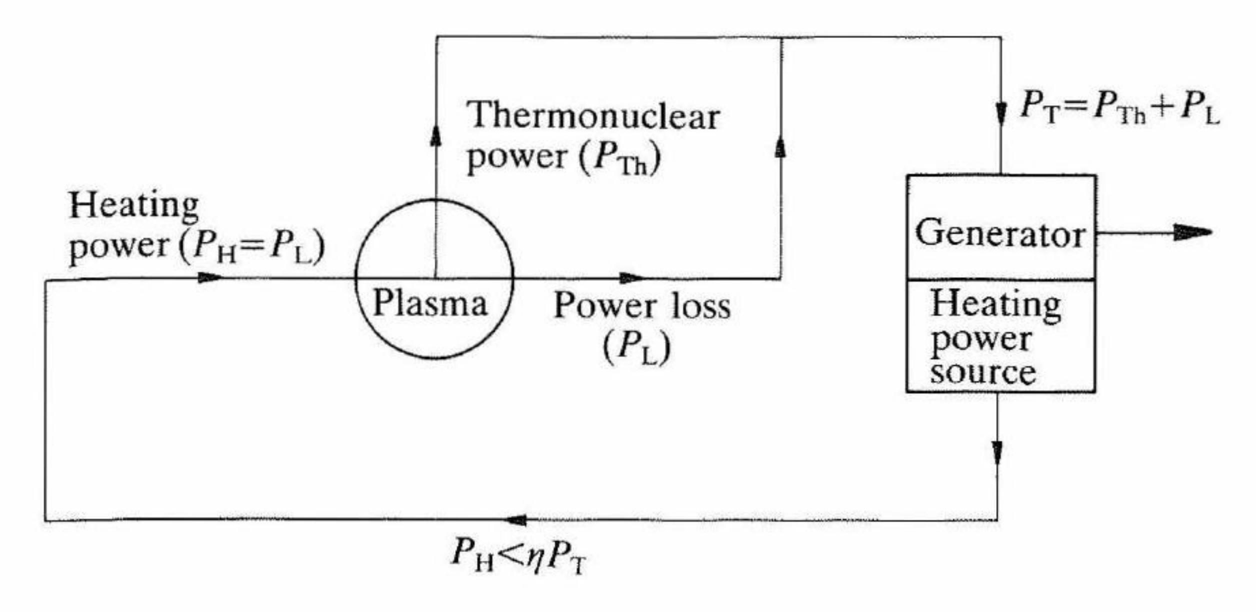
Thermonuclear power (P_{Th})
$P_{\mathrm{T}}=P_{\mathrm{Th}}+P_{\mathrm{L}}$
Heating power ($P_{\mathrm{H}}=P_{\mathrm{L}}$)
Generator
Plasma
Power loss (P_{L})
Heating power source
$P_{\mathrm{H}}<\eta P_{\mathrm{T}}$

Figure 2.9. The simplified schematic proposed by Lawson, showing the energy flow of a fusion power plant. Figure from [Wesson 1987].

It should be borne in mind, however, that the calculation of the criterion assumes a particular mode of operation of the reactor. If the thermonuclear power released in charged particles is retained within the plasma it is possible to envisage a reactor in which continuous external heating is unnecessary. The requirement for the achievement of such conditions will be discussed in *section 2.2.1*. The thermonuclear power generated from D-T fusion reaction is given as:

$$P_{Th} = \frac{n^2}{4}\langle \sigma v \rangle \mathcal{E} \qquad (2.40)$$

Where n is the total ion density, $\langle \sigma v \rangle$ is the reaction cross-section, $\mathcal{E}$ is the fusion energy released per reaction. Thus, the energy leaving the plasma through the energy losses may be written as:

$$P_L = \alpha n^2 T^{\frac{1}{2}} + \frac{3nT}{\tau_E} \qquad (2.41)$$

Where the first term represents the bremsstrahlung radiative losses, the second term represent the conductive losses and the energy confinement time τ_E. Thus, the total power leaving the plasma is:

$$P_T = n^2 \left(\frac{\langle \sigma v \rangle \mathcal{E}}{4} + \alpha T^{\frac{1}{2}} \right) + \frac{3nT}{\tau_E} \qquad (2.42)$$

After recycling the outgoing power into electrical power and the then re-injected into plasma heating with a combined efficiency η, the maximum power available to provide the heating power $P_H = \eta P_T$. Since for the power balance within the plasma $P_H = P_L$, it is at least necessary that $\eta P_T > P_L$. Substitution of $Eq.(2.41)$ and $Eq.(2.42)$ into this requirement gives:

$$n\tau_E > \frac{3T}{\frac{\eta}{1-\eta} \cdot \frac{\langle \sigma v \rangle \mathcal{E}}{4} - \alpha T^{\frac{1}{2}}} \qquad (2.43)$$

Where for a D-T fusion reactor, $\langle \sigma v \rangle = \langle \sigma v \rangle_{DT}$, $\alpha = 3.8 \times 10^{-29}\, J^{1/2} m^3 s^{-1}$, $\mathcal{E} = 17.6\, MeV$ and $\eta = 1/3$, which the values are chosen by Lawson. From the right-hand side of this inequality, we can see that at low temperatures the fusion power is small and at high temperatures the energy losses at a given τ_E increase more rapidly with temperature than does the fusion power. It is clear that for a reactor $n\tau_E$ must exceed this minimum value. Then the requirement becomes: $n\tau_E > 6 \times 10^{19}\, m^{-3} s$.

In practice, only a small part of the power produced could be recycled for plasma heating. Furthermore, the overall efficiency of providing such heating would probably be substantially lower than $1/3$ assumed above. Lawson's criterion is thus only a necessary criterion.

2.2.2 Plasma-surface interaction

In a tokamak discharge, the plasma particles inevitably escape the confinement at a certain moment (plasma transport, disruptions, run-away electrons etc.), and eventually strike the material boundary surface. When a hydrogenic ion or atom, or an electron reaches a solid surface, there would be three possible results:

(a) The particle may be directly back-scattered or reflected into the plasma, with a certain fraction of the impact energy.
(b) The particle may become implanted in the surface, undergoing thermal relaxation and eventually being released again under some form.
(c) Similar as (b), but the particle may remain trapped in the solid surface for an extended period, or permanently.

A hydrogenic incoming ion will extract an electron from the surface as it enters, and become neutral. At same time, electrons can also stick to surfaces of plasma-facing components (PFC). The surface therefore could act as a sink for plasma particles, although it is not a mass sink, since most of the particles are finally released again in a neutral atom or molecule. A steady-state situation arises where particles are captured by the surface at the same rate as recombined neutrals enter the plasma, called *recycling*.

The PFC surfaces, e.g. limiters or divertor surfaces, which are the main surfaces that come into contact with the plasma, have to be made of special materials that are resilient enough to heat load peaks. Many tokamaks' PFC surface material consist of carbon fiber composite (CFC). CFC has high thermal conductivity, good resilience to heat fluxes and lower economical cost. On the other hand, the CFC material may be subjected to various plasma-surface interaction processes, which can trigger the damage back to the surface. For the incoming ions or atoms, the principal mechanisms are physical and chemical sputtering. Physical sputtering occurs when the incoming particle is sufficiently energetic to transfer enough momentum to an atom in the first-wall that can reject it. Thus, gradually particles from the wall are released from the surface. Chemical sputtering refers to the process that the chemical potential energy of the incoming ion or electron is enough to break C-C bonds, and create C-H bonds. This leads to the formation of compounds such as $\mathrm{CH_4}$, which are released from the surface into the plasma as gas state. Especially, for the chemical sputtering, the incoming particle does not even need to be very energetic to trigger the process. Besides the sputtering, evaporation of plasma-facing structural components is another important source of wall particles in the plasma.

With above concerns and as well the crucial disadvantages of CFC material by means of tritium retention, many tokamaks supporting R&D for ITER (JET, AUG, WEST) have switched from CFC walls to metallic walls, mainly tungsten (W) and beryllium (Be). ITER has selected beryllium for the main chamber surface material and tungsten in the divertor and PFC. Similar to CFC, W has a good thermal conductivity and can handle heat fluxes up to $10-20\ \mathrm{MW/m^2}$ in steady-state with active cooling; at same time, W has a very low tritium retention and higher physical sputtering threshold compared to CFC. Beryllium has been selected for the main chamber wall due to its low atomic number and low tritium retention [Brezinsek 2014]. The ITER-like wall (ILW) concept has been adopted in JET with W in the divertor and Be for the first wall, as presented on **Figure 2.10**, which is an important facility to study plasma-wall interaction and resilience of metallic PFCs to high heat fluxes in conditions relevant for ITER.

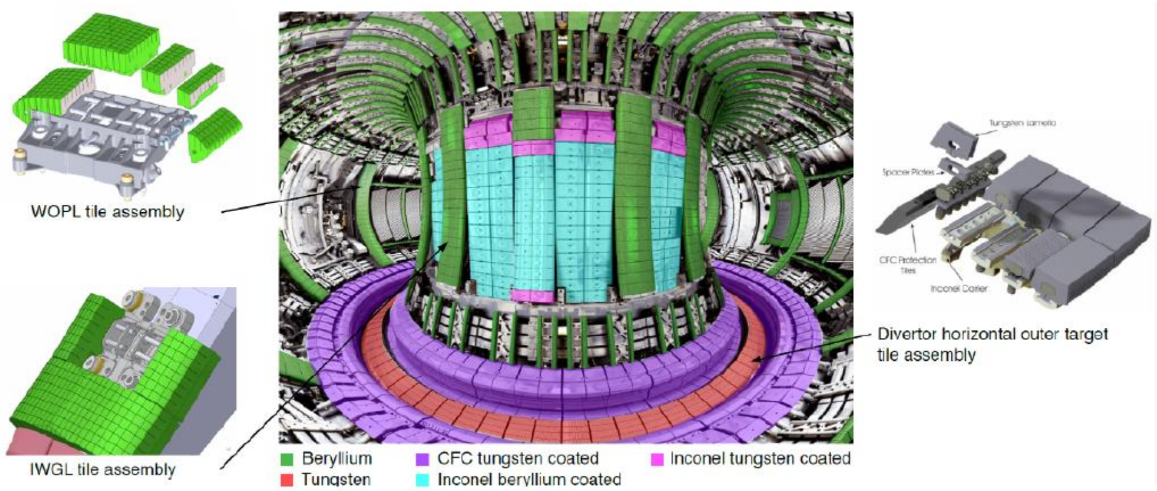
WOPL tile assembly
IWGL tile assembly
Tungsten lamella
Spacer Plates
CFC Protection Tiles
Inconel Carrier
Divertor horizontal outer target tile assembly
🟩 Beryllium
🟥 Tungsten
🟪 CFC tungsten coated
🟦 Inconel beryllium coated
🟪 Inconel tungsten coated

Figure 2.10. JET ITER-like wall components. Figure reprinted from [Arnoux 2014].

The characterization of the W source due to PFC erosion is a crucial issue to determine the lifetime of PFCs and the potential plasma core accumulation of W impurities. Under steady-state conditions (ELM-free or during inter-ELM periods), extrinsic and intrinsic impurities like argon (Ar), oxygen (O) or C have been identified [Brezinsek 2011] as the dominant source of W sputtering rather than the fuel species, due to their lower physical sputtering threshold on W of a few 10 eV (which can be easily achieved in typical tokamak edge plasmas temperature, corresponding to $10 \sim 100\ \mathrm{eV}$), compared to hydrogen isotopes (over $100\ \mathrm{eV}$). However, ELMs are expected to occur in most ITER baseline plasmas where the threshold can be potentially achieved with the presence of ELMs. Recently, the ion energy impact of ELM filaments on divertor targets and associated W sputtering have been recently investigated on JET [Jardin 2014, Guillemaut 2015] using ECE, infrared and Langmuir probes measurements in order to determine the ion impact energies. Impinging ion energies of several keV were estimated during ELMs (well above the W sputtering threshold), and indicating that D ions could be the dominant source of W sputtering during ELMs, and potentially over the whole discharge depending on the ELM regime, in unseeded H-mode discharges. Good agreement on W sputtering flux was later found between estimates using Langmuir probes and traditional tungsten spectroscopy measurements.

Ideally, the plasma would only make contact with the limiters and divertor targets. However, in realistic this is not always true, and particles may also be released from other parts of the vacuum vessel. Even without direct plasma-wall contact, neutral particles resulted from charge exchange process would also bombard to all vessel surfaces, causing chemical sputtering.

2.2.3 Effects of plasma impurities

In the ideal images, there's only hydrogenic ions would be present in a fusion plasma. In reality, plasma impurities, i.e. non-fuel ions, are unavoidably present and play an important role. Under reactor conditions, helium 'ash' will of course be present, as a part of the product of the fusion reaction. At the same time, due to the plasma-surface interaction as already mentioned above, atoms and molecules from the solid structural components surrounding the plasma, are released into the plasma. Impurities that are deliberately injected into the plasma (for various purposes) are called extrinsic impurities, as opposed to the ever present intrinsic impurities, such as carbon from CFCs, W from metallic surfaces etc.

Plasma impurities have a number of properties which are harmful for plasma operation. Firstly, impurities cause a considerable radiative power loss from the plasma core, such as bremsstrahlung radiation, recombination radiation and atomic line radiation. This is also true for the hydrogenic fuel species, but to a far lesser degree due to their lower atomic number. Depending on the different atomic number and ionization and excitation potential, different impurity species will radiate quite differently inside the plasma. Generally, the power is preferentially radiated stronger from hotter regions and by impurities with higher charge number. Bremsstrahlung emissivity is proportional to Z^2 (further information is given in *Chapter 3*), while the energy loss from line radiation is proportional to $\mathrm{Z}^3 - \mathrm{Z}^4$. Moreover, impurities can also dilute the burning fuel. Both the effects of power radiation and fuel dilution, when extrapolated to reactor conditions, would prevent the ignition. Concentrations of 3% for low-Z elements (like carbon or oxygen), 1% for intermediate-Z elements (like iron), and 0.1% for high-Z elements (like tungsten) would already be sufficient threatening to power plant future[Jensen 1977].

Apart from particle impurities, larger conglomerates of particles, referred to as *dust*, can also be formed through plasma-wall interactions. This can present significant issues for ITER and for reactor-like devices such as DEMO. The maximum amount of dust that can be tolerated in ITER is still under investigation. [Krasheninnikov 2011] The main issues related to dust are:

- dust chemical activity, tritium retention and radioactivity (in case of loss-of-vacuum accident),
- potential degradation of in-vessel diagnostics,
- increase of the wall erosion due to impinging impurity particles,
- mobile dust can release impurities that can accumulate in the plasma core, decrease its performances through radiation and even cause termination of the discharge.

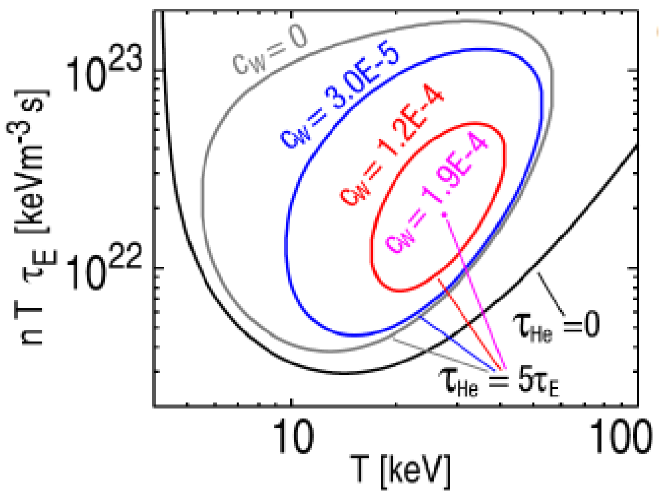

Figure 2.11. Shrinking ignition domain of fusion plasmas as the tungsten (W) impurity concentration increases. The dilution caused by helium ashes is included assuming a confinement time of helium five times greater than the plasma energy confinement time: $\tau_{He} = 5\tau_E$. [Putterich 2010].

Reliable diagnostic tools are essential to trace the dust's or impurity's velocities and trajectories and thus study their formation and transport, and resulting plasma core pollution. [Ratynskaia 2011] Several impurity transport codes have been successfully developed by the fusion community, e.g. MIGRAINe [Vignitchouk 2014] at KTH, Sweden or DUMBO [Autricque 2016] at IRFM, France. On WEST, the long-pulse discharge experiments will offer a great opportunity to study the formation of hot spots or potential flaking of W coatings, and their impact on impurity generation and its effects on plasma performance.

Apart from the detrimental effects, impurities can also have a number of beneficial effects. During plasma discharges, impurities can be injected for diagnostic purposes, for affecting edge plasma conditions leading to confinement enhancement and for decreasing power loads on the plasma-facing components. Indeed, impurities radiating in the scrape-off layer (SOL) or near the periphery of the main plasma, can lead to a diminishing power load and reduced plasma-wall interaction on the plasma-facing components, without affecting plasma confinement. This natural effect can be enhanced by the deliberate injection (also called puffing) of low-Z impurities like nitrogen or neon, giving rise to so-called *cold plasma mantel* at the periphery of the main plasma. The reason to prefer low-Z species is that they radiate mainly near the plasma periphery, much more than in the core plasma. On the other hand, this is an advantage for plasma-facing components made of a low-Z material.

2.2.3.1. Power loss through impurity radiation

The radiation in tokamak plasmas contains both continuum radiation and line radiation (bound-bound radiation) with wavelengths from the visible to the X-ray region. The continuum radiation is dominated by recombination radiation (free-bound radiation) and bremsstrahlung radiation (free-free radiation). Many of these lines can be used for detailed spectroscopic studies, while measurements of the power emitted over the entire wavelength region provides important information for power balance studies. Indeed, for non-fully stripped ions (like tungsten, which has an atomic charge of 74), the line-emission and radiative recombination radiate very significant amounts of power out of the plasma center. In addition, highly-charged ions radiate more than deuterium and tritium through bremsstrahlung because of their higher charge. These properties mean that, impurities, even when a very small concentration is present, can lead to radiative collapse and strongly affect confinement. We will come back to this topic in *Chapter 3*.

2.2.3.2. Impurity transport

The most part of impurity ions are released from first walls and quickly return to the surfaces, namely the *recycling process*, but some are transported further inside the plasma, and some may even reach the plasma core area, causing impurity accumulation. Eventually, all the impurity ions will return to the particles sinks. Once the particles enter the relatively deeper plasma region, they shall be ionized, and follow the law of impurity transport. Traditionally, a distinction has to be made between edge transport and core transport by regarding their different assumptions.

In the context of transport, the plasma 'edge' may be defined in two ways:

a. In the case that the ionization of neutrals occurs entirely outside the last-closed flux surface (LCFS), then edge transport can be considered as the transport outside the LCFS.
b. If the ionized neutrals extend inside the LCFS with certain depth λ_{iZ}, then edge tranport can be considered as the transport outside the radius (a $-\lambda_{iZ}$), where λ_{iZ} is the typical ionization depth of an impurity, depending on charge number Z.

The edge impurity transport can be modelled using the quasi-one-dimensional Engelhardt model [Engelhardt 1978], as one of the simplest description. However, due to the complexity of material content and unpredictable boundary conditions in the plasma edge, the edge transport is usually inherently more complex than transport in the plasma core. We will not go further into edge transport, and rather refer to [Stangeby 2000] for an overview.

Transport in the plasma core (i.e. the inboard of the edge region) has been extensively studied both theoretically and experimentally. The transport activity at plasma core area is usually seen as a 1D cross-field picture (profile view), described by the following equation, which contains a diffusion and convection term individually:

$$\Gamma_\perp = -D_\perp \frac{dn}{dr} - V_{pinch} n. \qquad (2.43)$$

Here, $\Gamma_\perp$ is the transport flux of impurity species with density n in perpendicular direction to the magnetic equilibrium surfaces, and V_{pinch} is the convection (pinch) velocity. The transport coefficients $D_\perp$ and V_{pinch} cannot yet be calculated from first principles, since from the experimental measurements, they are anomalous, and much higher than the neoclassical expected values. Typically, $D_\perp \approx 0.1 - 10\ m^2/s$, while $V_{pinch} \approx 10$ m/s [Wesson 1987].

The transport behavior of helium ions is of primary interest for reactor-grade plasma, which is relevant to the studies of efficient exhaust of helium ash from plasma. In order to achieve a stationary and ignited burning D-T plasma, it is necessary that:

$$\frac{\tau_\alpha^*}{\tau_E} \leq 10, \qquad (2.44)$$

with τ_α^* the global alpha particle confinement time, while τ_E is the global energy confinement time. Thus, the unwanted particle confinement time should not be "too good". Also, helium neutrals need to be pumped away effectively from some region at the edge.

2.2.3.3. Impurity measurement

From the above discussions, we can clearly see that impurities play an important and complex role in tokamak physics. On one hand, impurities cause a number of harmful effects to confinement and energy balance. On the other hand, impurities can be exploited to provide valuable information from the diagnostic point of view, they can help protecting plasma-facing components, and sometimes they can even improve plasma confinement. As a consequence, the reliable measurements of the impurity properties and behavior in plasma is a key element. In the past decades, many sophisticated techniques have been developed, the enforces not only characterized impurities themselves, but also used impurities as certain diagnostic tool, to study particle confinement and deduce such properties as ion temperature and plasma rotation.

Considerable information on impurity transport can be deduced from measuring impurity density or impurity concentration. Generally, the impurity concentration refers to the ratio of impurity density to electron density, where $c_{im} = n_{im}/n_e$. The impurity density or concentration information can be obtained using various active or passive spectroscopic techniques [Hutchinson 2002], such as UV and VUV spectroscopy, bremsstrahlung spectroscopy, active beam spectroscopy, etc. Especially, soft-X ray spectroscopy is another key technique to obtain impurity densities, due to its good temporal resolution and spatial resolution. It is part of the focus for this Ph.D. work and will be discussed in *Chapter 3*.

Chapter 3 Soft X-ray diagnostic on WEST

Progress in nuclear fusion programmes requires application of diagnostic techniques for measurements of high temperature plasma paramters and for basic control of discharge performance. Monitoring of plasma discharge performance by measurement of hydrogen Balmer lines or by lines of intrinsic ligh impurities proved to be very useful at various stages of controlled fusion studies. Investigation of the spatial distribution of emitters, absolute measurement of atom (or ion) line emission, development of interpretative models (collisional-radiative model, which we will discuss in *section 3.1.2*) provided an opportunity to obtain a number of plasma parameters of great importance for plasma studies. Nowadays, there is considerable activity on the ITER diagnostic suite, including a number of spectroscopic techniques [Donné 2007]. For instance, the impurity influx monitor is a spectroscopic system for the investigation of impurities and hydrogen isotopes in ITER divertor plasmas [Sugie 2003]. The expected impurities correspond to the main ITER wall materials, like Be, W, C, Cu (the materials of the vacuum vessel and divertor target plates), He ('ash' from nuclear fusion reactions) and extrinsic impurities such as the noble gases (Ne, Ar, Kr) and nitrogen.

The investigation of soft X-ray (SXR) radiation is a very important part of spectroscopic diagnostics in fusion devices. It originates from ion-electron Coulomb interaction, i.e. Bremsshtralung radiation for fully ionized species (hydrogenic species, α-particles and light impurities), but also from radiative recombination and line radiation for non-fully ionized species like metallic impurities. Furthermore, as the plasma optical absorption is quite low in the SXR range, SXR diagnostics are a suitable method to deliver information from the plasma core. In tokamaks, SXR radiation is observed in the plasma core where the plasma temperature $T \sim 1 - 15\ \mathrm{keV}$.

In this chapter, we will look into details of the SXR radiation mechanism in tokamak plasma, introduce present detection methods and give readers insight in the newly developed soft X-ray diagnostic based on Gas Electron Multiplier (GEM) cameras at the WEST tokamak.

3.1. Soft X-ray emission

Traditionally, the name 'X-ray radiation' is connected with a photon spectral wavelength shorter than $5\mathrm{nm}$, corresponding to a photon energy above $250\ \mathrm{eV}$. The photon energy of soft X-rays is less than $10\ \mathrm{keV}$. Highly energetic particles such as supra-thermal electrons or fast α -particles lead to emission of hard X-rays and γ-rays. On the other side of the electromagnetic spectrum, visible-ultraviolet (VUV) radiation is observed in the plasma edge while plasma-facing components heated by the plasma radiate in the visible and infrared ranges. Radio waves and microwaves are used to heat the plasma at the cyclotron resonance frequencies of ions (several tens of MHz) and electrons ($\sim 100\ \mathrm{GHz}$). Thus, the whole electromagnetic spectrum from $10^{-7}\ \mathrm{eV}$ to $10^{6}\ \mathrm{eV}$ is used in tokamaks for heating or diagnostics purposes.

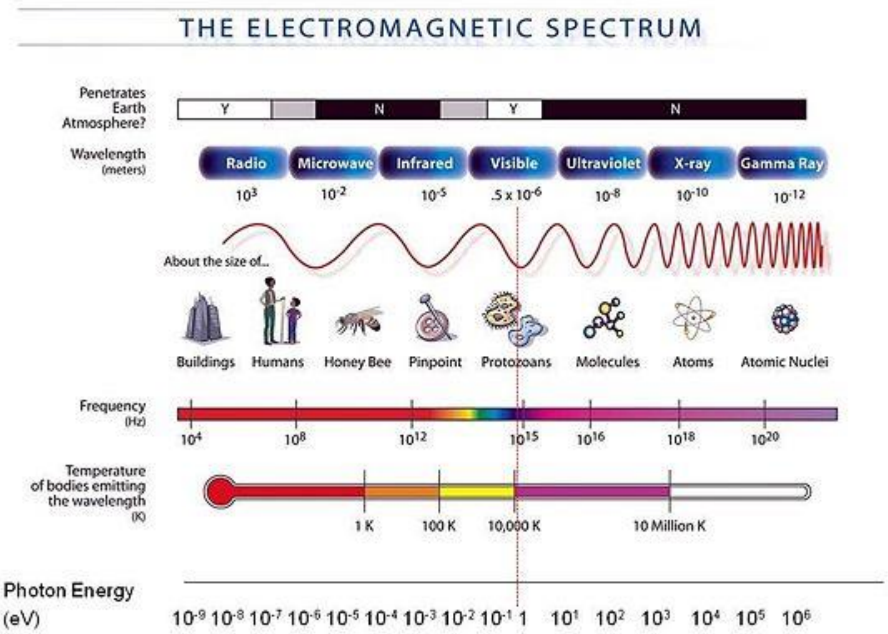
THE ELECTROMAGNETIC SPECTRUM
Penetrates Earth Atmosphere?
Y
N
Y
N
Wavelength (meters)
Radio
Microwave
Infrared
Visible
Ultraviolet
X-ray
Gamma Ray
10^3
10^-2
10^-5
.5 x 10^-6
10^-8
10^-10
10^-12
About the size of...
Buildings
Humans
Honey Bee
Pinpoint
Protozoans
Molecules
Atoms
Atomic Nuclei
Frequency (Hz)
10^4
10^8
10^12
10^15
10^16
10^18
10^20
Temperature of bodies emitting the wavelength (K)
1 K
100 K
10,000 K
10 Million K
Photon Energy (eV)
10^-9 10^-8 10^-7 10^-6 10^-5 10^-4 10^-3 10^-2 10^-1 1 10^1 10^2 10^3 10^4 10^5 10^6

Figure 3.1. Illustration of the electromagnetic spectrum, from radio waves to gamma rays, courtesy of NASA website.

It is believed that the first soft X-ray radiation investigations in plasma physics were carried out in 1949, when the solar corona X-ray radiation was visualized. The plasma radiative spectrum consists of both continuum radiation and discrete spectral lines. The continuum radiation consists of bremsstrahlung and recombination radiation. Until the times where laboratory plasma temperatures did not exceed $100\ \mathrm{eV}$, the possibility of experimental investigations of plasma X-ray radiation were very limited. With the plasma electron temperature in many present experiments exceeding several keV, the value of such research has increased considerably. If the plasma electron temperature is greater than $200\ \mathrm{eV}$ and the amount of impurities is low, the influence of recombination radiation may be ignored. In this situation, the continuum spectrum is determined generally by bremsstrahlung, which arises due to scattering of free electrons by plasma ions. We will discuss bremsstrahlung radiation in detail in the next section.

3.1.1. Line radiation, recombination radiation and Bremsstrahlung radiation

As mentioned above, fusion plasma radiation is dominated by three main processes: free-free interaction called Bremsstrahlung radiation, free-bound interaction via radiative recombination and bound-bound interaction by line transition. In this section, we will introduce in more detail these three processes and calculation of the total soft X-ray emissivity.

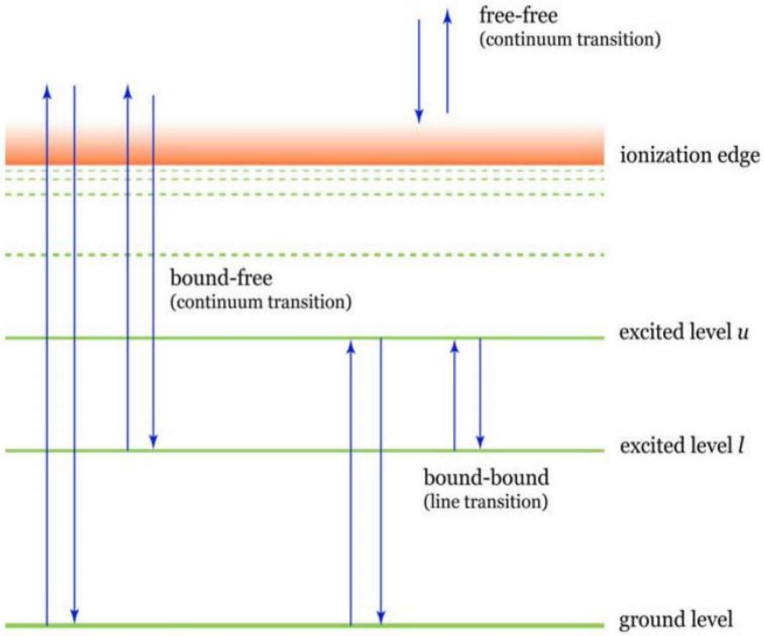

Figure 3.2. Radiation processes in plasmas: Bremsstrahlung (free-free), line emission (bound-bound) and radiative recombination (free-bound).

Line Emission (bound-bound interaction)

Line emission occurs when ions are excited to higher energy levels and then relax to lower levels via radiative decay. Schematically, it can be seen as one bound electron has been lifted to a higher energy level, making the whole system (ion or atom) more energetic than its ground state. The excitation process (or receiving energy process) can be driven by absorption of photons or collision with energetic electrons. These processes can be described as:

$$\text{photo} - \text{absorption:} \qquad \mathrm{A}^{(Z)+} + h\nu \xrightarrow{\text{excitation}} \left(\mathrm{A}^{(Z)+}\right)^{*} \qquad (3.1)$$

$$\text{electron} - \text{collision:} \qquad \mathrm{A}^{(Z)+} + e \xrightarrow{\text{excitation}} (\mathrm{A}^{(Z)+})^{*} + e' \qquad (3.2)$$

$$\text{emission:} \qquad (\mathrm{A}^{(Z)+})^{*} \xrightarrow{\text{emission}} \mathrm{A}^{(Z)+} + h\nu^{(b-b)} \qquad (3.3)$$

Here, $\mathrm{A}^{(Z)}$ denotes an ion with charge Z in the ground state, $(\mathrm{A}^{(Z)})^{*}$ denotes the ion or atom in excited energetic state, $h\nu$ denotes a photon with frequency ν, e and e' denote electrons with different kinetic energy.

Line emission is referred to as bound-bound interaction because the excited electron is still bound to its atom after the radiative relaxation. Its spectral emission is composed of numerous discrete lines corresponding to spontaneous transitions from upper levels u to lower levels l:

$$h\nu_{u\to l}^{(b-b)} = \Delta E_{ul} = E_u - E_l \tag{3.4}$$

The emission coefficient $\epsilon_{ij}^{(Z)}$ of the emission from level i to level j with units of energy/time/volume/solid angle is defined as:

$$\epsilon_{ij}^{(Z)} = n_i^{(Z)} A_{ij}^{(Z)} \frac{h\nu_{ij}}{4\pi}, \tag{3.5}$$

where n_i denotes the density of ions with charge Z at energy level i, and $A_{ij}^{(Z)}$ denotes the Einstein coefficient for spontaneous emission from level i to level j.

According to Kirchhoff's Law, the rate of change of the density $n_i^{(Z)}$ of the energy level i is given by:

$$\frac{\mathrm{d}n_i^{(Z)}}{\mathrm{dt}} = -\sum_{k<i} n_i^{(Z)} A_{ik}^{(Z)} - n_e \sum_{k\neq i} n_i^{(Z)} X_{ik}^{(Z)} + \sum_{k>i} n_k^{(Z)} A_{ki}^{(Z)} + n_e \sum_{k\neq i} n_k^{(Z)} X_{ki}^{(Z)} \tag{3.6}$$

Here, $X_{ki}^{(Z)}$ denotes the excitation coefficient due to the electron collision and $X_{ik}^{(Z)}$ is the de-excitation coefficient due to the electron collision.

As tokamak plasmas follow the collisional-radiative model, which we will come back to in *section 3.1.2*, equilibrium between internal energy levels of any ionization state is eventually reached ($dn_i^{(Z)}/dt = 0$) and Eq. (3.6) can be reformulated as:

$$n_i^{(Z)} A_{ij}^{(Z)} = n_e n_Z \left[\sum_{k\neq i} f_i^{(Z)} X_{ik}^{(Z)} - \frac{1}{n_e} \sum_{k>i} f_k^{(Z)} A_{ki}^{(Z)} - \sum_{k\neq i} f_k^{(Z)} X_{ki}^{(Z)} \right] B_{ij}^{(Z)} \tag{3.7}$$

Herein the $f_i^{(Z)} = n_i^{(Z)}/n_Z$ are the fractional abundances of energy level i in ionization state Z and $B_{ij}^{(Z)} = A_{ij}^{(Z)} / \sum_{k<i} A_{ik}^{(Z)}$ the branching ratio of transition i to j.

Thus, using Eq. (3.5), the $\epsilon_{ij}^{(Z)}$ depend on n_e, n_Z and a term depending on n_e and T_e with respect to the fractional abundance factor. Therefore, a photon emissivity coefficient (PEC) provided by the Atomic Database and Analysis Structure (ADAS) [Open-ADAS 2017] can be defined as:

$$\epsilon_{ij}^{b-b,(Z)}(h\nu) = n_e n_Z PEC_{ij}^{(Z)} \tag{3.8}$$

Summarizing, the total line emissivity $\epsilon_{S,Z}^{b-b,(Z)}$ of any species S^{Z+} in the plasma is given by the formula:

$$\epsilon_{S,Z}^{b-b,(Z)}(h\nu) = n_e n_{S,Z} \sum_{i<j} PEC_{ij}^{(Z)} = n_e n_{S,Z} k_{S,Z}^{b-b} \tag{3.9}$$

Specifically, the hydrogenic isotopes, helium and other light impurities are fully ionized in the tokamak plasma core, hence their line radiation does not contribute significantly to the background soft X-ray emission in the plasma core where $T_e \geq 1$ keV, but is only significant for medium and heavy impurities.

Recombination radiation (free-bound interaction)

Radiative recombination occurs when free plasma electrons are captured by ions of charge $\mathrm{Z}+1$. It is virtually negligible for hydrogen isotopes, however, it can be a significant contribution to soft X-ray radiation when ionized impurities are present. The radiative recombination process could be described as:

$$\mathrm{A}^{(Z+1)+} + e \xrightarrow{\text{reconbination}} \mathrm{A}^{(Z)+} + h\nu^{(f-b)} \qquad (3.10)$$

The inverse process of radiative recombination is photo-ionization:

$$\mathrm{A}^{(Z)+} + h\nu \xrightarrow{\text{ionization}} \mathrm{A}^{(Z+1)+} + e \qquad (3.11)$$

This radiation leads to the photon emission in a semi-continuum spectrum:

$$h\nu_{\infty\to i}^{(f-b)} = E_{kinetic} + \left[E_{\infty}^{(Z)} - E_{i}^{(Z)}\right] = E_{kinetic} + \Delta E_{\infty\to i}^{(Z)} \qquad (3.12)$$

Here, $E_{kinetic} > 0$ is the initial free electron kinetic energy and $\Delta E_{\infty\to i}^{(Z)}$ is the energy gap between the ionization limit and the energy level i of the recombined electron. It is called as free-bound interaction since the initially free electron is bound to the atom after the photon emission and it corresponds to a semi-continuum spectrum in the sense that the photon energy is the sum of a continuous component $E_{kinetic}$ (with Maxwellian distribution of the electron kinetic energy) and a discrete component $\Delta E_{\infty\to i}^{(Z)}$ for the recombination edge.

For impurities with high charge number Z, the partial screening effect of bound electrons plays a role in the radiative recombination process and specific interaction cross-sections should be used. Nevertheless, for recombination of bare nuclei z + 1 = Z into their hydrogenic ions z, we substitute the ionization energy by:

$$E_{\infty}^{(Z)} - E_{i}^{(Z)} = \frac{Z^2 E_R}{{n_i}^2}, \qquad (3.13)$$

where n_i is the principle quantum number of energy level i. A simplified expression for the recombination spectral emissivity can be found in [Kunze 2009]:

$$\epsilon_{S,Z}^{f-b,(Z)}(h\nu) = n_e n_{S,Z} Z^4 \frac{64\sqrt{\pi}(\alpha a_0)^3 E_R}{3\sqrt{3}hc} \left(\frac{E_R}{k_B T_e}\right)^{\frac{3}{2}} \exp\left[-\frac{h\nu}{k_B T_e}\right] \sum_{n>n_{min}} \frac{1}{{n_i}^3} \exp\left[\frac{E_R}{{n_i}^2 T_e}\right] G^{f-b}, \quad (3.14)$$

where α is the fine structure constant, a_0 is the first Bohr radius, E_R is the Rydberg Energy, G^{f-b} is the free-bound Gaunt factor also, which is of order unity in the SXR range.

The integration of the free-bound emission coefficient in Eq. (3.14) over the whole spectrum can be expressed in $\mathrm{W}\cdot\mathrm{m}^{-3}\cdot\mathrm{sr}^{-1}$, as:

$$\epsilon_{S,Z}^{f-b,(Z)}(h\nu) = 1.08 \times 10^{-38} n_e n_{S,Z} Z^4 \left(\frac{E_R}{T_e}\right)^{\frac{1}{2}} \qquad (3.15)$$

Figure 3.3 illustrates the recombination spectrum of an optically thin hydrogen plasma of $\mathrm{k}_B\mathrm{T}_e = 5\mathrm{eV}$ with the Gaunt factors set to unity. The edge structure imposed by recombination into the different shells (n_i) is characteristic. Due to the $1/n_i^3$ factor, recombination into the ground state gives by far the strongest contribution. At short wavelengths (large $h\nu$) the exponential term $\exp(-\mathrm{h}\nu/\mathrm{k}_B\mathrm{T}_e)$ determines the spectrum, at long wavelengths a $1/\lambda^2$ dependence emerges between the edges.

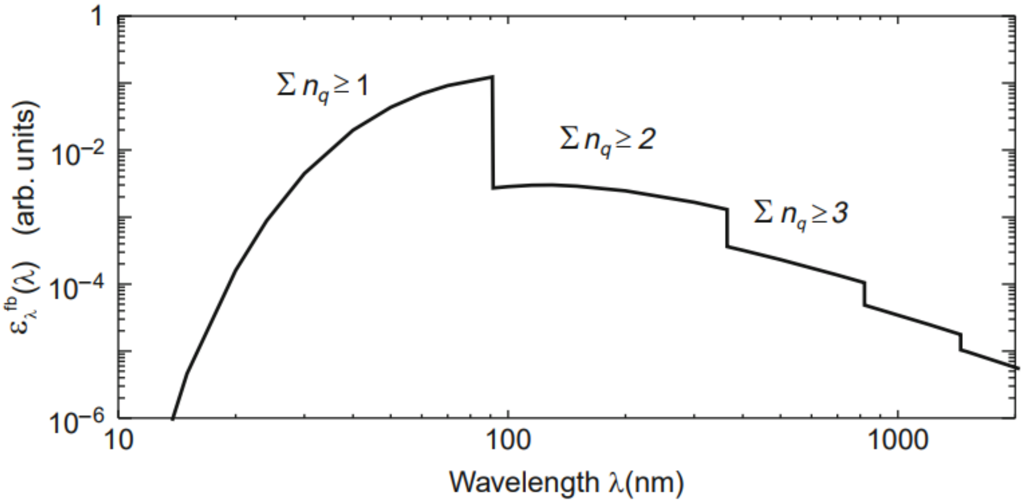

Figure 3.3. Emission coefficient of radiative recombination of a hydrogen plasma of $\mathrm{k}_B\mathrm{T}_e = 5\mathrm{eV}$, [Kunze 2009] .

Bremsstrahlung radiation (free-free interaction)

Deflection of electrons in the field of ions leads even in the classical picture to the emission of radiation, which corresponds quantum mechanically to transitions between continuum states. The spectrum of all the free–free transitions in the plasma is continuous and the radiation is called *Bremsstrahlung*. This process can be described as:

$$\mathrm{A}^{(Z)+} + e \xrightarrow{\text{coulomb collision}} \mathrm{A}^{(Z)+} + e' + h\nu^{(f-f)} \qquad (3.16)$$

In tokamaks, the Bremsstrahlung radiation in soft X-ray rang is caused by Coulomb collisions between free electrons and ions. Due to the electron energy distribution follows a continuous shape (namely Maxwellian distribution), the corresponding Bremsstrahlung radiation has a continuous spectrum as well. This is a free-free interaction because the interacting particles are free before and after the photon emission. In a fully ionized plasma, the Bremsstrahlung spectral emissivity is given by:

$$\epsilon_{S,Z}^{f-f,(Z)}(h\nu) = n_e n_{S,Z} Z^2 \frac{32\sqrt{\pi}(\alpha a_0)^3 E_R}{3\sqrt{3}hc} (\frac{E_R}{T_e})^{\frac{1}{2}} \exp\left[-\frac{h\nu}{T_e}\right] G^{f-f}, \qquad (3.17)$$

where α is a constant which represents the fine structure effect, a_0 is the first Bohr radius, E_R is the Rydberg Energy, G^{f-f} is the free-free Gaunt factor close to unity in the soft X-ray range. For non-fully ionized species, an additional correction factor should be included to consider the ion internal structure, which can influent the Bremsstrahlung cross-section if the electron is close enough to the ion such that the charge seen by the free electron cannot be described as the total ion charge, considering screening by the bound electrons. This effect becomes more important with increasing velocity of the electrons. The general correspondence between a spectral emissivity ϵ_λ in $\mathrm{W \cdot m^{-3} \cdot nm^{-1}}$ and ϵ_{hv} in $\mathrm{W \cdot m^{-3} \cdot eV^{-1}}$ is given by:

$$\epsilon_\lambda = \epsilon_{hv} \cdot \frac{hc}{\lambda^2} \tag{3.18}$$

An example of Bremsstrahlung radiation spectrum from hydrogen has been shown in **Figure 3.4** at different electron temperatures, which indicates that the spectrum is shifted to higher energies at higher temperature regime. Besides, the maximum value of ϵ_λ is reached for $\lambda_{max} = \mathrm{hc/2Te}$. The numerical estimation of Eq. (3.17) gives:

$$\epsilon_{S,Z}^{f-f,(Z)}(hv) = 1.54 \times 10^{-38} n_e n_{S,Z} Z^2 \frac{\exp\left[-\frac{hv}{T_e}\right]}{\sqrt{T_e}} G^{f-f} \tag{3.19}$$

Where ion charge Z^2 can be approximately replaced by the effective charge $\mathrm{Z}_{eff}^2 = \sum_i n_i \mathrm{Z}_i^2 / n_e$ during the calculate of spectral power. After the integration of $\epsilon_{S,Z}^{f-f,(Z)}(hv)$ over the whole spectrum, the total radiated power expressed in $\mathrm{W \cdot m^{-3} \cdot sr^{-1}}$ gives:

$$\epsilon_{S,Z}^{f-f,(Z)} = 4.51 \times 10^{-39} n_e n_{S,Z} Z^2 \frac{T_e}{E_R} \tag{3.20}$$

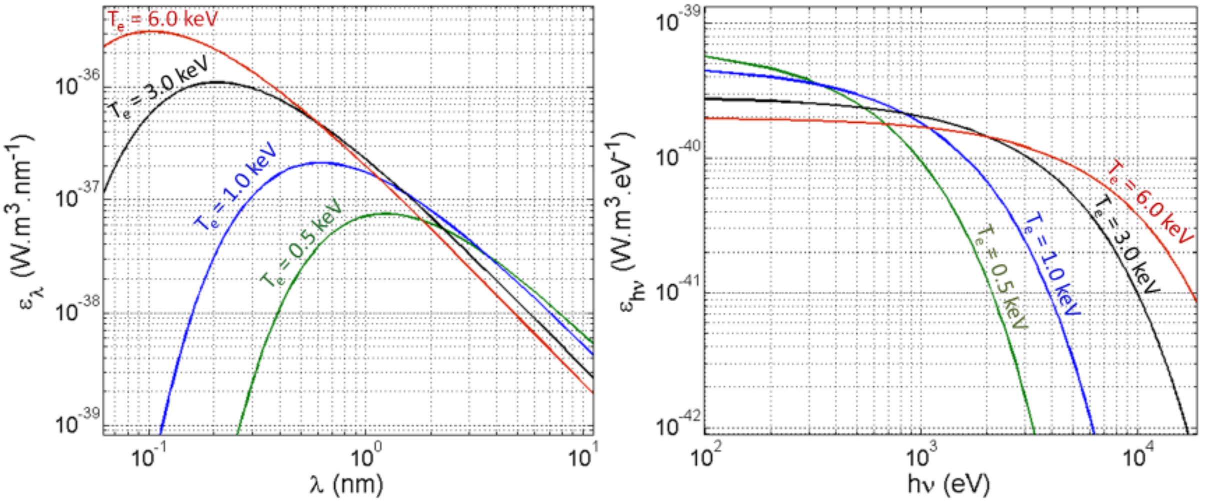

Figure 3.4. An example of Bremsstrahlung radiation spectrum from hydrogen in function of wavelength (on left) and frequency (on right) at different electron temperatures [Jardin 2017].

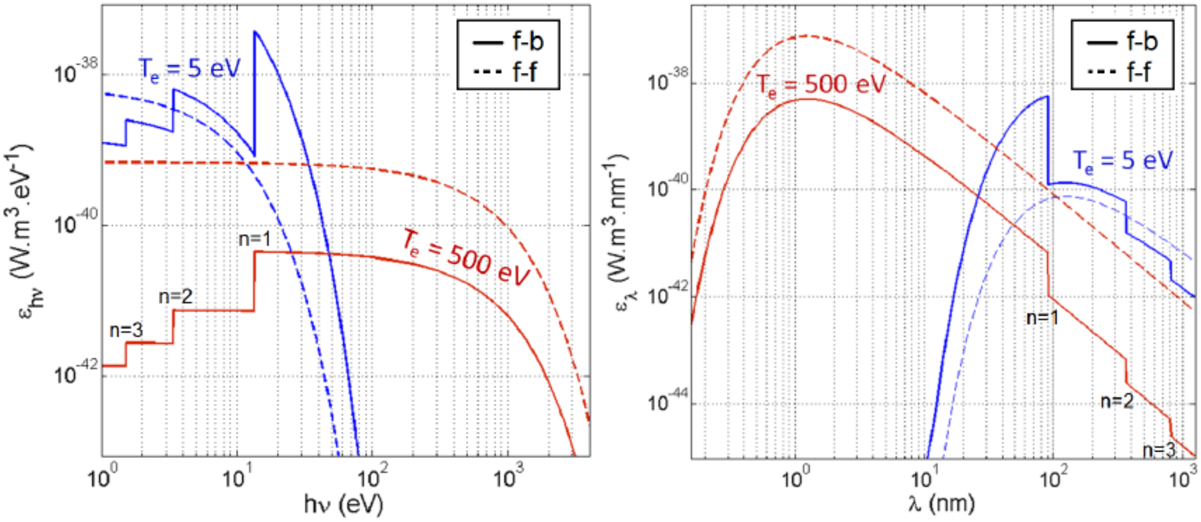

Figure 3.5. Spectral emission coefficient of radiative recombination (solid line) for hydrogen as a function of frequency (left) and wavelength (right). Bremsstrahlung radiation as defined in Eq. (3.19) is plotted (dashed line) for comparison [Jardin 2017].

As shown in **Figure 3.5**, the radiative recombination contribution becomes weaker compared to Bremsstrahlung with increasing temperature and therefore with increasing fractional abundance of the fully stripped ion. It can also be seen in Eq. (3.14) that contribution of atomic orbits $\mathrm{n} > \mathrm{n}_{min}$ diminishes very rapidly with increasing n, so the summation can be truncated at $\mathrm{n}_{max} \leq 10$. Spectrally integrated emission coefficients (PRB) are provided by ADAS to include the free-free (Bremsstrahlung) and free-bound (recombination) radiation of each ionization state of a given species. This is very useful to estimate power losses due to the presence of impurities in plasma simulations.

3.1.2. Ionization equilibrium

Before considering the spectral emissivity of the plasma, first the ionization equilibrium of each relevant species must be solved, including the population of atomic levels inside the ionization states (referred to as the fractional abundance). Using Kirchhoff's law, the kinetics of the local population of atomic states (i) of ions of charge (Z) in plasmas is governed by coupled rate equations of the type:

$$\frac{\mathrm{d}n_i^{(Z)}}{\mathrm{dt}} = -\mathrm{R}_Z(i \rightarrow) + \mathrm{R}_Z(\rightarrow i) + \Gamma_Z(i) \qquad (3.21)$$

Here, $\mathrm{R}_Z(i \rightarrow)$ and $\mathrm{R}_Z(\rightarrow i)$ represent the sums of all rates of possible radiative and collisional transitions out of level (i) and into that level, respectively, and $\Gamma_Z(i)$ is the external flux of level (i) population by diffusion and convection. It is clear that a general solution is practically impossible not only because of the large number of transitions which have to be considered, but also for the fact that for many transitions the probabilities and rate coefficients are not known with sufficient accuracy (especially for high-Z elements). It is therefore a common approach to reduce the number of rate equations to a set of tractable size by considering only the most relevant processes and by considering the pertinent time scales. These so-called *collisional-radiative* models may differ for different atomic and ionic species and certainly for molecules, and they depend on the regime of plasma parameters.

The longest time constant to reach steady-state population for an excited level (i) is given by the lifetime for pure radiative decay $\tau = 1/A_Z(i \rightarrow)$. Since in atomic systems these are typically very short compared to changes of the plasma conditions, usually $dn_i^{(Z)}/dt = 0$ can be assumed. Hence, the time dependence needs to be kept only for metastable levels (m) and ground states (g), which reach steady-state by ionization and recombination on longer time scales. The influx of level population $\Gamma_Z(i)$ is low and even negligible in most cases. If it becomes relevant, this is also true for the ground state and metastable levels. Radiative relaxation times for the ground state vibrational levels of molecules are typically long, too, and the above quasi-steady-state approximation may not be appropriate.

The first approach to a manageable collisional radiative (CR) model for the population densities of an ion (atom, molecule) is to solve Eq. (3.21) considering the following processes (omitting photoexcitation and photoionization):

- Electron collisional transitions out of the level (i) and into the level from all other levels of the ion,
- Radiative decay to all lower levels and cascading contributions from all higher levels,
- Collisional ionization to the ground state (g) of the next ionization state $(Z + 1)$ and three-body recombination from those states,
- Radiative recombination and dielectronic recombination.

Detailed information about three-body recombination and dielectronic recombination available in [Kunze 2009]. Thus, the collisional-radiative model gives:

$$
\begin{aligned}
\frac{\mathrm{d}n_i^{(Z)}}{\mathrm{dt}} = \quad & -\sum_{k<i} n_i^{(Z)} A_{ik}^{(Z)} && + && \sum_{k>i} n_k^{(Z)} A_{ki}^{(Z)} \\
& -n_e \sum_{k\neq i} n_i^{(Z)} X_{ik}^{(Z)} && + && n_e \sum_{k\neq i} n_k^{(Z)} X_{ki}^{(Z)} \\
& -n_e n_i^{(Z)} S_{i\infty}^{(Z)} && + && n_i^{(Z+1)} n_e \alpha_{(Z+1)}^{RR}(\infty \rightarrow i) \\
& && + && n_i^{(Z+1)} n_e \alpha_{(Z+1)}^{DR}(\infty \rightarrow i) \\
& && + && n_i^{(Z+1)} n_e^2 \alpha_{(Z+1)}^{TR}(\infty \rightarrow i) \qquad (3.22)
\end{aligned}
$$

Here, $S_{i\infty}^{(Z)}$ denotes the electron impact ionization coefficient, $\alpha_{(Z+1)}^{RR}(i \rightarrow \infty)$ denotes the **radiative recombination** coefficient, $\alpha_{(Z+1)}^{DR}(i \rightarrow \infty)$ denotes the **dielectronic recombination** coefficient, $\alpha_{(Z+1)}^{TR}(i \rightarrow \infty)$ denotes the **three-body recombination** coefficient.

For the derivative of the ground state density $n_g^{(Z)}$, in principle terms with ionization from and recombination into levels of the lower ionization stage $(Z - 1)$ should be added. They are redundant only for neutral atoms (molecules), but a corresponding equation holds for $n_\infty^{(Z+1)}$. Mathematically this set of rates $Eq.$ (3.22) describes the dynamics of the population vector $\bar{n}_Z = \{n_g^{(Z+1)}, \cdots, n_{i=\infty}^{(Z)}, \cdots, n_g^{(Z)}\}$,

$$\frac{d}{dt}\begin{pmatrix} n_g^{(Z+1)} \\ \vdots \\ n_{i=\infty}^{(Z)} \\ \vdots \\ n_g^{(Z)} \\ \\ \end{pmatrix} = \begin{pmatrix} 0 & \cdots & n_e S_{i\infty}^{(Z)} & \cdots & \cdots \\ \vdots & \vdots & \vdots & \vdots & \vdots \\ \cdots & \cdots & \cdots & \cdots & \cdots \\ \vdots & \vdots & \vdots & \vdots & \vdots \\ \cdots & \cdots & \cdots & \cdots & \cdots \\ \\ \end{pmatrix}\begin{pmatrix} n_g^{(Z+1)} \\ \vdots \\ n_{i=\infty}^{(Z)} \\ \vdots \\ n_g^{(Z)} \\ \\ \end{pmatrix} \qquad (3.23)$$

and the matrix contains all the possible radiative and collisional transition.

As discussed above, excited states reach quasi-steady state on very short time scales compared to the changes of the densities of the ground states and metastable states and of the plasma parameters, $\tau_{transition} \ll \tau_{plasma}$. This allows a realistic approximation where the time variation is kept only for the ground states and perhaps metastable states, and all excited levels are considered being in quasi-equilibrium with their ground state: $dn_g^{(Z)}/dt = 0$. This implies that they follow instantaneously the variation of the ground-state density. Therefore, the matrix equation may be replaced by a set of coupled linear equations which can be solved for assumed input ground-state densities $n_g^{(Z)}$ and $n_g^{(Z+1)}$. The results are substituted into $Eq.$ (3.22) for the ground-state density leading to an equation of the type:

$$\frac{\mathrm{d}n_g^{(Z)}}{\mathrm{dt}} = -n_e n_g^{(Z)} S_{(Z)}^{eff}(T_e, n_e) + n_g^{(Z+1)} n_e \alpha_{(Z+1)}^{eff}(T_e, n_e) \qquad (3.24)$$

$S_{(Z)}^{eff}$ and $\alpha_{(Z+1)}^{eff}$ are called effective collisional-radiative ionization and recombination coefficients, and both are functions of electron temperature T_e and weakly depend on density n_e. $S_{(Z)}^{eff}$ considers multi-step excitation and de-excitation followed finally by ionization, and discounts electrons which return to the ground state. Likewise, $\alpha_{(Z+1)}^{eff}$ accounts for all recombination processes ending in the ground state. In the other energy states:

$$\frac{\mathrm{d}n_i^{(Z)}}{\mathrm{dt}} = -n_e n_i^{(Z)}\left(S_{(Z)}^{eff} + \alpha_{(Z+1)}^{eff}\right) + n_i^{(Z+1)} n_e \alpha_{(Z+1)}^{eff} + n_e n_i^{(Z-1)} S_{(Z-1)}^{eff} \qquad (3.25)$$

For a given species S at steady state, the fractional abundances $f_{S,i}$ can be calculated by summing iteratively $Eq.$ (3.25) for each ionization state (i):

$$f_{S,i} = \frac{n_{S,i}}{n_S} \qquad (3.26)$$

A number of collisional-radiative models have been developed, in many cases adapted to specific needs. We shall mention only some examples of broader interest. In the model for hydrogen-like ions by

[Ljepojevic 1984], fine structure components were treated separately and proton collisions between the fine structure levels were included. This is necessary for hydrogen-like ions in tokamak plasmas and solar flares.

A generalized collisional-radiative model has been setup by [Summers 2006] that includes dielectronic recombination and accounts for metastable levels, which requires a detailed specific classification of the level structure for both recombining and recombined ions. Bundling of levels was used whenever meaningful. Atomic structure data and radiative and collisional data are taken from ADAS. Several models of varying complexity have been set up for helium-like ions because of their usefulness in diagnostic applications, especially at low and intermediate densities [Fujimoto 1984, Rosmej 1997]. Dielectronic capture from hydrogen-like ions and inner shell excitation from lithium-like and beryllium-like ions were included, as were charge exchange with neutral hydrogen and particle transport, and even a non-Maxwellian velocity distribution was allowed for. A very useful tool is provided by the FLYCHK code [Chung 2005], which allows steady-state and time-dependent calculations of population and charge-state distributions from low to high-Z elements.

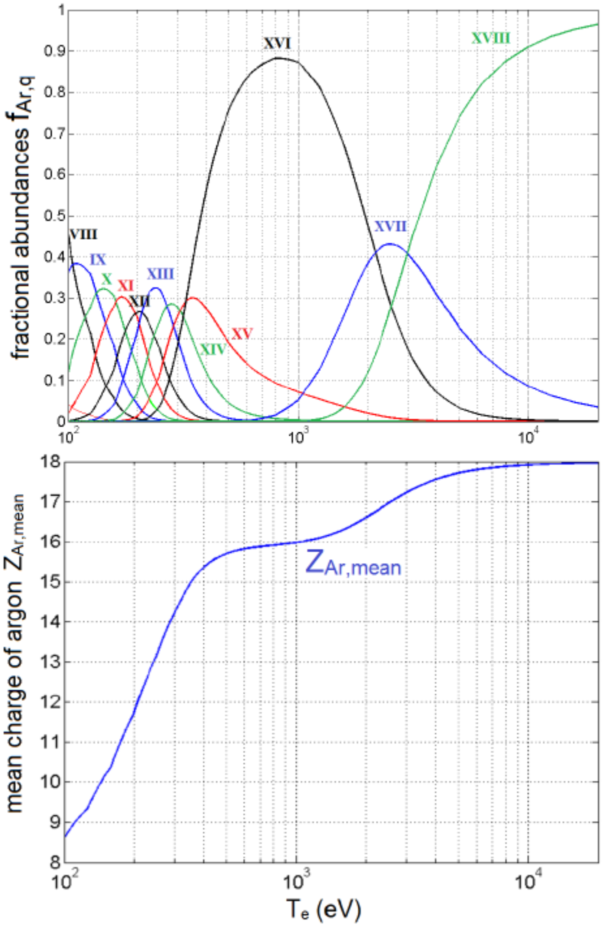

Figure 3.6. Top: Ionization equilibrium of argon as a function of electron temperature. Bottom: average charge of argon in the temperature range 0.1 - 20 keV, calculated using the ADAS CR effective ionization and recombination coefficients. Figure reprinted from [Jardin 2017].

3.1.3. Cooling factor

Up to now, we have discussed the mechanism of soft X-ray radiation in fusion plasmas, which follows the collisional-radiation model and gives the ionization equilibrium. Therefore, the contribution of one species S of the plasma to the local soft X-ray (SXR) emissivity is as follows:

$$\varepsilon_S\left(h\nu, T_e, n_e, \vec{\Gamma}_{S,q}\right) =$$

$$n_e n_S \sum_{i=0}^{Z_S} f_{S,q}\left(T_e, n_e, \vec{\Gamma}_{S,q}\right).\left[\epsilon_{S,i}^{f-f}(T_e, n_e, h\nu) + \epsilon_{S,i}^{f-b}(T_e, n_e, h\nu) + \epsilon_{S,i}^{b-b}(T_e, n_e, h\nu)\right], \qquad (3.27)$$

where $f_{S,q}$ is the fractional abundance of the q-th ionization state of S which is obtained from Eq. (3.26), $\vec{\Gamma}_{S,q}$ its local particle flux and $\epsilon_{S,q}^{f-f}$, $\epsilon_{S,q}^{f-b}$, $\epsilon_{S,q}^{b-b}$ are its free-free, free-bound and bound-bound emissivity coefficients. Ignoring the dependence on n_e, which is weak anyway, while in the core the electron density profile is relatively flat, and disregarding transport effects governed by $\vec{\Gamma}_{S,q}$ (see *Chapter 6*), the calculation simplifies as:

$$\varepsilon_S(h\nu, T_e) = n_e n_S \sum_{i=0}^{Z_S} f_{S,i}(T_e).\left[\epsilon_{S,i}^{f-f}(T_e, h\nu) + \epsilon_{S,i}^{f-b}(T_e, h\nu) + \epsilon_{S,i}^{b-b}(T_e, h\nu)\right] \qquad (3.28)$$

By defining the cooling factor of S:

$$L_S(h\nu, T_e) = \sum_{i=0}^{Z_S} f_{S,i}(T_e).\left[\epsilon_{S,i}^{f-f}(T_e, h\nu) + \epsilon_{S,i}^{f-b}(T_e, h\nu) + \epsilon_{S,i}^{b-b}(T_e, h\nu)\right], \qquad (3.29)$$

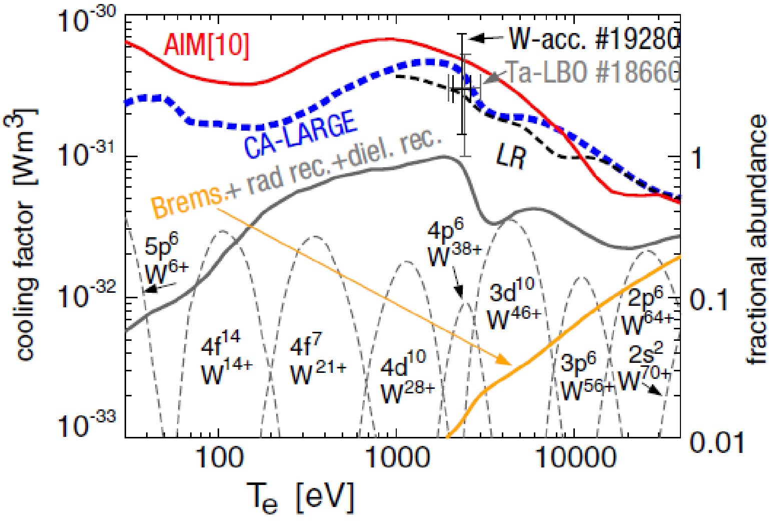

Figure 3.7. The spectrally integrated cooling factors of W from AIM [Post 1955] (red, thick, solid) and those derived from the LR (black, thin, dashed) and CA-LARGE (blue, thick, dashed) calculations are presented. The summed contributions (contained in the total cooling factors from LR and CA-LARGE) due to radiative and dielectronic

recombination and by bremsstrahlung are given as an additional curve (grey, thick, solid). The bremsstrahlung contribution is also presented separately (orange, thick, solid). The fractional abundances are presented for a few ionization stages [Putterich 2010].

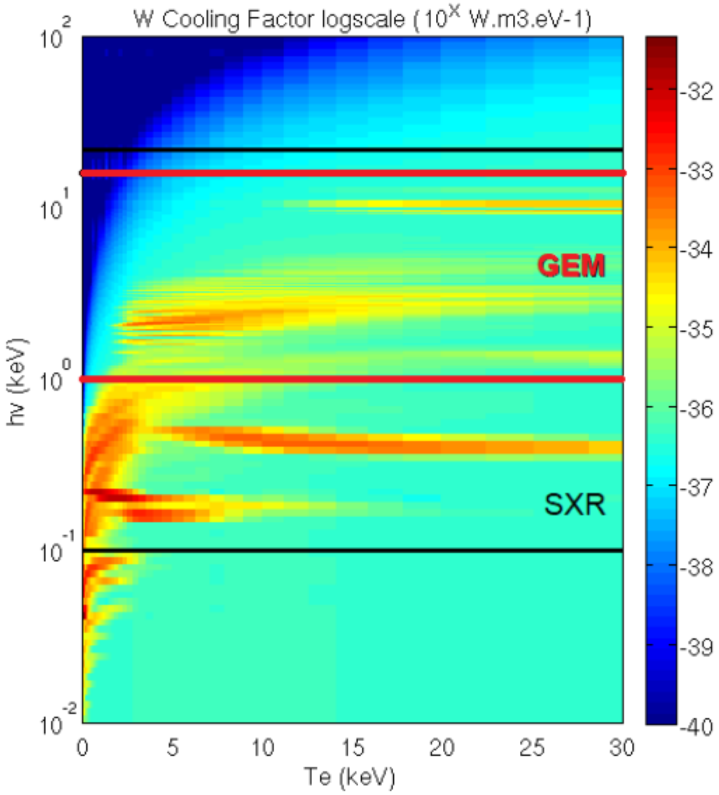

Figure 3.8. Estimated tungsten spectral radiation (W.m3.eV-1) as a function of photon energy and plasma temperature (semi-log scale). The black line indicates the soft X-ray radiation range and the red line indicates the Gas Electron Multiplier (GEM) camera measuring range. Figure reprinted from [Jardin 2017].

we obtain the final simplified expression, in which the SXR emissivity depends only on the density of the considered species and on the electron density and temperature:

$$\varepsilon_S(h\nu, n_S, n_e, T_e) = n_e . n_S . L_S(h\nu, T_e) \tag{3.30}$$

This is a most valuable parameter that offers the possibility to distinguish the contributions from different species in the plasma. For example, in a hydrogen plasma with tungsten impurities only, the total SXR emissivity observed by the detection system (without considering the detector spectral response) is:

$$\varepsilon_{SXR}(h\nu) = n_e^2 . [L_H(h\nu, T_e) + c_W . L_W(h\nu, T_e)], \tag{3.31}$$

were $c_W = n_W / n_e$ is the tungsten concentration. Indeed, the local tungsten concentration can be estimated from SXR emissivity measurements as:

$$c_W \simeq \frac{\varepsilon_{SXR}(h\nu) - n_e^2 . L_H(h\nu, T_e)}{n_e^2 . L_W(h\nu, T_e)} \tag{3.32}$$

3.2. SXR diagnostic on Tokamak

It is an established fact that the knowledge gained with and the performance of present fusion machines is directly linked to its diagnostic capability. Diagnostics for tokamak plasmas have generally been developed to study particular problems in tokamak research. Four major problem areas have been proposed by [Wesson 1987]:

- Methods of setting up grossly stable plasmas,
- Determination of the plasma energy and particle confinement time,
- Development of supplementary plasma heating methods,
- Study and control of plasma impurities.

With the mentioned concerns, the soft X-ray diagnostic plays an important role in tokamak research. In this section, we review the different detector technologies that can be used in tokamak plasmas for SXR detection. We also introduce the former SXR diagnostic of Tore Supra and the implementation of its new GEM-based diagnostic for WEST.

3.2.1. SXR detectors

Spectroscopy detectors can be classified according to their application, such as semiconductor detectors, photoionization detectors (gaseous detectors) and other miscellaneous detectors. The detectors convert radiant flux $\Phi(\lambda)$ in a spectral interval $\Delta\lambda$ into a current signal I_c, as presented in Figure 3.9, the magnitude of current signal which depends on the wavelength. The conversion efficiency is described by the spectral sensitivity $S(\lambda)$ which is defined as the ratio of output current of the detector to incident radiant flux,

$$S(\lambda) = \frac{I_c}{\Phi(\lambda)} \qquad (3.33)$$

$S(\lambda)$ [A/W] is also known as the responsivity of the detector.

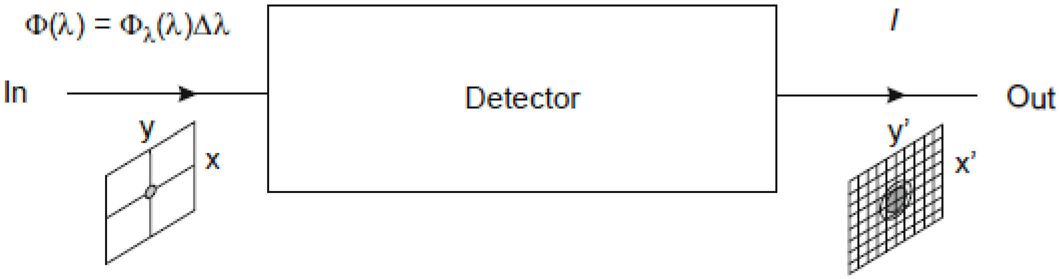

Figure 3.9. Schematic of a detector. Figure reprinted from [Kunze 2009].

It is convenient to introduce the quantum efficiency (or spectral response function) $\eta(\lambda)$ for photoemissive detectors, which gives the fraction of electrons released from the photocathode by one incident photon:

$$\eta(\lambda)=\frac{I_c}{\Phi(\lambda)}\frac{hc}{e\lambda}=S(\lambda)\frac{hc}{e\lambda} \qquad (3.34)$$

The quantum efficiency, i.e. spectral response of photodiodes used in the TCV tokamak is presented in Figure 3.10 as an illustration. A beryllium window cuts the signal below $\sim 1\ keV$. The discontinuity at $1.8\ keV$ is due to the K-alpha absorption line of silicon.

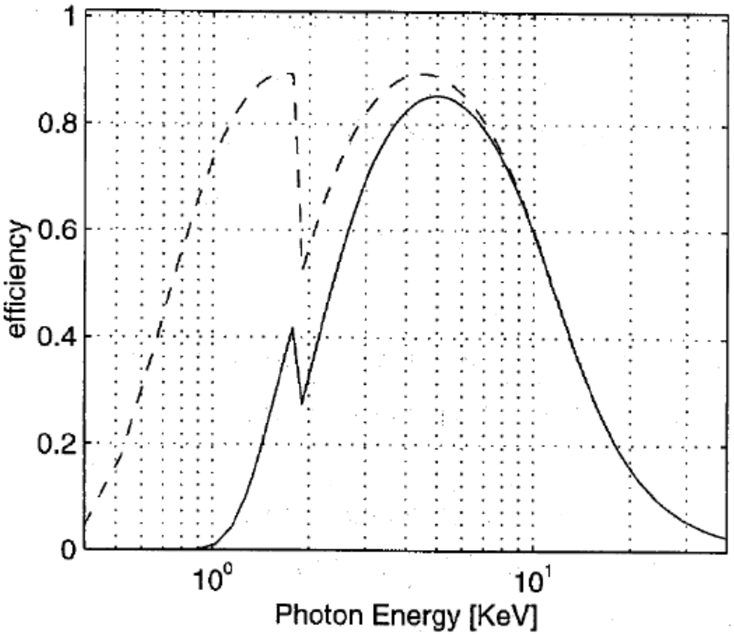

Figure 3.10. Spectral response of the SXR photodiodes of the TCV tokamak (dashed line: without the Beryllium filter). Figure reprinted from [Furno 2001].

The time response of the detector is crucial in case of rapidly varying radiation. This response is characterized either by the rise time T_r or by the bandwidth f_{bw}. The rise time refers to the time of the output current I to rise from 10 to 90% of the peak value if the input radiation is described by a step function. The bandwidth is defined as the cut-off frequency in Hertz at which the amplitude of the current is reduced to $1/\sqrt{2}$ of the value at low frequencies. Both are connected with each other by the relation [Kunze 2009]:

$$f_{bw}T_r \approx 0.35 \qquad (3.35)$$

Some detectors have an internal delay time which has to be taken into account when correlating signals. The output current in the absence of incident flux is called *dark current* which limits measurements at low flux levels. In most cases it is essentially thermal in origin and can be reduced by cooling the detector. The linearity of the system is another important characteristic. To quote the maximum linear output current is one possibility, the dynamic range is the other quantity used in that context. It is defined as the ratio of maximum to minimum detectable linear output current. In some applications the *time stability* could also be important as well as the *life time* of the detector.

Array detectors record the spectrum (object) in the exit plane (x, y) of a spectrograph and produce a digitized image (x', y'), which can be viewed on a screen or further processed by a computer. The imaging quality of an array detector is characterized by a respective point-spread function $F(x', y')$, which describes the intensity distribution of a point object $f(x_0, y_0)$ in the image (x', y') plane of the detector:

$$f(x_0, y_0) \rightarrow F(x' - x'_0, y' - y'_0) \qquad (3.36)$$

Convolution with the instrument function of the spectrograph gives the instrument function of the entire spectrographic system.

3.2.1.1. Semiconductor photodiode detectors

The silicon-based semiconductor photodiodes for SXR diagnostic purpose has been widely adopted on tokamak devices, due to their simplicity of operation and relatively low economical cost, like Tore Supra, [Mazon 2012b] AUG, [Igochine 2010] TCV, [Anton 1996] JET [Alper 1994] and COMPASS. [Weinzettl 2010]. The photodiode is a kind of semiconductor detector which can convert the light signal into electrical current. This is based on the semiconductor features where the semiconductor materials have an electrical conductivity lower than conductors and higher than insulators, and the conductivity relies on the capacity of the electrons of the valence band to flow towards the conduction band. Thus the photoelectric effect exhibits an energy threshold. For instance, the energy gap between the conduction and valence bands of silicon is about 1.2 eV, while it is typically of several eV for insulators. Metallic materials generally have a higher conductivity due to their partially filled bands which play both the role of valence and conduction band. Semiconductors act like insulators at rest and at temperature $\mathrm{T} = 0\ \mathrm{K}$, however with increasing temperature thermalized electrons can flow more easily to the conduction band. External excitation like absorption of incident photons can also provide the energy necessary to make electrons of the valence band go to the conduction band.

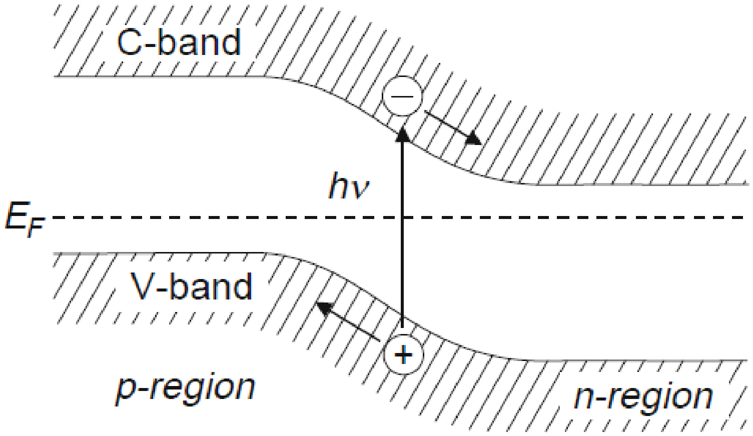

Figure 3.11. Energy diagram of a P–N junction. Figure reprinted from [Kunze 2009].

A photodiode is a P–N junction or PIN structure. When a photon of sufficient energy strikes the diode, it creates an electron-hole pair. This mechanism is also known as the inner photoelectric effect [Einstein 1905]. If the absorption occurs in the junction's depletion region, or one diffusion length away from it, these carriers are swept from the junction by the built-in electric field of the depletion region. Thus holes move toward the anode, and electrons toward the cathode, and a photocurrent is produced. The total current through the photodiode is the sum of the dark current (current that is generated in the absence of light) and the photocurrent, so the dark current must be minimized to maximize the sensitivity of the device.

Figure 3.11 shows the respective energy diagram with conduction and valence bands. The Fermi level is indicated by the Fermi energy E_{Fermi}. The transition region is characterized by a depletion of charge carriers: diffusion of holes from the *P*-region into the *N*-region and in the opposite direction of electrons into the *P*-region leads to the buildup of an electric double layer and a corresponding electric field, which drives an opposite current that finally compensates the diffusion current. Depletion regions can be made large.

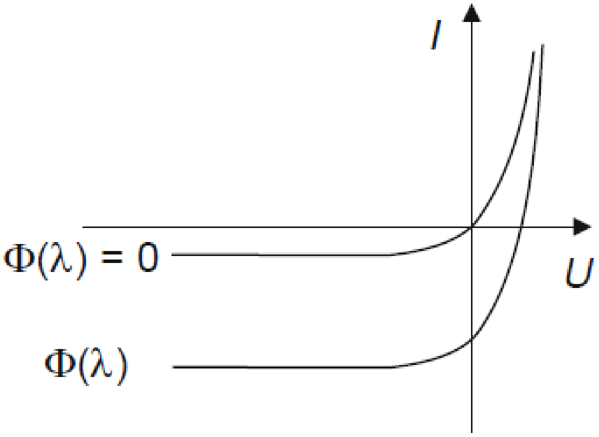

Figure 3.12. current–voltage characteristics of a photodiode. Figure reprinted from [Kunze 2009].

Electrons and holes produced by absorption of photons in the depletion region result in a current which depends on the applied voltage. In the Figure 3.12, the current–voltage characteristic $I = f(U)$ for an arbitrary flux $\Phi(\lambda)$ and for no illumination have been presented. As detectors, these photodiodes are operated with reversed bias voltage $\mathrm{U} < 0$. The current becomes independent of the voltage as long as it is large enough:

$$I_c = -e\frac{\eta(\lambda)\Phi(\lambda)}{hv} + I_d \qquad (3.37)$$

where I_d is the dark current. Noise of the dark current, which also here limits the sensitivity, can again be significantly reduced by cooling.

For photodiodes, the high quantum efficiency or spectral response $\eta(\lambda)$ (typically 80%) is one of the most important advantages, an example of TCV SXR photodiode response function has been presented in Figure 3.10. The photodiodes are compact, rugged, and insensitive to magnetic fields. The bandwidth of the frequency response is essentially determined by the load resistance and the capacitance of the depletion layer. Since its width increases with increased reversed bias voltage, thus decreasing the capacitance, photodiodes can be made very fast, where the drift time of the carriers through the depletion layer determines the final cut-off.

Several variations of the basic type of photodiode have been developed and are used in spectroscopy. The *PIN* diodes are an extension of the *P–N* junction: an un-doped zone (*I*) of the intrinsic semiconductor separates the *P*- and *N*-regions, which are produced by having the respective dopants diffused into the intrinsic semiconductor. Absorption is now in the *I*-zone, which can be made very wide and thus allows a fast response. Photodiodes with bandwidths of gigahertz are possible. Silicon PIN diodes can therefore be fast enough to operate in photon-counting mode, with dedicated acquisition systems such as multi-channel analyzers [Vezinet 2013].

Table. 3.1. Photodiodes based on different materials and working temperature. [Kunze 2009]

Material	Spectral range μm	T K	Material	Spectral range μm	T K
Si	0.4–1.1	295	InAs	0.6–3.2	77
Ge	0.5–1.8	295	InSb	0.6–5.6	77
InGaAsP	1.0–1.7	295	HgCdTe	2–15	77
InAs	0.9–5.2	295	PbSnTe	8–12	77

There exists a large variety of photodiodes offered by manufacturers. Silicon is the most important semiconductor material. On the other hand, germanium diodes have a wider spectral sensitivity but a larger dark current. Table 3.1 displays examples of photodiodes. The alloy HgCdTe is included, whose bandgap depends on its stoichiometry. For the vacuum-ultraviolet and soft X-ray spectral applications, silicon photodiodes with thin oxide layers have been proved to be stable and suitable detectors for absolute flux measurements [Gullikson 1996, Canfield 2000]. Reverse-biased *PIN* diodes of silicon and germanium can also make excellent energy-resolving detectors of single X-ray photons from about $1\ \mathrm{keV}$ to few hundreds of keV. The diode is nearly fully depleted and thus provides a large detector volume. The photons interact in the intrinsic region and produce the tracks of electron-hole pairs. $3.6\ \mathrm{eV}$ are needed to generate one electron-hole pair in silicon, and $2.98\ \mathrm{eV}$ in germanium. The recorded current pulse of a single photon is a direct measure of its energy, which thus can be obtained via pulse-height analysis. A variant is the lithium-drifted silicon, Si(Li), detector, where a large sensitive volume is created by having lithium atoms drifted into slightly *P*-doped silicon. The energy resolution is often limited, typically to about $150\ \mathrm{eV}$, but no spectrograph is needed. The resolution suffices for measurements of the continuum radiation of long-lived hot plasmas like those of tokamaks.

3.2.1.2. Gaseous detectors

Gaseous detectors have been widely applied in nuclear related industry or high energy physics, for example at CERN for the detection of ionizing particles. They are descendant of the previously mentioned semiconductor detectors and have even more promising capabilities in terms of spatial resolution, signal amplification, resilience to sparks and above all reliability under harsh operating conditions and high flux environment.The fundamental process in these detectors is the ionization of gases by photons and subsequent measurement of the produced charges. The probability of absorbing the incident photons within the gas volume may approach 100% if gas type and dimensions of the device have been properly designed. A long wavelength limit is naturally given by the ionization energy of the gas atoms or molecules. Such detectors are thus suited for the X-ray region. Two schemes used in spectroscopy are *ionization chambers* and *proportional chambers*.

LOW VOLTAGE IONIZATION CHAMBER

A low voltage ionization chamber (LVIC) detector as an X-ray diagnostic concept has been reported of particular interest for ITER [Hu 2017]. The ITER Radial X-ray Camera (RXC) will be operable under conditions of high neutron and γ-ray fluxes that are expected to exist in D–T operation. Since it is impossible to use any electronic devices near the tokamak under these conditions, amplifiers must be located several tens of meters away from detectors. In this case, stray and other pickups present a serious problem. From this point of view, it is desirable, on the one hand, that a means for raising the detector signal be provided and, on the other, that a system for noise rejection be developed. The VPD system described in [Gott 2005] and using successive parallel anode and cathode plates separated by about $1 - 5\ \mathrm{mm}$ was filled with air (and some noble gases) and operated as an ionization chamber [Gott 2009]. The supplied voltage was about $10\ \mathrm{V}$, making it possible to place the amplifier at several tens of meters from the detector to protect it from plasma radiation. It could be coupled with a high frequency noise suppression system. Under similar experimental conditions, the sensitivity of the LVIC filled with air at atmospheric pressure was found $100 - 200$ higher than in the VPD configuration. This was increased even more by using noble gases like Ar, Ne and Xe instead of air. The LVIC technology seems to present significant advantages in terms of gamma and neutron resilience compared to traditional semiconductor technologies, and could be a potential candidate for ITER.

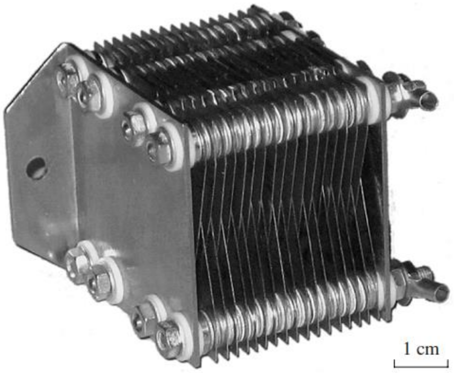

Figure 3.13. Picture of the LVIC electrode system. Figure reprinted from [Gott 2009].

MULTI-WIRE PROPORTIONAL CHAMBER

When increasing the voltage applied to an ionization chamber the electrons gain enough energy to ionize further atoms, and at sufficiently high voltages an electron avalanche will finally develop. Within some voltage range known as *proportional regime* the magnitude of the current pulse varies linearly with the voltage and the amplification is typically $10^3 - 10^5$. At still higher voltages, a discharge develops and the device becomes a Geiger–Muller counter. Proportional chambers can be used in the photon counting or in the current mode. Counting rates can be as high as $10^6\ \mathrm{s}^{-1}$. For the spectroscopy of hot magnetically confined fusion plasmas, the multi-wire proportional chambers (MWPCs) are widely employed detectors in the exit plane of X-ray spectrographs[Weinheimer 2001]. In a simple picture, MWPCs are many single wire units closely placed in parallel. The present designs consist of a grid of uniformly spaced anode wires sandwiched between two cathode planes, where the cathode on the entrance side behind the window is usually a wire grid; while the second cathode can be a series of strips or again a wire grid. Absorption of the photons is in the drift region after the first cathode; the very localized electron pulses on the anode wires induce image pulses on the cathode wires or strips that are the basis of position encoding; early designs also utilized readout from anode wires. The most highly developed and most frequently used techniques utilize a delay line [Boie 1982, Smith 2006]: all cathode wires or strips feed the nodes of the line, and the difference of the arrival times at both ends yields the position. For the analysis, the time information is converted into position by time-to-digital converters (TDCs), which are a crucial part of the detectors. By determining the centroid of the cathode charges, a spatial resolution approaching $0.1\mathrm{mm}$ is possible.

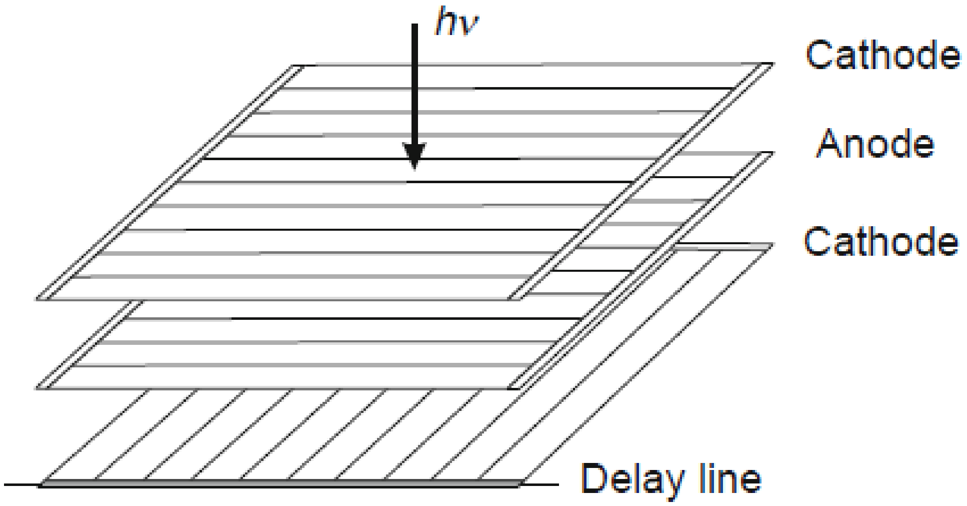

Figure 3.14. Scheme of a multi-wire proportional chamber (MWPC).

GAS ELECTRON MULTIPLIER

The gas electron multiplier (GEM) is another good detector candidate for the ITER RXC system, which is a quite recent technology developed at CERN by F. Sauli [Sauli 1997]. GEMs are very promising since they are cheap and quite robust against radiation damage. The basic element of a GEM is an insulating polymer foil, metalized on both sides and punched with an array of holes, which are typically of bi-conical shape. A voltage applied between both sides of the foil produces very high electrical fields (in order of $50 - 100\ \mathrm{kV \cdot cm^{-1}}$) in the holes, and electrons produced by the incident X-rays in the upper gas volume drift into the channels where they are accelerated and multiplied by collisional ionization: an avalanche develops over a very short distance and moves towards the electrodes in the lower volume. Electron multiplication up to 10^3 is possible. Figure 3.15 illustrates one variant of a two-stage array detector. A suitable resistor chain provides the voltages to the cathode, the two GEMs and to a matrix of readout pads, which are hit by the electron avalanches. The intrinsic advantage is obvious: the multiplication region is separate from the readout electrodes. A time resolution in the microsecond domain seems feasible.

The technology chosen for WEST's new soft X-ray diagnostic array system is a triple-GEM detector, which we will discuss in detail in *section 3.3*. Compared to the semiconductor detectors, gaseous detectors have the advantage of working with a constantly renewed detection volume not affected by aging (only electrodes and surrounding materials). They exhibit high sensitivity compared to semiconductor and vacuum photodiodes, but they have a low quantum efficiency and are slightly more complex to design with their gaseous part compared to solid-state detectors. LVIC [Gott 2009] has an advantage over the GEM due to its operation at low voltage, and because it allows the amplifiers to be placed several tens of meters away from the plasma. However, it is not designed to work in photon-counting mode.

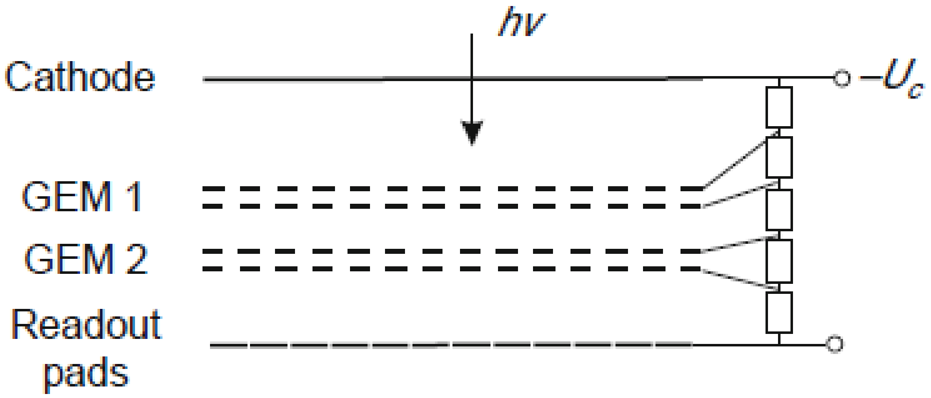

Figure 3.15. Scheme of a two-stage GEM detector.

3.2.2. Detector calibrations

Before the installation on experimental devices, the calibration of detectors, as well as defining and gradually refining a reliable experimental protocol, are necessary processes. In general, the calibration of a spectroscopic diagnostic includes *wavelength calibration* and *sensitivity calibration*.

The spectrographic systems are often supplied with wavelength calibration, but it is essential that the experimenter perform his own calibration for reliable measurement. A number of sources emitting well-known emission lines are available, and the best values of their wavelengths may be taken from databases accessible online. Data have been critically evaluated for many decades by the US National Institute of Standards and Technology (NIST). Optimal calibration is achieved if traces of these or other suitable elements can be added to the plasma to be investigated. For all spectral regions, such in situ calibration is inherently possible in a number of cases since many plasmas contain already small amounts of impurities from the walls such as carbon, oxygen, and their ions, whose spectra are very well known down to the soft X-ray region. In all cases, however, attention must be paid to possible Doppler shifts, which can be serious even for heavy ions in hot plasmas.

In particular, absolute spectral calibration of photodetectors remains a delicate task that requires a lot of precautions, the result of which depends on parameters such as the bias voltage (for semiconductor junctions), operating temperature, quality of the source, electromagnetic environment etc. Any photo-detector can be roughly described as a black box issuing a measurement M as a result of the spectral convolution of the incident photon flux $\Phi(\lambda)$ with a detector spectral response function $\eta(\lambda)$ as:

$$M = C \int_0^\infty \Phi(\lambda)\, \eta(\lambda)\, d\lambda. \qquad (3.38)$$

Here C is the appropriate conversion coefficient considering the electronic noise etc.

3.3. Gas Electron Multiplier (GEM) on WEST

As mentioned above, the triple-GEM detector has been chosen for WEST's new soft X-ray diagnostic array system [Mazon 2016]. The WEST SXR system is composed of two sets of 1D array cameras (vertical and horizontal views respectively), located in the same poloidal cross-section to allow for tomographic reconstruction, as presented in **Figure 3.16**. An array (about $20\ cm \times 2\ cm$) consists of up to 128 detecting pixels in front of a $50\ \mu m$ wide Beryllium pinhole (with a $1\ mm$ diameter diaphragm) inserted in the case of the vertical camera at about $50\ cm$ depth inside an optimized water-cooled thimble.

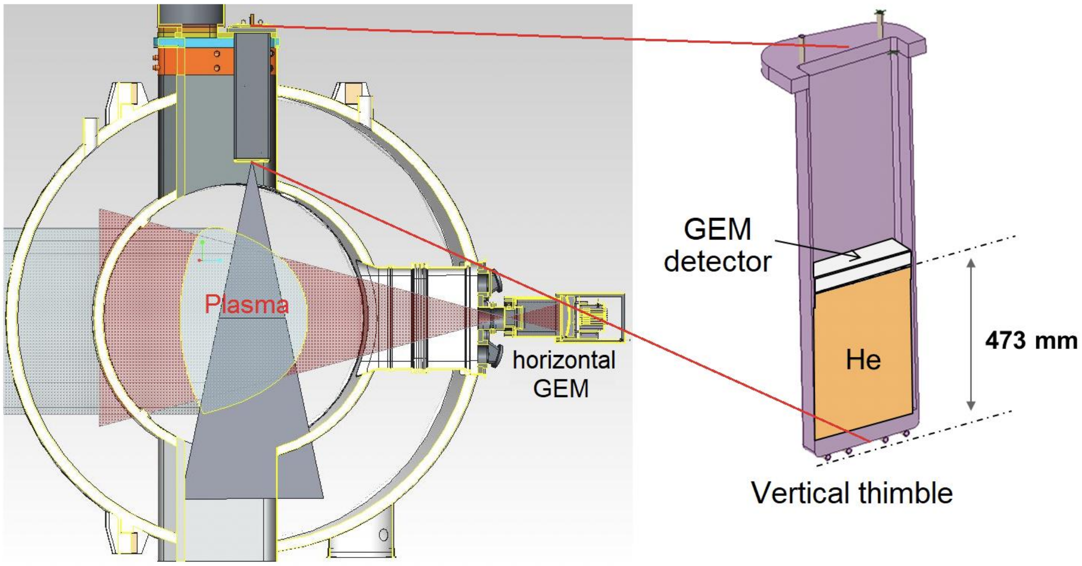

Figure 3.16. Left: Integration and geometric coverage of the new SXR diagnostic of WEST, composed of two GEM-based cameras. Right: Illustration of the GEM detector and helium buffer inside the vertical thimble. Figure reprinted from [Mazon 2016].

The horizontal camera remains outside the port as illustrated in **Figure 3.16**. The time resolution has been selected as follows: $\sim\ 1\ kHz$ for real-time (online) application and $0.1\ kHz$ for non-real-time (offline) application. Acquisition of the low-energy spectrum is insured by a helium buffer installed between the pinhole and the detector. Without the helium buffer, the 47 cm of air would absorb the SXR spectrum below $4\ \mathrm{keV}$. Internal to the He buffer a supporting structure for two Fe^{55} radioactive sources will insure permanent calibration of the GEM detector, as shown in **Figure 3.17**. Below these sources, a motorized slit (piezoelectric motors) is installed in order to protect the GEM in case of high photon fluxes and thus avoid saturation ($\sim\ 10^7\ ph/s/mm^2$). Complementary cooling systems (water) are used to maintain a constant temperature (27^oC) inside the detector. The GEM detector operates slightly above atmospheric pressure. An extraction system of the cassette containing the GEM detector for the horizontal camera has been designed in order to extract the detector easily during baking and maintenance phases. A spatial resolution of $1cm$ in the equatorial plane was estimated to be sufficient for obtaining accurate information about the location of the magnetic axis, the sawteeth inversion radius, impurity density gradients, and more generally to get a good tomographic image. This new spatial resolution of $1\ cm$ is to be compared with the former one of $4\ cm$ used for Tore Supra discharges, which was already sufficient for studies of impurity transport and MHD activity (10-100 kHz).

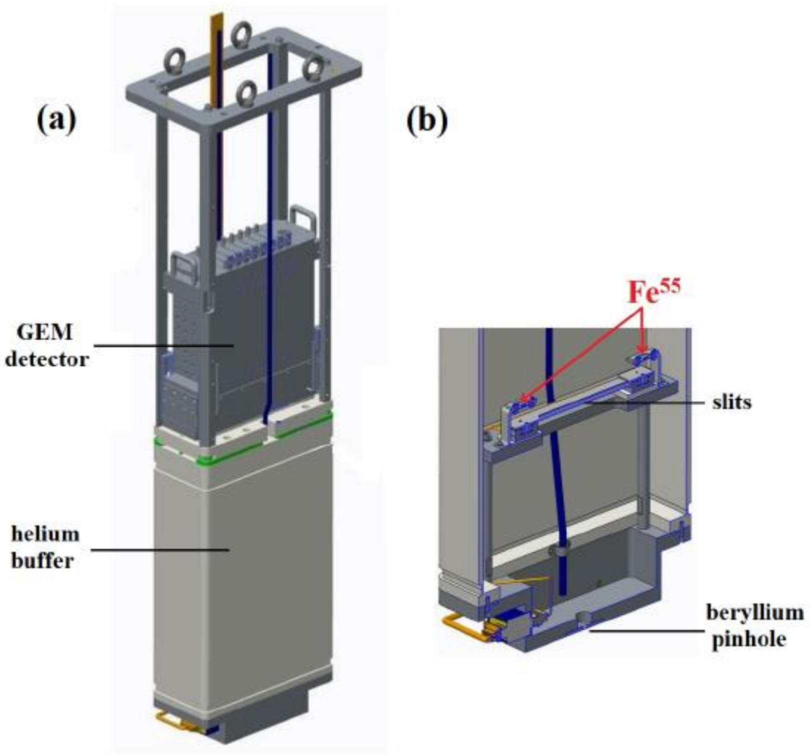

Figure 3.17. a) GEM detector with electronics and He buffer inside the cassettel b) internal structure of the He buffer with the supporting Fe55 sources structures and slits [Mazon 2016].

Furthermore, the GEM system was requested to enable spectral discrimination of the signal, i.e. to perform photon counting in several energy bands. A radioactive iron source (Fe^{55}) emitting $5.9\ \mathrm{keV}$ photons was commonly used to perform acquisition tests on the GEM as presented in **Figure 3.18**.

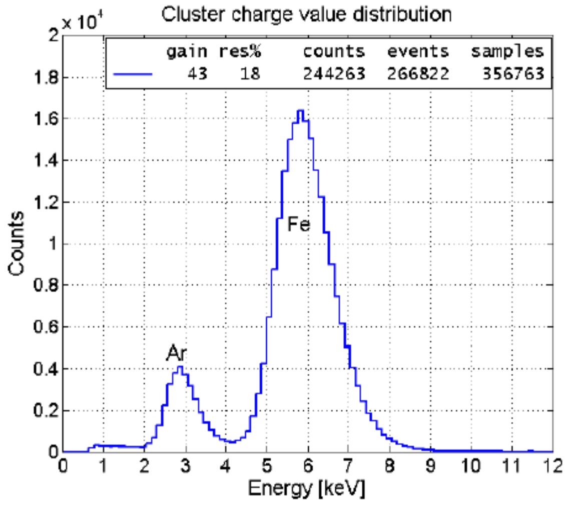

Figure 3.18. GEM acquisition of a Fe55 source ($5.9\ \mathrm{keV}$). The presence of an argon peak is due to the gas mixture inside the GEM. Figure reprinted from [Jardin 2017].

Such a Fe55 source is crucial for the GEM spectral calibration since the detector gain varies with pressure, purity of the flowing gas mixture or applied voltages.

Figure 3.19 presents the operation principle inside triple-GEM detectors:

1) The incident photon passes through the cathode (usually manufactured by aluminized Mylar foil with a thickness of few $10\ \mu m$) and has a certain possibility to generate an ion-electron pair by photoionization of an atom from the GEM gas mixture (here as an example composed of Argon at 70% and $\mathrm{CO_2}$ at 30%).
2) This photo-electron pair produces a primary electron cloud in conversion region, and then the generated electron cloud drifts toward the amplification area.
3) The primary cloud is amplified by successive electron avalanches in the 3 GEM foils (micrometric perforated copper-clad Kapton foils) under high voltage $\mathrm{V}_{GEM} \approx 400\ \mathrm{V}$, leading to an electric field of $\sim 50 - 100\ \mathrm{kV/cm}$.
4) The electron cloud drifts and diffuses in the gas toward the anode due to the imposed electric fields $\vec{\mathrm{E}}_I, \vec{\mathrm{E}}_T, \vec{\mathrm{E}}_C$ of a few $\mathrm{kV/cm}$.
5) The resulting current is finally detected on the anode strips (pixels) above the electronic noise. Indeed, the multiplicative foils allow the GEM to be sensitive enough (and fast enough with dedicated electronics) to work in photon-counting mode.
6) The detector works in proportional regime and the detector gain is determined by the high voltage applied on the GEM foils used for avalanche, such that the photon energy can be inferred from the total collected charge Q_{tot} of the cluster, provided that the detector has been calibrated and the photon rate is sufficiently low to avoid pile-up effects. Thus, the charge, time and position values of each cluster are finally computed and stored.

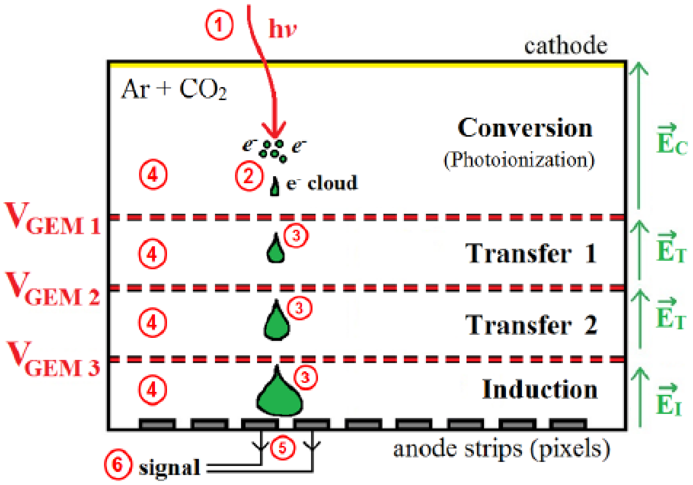

Figure 3.19. Basic sketch of the GEM detector principle with 1) the SXR source, 2) photoionization in the gas mixture, 3) electron avalanches through GEM holes, 4) electron cloud transport in the drift regions, 5) collection of the electron cloud on the anode and 6) post-processing of the GEM signal to compute the charge, time and position of each incident photon. Figure reprinted from [Jardin 2017].

Due to the interest in inferring tungsten impurity distributions, the energy resolution of the WEST GEM has been designed in terms of 5 energy bands, as presented in Figure 3.20, where

- the first energy band is characterized by $h\nu \ < \ 1.8\ keV$,
- second energy band $1.8\ keV \ \leq h\nu \ < \ 2.8\ keV$
- third energy band $1.8\ keV \ \leq h\nu \ < \ 4\ keV$,
- fourth energy band $4\ keV \ \leq h\nu \ < \ 8\ keV$
- and fifth energy band $8\ keV \ \leq h\nu \ < \ 15\ keV$.

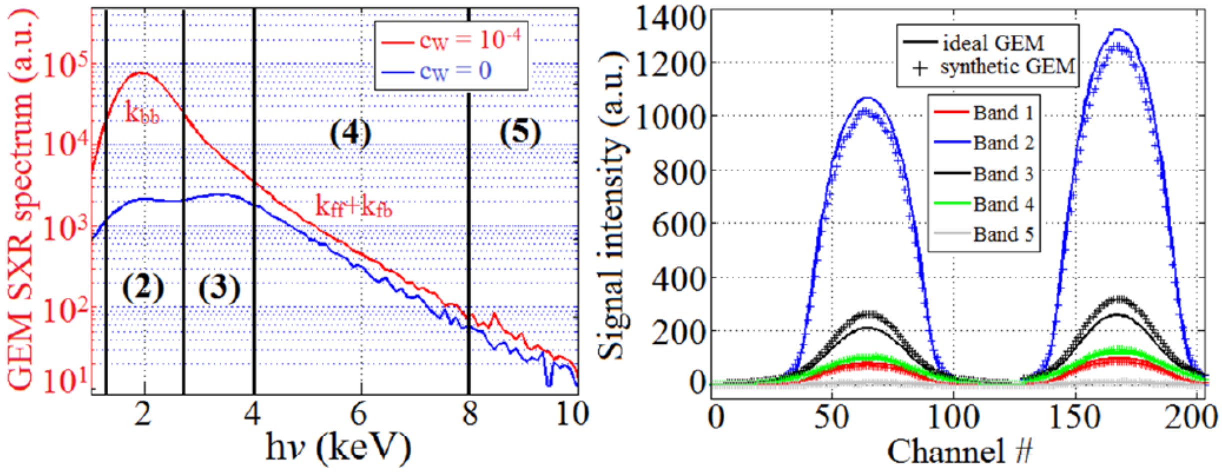

Figure 3.20. Left: GEM cumulated spectrum obtained from a simulation. Right: GEM signal in 5 energy bands . Figure reprinted from [Jardin 2017].

Chapter 4 Tomography and Bayesian inference

Tomography is a well-known term from application in medical imaging, more particularly the computer tomography (CT) scan. It involves combination by a computer of many X-ray measurements taken from different angles to produce cross-sectional (tomographic) images (virtual 'slices') of specific areas of a scanned object, allowing the user to see inside the object without cutting. In the fusion area, this technique has also been widely used for reconstruction of the distribution of a quantity in a poloidal cross-section based on line-integrated measurements. Particularly for soft X-ray diagnostics, the technique was pioneered by groups in several laboratories starting with a single camera, exploiting the natural plasma rotation. This is the concept of Abel inversion [Bockasten 1961], which is actually a 1-D reconstruction. After a while, the 2-D full tomography with at least two cameras was developed at MIT [Camacho 1986, Granetz 1988]. With requirement to observe the details of an asymmetric distribution in the plasma, the SXR system was updated with even more cameras afterwards [Decoste 1985, Cruz 1994, Alper 1997, Anton 1995]. In this chapter, we begin our discussion with a detailed introduction of the tomography problem in the context of soft X-ray measurement. In addition, the framework of Bayesian inference be presented, explaining how it is used for tomographic reconstruction.

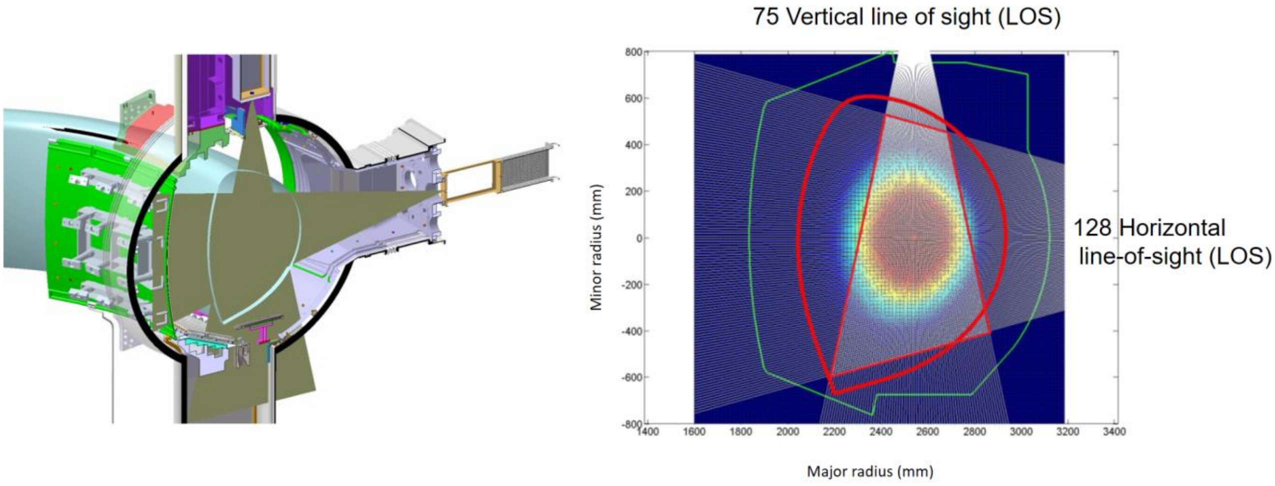

Figure 4.1. Tomographic capabilities of the WEST SXR system based on GEM detectors. The horizontal camera views along 128 lines-of-sight. The vertical camera is inside the vertical port and is coupled to 75 sight lines.

4.1. Tomography of line-integrated measurements

Reconstruction of a space-resolved image or profile of a plasma quantity using tomography has been considered on many fusion devices. Due to the high temporal resolution requirement, the tomography measurement on fusion devices is obtained from fixed detector arrays, in contrast to medical tomography. The measurement represents line-integrated emissivity through the approximated line-of-sights, determined by pin-hole positions. The line-of-sight approximation is based on [Ingesson 2000].

The tomographic problem essentially involves inference of a large set of physical parameters, namely the quantity of interest in a set of pixels in a two-dimensional cross-section, based on a limited number of measurements. This is an ill-posed problem, as the number of measurements is always lower than the number of unknowns. It is also often referred to as an *inverse problem*, as the goal is to invert the *forward model* that allows, in principle, to calculate the measurements ('effect') from the unknown parameters ('cause'). Other examples of inverse problems are source reconstruction in acoustics or calculating the density of the Earth from measurements of its gravitational field. Inverse problems are some of the most important mathematical challenges in science and mathematics, which involves to infer the parameters that we cannot directly observe.

In the context of this thesis, we consider tomography for a soft X-ray diagnostic at Tore Supra/WEST. The WEST SXR diagnostic system is presently being commissioned with two triple-gas electron multiplier (GEM) cameras, located in the same poloidal cross-section to allow tomographic reconstruction. As shown in Figure 4.1, one of the cameras of the WEST SXR diagnostic views along the horizontal direction through 128 lines-of-sight (LOS) from the low-field-side to the high-field-side. The other camera is located at the top of the device, viewing downwards along 75 lines-of-sight. Hence, the majority of the core plasma region is covered with a good spatial resolution (∼1 cm in the equatorial plane).

4.1.1. Modeling of SXR tomography

Generally, tomographic systems on fusion device have a relatively small aperture. Consequently, the measurement of the SXR emissivity (in W.m^{-2}) of the j-th detector $\boldsymbol{d_j}$ of a tomographic system can be approximated by the integration of the emissivity, filtered by the detector, along the corresponding line-of-sight:

$$d_j = \int_{LoS_j} E(r)\, dr \qquad (4.1)$$

Where $E(r)$ is the emissivity function at location r, LoS_j is the trajectory corresponds to j-th detector's line-of-sight. Spatial discretization of the poloidal cross-section is achieved by means of a square grid (with dimensions 1.6 × 1.6 m^2) comprising 100 × 100 square pixels, each associated with a homogeneous emissivity value. Then, the total SXR line-integrated measurement $\bar{d}_m$ can be written as:

$$\bar{d}_m = \bar{\bar{R}}_{m\times n} \cdot \bar{E}_n + \bar{\varepsilon}, \qquad (4.2)$$

where E_n is the local SXR emissivity in pixel n. In addition, $\bar{\bar{R}}_{m\times n}$ is the response matrix, wherein element (i,j) denotes the path length of the j-th LOS through the i-th pixel, as shown in Figure 4.2. Furthermore, $\bar{\varepsilon}$ represents a noise term, arising from various uncertainties, including detector noise.

As mentioned before, tomographic reconstruction (or inversion) is an ill-posed problem. Without additional information, there is an infinity of solutions. Regularization is the process of adding a priori information, often in the form of requirements or constraints on the solution, in order to render the problem well-posed with a less-broad regime of solutions, preferably converge to one single solution. We now go deeper into several standard regularization methods., before embarking on a discussion of the approach used in the present work, using Bayesian inference and Gaussian processes.

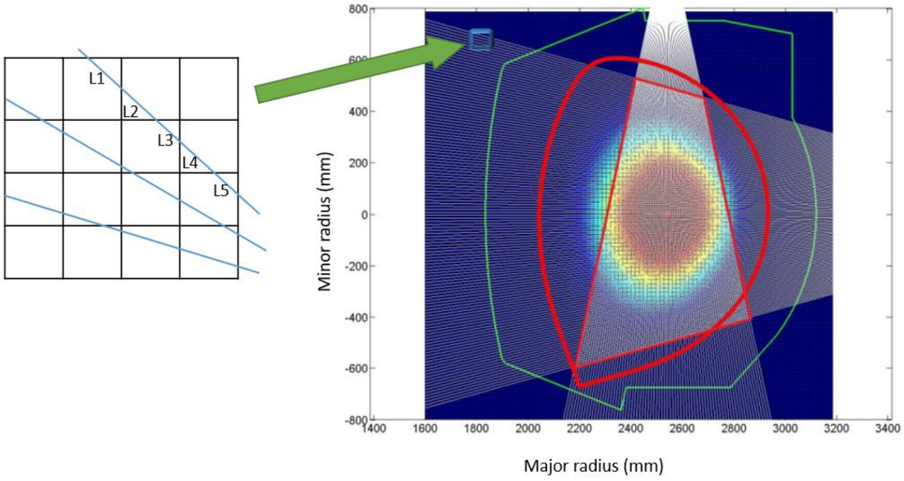

Figure 4.2. Illustration of the line-of-sight geometry in a poloidal cross-section.

4.1.2. Standard regularization approaches

In a standard tomographic solution, the objective is to find the optimized emissivity distribution based on the standard χ^2 criterion for the line-integrated measurements:

$$\chi^2(\bar{E}_n) = (\bar{d}_m - \bar{\bar{R}}_{m\times n}\cdot \bar{E}_n)^T(\bar{d}_m - \bar{\bar{R}}_{m\times n}\cdot \bar{E}_n) \tag{4.3}$$

This involves least squares minimization between the measured and modeled line-integrated emissivities. One common regularization technique is *Tikhonov regularization*, which involves adding a priori information on the expected emissivity profile [Tikhonov 1977]. In particular, a term ${\bar{E}_n}^T\bar{\bar{H}}\bar{E}_n$ is added to the cost function, imposing an additional constraint of smoothness of the solution. The optimization problem becomes

$$\bar{E}_{reconstructed} = arg\min_{\bar{E}_n}[\,\chi^2(\bar{E}_n) + \lambda\cdot {\bar{E}_n}^T\bar{\bar{H}}\bar{E}_n\,], \tag{4.4}$$

where the $\bar{\bar{H}}$ matrix is the regularization operator and λ denotes the regularization parameter. Thus, the tomographic reconstruction is a compromise between minimization of the residual and regularization of the solution. A vector derivative of the above equation allows determining a closed-form solution:

$$\bar{E}_{reconstructed} = (\bar{\bar{R}}^T\,\bar{\bar{R}} + \lambda \cdot \bar{\bar{H}})^{-1} \cdot \bar{\bar{R}}^T \cdot \bar{d}_m \tag{4.5}$$

The regularization parameter λ is a free parameter that quantifies the level of smoothness of the reconstructed profile. λ can be determined empirically, by adjusting χ^2 according to the experimental noise level, or via the L-curve method [Hansen 1992].

Depending on different choices of regularization term $\bar{\bar{H}}$ and optimization method for the regularization parameter λ, various tomography techniques can be distinguished. This includes the Fourier-Bessel method [Wang 1991], the Phillips-Tikhonov Regularization (PTR) method [Bielecki 2015], the minimum Fisher information (MFI) method [Anton 1996, Mazon 2012b], etc. Particularly the minimum Fisher information (MFI) technique has been widely adopted in the fusion community. This reconstruction method involves χ^2 optimization, regularized by the Fisher information (FI), defined as follows:

$$FI(\theta) = E\left([\frac{\partial}{\partial\theta} log\, f(X;\theta)]^2 \middle| \theta\right) = \int [\frac{\partial}{\partial\theta} log\, f(X;\theta)]^2 dX \tag{4.6}$$

Where θ is the unknown parameter, X is the measurement. Applied to the case of our discretized tomography model, the MFI regularization operator $\bar{\bar{H}}_{MFI}$ is given by

$$\bar{\bar{H}}_{MFI} = \bar{\bar{\nabla}}^T \bar{\bar{W}} \bar{\bar{\nabla}}, \tag{4.7}$$

where $\bar{\bar{\nabla}}$ denotes the discretized gradient operator and $\bar{\bar{W}}$ denotes the weight matrix:

$$\begin{cases} W_{ij} = \dfrac{1}{E_i}\delta_{ij}, & E_i \geq E_{min} \\ W_{ij} = \dfrac{1}{E_{min}}\delta_{ij}, & E_i < E_{min} \end{cases} \tag{4.8}$$

Here, δ_{ij} is Kronecker's delta and $E_{min} > 0$ the lower bound used for the zero emissivity regions to avoid unphysical results. The weight matrix $\bar{\bar{W}}$ imposes flatness at the plasma edge where the emissivity is close to zero, and decreases the constraint on the first derivative in the plasma core where, the emissivity is maximal, to avoid over smoothing in the core. Since the regularization operator $\bar{\bar{H}}_{MFI}$ depends on the unknown emissivity $\bar{E}_n$, an iterative algorithm is needed to converge to a stable solution, usually in $\mathrm{n} \sim 4-6$ steps from a first guess $\bar{E}_n{}^{(0)}$. Thus, the k-th iteration gives:

$$\begin{cases} W_{ij}{}^{(k)} = min\left(\dfrac{1}{E_i{}^{(k)}}, \dfrac{1}{E_{min}}\right)\delta_{ij}, \\ \bar{\bar{H}}_{MFI}{}^{(k)} = \bar{\bar{\nabla}}^T\, \bar{\bar{W}}^{(k)}\, \bar{\bar{\nabla}} \\ \bar{E}_n{}^{(k)} = (\bar{\bar{R}}^T\,\bar{\bar{R}} + \lambda \cdot \bar{E}_n{}^{(k-1)} \bar{\bar{H}}_{MFI}{}^{(k)} \bar{E}_n{}^{(k-1)})^{-1} \cdot \bar{\bar{R}}^T \cdot \bar{d}_m \end{cases} \tag{4.9}$$

Note that, in the above discussion, the magnetic equilibrium flux surface information has not been used yet. To do this, [Jardin 2017] has decomposed the regularization operator $\overline{\overline{H}}_{MFI}$ in a parallel and perpendicular part, w.r.t. the magnetic flux surfaces in the cross-section of interest:

$$\overline{\overline{H}}_{MFI} = (1-\tau)\,\overline{\overline{\nabla}}_{/\!/}^{\,T}\,\overline{\overline{W}}\,\overline{\overline{\nabla}}_{/\!/} + \tau\,\overline{\overline{\nabla}}_{\perp}^{\,T}\,\overline{\overline{W}}\,\overline{\overline{\nabla}}_{\perp} \qquad (4.10)$$

The associated factor of anisotropic smoothing τ is introduced, with $0 < \tau < 0.5$, in order to account for the dominant parallel transport.

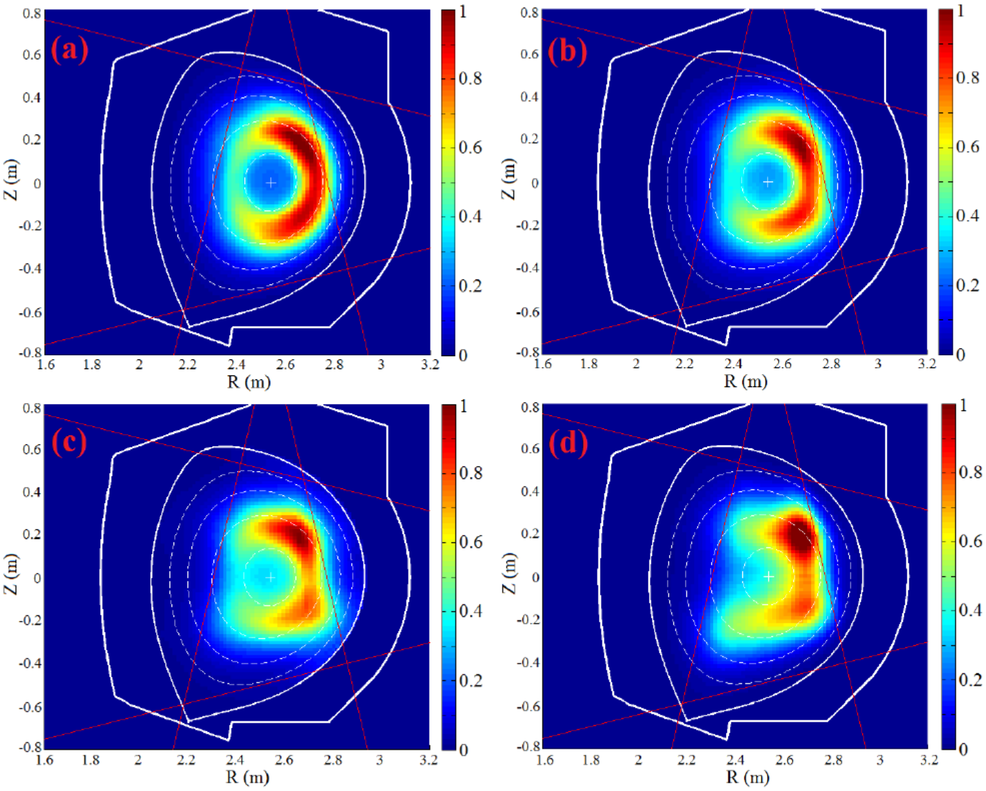

Figure 4.3. The effect of anisotropy factor τ on the reconstruction of a banana shape phantom test with (a) $\tau = 0.01$ (b) $\tau = 0.1$ (c) $\tau = 0.25$ (d) $\tau = 0.5$, the latter corresponding to the isotropic case. Figure reproduced from [Jardin 2016].

4.1.3. Singular-value decomposition

Singular-value decomposition (SVD) is a powerful mathematical tool, which is widely applied to investigate the spatial-temporal behavior of fluctuating quantities, such as magnetic field and SXR emissivity in fusion plasmas [Dudok 1994, Nardone 1992]. This method takes the data which appears in a matrix form (defined as M with dimension of *n* x *p*) in which the *n* rows represents certain physical quantity for different locations, and the *p* columns represents the time tracing. The SVD gives:

$$\bar{\bar{M}}_{n\times p} = \bar{\bar{U}}_{n\times n}\bar{\bar{S}}_{n\times p}\bar{\bar{V}}^{T}_{p\times p}, \qquad (4.11)$$

where U and V are in orthogonal form:

$$\bar{\bar{U}}^{T}\bar{\bar{U}} = \bar{\bar{I}}_{n\times n} \qquad (4.12)$$

$$\bar{\bar{V}}^{T}\bar{\bar{V}} = \bar{\bar{I}}_{p\times p} \qquad (4.13)$$

The columns of $\bar{\bar{U}}_{n\times n}$ represent spatial eigenvectors or *topos*, whereas the columns of $\bar{\bar{V}}_{p\times p}$ can be considered as temporal eigenvectors or *chronos* [Dudok 1994]. $\bar{\bar{S}}_{n\times p}$ (the same dimensions as $\bar{\bar{M}}_{n\times p}$) has singular values and is diagonal (*mode significance*), as the singular values are posted as a descending order, $\bar{\bar{M}}_{n\times p}$ is decomposed into different components of descending relative importance. Thus, the first pairs of these topos/chronos contain most part of the information from $\bar{\bar{M}}_{n\times p}$, whereas the components with the smallest singular values represent noises, as a consequence, the SVD can be used for filtering purpose of interest. For example, If we are only interested in the *k-th* component (of perturbation or mode) we obtain a 'filtered' matrix by:

$$\bar{\bar{M}}^{(k)}_{n\times p} = \bar{u}^{(k)}_{n} * s^{(k)} * {\bar{v}^{(k)}_{p}}^{T} \qquad (4.11)$$

where $\bar{u}^{(k)}_{n}$ and $\bar{v}^{(k)}_{p}$ stand for the *k-th* topos and chronos, i.e. the *k-th* columns of $\bar{\bar{U}}_{n\times n}$ and $\bar{\bar{V}}_{p\times p}$, respectively, and $s^{(k)}$ is the corresponding singular value.

Following the suggestion from [Anton 1996], in time-dependent applications, we apply SVD after the tomographic inversion, which means the columns of $\bar{\bar{\mathrm{A}}}_{n\times p}$ are emissivity vectors $\bar{E}_{n}$ at different *p-th* times instead of raw data column vectors $\bar{d}_{m}$. The advantage of 'post-inversion' SVD is that the reconstruction itself has already provided a filtering process: contributions of parasitic signal components such as SXR measurement, are eliminated due to smoothing and built-in boundary conditions. Especially in the case where this kind of 'noise' is not randomly produced (due to certain reason hard to estimate), the suppression by SVD filtering of the raw data is not always possible.

4.2. A conceptual introduction of Bayesian probability theory

In this section, we explain how the tomographic problem can be modelled in the framework of Bayesian probability theory. We begin our discussion with a short note about the view we choose to adopt on probability. Over time, various interpretations of probability have been proposed, the most popular by far being the *frequentist* and the *Bayesian* approaches. Both interpretations come with their associated set of methods and tools, although practices vary across disciplines (e.g. social sciences vs. physical sciences). In addition, there exist various flavours of Bayesian thinking, some of which are half frequentist and use frequentist terminology. However, in the physical sciences and fusion in particular, the point of view of [Cox 1961, Jaynes 2004] has come to prevail, wherein probability theory is considered as an extension of logic to uncertain propositions. The theory is based on a set of common-sense axioms (or desiderata), including the basic requirement of consistency. In other words, different observers should arrive at the same conclusions when providing the same information. From this point of view, a probability always depends on two pieces of information: the proposition or hypothesis A, the probability of which we seek, and the information B, conditioning the probability. The standard notation used to denote such a probability is $P(A|B)$ and corresponds to a real number in the interval $[0,1]$ expressing the plausibility of A provided B is true. Put differently, it is a measure of the extent to which B *implies* A. As such, a probability denoted by $P(.|.)$ always has two slots that need to be filled to produce a meaningful numerical output. The conditioning information B can be a problem statement, some measured data or any other available background information. The whole of information on which a probability statement is conditioned is often summarized by the generic symbol I, e.g. $P(.|I)$. Specific additional information conditioning the probability may be stated explicitly, e.g. $P(.|B,I)$.

The classical frequentist definition of probability is based on the frequency of an event in the long run and necessitates identical repeats of experiments or ensembles of the system under study. As such, it contrasts with the Bayesian interpretation, which enables a direct evaluation of the probability of any statement or single event. Examples include the probability of the plasma density in a fusion machine being within certain bounds or the probability that a plasma is in the H-mode. In the Bayesian view, probabilities are useful whenever there is a general lack of certainty, e.g. details of plasma particle orbits causing fluctuations in the macroscopic quantities or the electron thermal motion in a detector introducing noise in the measurement. We will not follow the habit of using capital letters to denote random variables since, from our point of view, the information carried by any physical variable is subject to uncertainty. Furthermore, while the concept of a *statistic* as a function of the data is technically well-defined, its definition is not required in Bayesian analysis. Indeed, whereas the field of statistics is essential for frequentist inference and some practitioners of (partly) Bayesian methods use the term 'Bayesian statistics', frequentist terminology is better not used to avoid confusion. This approach is adopted by several excellent textbooks on Bayesian probability theory geared to physicists; see [Sivia 2006, von der Linden 2014, Gregory 2005, Jaynes 2004].

4.2.1. Inverse problems in the Bayesian approach

In the context of the SXR tomography problem, suppose one would know the SXR emissivity distribution throughout the plasma cross-section, then the forward model would allow deduction of the line-integrated emissivities, as schematized in **Figure 4.4** from right to left; i.e. this is the forward problem. Conversely, given the noisy SXR line integrals, compatible two-dimensional emissivity distributions can be inferred. This corresponds to the sense from left to right in **Figure 4.4**, i.e. the inverse problem. Without further constraints, there is an infinite number of solutions.

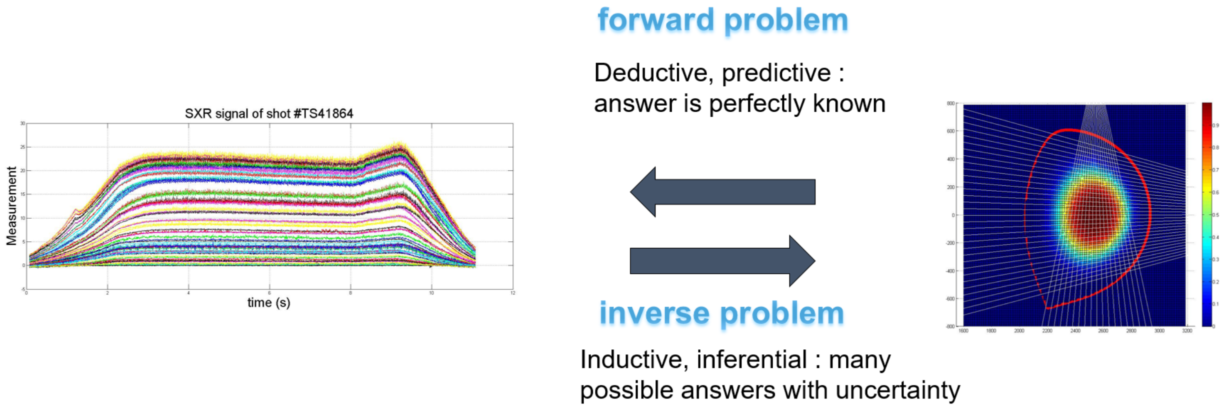
SXR signal of shot #TS41864
Measurement
time (s)
forward problem
Deductive, predictive :
answer is perfectly known
inverse problem
Inductive, inferential : many
possible answers with uncertainty

Figure 4.4. The forward problem and inverse problem in SXR tomography, illustrated for a set of SXR line integrals available at multiple time instants.

4.2.2. Bayes' theorem

We introduce some basic concepts from Bayesian probability theory in this section. We do this in the context of a simple example involving the estimation of the parameters of a normal distribution based on suitable prior information and the repeated measurement of a physical quantity.

In fusion, as in many scientific activities, we do not have a direct access to the physical properties of the plasma. The experimentalist must instead devise a measurement technique for a diagnostic, which returns numbers (usually voltages) that are related to the quantity of interest. If the properties of a physical system were known precisely, together with the full details of the measurement process, the corresponding measurement values could be computed straightforwardly. This would require the measurement process to be encoded in a mathematical model: the *forward model*. However, since the microscopic details of the physical system and the measurement process are unknown, the raw measurement itself is never a truly precise number.[1] We may nevertheless be able to model this uncertainty by assigning a probability for the measured value to lie within certain bounds. Representing the measurement by a real number x, it is convenient to introduce the *probability density function* (PDF) of x.[2] The PDF is usually denoted $p(x)$, where $p(x|I)\mathrm{d}x$ can be interpreted as the probability to find the measurement value between x and $x + \mathrm{d}x$, given the background information I.[3] Strictly speaking, for continuous variables, the term *distribution function* refers to the cumulative distribution function; it is nevertheless used colloquially to denote the PDF. To indicate that a variable x is assumed to be distributed according to (or sampled from) the model with PDF $p(x|I)$, one writes $x \sim p$. One of the most common models is the *normal* or *Gaussian distribution*, the density function of which is the well-known function:

$$p(x|\mu,\sigma,I)=\frac{1}{\sqrt{2\pi}\sigma}\exp\left[-\frac{(x-\mu)^2}{2\sigma^2}\right]. \qquad (4.15)$$

This is often written as $x \sim \mathcal{N}(\mu,\sigma^2)$, where μ is the mean (expectation value) of the distribution and σ the standard deviation. Note that, in the Bayesian spirit, we have explicitly written the PDF as a two-slot function $p(x|\mu,\sigma,I)$, where the second slot emphasizes that the probability density can only be calculated for known values of μ and σ. Any additional information (e.g. the fact that it is a Gaussian distribution) has been summarized in the symbol I. With the same knowledge, the probability that x is found to lie within two given bounds can be calculated by integration (involving the error function erf). Again, it is important to stress that, in characterizing the uncertainty in x, we have not invoked the concept of randomness. We simply do not know x exactly, although we claim that we have a certain idea where x can be found with appreciable probability. This viewpoint does not exclude the practical situation of a series of measurements of x, where one realization of x appears to be unrelated to any other, and where most values lie close to μ in a pattern that can be summarized by Eq. (4.15). This feature is related to the frequentist interpretation of probability. However, in the Bayesian view, the frequency distribution is an observed consequence of the underlying characteristics of the system rather than the basis for the definition of probability. The measurement uncertainties that can be described by probability models such as Eq. (4.15) are often referred to as *stochastic* or *statistical uncertainties*. This is opposed to *systematic uncertainties*, which result in a ‘deterministic’ deviation of the result from the ‘correct’ measurement.

An entirely different question concerns the assignment of probabilities to the parameters μ and σ, given a set of measurements for the variable x, denoted by $\vec{x}$. The solution, known as *Bayes’ rule* or *Bayes’ theorem*, is generally credited to Thomas Bayes (1763) and Pierre-Simon Laplace (1812). This is a direct consequence of the well-known product rule of probability theory, which in this context reads

---

[1] At a certain point, one also hits the rather philosophical question of whether there is such a thing as an ‘exact value’ of a (microscopic) physical quantity.

[2] We will treat only continuous variables here. This represents the most common situations in physical sciences.

[3] We will follow the common slight abuse of notation of using the symbol p to denote a specific model (e.g. Gaussian) of the probability density of a specific variable or, in general, the probability density of a variable, possibly unknown or unspecified.

$$p(\vec{x}, \mu, \sigma | I) = p(\vec{x} | \mu, \sigma, I) p(\mu, \sigma | I). \qquad (4.16)$$

Of course, the same rule also yields

$$p(\vec{x}, \mu, \sigma | I) = p(\mu, \sigma | \vec{x}, I) p(\vec{x} | I), \qquad (4.17)$$

which Eq. (4.17) together with Eq. (4.16), results in Bayes' rule in the current example:

$$\overbrace{p(\mu, \sigma | \vec{x}, I)}^{\text{posterior}} = \frac{\overbrace{p(\vec{x} | \mu, \sigma, I)}^{\text{likelihood}} \overbrace{p(\mu, \sigma | I)}^{\text{prior}}}{\underbrace{p(\vec{x} | I)}_{\text{evidence}}}. \qquad (4.18)$$

Thus, the rules of probability theory naturally enable solving the inverse problem by using a forward model. Determining appropriate values for the quantities of interest – μ and σ – from Eq. (4.18) is referred to as the task of *parameter estimation*. We will discuss this task in more detail below, still in the context of a normal distribution.

Bayes' rule can also be interpreted in terms of a learning process. In this sense, the knowledge of the parameters μ and σ is considered before the data is acquired: the so-called *prior distribution*, indicated in Eq. (4.18) The prior can be obtained from background knowledge about the problem or other experiments. Alternatively, we may choose an *uninformative prior*, which, as the term implies, allows us to adopt a maximally ignorant point of view before performing the experiment. However, one should be careful in keeping the problem well-posed (or *identifiable*), i.e. there should be sufficient information in the data and the prior to estimate the parameters with reasonable accuracy (e.g. the discussion in [Verdoolaege 2010]). Various criteria and methods exist to assign uninformative prior distributions (see [Sivia 2006, von der Linden 2014] for practical advice and [Jaynes 2004] for more in-depth discussions). Whether one chooses an uninformative or informative prior, in the objective Bayesian view the prior distribution is not a subjective judgment by an individual scientist, but rather the result of quantifying the available prior information. In this sense, two individuals, given the same information prior to the experiment, should arrive at the same prior distribution, hence should obtain the same conclusions. Many practitioners use a very pragmatic rule to assign prior distributions, which is related to the analytical tractability of the posterior. This gives rise to the so-called *conjugate priors*, described for instance in [Gelman 2013]. However, one could object that more objective prior information is to be preferred over a criterion based on computational ease, especially as the likelihood and the experimental setup also depend, to some extent, on 'subjective' choices.

Continuing with our example of inferring the parameters of a normal distribution, we could next perform a series of n measurements, here described by $\vec{x}$. We will assume, given a common μ and σ, that the measurements are performed independently from each other. Fixed model parameters μ and σ imply stationary system and measurement conditions. Under these assumptions, the distribution of $\vec{x}$, conditioned on μ and σ, can be factorized into a product of marginal distributions for each of the x_i components of $\vec{x}$ ($i = 1 \dots n$):

$$p(\vec{x}|\mu,\sigma,I)=\prod_{i=1}^{n}\frac{1}{\sqrt{2\pi}\sigma}\exp\left[-\frac{(x_i-\mu)^2}{2\sigma^2}\right]=\frac{1}{(2\pi)^{n/2}\sigma^n}\exp\left[-\sum_{i=1}^{n}\frac{(x_i-\mu)^2}{2\sigma^2}\right]. \qquad (4.19)$$

This is the *likelihood distribution*. According to Eq. (4.18), the product of the likelihood and the prior is proportional to the *posterior distribution* for the quantities of interest. In this respect, an important observation is that, in estimating μ and σ, we do not need to care about the normalization of the posterior. Only the posterior's dependence on μ and σ matters, since it determines the shape of their joint distribution. For this reason, the denominator in Eq. (4.18) is irrelevant in the context of parameter estimation and may be absorbed in a proportionality constant. The denominator is referred to as the *evidence* since it gives the probability of the data in the light of the background information, which includes knowledge about the model that we use for the physical and measurement systems. This term provides evidence for our model and becomes important in comparing different models. In the Bayesian approach, the task of *model selection* is also performed according to Bayes' rule; we will not go deeper into this topic here, but the reader may refer to [von der Linden 2014].

4.2.3. Marginalization

In the case where there is more than one parameter in the model, Bayes' theorem yields a joint PDF for parameter vector $\bar{\theta}$:

$$p(\bar{\theta}|\bar{x},I) = p(\theta_1,\theta_2 \dots \theta_p|\bar{x},I), \qquad (4.20)$$

where p is the number of parameters. However, we typically want to make inferences about individual parameters $\theta_i, \mathrm{i} = 1,2,\dots,\mathrm{p}$. In fact, the posterior often depends also on the parameters we are not interested in, but that necessarily enter the data descriptive model. These are called *nuisance parameters*. In order to obtain the PDF for an individual parameter θ_i, we have to marginalize the joint PDF, i.e. integrate out the other parameters:

$$p(\theta_i|\bar{x},I) = \int p(\bar{\theta}|\bar{x},I)\, d\theta_1 \dots d\theta_{i-1} d\theta_{i+1} \dots d\theta_p$$

$$\sim \int \frac{p(\bar{x}|\bar{\theta},I)p(\bar{\theta}|I)}{p(\bar{x})} d\theta_1 \dots d\theta_{i-1} d\theta_{i+1} \dots d\theta_p \qquad (4.21)$$

The integral is over the complete parameter space spanned by the parameters $\theta_1, \dots \theta_{i-1}, \theta_{i+1}, \dots, \theta_p$, and it may also be a sum in the case of discrete parameters:

$$p(x) = \sum_i p(x, y_i) \qquad (4.22)$$

4.2.4. An example of Bayesian Gaussian process regression

Briefly, a Gaussian process (GP) is a generalization of the multivariate normal (Gaussian) distribution to a function space. It is described by a mean function $\bar{\mu}$ and a covariance function $\bar{\bar{\Sigma}}$, where

$$GP \sim \mathcal{N}(\bar{\mu}, \bar{\bar{\Sigma}}) \qquad (4.23)$$

We give an example of the Bayesian Gaussian process regression of a simple standard linear regression model:

$$y = \bar{x}^T \bar{w} + \varepsilon \qquad (4.24)$$

where y is the observed output value, $\bar{x}$ is the input vector, $\bar{w}$ is a vector parameters of the linear model, and ε is a Gaussian noise. We assume that the observation values y is different from the function values $f(\bar{x}) = \bar{x}^T \bar{w}$ by the presence of noise, and the noise follows an independent, identically distributed Gaussian distribution with zero mean and variance σ_n^2:

$$\varepsilon \sim N(0, \sigma_n^2) \qquad (4.25)$$

This assumption together with the linear model naturally gives rise to the likelihood, the probability density function of the observations given the parameters $\bar{w}$, which can be factored over the available observation data set to give:

$$p(\bar{Y} | \bar{\bar{X}}, \bar{w}) = \prod_{i=1}^{n} p(y_i | \bar{x}_i, \bar{w}) = \prod_{i=1}^{n} \frac{1}{\sqrt{2\pi}\sigma_n} \exp\left(-\frac{\left(y_i - \bar{x}_i{}^T \bar{w}\right)^2}{2\sigma_n^2}\right)$$

$$= \frac{1}{(2\pi\sigma_n^2)^{n/2}} \exp\left(-\frac{\left|\bar{Y} - \bar{\bar{X}}^T \bar{w}\right|^2}{2\sigma_n^2}\right) = \mathcal{N}(\bar{\bar{X}}^T \bar{w}, \sigma_n^2 \bar{\bar{I}}) \qquad (4.26)$$

where $|\cdot|$ denotes the Euclidean length of a given vector. In the Bayesian formalism we need to specify a prior over the parameter $\bar{w}$s, expressing our beliefs about the parameters $\bar{w}$ before we look at the observations $\bar{Y}$. We put a zero mean Gaussian process prior with covariance matrix $\bar{\bar{\Sigma}}_{\mathrm{p}}$ on parameters $\bar{w}$ to be inferred,

$$\bar{w} \sim \mathcal{N}(\bar{0}, \bar{\bar{\Sigma}}_{\mathrm{p}}) \qquad (4.27)$$

The role and properties of this uninformative prior will be discussed in *Section 4.3* together with the SXR tomography background. The Bayesian inference in linear model is based on the posterior distribution over the parameters $\bar{w}$, computed by Bayes' rule, as

$$\overbrace{p\left(\bar{w}\middle|\bar{Y},\bar{\bar{X}}\right)}^{\text{posterior}} = \frac{\overbrace{p\left(\bar{Y}\middle|\bar{\bar{X}},\bar{w}\right)}^{\text{likelihood}}\overbrace{p(\bar{w})}^{\text{prior}}}{\underbrace{p\left(\bar{Y}\middle|\bar{\bar{X}}\right)}_{\text{evidence/marginal likelihood}}} \sim\ p\left(\bar{Y}\middle|\bar{\bar{X}},\bar{w}\right) p(\bar{w}) \qquad (4.28)$$

where the normalizing factor, also known as the evidence or marginal likelihood, is independent of the parameters $\bar{w}$ and given by

$$p\left(\bar{Y}\middle|\bar{\bar{X}}\right) = \int p\left(\bar{Y}\middle|\bar{\bar{X}},\bar{w}\right) p(\bar{w})\, d\bar{w} \qquad (4.29)$$

The posterior in Eq. (4.28) combines the likelihood and the prior, and captures everything we know about the parameters. Writing only the terms from the likelihood and prior which depend on the weights, and "completing the square" we obtain the posterior:

$$p\left(\bar{w}\middle|\bar{Y},\bar{\bar{X}}\right) \sim \exp\left(-\frac{1}{2\sigma_n^2}\left(\bar{Y}-\bar{\bar{X}}^T\bar{w}\right)^T\left(\bar{Y}-\bar{\bar{X}}^T\bar{w}\right)\right)\cdot\exp\left(-\frac{1}{2}\bar{w}^T\bar{\bar{\Sigma}}_{\mathrm{p}}{}^{-1}\bar{w}\right)$$

$$\sim\ \exp\left(-\frac{1}{2}(\bar{w}-\bar{w}^*)^T\bar{\bar{\Sigma}}_{\mathrm{p}}{}^{*-1}(\bar{w}-\bar{w}^*)\right) \qquad (4.30)$$

Here,

$$\bar{w}^* = \frac{1}{\sigma_n^2}\left(\frac{1}{\sigma_n^2}\bar{\bar{X}}\bar{\bar{X}}^T + \bar{\bar{\Sigma}}_{\mathrm{p}}{}^{-1}\right)^{-1}\bar{\bar{X}}\bar{Y} = \frac{1}{\sigma_n^2}\bar{\bar{\Sigma}}_{\mathrm{p}}{}^{*-1}\bar{\bar{X}}\bar{Y} \qquad (4.31)$$

$$\bar{\bar{\Sigma}}_{\mathrm{p}}{}^{*} = \frac{1}{\sigma_n^2}\bar{\bar{X}}\bar{\bar{X}}^T + \bar{\bar{\Sigma}}_{\mathrm{p}}{}^{-1} \qquad (4.32)$$

We recognize the form of the posterior distribution as Gaussian with mean vector $\bar{w}^*$ and covariance matrix $\bar{\bar{\Sigma}}_{\mathrm{p}}{}^{*-1}$ as:

$$p\left(\bar{w}\middle|\bar{Y},\bar{\bar{X}}\right) \sim \mathcal{N}\left(\bar{w}^*,\bar{\bar{\Sigma}}_{\mathrm{p}}{}^{*}\right) \qquad (4.33)$$

Notice that for this model (and indeed for any Gaussian posterior) the mean of the posterior distribution $p\left(\bar{w}\middle|\bar{Y},\bar{\bar{X}}\right)$ is also its mode, which is also called the maximum a posteriori (MAP) estimate of $\bar{w}$.

4.3. Gaussian Process Tomography (GPT)

Given a forward model like the one in Eq. (4.2), the optimization criterion minimizes the difference between the measured line integrals and the prediction by the model. Because of the ill-posedness, the optimization has to be combined with some regularization technique, e.g. assuming a spline model for the local emissivity field, or by optimizing at the same time some information measure like the Fisher information. In this section, we choose the probabilistic methodology, which provides a probability distribution $p(\bar{E}_n)$ of the emissivity in all cells rather than a single solution. In Bayesian inference, one starts from the prior probability distribution of the emissivity field, which can be used to encode the regularization. This is then updated through Bayes' theorem as data become available:

$$p(\bar{E}_n|\bar{d}_m) = \frac{p(\bar{d}_m|\bar{E}_n)\, p(\bar{E}_n)}{p(\bar{d}_m)} \sim p(\bar{d}_m|\bar{E}_n)\, p(\bar{E}_n) \qquad (4.34)$$

$$p(\bar{d}_m) = \int p(\bar{d}_m, \bar{E}_n) d\bar{E}_n = \int p(\bar{d}_m|\bar{E}_n)\, p(\bar{E}_n) d\bar{E}_n \qquad (4.35)$$

In Eq. (4.34), the likelihood term $p(\bar{d}_m|\bar{E}_n)$ measures the mismatch between the measured line integrals $\bar{d}_m$ and their predictions by the forward model, under the assumption of some emissivity field $\bar{E}_n$. The evidence (marginal likelihood) $p(\bar{d}_m)$ depends on the particular forward measurement model, which we will assume to be fixed. Therefore, it can be considered as a normalization factor, independent of the emissivity. The posterior probability distribution $p(\bar{E}_n|\bar{d}_m)$ quantifies our uncertainty on the estimated emissivity field, given our model, prior knowledge and the measured data. Thus, Bayesian inference yields probabilities for all possible results consistent with our model. In principle, systematic uncertainties can also be estimated, provided some knowledge is available about them from other sources of information, such as other experiments. Another important advantage is the ease with which heterogeneous sources of information can be integrated into a single coherent model. This is particularly relevant in deriving local plasma quantities from line-integrated data, as in SXR spectroscopy, since the raw information on the plasma equilibrium, which itself is uncertain, can be combined with the raw spectroscopic data. Although outside the scope of the present work, such an approach enables self-consistent estimation of the local impurity concentrations together with the magnetic equilibrium.

4.3.1. Bayesian Formalization

Gaussian process tomography (GPT) [Svensson 2011, Li 2013, Wang 2018a] is a technique whereby the prior distribution regularizes the tomographic reconstruction process, by imposing a smoothness level dictated by the correlation between pixels.

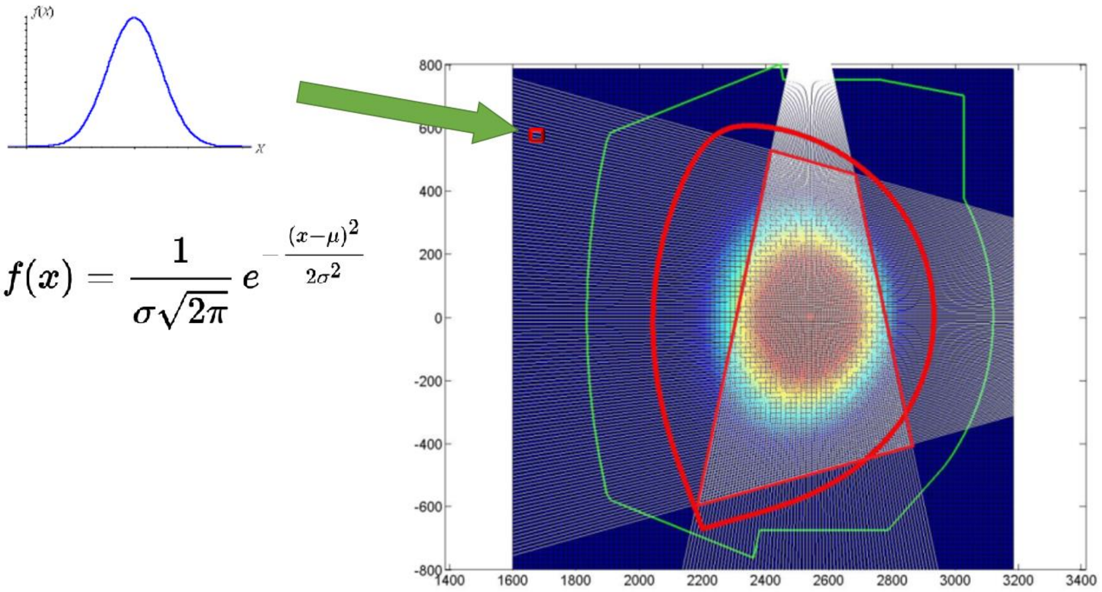

Figure 4.5. In the Gaussian process framework, the emissivity in each cell follows a Gaussian distribution, while the joint distribution of every subset of pixels is multivariate normal. This imposes structure on the emissivity field, avoiding wildly fluctuating emissivity in neighboring cells.

The distribution of a Gaussian process is the joint distribution of infinitely many normally distributed random variables, and as such, it is a distribution over functions with a continuous domain, e.g. time or space. GPT is related to Gaussian process regression, a nonparametric regression technique widely used in machine learning. Being nonparametric, Gaussian process regression does not assume any functional form for the regression function, hence leaving a lot of flexibility. Instead, the regression surface is regularized through the covariance matrix of the Gaussian process. Likewise, GPT assumes that the prior joint distribution of the emissivity in the n cells with coordinates $\vec{r_i}$ is multivariate Gaussian with covariance matrix $\overline{\overline{\Sigma}}_E$ given by:

$$\overline{\overline{\Sigma}}_E = \begin{pmatrix} k(\overrightarrow{r_1},\overrightarrow{r_1}) & \cdots & k(\overrightarrow{r_1},\overrightarrow{r_n}) \\ \vdots & \ddots & \vdots \\ k(\overrightarrow{r_n},\overrightarrow{r_1}) & \cdots & k(\overrightarrow{r_n},\overrightarrow{r_n}) \end{pmatrix} \qquad (4.36)$$

Here, $k(\overrightarrow{r_i},\overrightarrow{r_j}) = cov[\,E(\overrightarrow{r_i}),\ E(\overrightarrow{r_j})\,]$, with $E(\overrightarrow{r_i}) = E_i$ the emissivity in pixel i, is the *covariance kernel function*, for which we choose the common squared-exponential form:

$$k_{SE} = {\sigma_f}^2 \exp\left(-\frac{d^2}{2{\sigma_l}^2}\right), d = \| \overrightarrow{r_i} - \overrightarrow{r_j} \| \qquad (4.37)$$

In turn, the kernel function depends on two parameters σ_f and σ_l, referred to as the signal standard deviation and characteristic length scale. In Bayesian terminology, any parameters of the prior distribution are called *hyperparameters* and in this case they determine the smoothness of the emissivity field. Summarizing σ_f and σ_l by $\bar{\theta}$, the Eq. (4.34) thus can be written as:

$$p\left(\bar{E}_n\middle|\bar{d}_m,\bar{\theta}\right) = \frac{p\left(\bar{d}_m\middle|\bar{E}_n,\bar{\theta}\right) \cdot p\left(\bar{E}_n\middle|\bar{\theta}\right)}{p\left(\bar{d}_m\middle|\bar{\theta}\right)} \sim p\left(\bar{d}_m\middle|\bar{E}_n,\bar{\theta}\right) \cdot p\left(\bar{E}_n\middle|\bar{\theta}\right) \qquad (4.38)$$

where the prior is given by:

$$p\left(\bar{E}_n\middle|\bar{\theta}\right) = \frac{1}{(2\pi)^{\frac{n}{2}}\left|\bar{\bar{\Sigma}}_E\right|^{\frac{1}{2}}}\, exp\left[-\frac{1}{2}(\bar{E}_n - \bar{\mu}_E)^T\, \bar{\bar{\Sigma}}_E^{-1}\, (\bar{E}_n - \bar{\mu}_E)\right] \qquad (4.39)$$

Here, $\bar{\mu}_E$ is the prior mean, which will be fixed at 0, or it may be chosen on the basis of earlier experiments or expert knowledge. In principle, the hyperparameters can be marginalized from the problem (i.e. integrated out), but this would greatly increase the computational complexity of the method. Instead, we will employ a common approximation wherein a fixed set of hyperparameters is determined by maximizing the evidence $p\left(\bar{d}_m\middle|\bar{\theta}\right)$, and plugging those estimates into Eq. (4.35)). This procedure is motivated in *Section 4.3.2*.

The next step in the inference process consists of choosing a likelihood function $p\left(\bar{d}_m\middle|\bar{E}_n,\bar{\theta}\right)$, containing the forward model. Under the reasonable assumption of a normal distribution of the measurement uncertainty on the emissivity line integrals, described by the variable $\bar{\varepsilon}$ in Eq. (4.2), the likelihood can be written as

$$p\left(\bar{d}_m\middle|\bar{E}_n,\, \bar{\theta}\right) = \frac{1}{(2\pi)^{\frac{m}{2}}\left|\bar{\bar{\Sigma}}_d\right|^{\frac{1}{2}}}\, exp\left[-\frac{1}{2}\left(\bar{\bar{R}} \cdot \bar{E}_n - \bar{d}_m\right)^T\, \bar{\bar{\Sigma}}_d^{-1}\, \left(\bar{\bar{R}} \cdot \bar{E}_n - \bar{d}_m\right)\right] \qquad (4.40)$$

Here, $\bar{\bar{\Sigma}}_d$ is the covariance of the emissivity, describing measurement uncertainty and correlation on the vector $\bar{d}_m$ of measured line-integrals. We will assume that the various line-integrated measurements are uncorrelated and choose a 5% noise level, based on historical statistic at Tore Supra.

Therefore,

$$\bar{\bar{\Sigma}}_d = \begin{pmatrix} (0.05 \cdot d_1)^2 & \cdots & 0 \\ \vdots & \ddots & \vdots \\ 0 & \cdots & (0.05 \cdot d_m)^2 \end{pmatrix}. \tag{4.41}$$

Finally, the posterior distribution reads up to a constant factor,

$$p(\bar{E}_n | \bar{d}_m, \bar{\theta}) \sim p(\bar{d}_m | \bar{E}_n, \bar{\theta}) \ \cdot p(\bar{E}_n | \bar{\theta})$$

$$\sim exp\left[-\frac{1}{2}(\bar{\bar{R}} \cdot \bar{E}_n - \bar{d}_m)^T \ \bar{\bar{\Sigma}}_d^{-1} \ (\bar{\bar{R}} \cdot \bar{E}_n - \bar{d}_m)\right] \cdot exp\left[-\frac{1}{2}(\bar{E}_n - \bar{\mu}_E)^T \ \bar{\bar{\Sigma}}_E^{-1} \ (\bar{E}_n - \bar{\mu}_E)\right] \tag{4.42}$$

The major advantage of normal distributions and a linear forward model now becomes clear. Indeed, it follows from standard probability calculus that the product of two normal distributions is also Gaussian, with mean vector and covariance matrix given by

$$\bar{\mu}_E^{post} = \bar{\mu}_E^{prior} + \left(\bar{\bar{R}}^T \bar{\bar{\Sigma}}_d^{\ -1} \bar{\bar{R}} + \bar{\bar{\Sigma}}_E^{\ -1}\right)^{-1} \bar{\bar{R}}^T \ \bar{\bar{\Sigma}}_d^{\ -1} \left(\bar{d}_m - \bar{\bar{R}} \cdot \bar{\mu}_E\right) \tag{4.43}$$

$$\bar{\bar{\Sigma}}_E^{post} = \left(\bar{\bar{R}}^T \bar{\bar{\Sigma}}_d^{\ -1} \bar{\bar{R}} + \bar{\bar{\Sigma}}_E^{\ -1}\right)^{-1}. \tag{4.44}$$

The posterior mean is thus available in a closed form and can be used as an estimate of the emissivity field, which can be calculated in real time. In addition, the diagonal elements of the posterior covariance matrix $\bar{\bar{\Sigma}}_E^{post}$ quantify the uncertainty on the inference result. These uncertainty estimates can further guide improvements in the design of the diagnostic, e.g. by optimizing the viewing geometry (see *Section 4.3.5*).

It should be noted that the GPT method implemented here only uses the SXR line integral measurements and no assumptions whatsoever are made regarding the magnetic equilibrium. This renders the method very flexible, potentially allowing detection of structures in the emissivity field (e.g. local impurity concentrations) that do not show up in the equilibrium reconstruction. It also prevents misguided information to enter the SXR reconstruction process in case the equilibrium information is incorrect, e.g. during sawtooth activity.

4.3.2. Bayesian Ockham's Razor

The choice of suitable hyperparameters is a key issue for the GPT method, as they determine the degree of smoothness of the reconstructed emissivity field. A full Bayesian analysis would determine the hyperparameters together with the emissivity parameters, but this would not be feasible in real time. As a workaround, we determine the hyperparameters $\bar{\theta}$ from the data by maximizing the evidence. The rationale is that the marginal posterior for the hyperparameters (i.e. with the parameters $\bar{E}_n$ marginalized) can be written as

$$p(\bar{\theta}|\bar{d}_m) \sim p(\bar{d}_m|\bar{\theta}) \cdot p(\bar{\theta}) \qquad (4.45)$$

Now, assuming a non-informative uniform hyperprior distribution:

$$p(\bar{\theta}) = \frac{1}{\Delta\bar{\theta}} = constant, \qquad (4.46)$$

and defining

$$Ockham\ factor \equiv \frac{\Delta\bar{\theta}}{\Delta^0\bar{\theta}} = constant, \qquad (4.47)$$

we see that the posterior for the hyperparameters is proportional to the evidence $p(\bar{d}_m|\bar{\theta})$, which also occurs in Eq. (4.38):

$$p(\bar{\theta}|\bar{d}_m) \sim p(\bar{d}_m|\bar{\theta}) \cdot \overbrace{p(\bar{\theta}) \cdot \Delta\bar{\theta}}^{\text{Ockham factor}} \sim p(\bar{d}_m|\bar{\theta}) \qquad (4.48)$$

Hence, by maximizing the evidence w.r.t. $\bar{\theta}$, we find the maximum *a posteriori* estimates of the hyperparameters. Using these values in the posterior Eq. (4.48) is usually a good approximation to the full Bayesian solution. From Eq. (4.35), the marginal posterior for the hyperparameters is given by

$$p(\bar{\theta}|\bar{d}_m) \sim p(\bar{d}_m|\bar{\theta}) = \int p(\bar{d}_m|\bar{E}_n, \bar{\theta})\ \ p(\bar{E}_n|\bar{\theta})\ \ d\bar{E}_n$$

$$= \mathcal{N}(\bar{d}_m|\bar{0}, \bar{\bar{\Sigma}}_d + \bar{\bar{R}}^T\bar{\bar{\Sigma}}_E\bar{\bar{R}}) \qquad (4.49)$$

This results in the following expression:

$$\log\left(p(\bar{\theta}|\bar{d}_m)\right) \sim \log\left(p(\bar{d}_m|\bar{\theta})\right) = \log(\mathcal{N}(\bar{d}_m|\bar{0}, \bar{\bar{\Sigma}}_d + \bar{\bar{R}}^T\bar{\bar{\Sigma}}_E\bar{\bar{R}})\ )$$

$$= -\frac{1}{2}\left\{\overbrace{m\log(2\pi)}^{\text{constant}} + \overbrace{\log\left|\bar{\bar{\Sigma}}_d + \bar{\bar{R}}^T\bar{\bar{\Sigma}}_E\bar{\bar{R}}\right|}^{\text{complexity penalty}} + \overbrace{\bar{d}_m{}^T(\bar{\bar{\Sigma}}_d + \bar{\bar{R}}^T\bar{\bar{\Sigma}}_E\bar{\bar{R}})^{-1}\bar{d}_m}^{\text{data fit}}\right\} \qquad (4.50)$$

The hyperparameters are contained in $\bar{\bar{\Sigma}}_E$ in the kernel function, see $\mathrm{Eq.}\,(4.37)$.

The term "Ockham's razor" originates from the perspectives of the fourteenth century English philosopher William of Ockham, to whom is attributed the following principle of parsimony in theory building:

"Numquam ponenda est pluralitas sine necessitate."

This is usually understood as:

"When multiple competing theories fit the data equally well, the one that introduces the fewest assumptions and parameters, should be selected."

An example of the evidence as a function of the two hyperparameters is given in **Figure 4.6**. The data were obtained from a hollow shape phantom test and the optimization results in a length scale $\sigma_l = 144$ mm and signal standard deviation value $\sigma_f = 0.2427$.

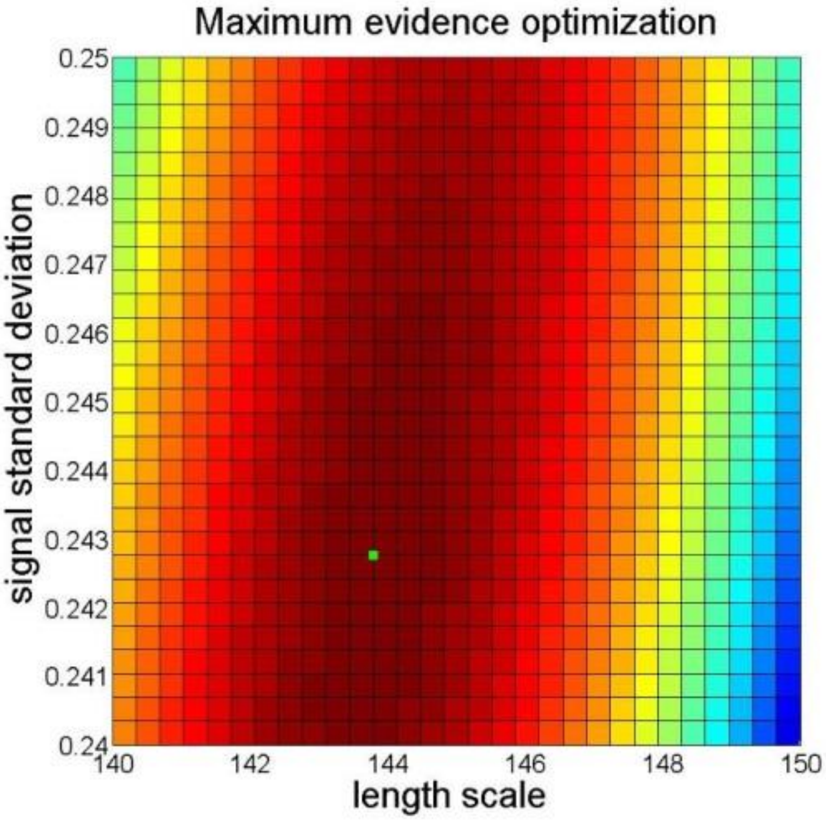

Figure 4.6. An example of log(evidence) maximization for a 5% noise level using a hollow shape phantom test. The maximum is obtained at the green point.

4.3.3. Phantom test with WEST SXR radiation field reconstruction case

The implementation of the GPT algorithm was validated using synthetic data. Also referred to as *phantoms*, these synthetic data sets contain synthetic SXR emissivity fields characterized by various emissivity patterns, some of which creating a challenging tomography problem. The phantoms are described on a grid of 100 × 100 pixels. Line integrals with added noise were calculated, followed by reconstruction of the emissivity field by GPT and comparison with the original emissivity phantom. In our study we employed two noise levels, 5% and 15%. The 5% noise level is the empirical reference obtained from Tore Supra measurements. Four different shapes were used for the phantom tests, corresponding to various situations that are expected to be relevant for WEST SXR emission: Gaussian shape, hollow shape, left-right kidney shape and up-down kidney shape, as shown in **Figure 4.7**.

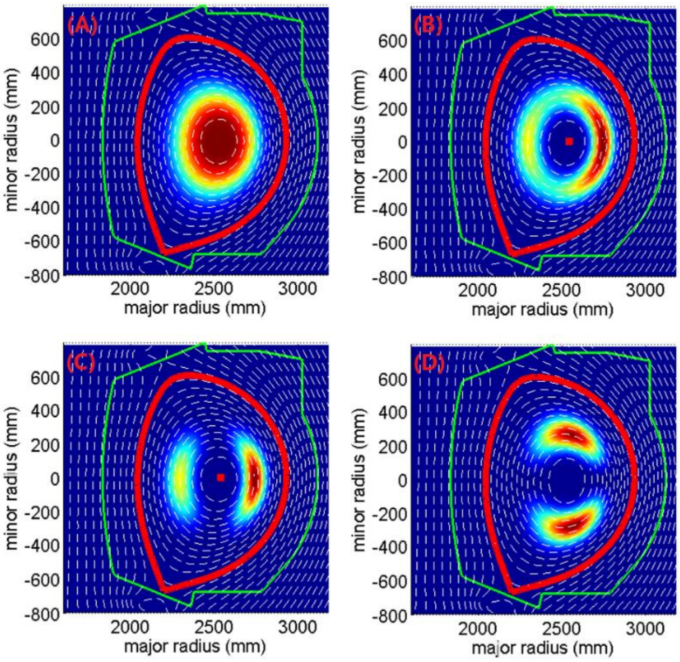

Figure 4.7. Four phantom emissivity fields are used in our test: (A) Gaussian shape, (B) hollow shape, (C) left-right kidney shape, (D) up-down kidney shape. The green curve in the figure represents the vacuum vessel and the red curve is the last-closed flux surface. The white dashed curves provide the flux surface geometry. Note that the phantom emissivity has been normalized for the benefit of numerical computation.

The reconstructed emissivity fields based on line integrals with a 5% noise level are shown in **Figure 4.8**. The quality of the reconstructions can be quantified through a relative error map, showing the difference between the phantom and reconstructed field, normalized by the maximum phantom emissivity:

$$\xi_i = \frac{\left|E_{n,i}^{(rec)} - E_{n,i}\right|}{max\{\bar{E}_n\}} \qquad (4.51)$$

In case of the Gaussian shape, the maximum relative error is around 6.9%, 15% for the hollow shape, 12% for the left-right kidney shape and 15% for the up-down kidney shape. In general, more asymmetric emissivity fields are more difficult to reconstruct, the error level depending greatly on the coverage and field of view of the optical system. Nevertheless, in all cases the characteristic shape of the phantom is recovered relatively well by GPT. In addition, one can compare the line integrals obtained from the original phantom, with those calculated from the reconstructed emissivity field. As shown in Figure 4.8, a good agreement is achieved in all cases. The results with the 15% noise level are shown in Figure 4.9. The maximum relative error is around 20% in all cases. Given the relatively high noise level, the quality of the reconstructions is quite good.

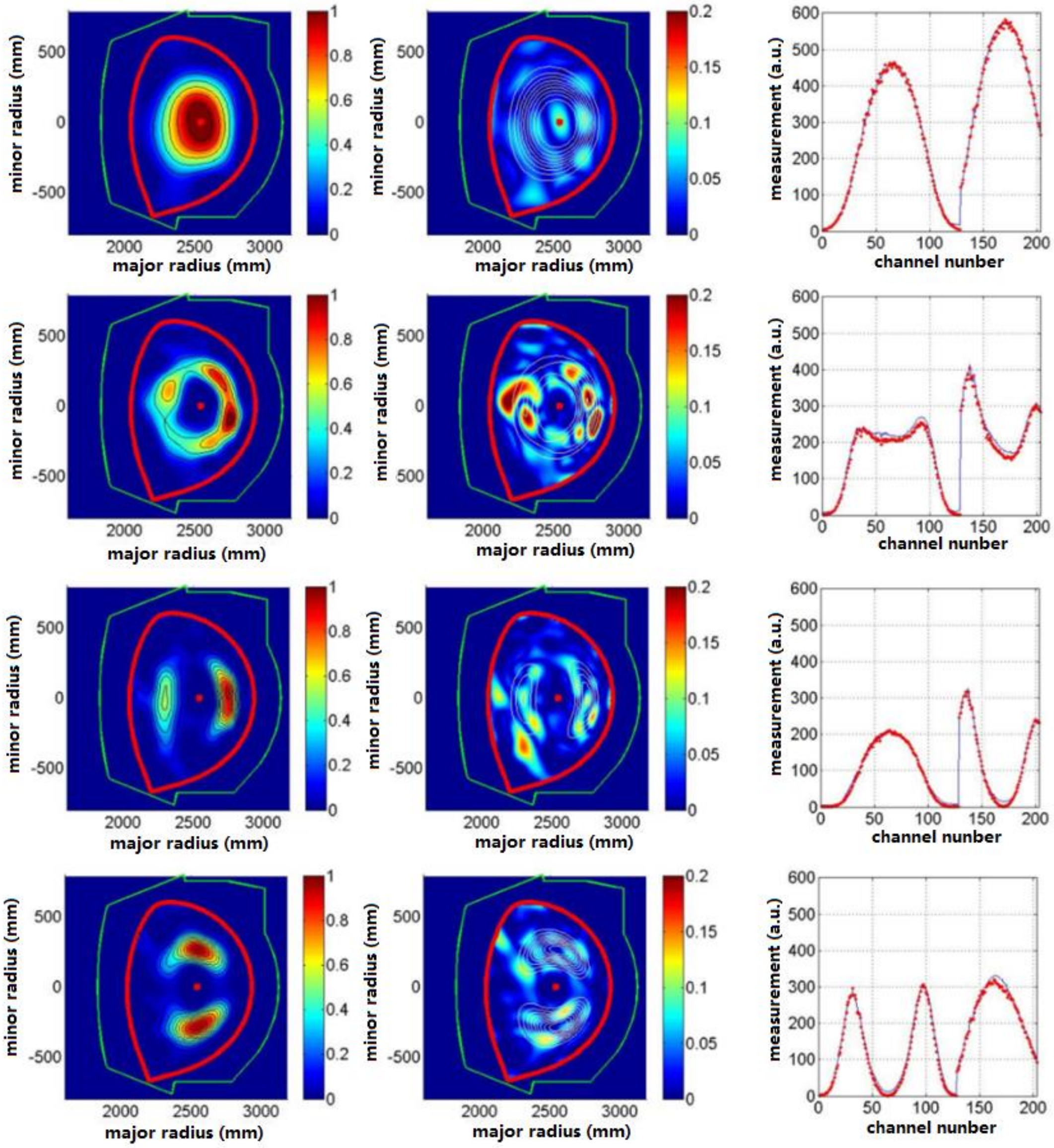

Figure 4.8. GPT phantom test with 5% noise level. From left to right, the first column contains the reconstructions **(normalized the a maximum of 1)**, the second column shows the relative error maps according to Eq. 4.51 (the white contours represent the original phantom), and the third column gives the comparison between the line integrals obtained from the phantom (red dots) and from the reconstructed emissivity fields (blue curves). Note that the phantom emissivity has been normalized for the benefit of numerical computation.

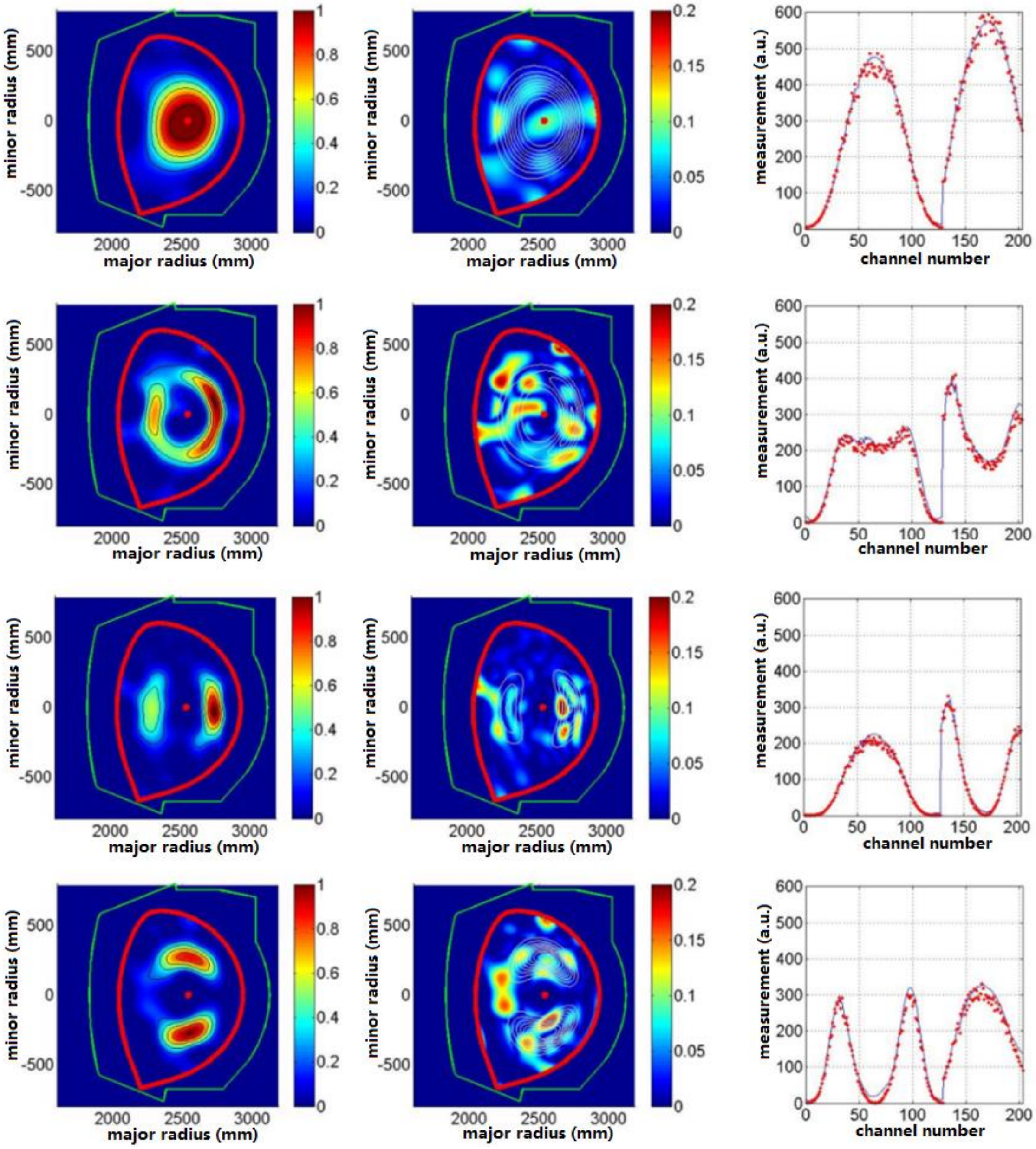

Figure 4.9. Similar to Figure 4.8, but for a 15% noise level on the line integrals.

4.3.4. Real-time calculation

The forward model for SXR tomography described above is linear. Consequently, as we have seen, the posterior probability distribution also takes on a Gaussian process form. Thus, the moments of the distribution are available in closed form, therefore sampling from the distribution, e.g. by means of MCMC is not necessary. As a result, GPT tomography is very fast compared to many traditional tomography methods based on optimization, involving an iterative process.

To estimate the calculation speed of GPT, the phantom tests were repeated 500 times and the GPT reconstruction times averaged between 44 ms and 45 ms, using a two-core PC with the Matlab environment. With a reduced spatial resolution, the computation could be sped up even more. For instance, in applications with real data from SXR and XUV diagnostics on EAST, GPT reached a reconstruction time of 8ms and 3ms with a resolution of 50 × 50 pixels (see Chapter 5).

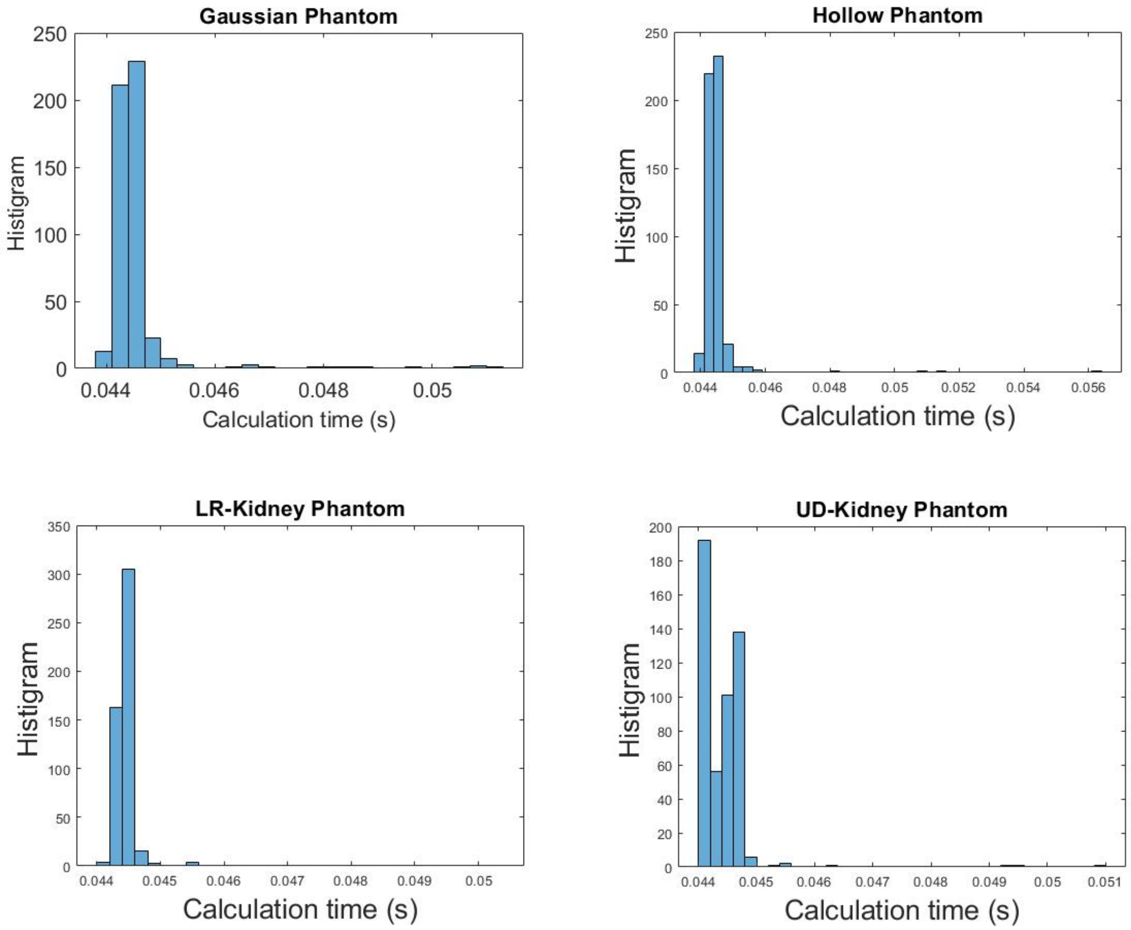

Figure 4.10. The histogram of calculation time for four phantom test with 500 times repetition.

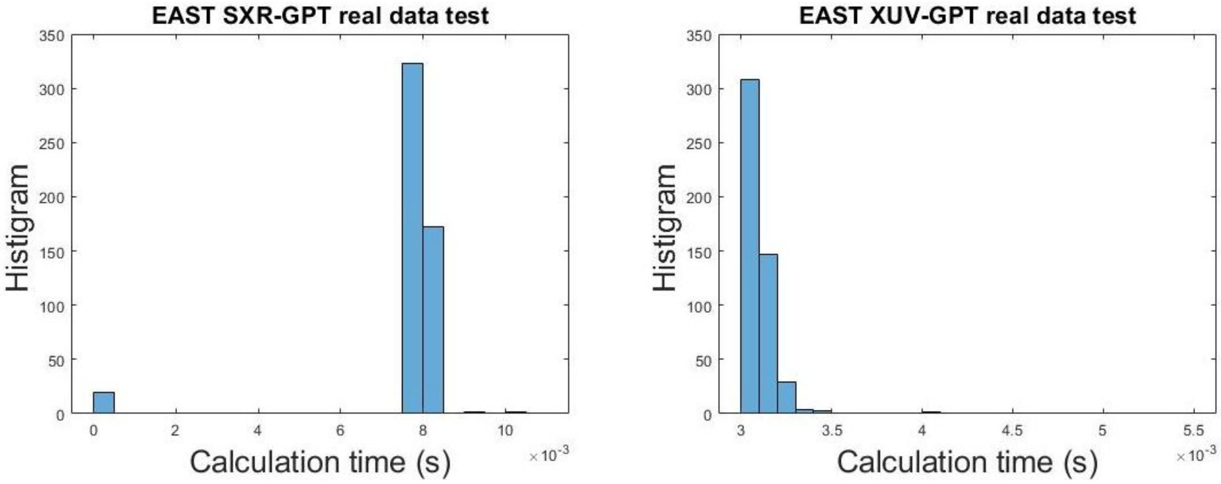

Figure 4.11. The histogram of calculation time for GPT on EAST SXR (left) and XUV (right) with 500 time slides.

4.3.5. GPT reconstruction uncertainty and Line-of-sight distribution

A valuable advantage of GPT is that it provides uncertainty estimates on the reconstructed emissivity field through the posterior covariance matrix; $\mathrm{Eq.}\,(4.44)$. This is confirmed by comparing the posterior variance map with the relative error field, as shown in **Figure 4.10**. In the uncertainty map, there is significant consistency between the uncertainty and the GPT reconstruction error, especially for the more complex structures: when the local uncertainty is lower, the local reconstruction error also reaches lower levels. Naturally, the relative error field will not be available when performing tomography on real WEST data, but the posterior variance can still be calculated.

In particular, the upper area in all panels in **Figure 4.10** marked by a red circle should be noted. The uncertainty in this area is low in all four cases, which is probably related to the geometric distribution of the lines-of-sight. This provides opportunities to optimize the viewing geometry of the diagnostic based on the uncertainty map, which could be part of future work.

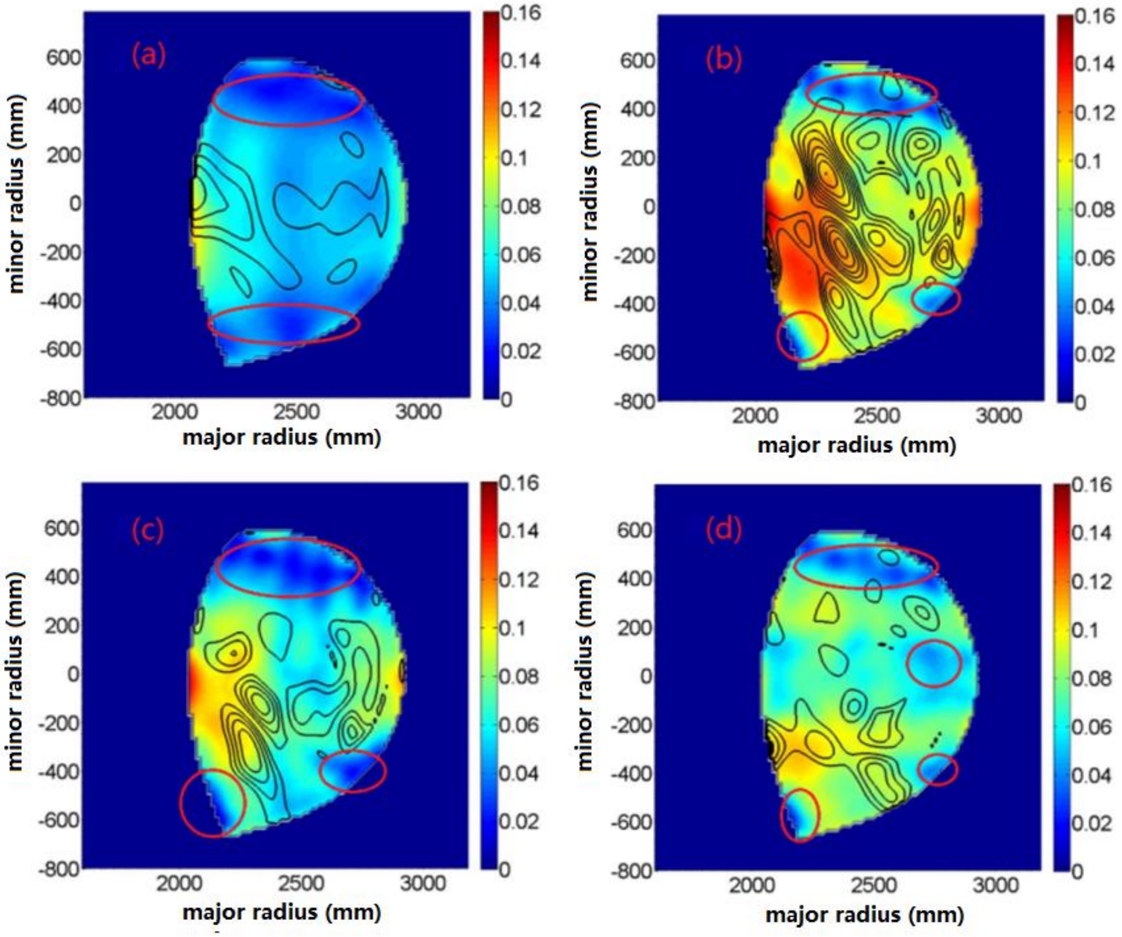

Figure 4.10. Examples of a comparison between the posterior variance map (color map) and relative error map (black contours) on a 5% noise level: (a) Gaussian shape, (b) hollow shape, (c) left-right kidney shape, (d) up-down kidney shape. In the areas marked by red ellipses, both the posterior variance and relative error are low. **The units of the uncertainty maps refer to emissivity probability density.**

4.4. Incorporating magnetic equilibrium information in GPT

Up to now we have not used information about the magnetic equilibrium, which can be useful in situations where the equilibrium is less reliable. On the other hand, routine tomography may benefit from equilibrium information, leading to more accurate reconstructions, decreasing the posterior uncertainty. Here, we introduce a method to incorporate magnetic equilibrium information in GPT.

4.4.1. Length scale following magnetic flux surfaces

The idea which we use to incorporate equilibrium information is that the correlation of the emissivity among any two pixels depends not only on the Euclidean distance between those pixels, but also on the time scales of the transport between those locations. In particular, let $d_\perp$ represent the perpendicular distance between the magnetic flux surfaces on which pixel i and j are located, and $d_{/\!/}$ the parallel distance between the pixels along one of the surfaces. Then we introduce a perpendicular length scale $\sigma_{l\perp}$ and a parallel length scale $\sigma_{l/\!/}$ in the Gaussian process kernel, as follows [WANG 2018b]:

$$k_{SE} = {\sigma_f}^2 \exp\left(-\left(\frac{{d_\perp}^2}{2{\sigma_{l\perp}}^2} + \frac{{d_{/\!/}}^2}{2{\sigma_{l/\!/}}^2}\right)\right). \qquad (4.52)$$

An example of a distance map is given in Figure. 4.11.

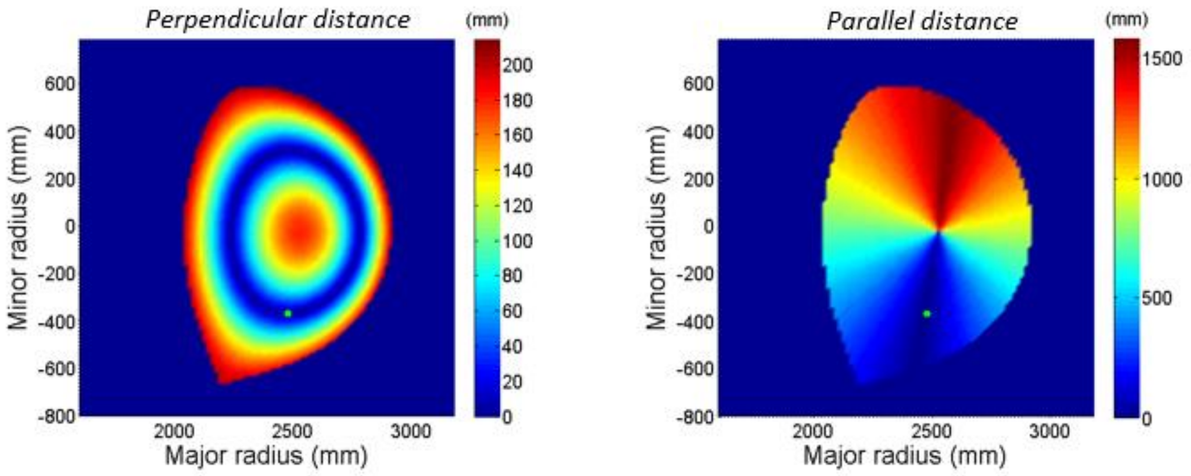

Figure 4.11. Example of a distance map w.r.t. to a reference pixel indicated by the green point. The color maps represent the perpendicular distance (left) and parallel distance (right) between the reference pixel and the other pixels.

In turn, the kernel function depends on three parameters (summarized by the vector $\bar{\theta}$ in the remainder): the signal standard deviation σ_f, and the perpendicular and parallel characteristic length scales $\sigma_{l\perp}$ and $\sigma_{l/\!/}$. These hyperparameters are again obtained by maximization of the marginal likelihood.

4.4.2. Equi-GPT on WEST

The GPT algorithm that incorporates magnetic equilibrium information using the two length scales will be referred to as *Equi-GPT* in the remainder. The reconstructed emissivity fields based on line integrals with a 5% noise level are shown in **Figure 4.12**. Equi-GPT performs significantly better than the bare GPT algorithm without equilibrium information.

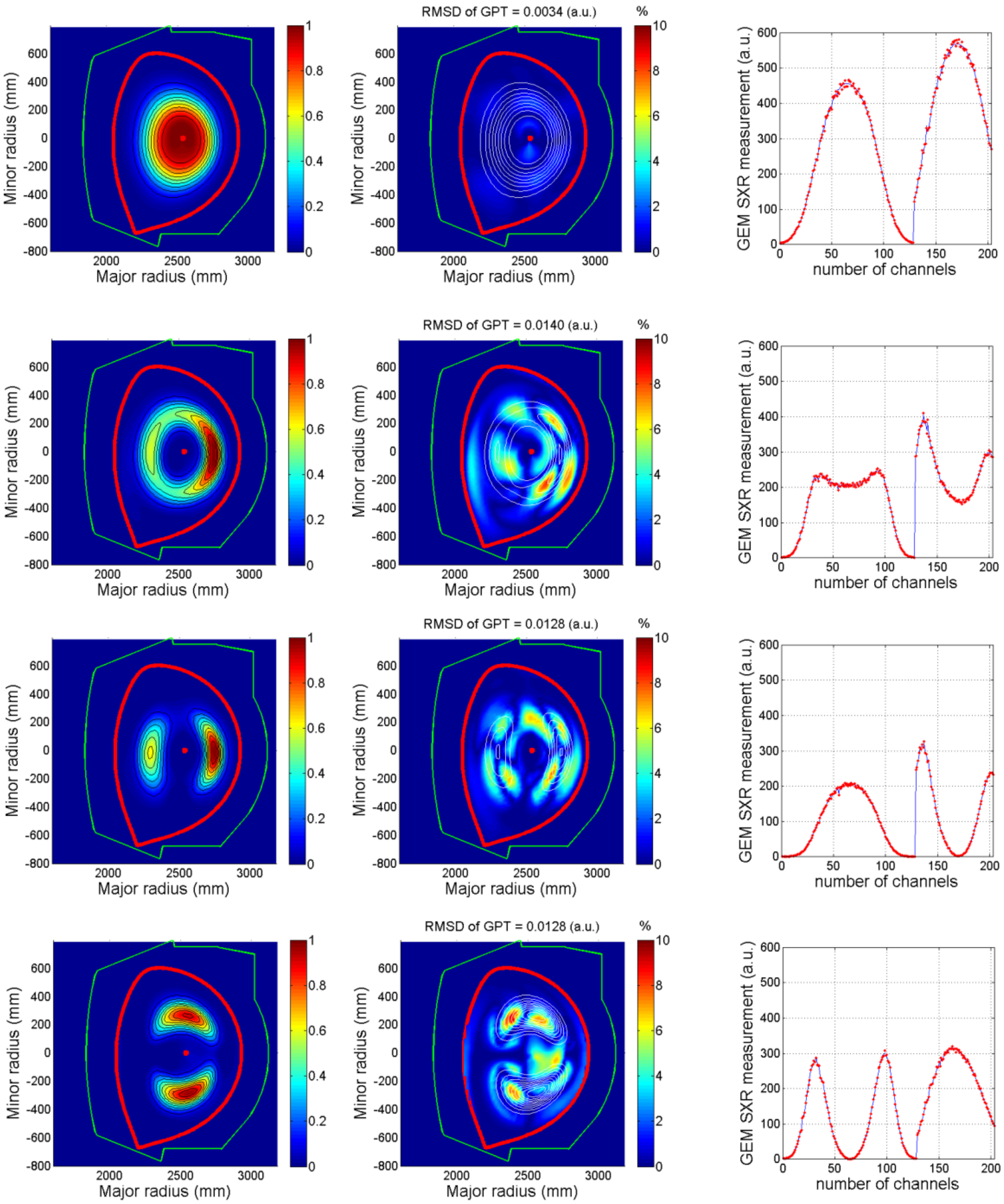

Figure 4.12. Equi-GPT phantom test with 5% noise level. From left to right, the first column contains the reconstructions, the second column shows the relative error maps (the white contours represent the original

phantom), and the third column gives the comparison between the line integrals obtained from the phantom (red dots) and from the reconstructed emissivity fields (blue curves).

Indeed, in case of the Gaussian shape, the maximum relative error is around 2%, 8% for the hollow shape, 8% for the left-right kidney shape and 8% for the up-down kidney shape. As shown in **Figure 4.12**, comparing the line integrals obtained from the original phantom with those calculated from the reconstructed emissivity field, good agreement is achieved in all cases.

The Equi-GPT posterior uncertainty plots are presented in **Figure 4.13**, corresponding well with the plots with reconstruction errors.

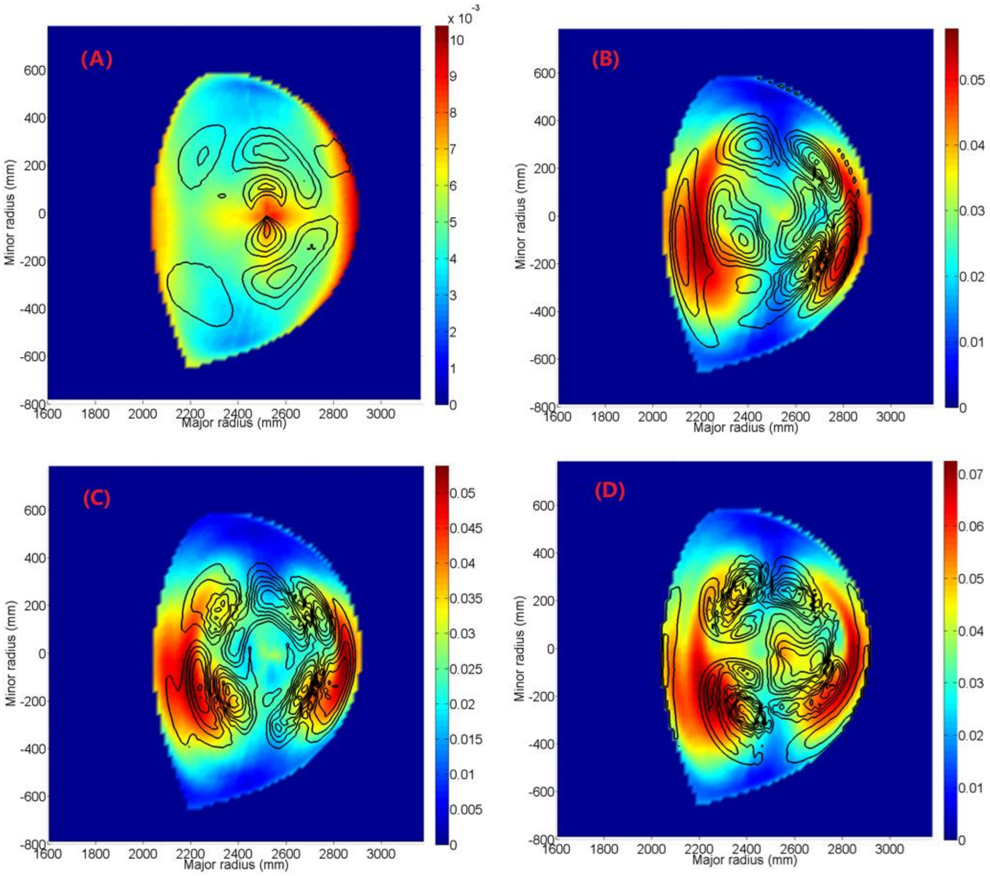

Figure 4.13. Comparison between the Equi-GPT posterior variance map (color map) and relative error map (black contours) on a 5% noise level: (a) Gaussian shape, (b) hollow shape, (c) left-right kidney shape, (d) up-down kidney shape. In the areas with lower posterior variance, relative error remains at low level also, similar to previous discussion.

4.5. Benchmark with GPT and MFI on WEST synthetic data

Minimum Fisher information (MFI) has been thoroughly tested for several fusion diagnostics, e.g. the SXR systems at JET, Tore Supra and TCV. At JET, minimum Fisher information tomography has performed successfully for over 20 years. In this sense, MFI is a perfect option to perform the benchmark with GPT. Here, MFI tomography including equilibrium magnetic information [Jardin 2016] has been demonstrated in Figure. 4.14, where the maximum relative error is 6% for the Gaussian shape, 14% for the hollow shape and over 20% for the left-right kidney shape.

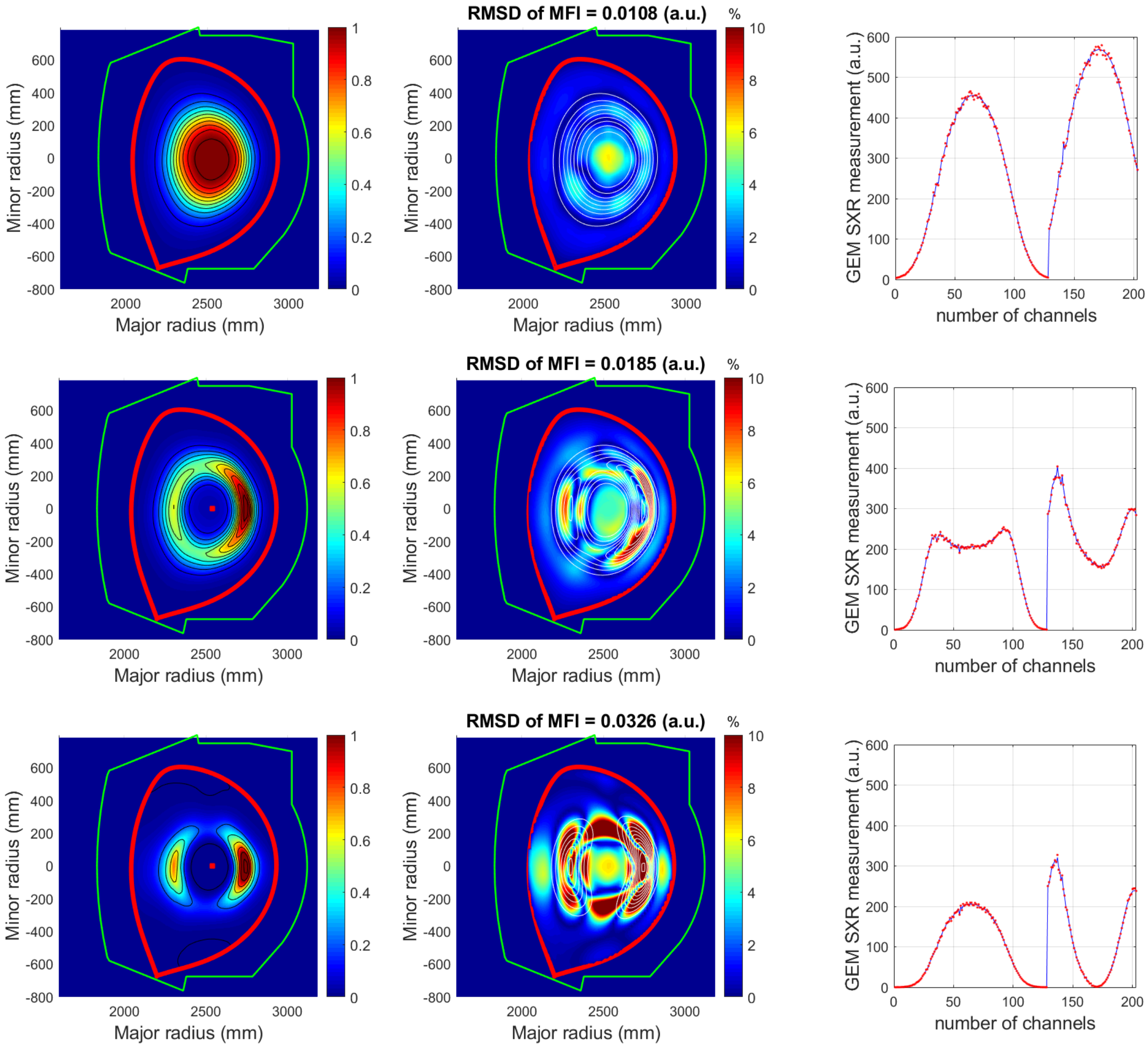

Figure. 4.14. MFI phantom test with 5% noise level for Gaussian shape, hollow shape and left-right kidney shape phantoms. From left to right, the first column contains the reconstructions, the second column shows the relative error maps according to Eq. 4.51 (the white contours represent the original phantom), and the third column gives the comparison between the line integrals obtained from the phantom (red dots) and from the reconstructed emissivity fields (blue curves).

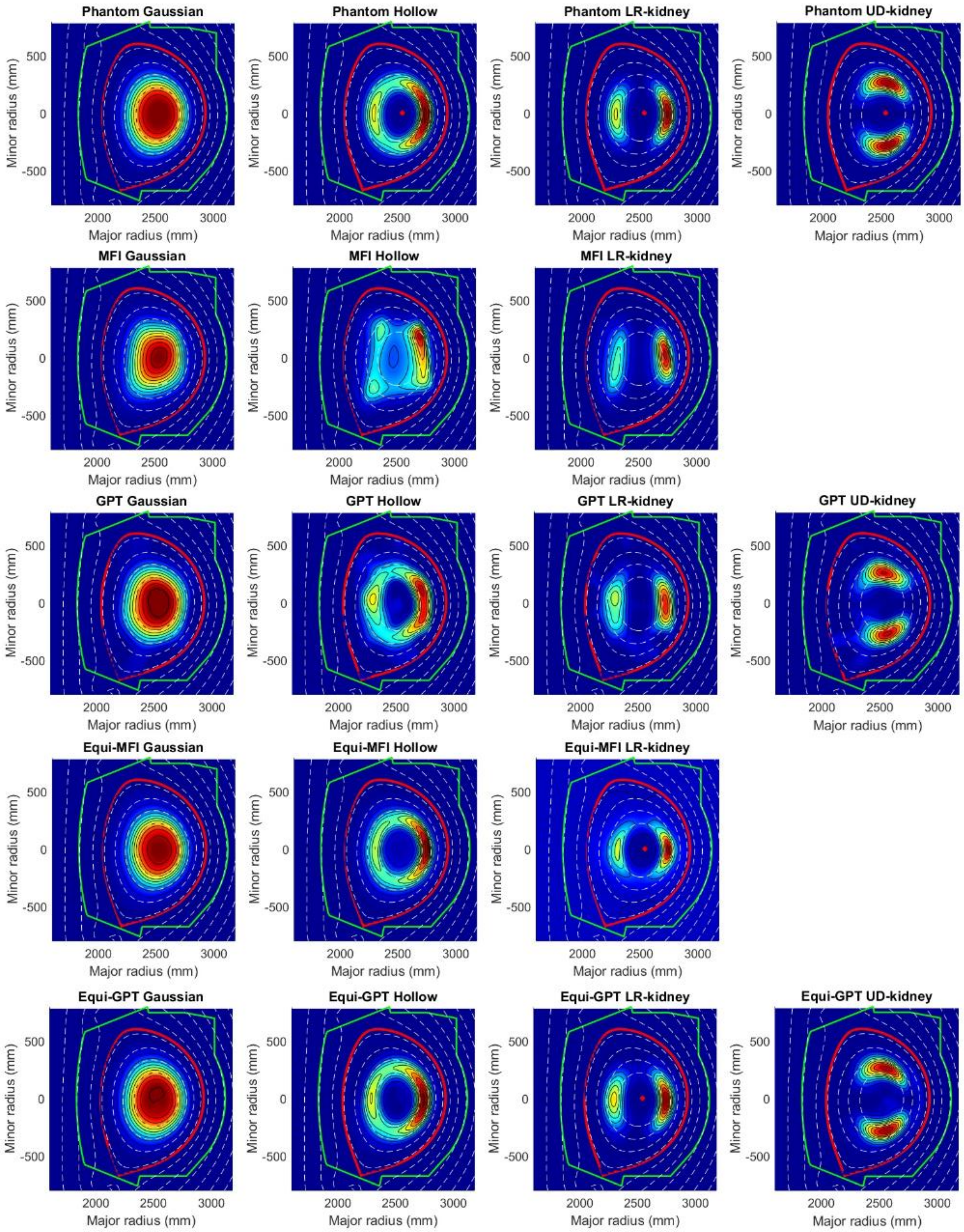

Figure. 4.15. Comparison of minimum Fisher information tomography and GPT. The green curve in the figure represents the vacuum vessel and the red curve is the last-closed flux surface. The white dashed curves provide the flux surface geometry.

Table 4.1. Error estimation and root-mean-square deviation.

Phantoms	Equi-GPT	Equi-MFI	GPT	MFI
Gaussian	2 % max error 0.0034 RMSD (a.u.)	6 % max error 0.0108 RMSD (a.u.)	6.9 % max error 0.0108 RMSD (a.u.)	~ 0.0264 RMSD (a.u.)
Hollow	8 % max error 0.0140 RMSD (a.u.)	14 % max error 0.0185 RMSD (a.u.)	15 % max error 0.0294 RMSD (a.u.)	~ 0.0772 RMSD (a.u.)
Left-right kidney	7 % max error 0.0128 RMSD (a.u.)	Over 20 % max error 0.0326 RMSD (a.u.)	12 % max error 0.0299 RMSD (a.u.)	~ 0.0383 RMSD (a.u.)
Up-down kidney	8 % max error 0.0128 RMSD (a.u.)		15 % max error 0.0287 RMSD (a.u.)	

A detailed benchmark plot is shown in Figure 4.15. In this comparison, the four phantom test data sets, Gaussian, hollow, left-right kidney, up-down kidney shapes, have been chosen as the input data for GPT under two different assumptions: with and without equilibrium information. Only the first three phantoms are shown for MFI. Without knowledge of the magnetic equilibrium, the MFI results can deviate quite strongly from the original phantom, sometimes concentrating the emissivity in localized areas related to the geometry of the line-of-sight. However, when taking into account the equilibrium information, MFI can provide proper reconstructions, and the characteristic shape of the phantom is recovered relatively well in all cases. On the other hand, the GPT method provides good results both with and without equilibrium information. Still, with equilibrium information the GPT reconstruction improves significantly, especially for the more complex structures. In order to quantitatively compare the quality of the reconstructions, the root-mean-square deviation (RMSD) was calculated for each result, given by

$$RMSD = \sqrt{\frac{\sum_{t=1}^{n}(E_{t,i}^{(rec)} - E_{t,i})^2}{n}}.$$

These values are mentioned in TABLE 4.1, confirming the superiority of the GPT technique compared to MFI. As the emissivity grid in this test was composed of 100 × 100 square pixels, the computational load of MFI was relatively high, with execution times up to several seconds. As mentioned before, the GPT reconstruction could be carried out much faster, taking around *45ms*, which is compatible with reconstruction in real time. An additional advantage of GPT is that it provides the posterior uncertainty.

Chapter 5 Implementation of Equi-GPT on experimental data

In experimental fusion science, tomography has application to various diagnostics that acquire line-integrated measurements. Having been validated using synthetic data in the previous chapter, in this chapter the Equi-GPT algorithm is applied to a bolometry diagnostic on the HL-2A tokamak.

5.1. Equi-GPT for bolometer in HL-2A H-mode plasmas

The first application of the Equi-GPT algorithm has been carried out on the bolometer diagnostic at the HL-2A tokamak. In accordance with the national nuclear fusion development program in China, the construction of HL-2A was approved in 1998 by the government as the largest tokamak in China during the period of the Ninth Five-year Plan (1995-2000). The vacuum vessel magnets and supports were based on ASDEX components. The pumping system, energy storage equipment and diagnostics were developed by the Southwestern Institute of Physics (SWIP), affiliated with the China National Nuclear Corporation. HL-2A was put into operation in 2002. The parameters of HL-2A are summarized in Table 5.1. Auxiliary heating with a total envisaged power of 10 MW is being developed (as shown in Table 5.2), of which 3 MW ECRH, 1.5 MW NBI and 1 MW LHCD have already been implemented. This presently allows access to H-mode.

Table 5.1. HL-2A parameters.

Major radius	1.65m	Safety factor	3
Minor radius	0.4m	Volt-second	5Vs
Plasma current	450kA	Plateau of plasma current	5s
Toroidal field	2.8T	Number of nulls	1 or 2
Triangularity δ_{95}	0.3		
Elongation κ_{95}	1.3		

Table 5.2. Auxiliary heating on HL-2A.

systems	Power (MW)	Energy/Frequency/Pulse duration
NBI	3	60 keV / 2s
LHCD	2	2.45 GHz / 2s
ECRH	5	4 x 0.55 kW / 68 GHz / 1s
		2 x 0.55 kW / 68 GHz / 1.5s
		2 x 1MW / 140 GHz / 3s

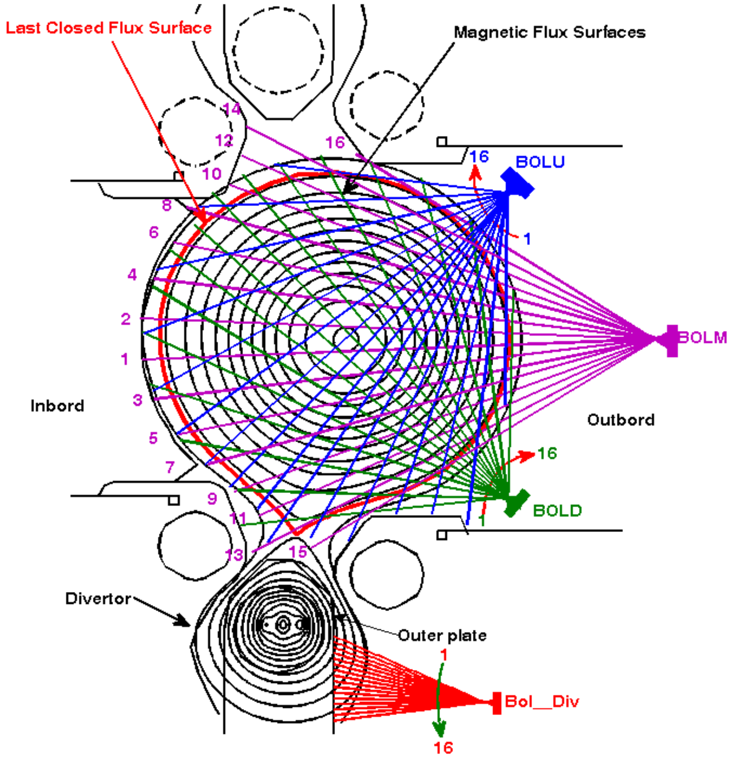
Last Closed Flux Surface
Magnetic Flux Surfaces
14
12
16
10
8
6
4
2
1
3
5
7
9
11
13
15
16
BOLU
1
BOLM
Inbord
Outbord
16
BOLD
1
Divertor
Outer plate
1
Bol__Div
16

Figure 5.1. Illustration of bolometer array line-of-sight distribution on HL-2A. [Pan 2006]

The bolometer diagnostic on HL-2A (geometry shown in **Figure 5.1**) consists of three AXUV linear arrays, each equipped with 16 p-n junction photodiodes, and characterized by flat spectral sensitivity from ultraviolet to X-ray energies ($1\text{eV}\sim10\text{keV}$), as well as a high temporal response ($0.5\mu\text{s}$).[Pan 2006]

5.1.1 ELM-induced divertor strike point shifting

The application of tomography of bolometry measurements using the Equi-GPT algorithm is related to a shift of the divertor strike points in HL-2A H-mode plasmas during the occurrence of edge-localized modes (ELMs). The strike point shift from the reference inter-ELM position (or during L-mode operation) was initially observed by an infrared camera viewing towards the divertor area, indicated in **Figure 5.4** (right). This footprint shift coincides, as expected, with other ELM indicators, such as a peak in the D_α recycling signal and a characteristic drop of the pedestal electron temperature T_e and electron density $\bar{\mathrm{n}}_e$, as presented in **Figure 5.2**. In addition, during the ELM crash, the heat flux at the new strike point position is 30% to 50% higher than in L-mode in the same discharge. Furthermore, a perturbation in the plasma current I_p is noted during ELMs, visible in **Figure 5.2** (b), which is strongly correlated to the shift of the strike point position. This is shown in **Figure 5.3** for data from several discharges and it is thought to result from a resonance effect.

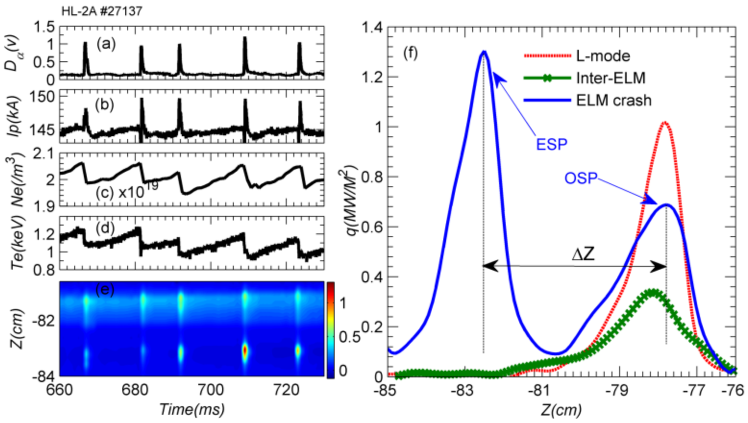

Figure 5.2. Example of HL-2A H-mode discharge #27137 with strike point shift. (a) D_α recycling; (b) plasma current I_p;(c) line-averaged density $\bar{\mathrm{n}}_e$ through the pedestal; (d) T_e from ECE at the pedestal; (e) divertor infrared camera measurement, indicating the strike point position and strike point shift; (f) A comparison of heat fluxes during an ELM at the ELM strike point (ESP), compared to L-mode and inter-ELM fluxes at the original strike point (OSP).[Gao 2019]

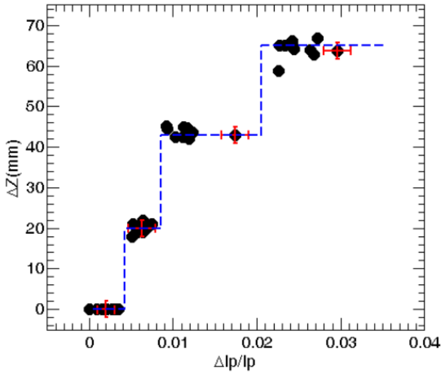

Figure 5.3. Resonance effect between the strike point shift and plasma current perturbation caused by the ELMs.[Gao 2019]

5.1.2. Deformation of local magnetic flux surfaces with evidence from bolometer tomography

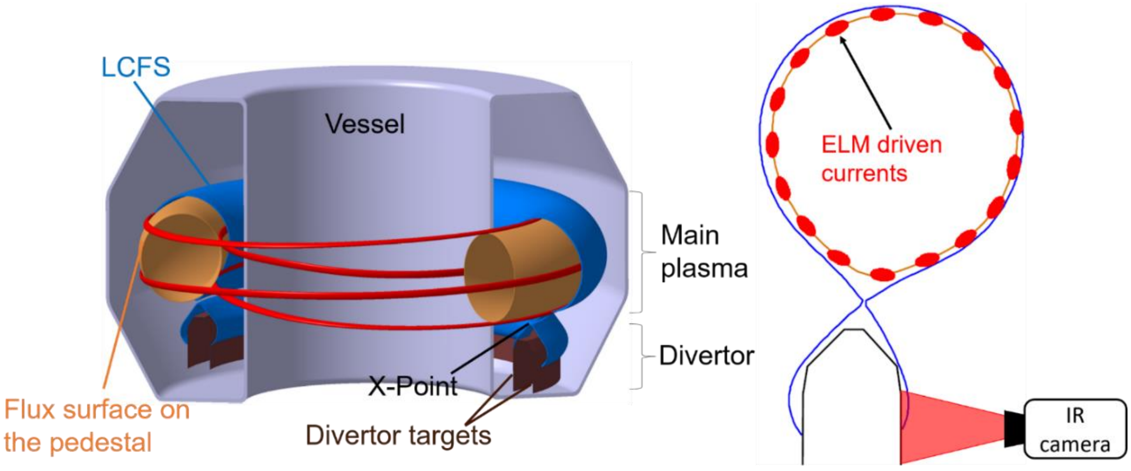

Figure 5.4. Illustration of ELM driven currents on pedestal flux surface position on HL-2A. [Gao 2019]

As one of the potential explanation for the strike point shift phenomena, [Gao 2019] has proposed that, regarding the resonance effect between plasma current perturbation and strike point shift distance, the shift is relevant to the ELM driven currents. After the ELM crashes, the fast electrons are generated on pedestal area and distributed as filements structure, which consists with ELM. These pedestal current filements formation could partially destroy the local magnetic equilibrium, and leading to an edge magnetic ergodization, as shown in **Figure 5.4**. The local edge magnetic ergodization would lead the internal confined heat escape through the saturated energy channels which have different direction from the L-mode, as shown in **Figure 5.6** (c), and offers an extra heat flux landing to divertor.

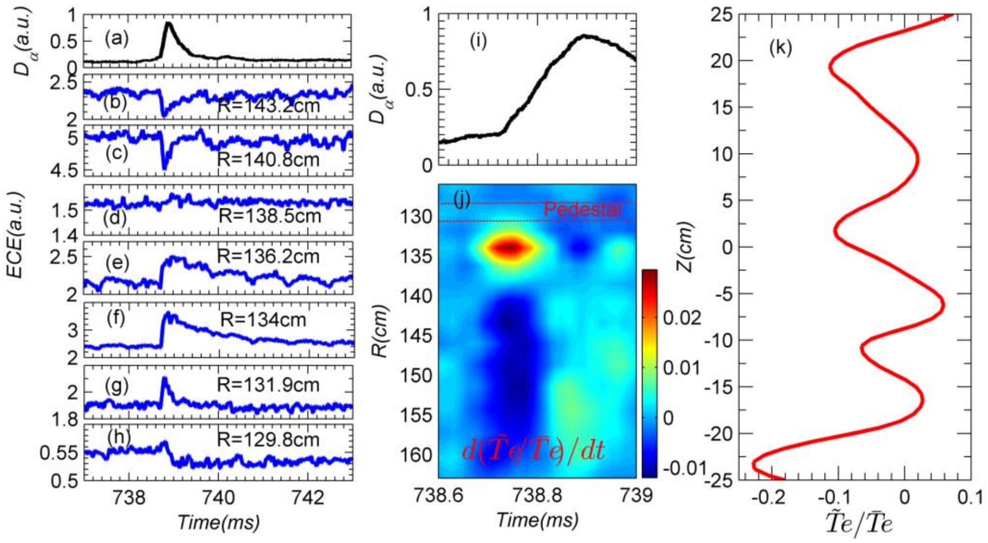

Figure 5.5. Example of HL-2A H-mode discharge #21930 with strike point shift. (a) D_α recycling; (b-h) T_e from ECE at different radial locations; (i) D_α recycling zoomed out and (j) electron temperature fluctuations from ECE measurements; (k) electron temperature fluctuations during an ELM at different vertical positions. [Gao 2019]

This is illustrated in **Figure 5.5**, where the radial location of the pedestal energy channel during an ELM has been detected through ECE, also seen in **Figure 5.5** (j), followed immediately by an increase in recycling visible in the D_α signal.

In order to provide further evidence for this hypothesis, using our Equi-GPT technique a reconstruction of the total radiated power has been performed based on bolometry measurements. In **Figure 5.6**, it can be clearly seen that for some ELMs coinciding with a strike point shift, the magnetic flux surfaces inside the pedestal can be broken up, causing heat transport along a path that is different from the case of an ELM without strike point shift. The difference in the geometry of the heat transport channels eventually leads to a shift of the strike point.

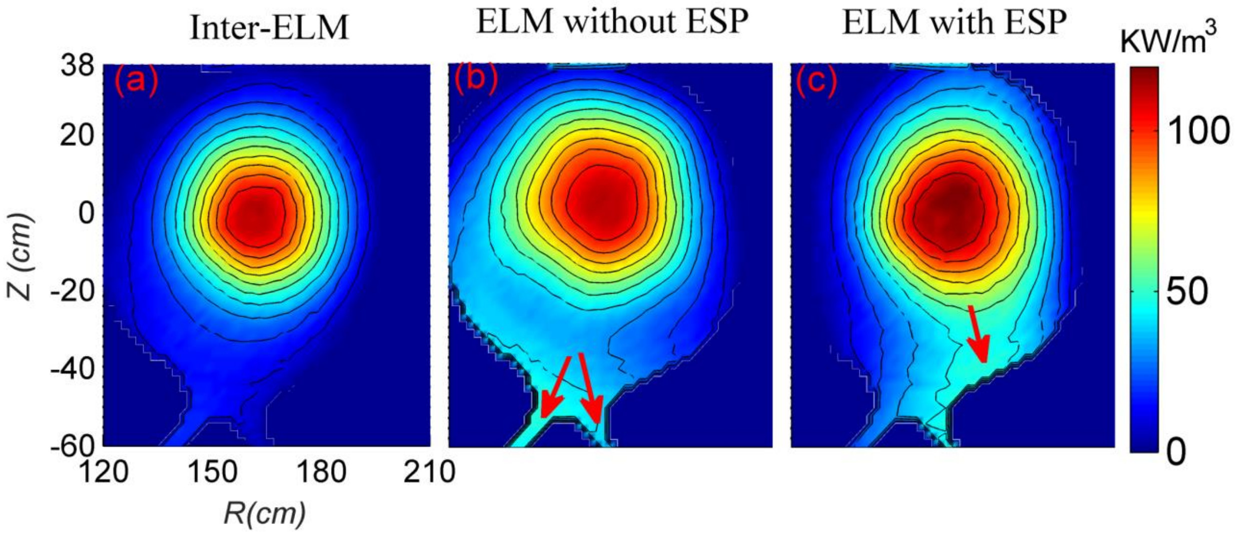

Figure 5.6. Example of the reconstructed radiated power distribution from bolometry using Equi-GPT (a) in between ELMs ,(b) during an ELM without strike point shift, (c) during an ELM with strike point shift. The red arrows indicate the predominant direct of the heat transport.

5.2. Equi-GPT on EAST

As another application of Equi-GPT with real data, we have selected soft X-ray tomography and bolometry tomography on the Experimental Advanced Superconducting Tokamak (EAST). The EAST device was developed by the Institute of Plasma Physics of the Chinese Academy of Sciences (abbreviated as ASIPP). The EAST device has three distinct features: non-circular cross-section, fully superconducting magnets and fully actively water-cooled plasma-facing components (PFCs). As such, EAST is well equipped for exploring advanced steady-state plasma operational modes. The device parameters are presented in Table 5.3.

Table 5.3. EAST parameters.

Major radius	1.85m	ICRH power	3 MW
Minor radius	0.45m	LHCD power	4 MW
Plasma current	1MA	Pules duration	1-1000s
Toroidal field	3.5T	Configuration	Double null divertor/
Triangularity δ_{95}	0.6-0.8		Pump limiter/
Elongation κ_{95}	1.6-2		Single null divertor

5.2.1. Observation of a sawtooth triggered kink mode by using SXR tomography

The current SXR system at EAST consists of three cameras, named U, D and V, as shown in Figure 5.7. All cameras are equipped with a single head, each head containing one diode array (S4114-46Q) and with its own pinhole and beryllium filter foil. The pinhole center corresponds to the middle of the diode array. The 3-array SXR diagnostic has a spatial resolution of about 2.5 cm and a temporal resolution up to 10 μs. The two horizontal cameras, U and D cameras, in port P are located in different poloidal positions but almost at the same toroidal position. The vertical camera V in port C is 67.5^o toroidally separated from the U and D arrays. Cameras U and D are up-down symmetrical in the poloidal cross-section. Both of them have 46 viewing lines which cover the whole plasma region.

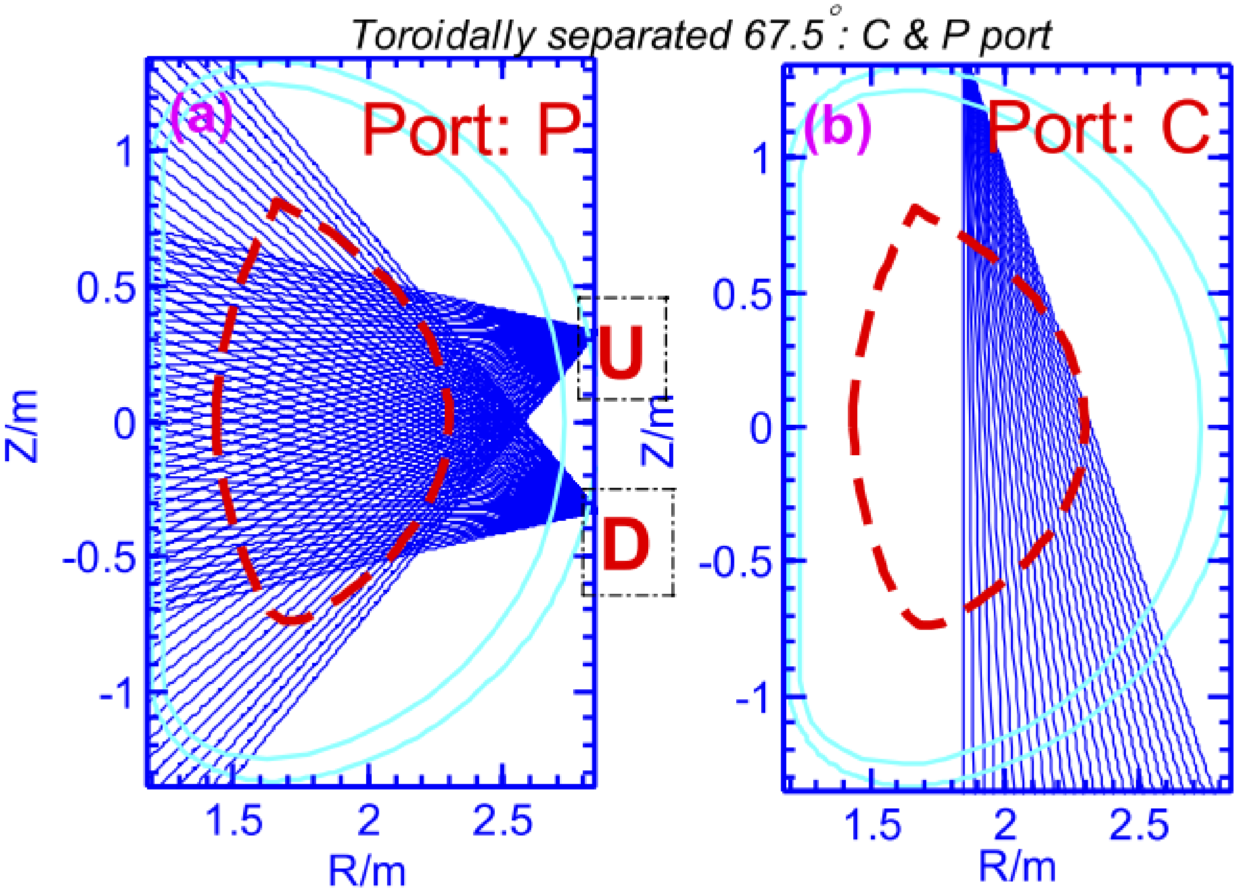

Figure 5.7. Projection of the lines-of-sight of the EAST SXR diagnostic in the poloidal cross-section in which the camera pinholes are located. The U and D cameras are located in port P and the V camera in port C. The red dotted circle marks the typical location of the last-closed flux surface in EAST. Figure reprinted from [Chen 2016].

Due to the different toroidal position of the C port camera, only measurements of the P port cameras are used in this work. The LOS distribution and flux surfaces position has been demonstrated in Figure 5.8. Data from a total of 92 LOS have been used and the SXR emissivity reconstruction grid consists of 50×50 pixels, each with a dimension of $17.8 \text{ mm} \times 29.1 \text{ mm}$.

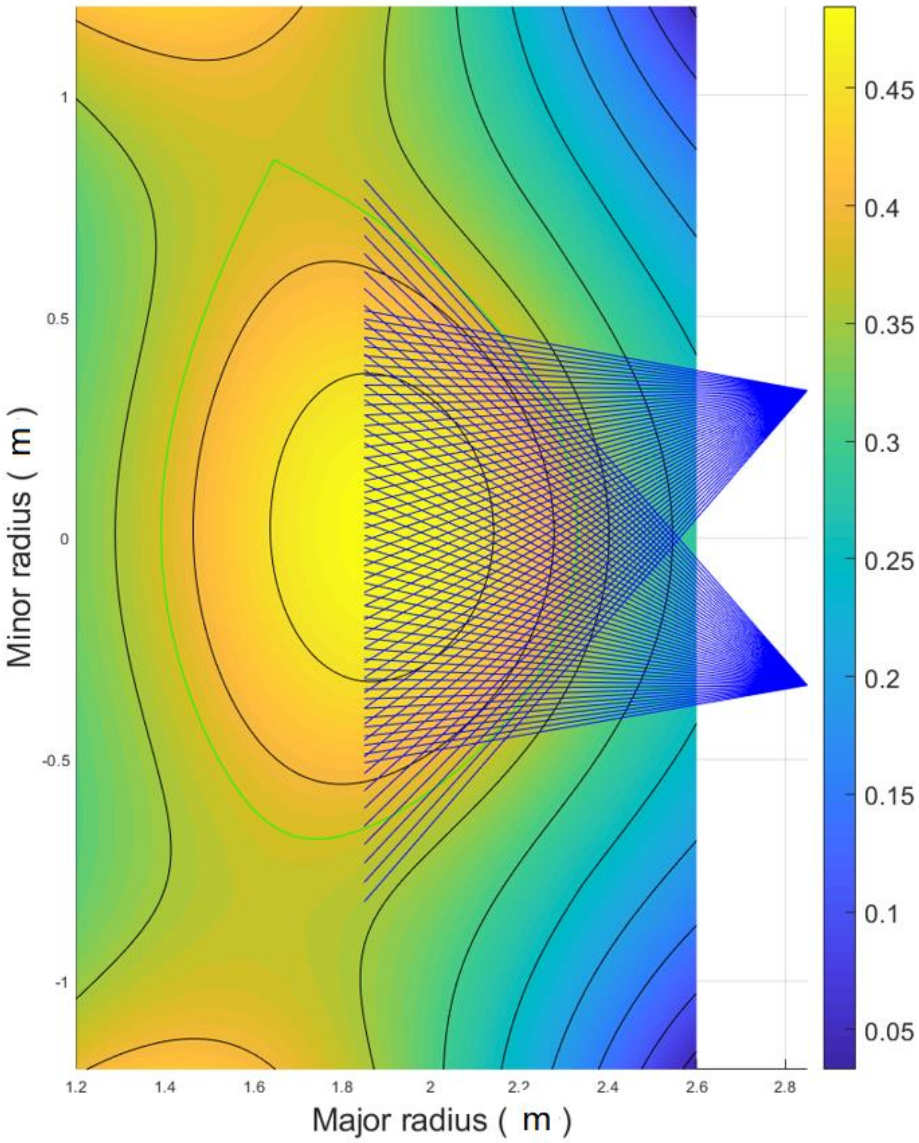

Figure 5.8. Illustration of LOS distribution of the two horizontal P port SXR cameras in an upper-single null configuration at EAST. The green curve indicates the position of the last-closed flux surface.

Equi-GPT reconstruction results are presented at different times during EAST discharge #70750 in **Figure 5.9**. This discharge exhibited MHD activity, which was later identified as a kink mode triggered by sawteeth. The reconstructions in the figure clearly show the sawtooth redistribution mechanism with core expulsion, followed by a kink mode. In addition, the MHD mode structure was analyzed using singular-value decomposition, as shown in **Figure 5.10**. The three first topos corresponding to the (1, 1) structure of the kink mode are shown.

Especially, for this case study, the Equi-GPT provides each time slide reconstruction result within computational time around 8ms, as shown in **Figure 4.11** a 500 time slides computational time statistic histogram has been given.

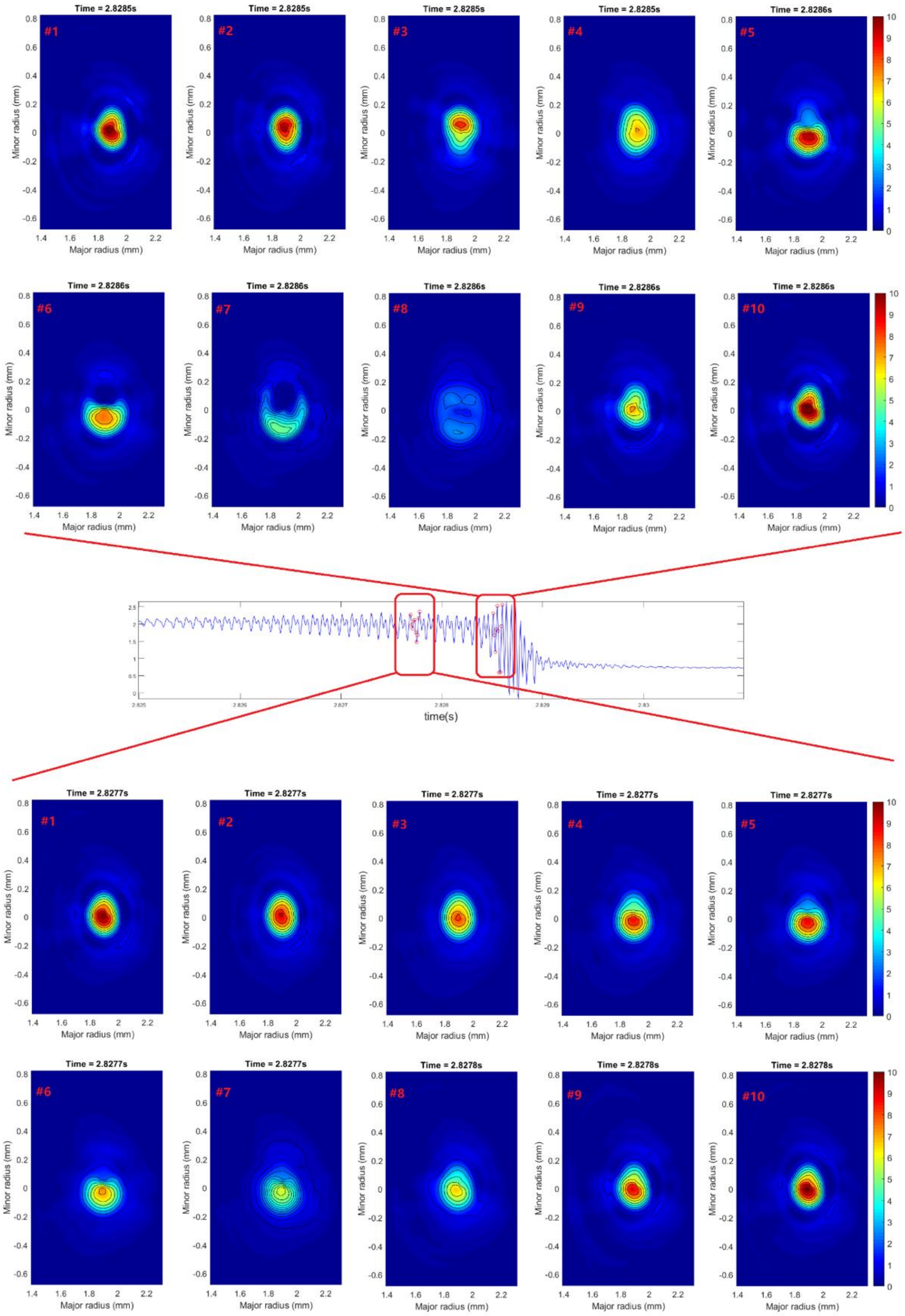

Figure 5.9. Application of Equi-GPT to SXR data in EAST discharge #70750 during a sawtooth-triggered kink mode event. The blue signal in the center represents the time evolution of SXR channel #23 (unit a.u.). The lower panels show the reconstructed SXR emissivity field during the sawtooth. The upper panels present the subsequent kink mode evolution, triggered by the sawtooth.

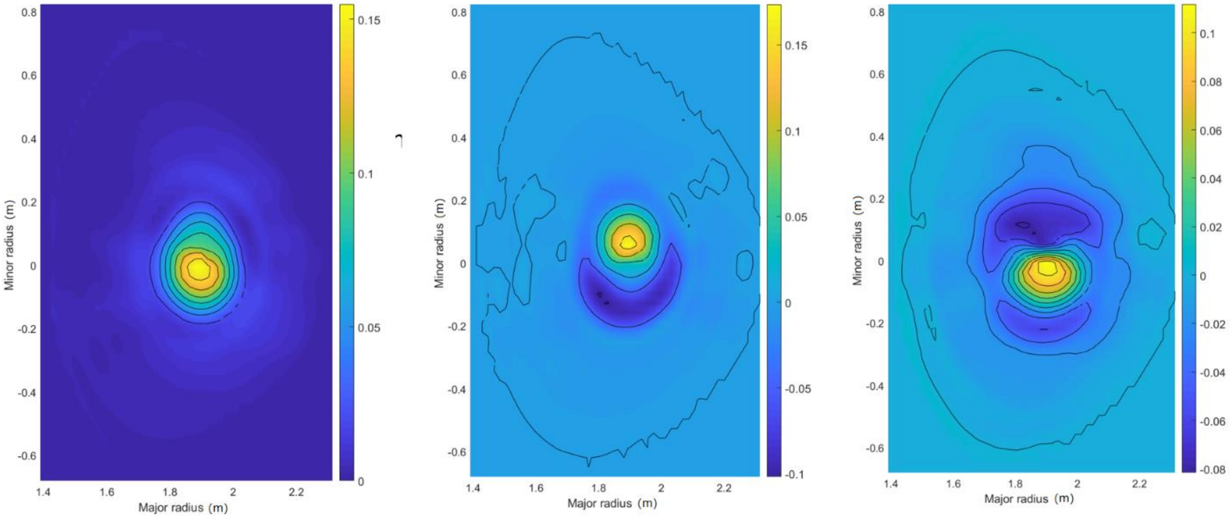

Figure 5.10. Singular-value decomposition analysis of the kink mode. The first three topos are shown, clearly showing the (1, 1) mode structure in the second topos.

5.2.2. Observation of low frequency oscillations using AXUV bolometer tomography during I-mode on EAST

The bolometer system installed on EAST [Duan 2013] has adopted a system of absolute extreme ultraviolet (AXUV) photodiode detectors. The AXUV photodiodes are of the type AXUV-16ELG linear array. Five pinhole cameras with a total of 80 channels have been developed, as shown in **Figure 5.10**. Each camera contains a 16-channel array with a spatial resolution of $3\ \mathrm{cm}$. Four cameras are installed in the horizontal port to fully cover the poloidal cross-section. The upper two cameras and the lower two cameras are symmetrical w.r.t. the equatorial plane. Another vertical camera is installed in the upper port to view the lower divertor through the bulk plasma. All detectors are placed inside the vacuum vessel. Due to the different calibration process of the horizontal and vertical cameras, only data from the four horizontal cameras is used in this work. The LOS distribution and flux surfaces position has been demonstrated in **Figure 5.12**. Thus 64 LOS has been implemented, and the radiation reconstruction grid has been designed as 50×50 pixels with dimension $17.8\ \mathrm{mm} \times 29.1\ \mathrm{mm}$.

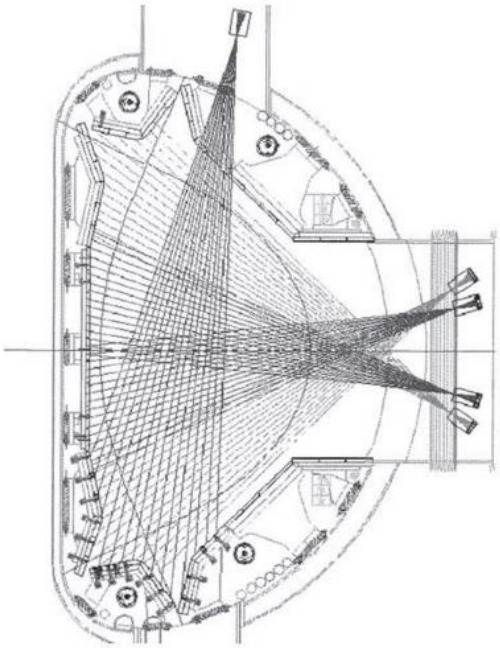

Figure 5.11. The geometry of AXUV bolometry on EAST. [Duan 2013]

In 2014, the EAST upper divertor was upgraded to full tungsten, while the lower divertor was conserved to be carbon. Consequently, all high-performance discharges were in the upper-single null (USN) shape to avoid large amounts of carbon impurities entering the main plasma. Thus, operations most frequently have a clockwise toroidal field, such that the ion $\vec{\mathrm{B}} \times \nabla\vec{\mathrm{B}}$ drift in the 'unfavorable' direction away from the active X-point, providing ample opportunities for I-mode studies.

The presence of I-mode in EAST has been confirmed very recently [Feng 2019]. It can be achieved in a relative wide parameter space with plasma currents of $\mathrm{I}_p \sim 0.45 - 0.7\ MA$ and toroidal magnetic field $\mathrm{B}_\phi = 2.26 - 2.49\ \mathrm{T}$, in USN geometry. In particular, at high-heating-power (above $1.8\ MW$) and high density (above $2.5 \times 10^{19}\mathrm{m}^{-3}$), the features of the I-mode become quite distinct. No heating method preference is observed, and the L-I transition can be triggered by many heating methods. A typical example of an I-mode discharge is shown in **Figure 5.13**, including sawtooth activity. The main heating methods are NBI and ECRH, and, as shown in **Figure 5.13**(b), the NBI power increases from $3\ \mathrm{MW}$ to $5\ \mathrm{MW}$ at approximately $2.5\ \mathrm{s}$, while $0.3\ \mathrm{MW}$ of ECRH turns on at $2.58\ \mathrm{s}$. The plasma current is approximately $500\ \mathrm{kA}$, and the line-averaged density from the HCN interferometer remains almost unchanged in the entire period as shown in **Figure 5.13**(a). However, the core and edge electron temperature T_e from ECE (**Figure 5.13**(c)) increase, as do the stored energy $\mathrm{W}_{\mathrm{MHD}}$ and poloidal beta β_p (**Figure 5.13**(e)). A new steady state sets in at approximately 2.6 s after the ECRH has turned on, indicating improved energy confinement. The energy confinement time increases by about 7% from 36.1 to $38.6\ \mathrm{ms}$. The fact that neither the density, nor the D_α signal undergo marked changes across the transition, suggests similar particle confinement as in L-mode. Finally, after the transition, the spectrogram of the edge radial electric field E_r which is obtained from DBS reveals a weakly coherent mode (WCM) with a frequency of $40 - 150\ \mathrm{kHz}$ (**Figure 5.13**(f)). Observed also on other devices, this E_r fluctuation is characteristic for I-mode operation.

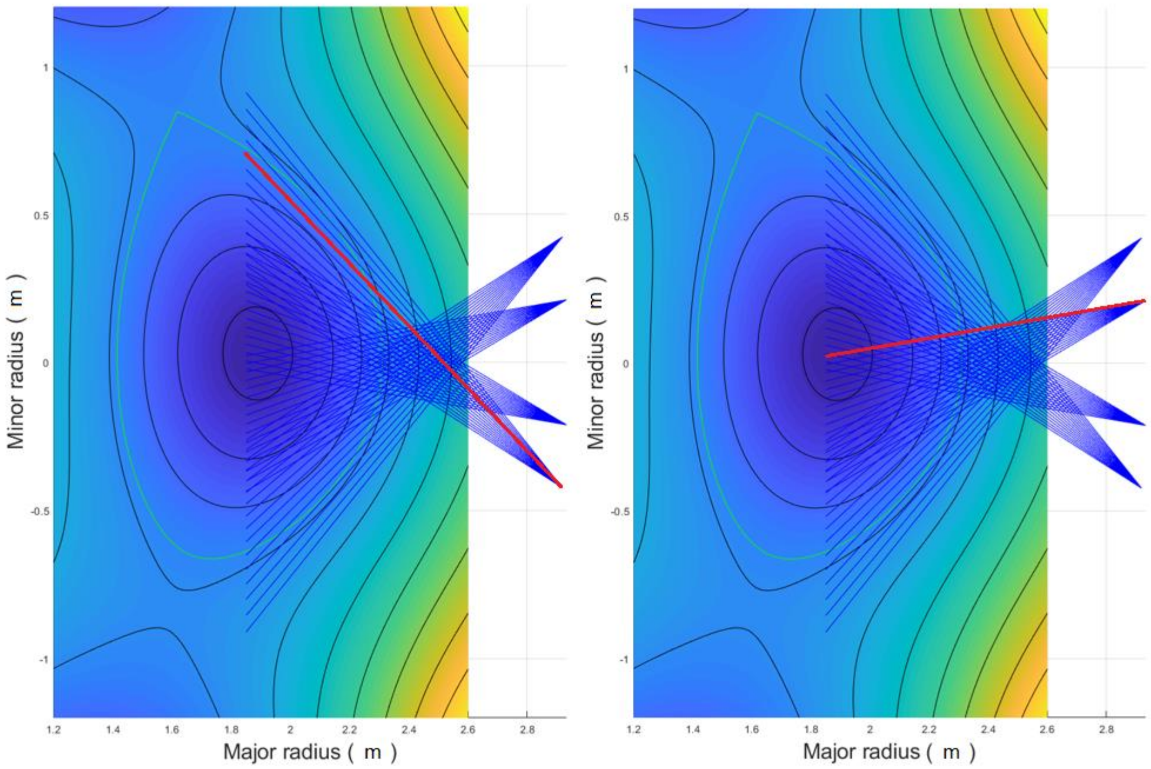

Figure 5.12. Viewing geometry of the four AXUV bolometer cameras in the horizontal port, in upper-single null configuration on EAST. The green line marks the last-closed flux surface. For later use, a LOS traversing the plasma edge has been marked in red in the left panel (channel #60) and another one traversing the plasma core in the right panel (channel #32).

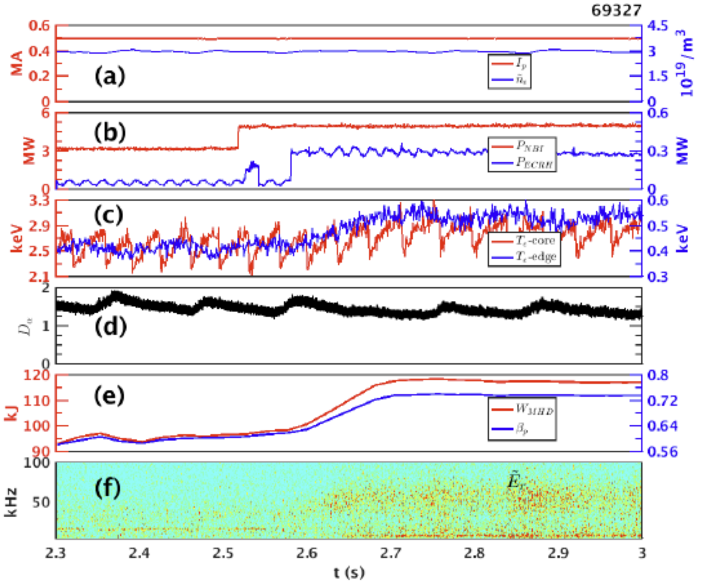

Figure 5.13. Example of EAST I-mode discharge #69327, upper single-null, $B_\phi = 2.23$ T, $q_{95} \sim 4$. The L-mode and I-mode phases are indicated from stored energy W_{MHD}, a L-I transition has been observed from 2.6s to 2.7s. (a) Plasma current and line-averaged density $\bar{n}_e$; (b) NBI and ECRH heating power; (c) T_e from ECE in core and edge; (d) D_α recycling; (e) stored energy W_{MHD} and poloidal beta β_p; (f) WCM in the E_r perturbation.[Feng 2019]

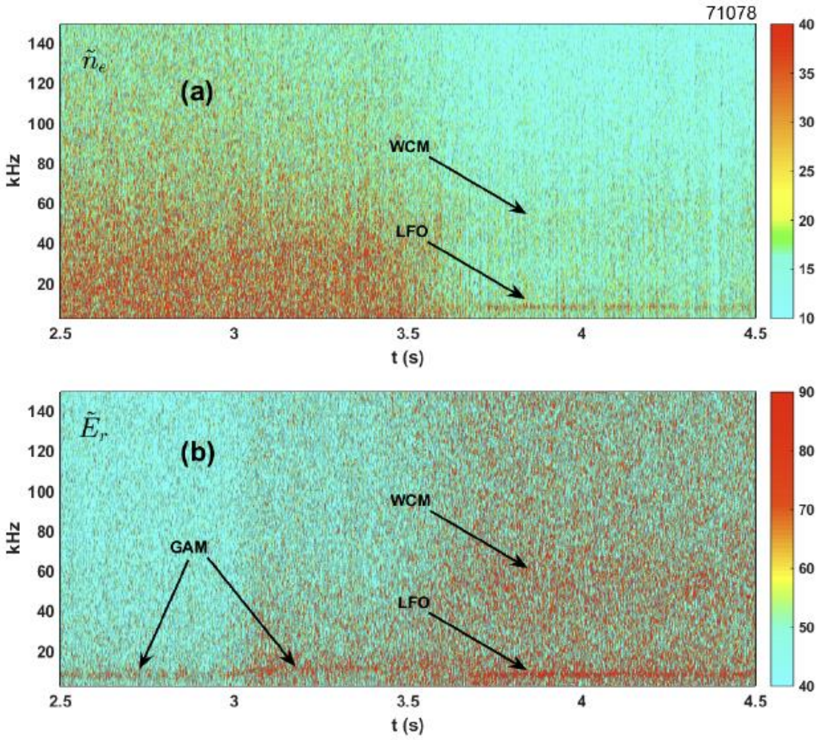

Figure 5.14. Spectrograms at normalized radius $\rho \sim 0.97$ of (a) density fluctuations (turbulence) and (b) E_r fluctuations during an L-I transition at $t = 3.5$s in EAST discharge #71078.[Feng 2019]

In particular, a low-frequency oscillation (LFO) with a frequency range of $5 - 10\ \mathrm{kHz}$ always accompanies the WCM in the EAST I-mode operation, as shown in **Figure 5.13** (f) (approximately $7\ \mathrm{kHz}$) and in **Figure 5.14** (a) and (b) (approximately $9\ \mathrm{kHz}$). Unlike the geodesic acoustic mode (GAM), the density perturbation and E_r perturbation of this type of low-frequency oscillations are significant. Many observations show that the LFO is another characteristic of the I-mode operation, in addition to the WCM in EAST. Even the LFO is similar to that observed in Alcator C-Mod and AUG, but it is obviously not a GAM, whose frequency range should be $15 - 25\ \mathrm{kHz}$ in these discharges. However, the details of the low-frequency oscillation remain unknown, and require further investigation.

Similar to the results from the Doppler backscattering system, the LFOs are also clearly observed by the AXUV bolometer system, an example of which is shown in **Figure 5.15**, corresponding to AXUV edge channel #60 marked in **Figure 5.12** (left). For comparison, the spectrogram of AXUV core channel #32 (**Figure 5.12** (right)) is also given in **Figure 5.16**. It is clear that this LFO mode occurs at the edge, not in the plasma core.

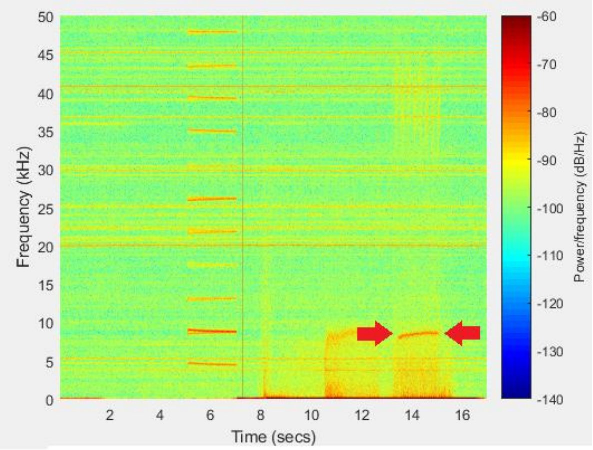

Figure 5.15. The power spectra of EAST I-mode discharge #69979 the AXUV radiation perturbation from edge, channel#60, the LFO has been recognized during I-mode period from 13.2s to 15.1s.

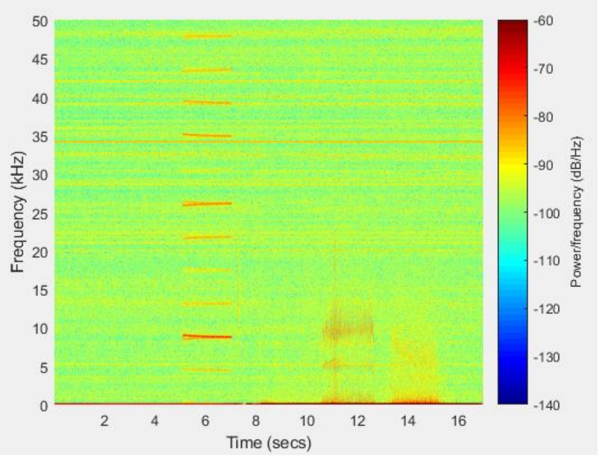

Figure 5.16. The power spectra of EAST I-mode discharge #69979 the AXUV radiation perturbation from core, channel#32, the I-mode period from 13.2s to 15.1s.

Equi-GPT reconstruction results from AXUV bolometry data in I-mode discharges #42880 and #69979 at EAST are presented in **Figure 5.17**. The LFO corresponds to a ring-shape radiation structure located at position $\rho \sim 0.9$. In addition, the mode structure has been revealed using SVD, **Figure 5.18** showing the three first topos. The second topos suggests that the LFO mode might be an $m = 0$ ring structure. Also, some additional (1, 1) mode structure from the core area is seen in the third SVD topos.

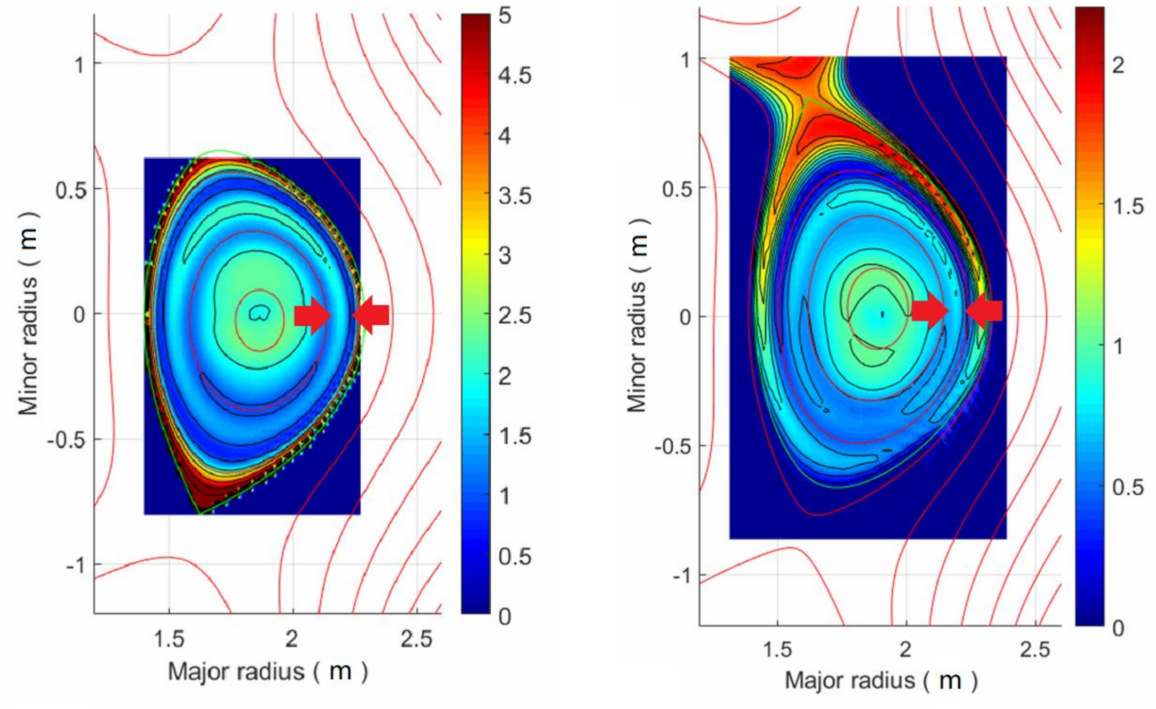

Figure 5.17. AXUV bolometer tomography reconstruction of EAST I-mode discharge #42880 (left) and discharge #69979 (right). A radiative ring can be recognized at the position of the LFO ($\rho \sim 0.9$), indicated by red arrows.

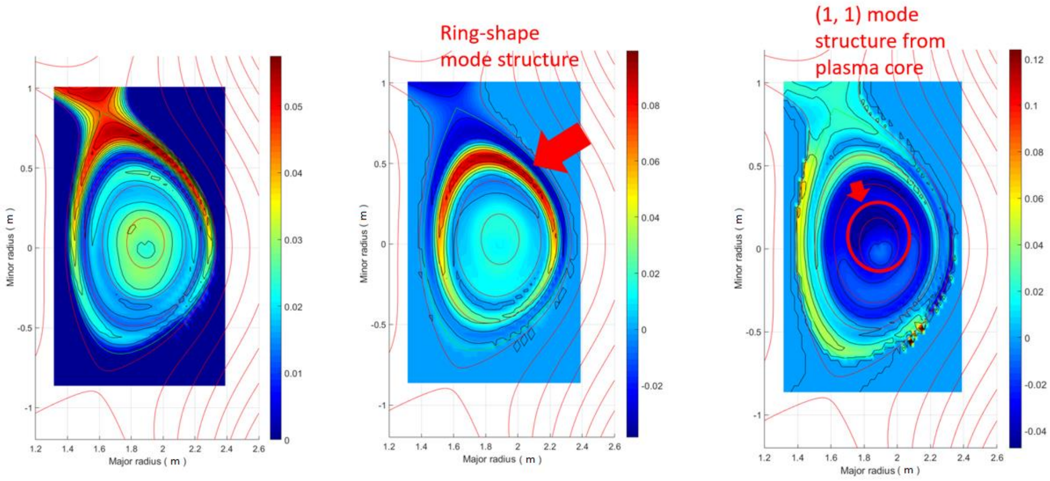

SVD first topos

SVD second topos

SVD third topos

Figure 5.18. SVD analysis of the LFO mode structure in EAST I-mode discharge #69979. The second topos hints at an $m = 0$ ring structure.

Chapter 6 Reconstruction of tungsten concentration profiles

In this chapter, we will introduce the basic method of impurity concentration reconstruction, particularly for high-Z impurities, using Gaussian process tomography. We will see that nonlinearities in the forward model complicate the reconstruction process in a first approach.

As mentioned before, it is expected that various plasma-facing components in fusion reactors will be manufactured using high-Z materials such as W, Mo or Fe. These materials provide advantages like a high melting point, small erosion rates, and low tritium retention. However, due to the interaction of the plasma with the wall, ions of this material will be inevitably present also in the main plasma. These ions are not entirely stripped even at fusion plasma temperatures, and therefore will emit strong line radiation, which can significantly degrade the performance of the fusion plasma. As a consequence, the understanding and control of impurity transport are of critical importance to the success of fusion. Moreover, the high mass and charge of the heavy impurities make them susceptible to some of the forces acting upon the plasma, resulting in a poloidal variation of their density. An example from AUG is shown in Figure 6.1. The most prominent are the centrifugal force arising from the plasma rotation and the electric force caused by magnetically trapped non-thermal ions. Poloidal asymmetries are expected to significantly impact the radial transport of heavy ions. Thus, it is crucial to quantify impurity distributions to establish a strategy for avoiding unacceptable high-Z impurity concentrations [Reinke 2012].

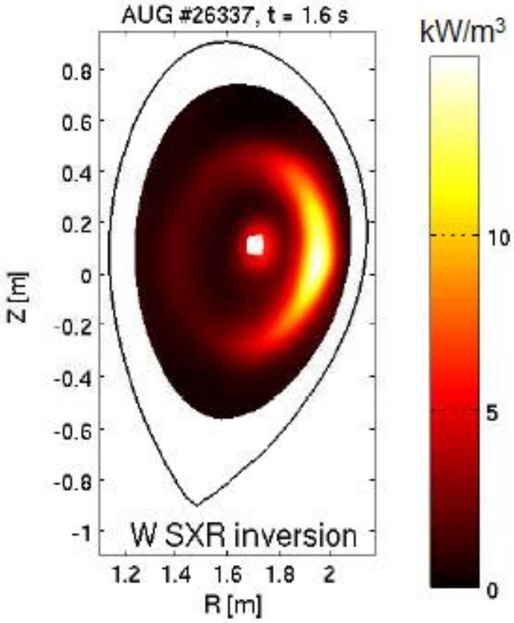

Figure 6.1. Two-dimensional SXR tomographic inversion with Bremsstrahlung subtracted, performed on AUG 26337 at $t = 1.6$ s in the presence of W impurities. [Casson 2014]

6.1. Effect of transport on tungsten impurity radiation

In the discussion about the cooling factor in Section 3.1.3, the effect of transport effects has been omitted. Because the transport time scale is much longer than that of excitation and ionization, the ionization equilibrium described in Eq. (3.21) has been simplified into collisional-radiative models in Eq. (3.22). This generally provides a good approximation for obtaining the fractional abundance of the various species and the cooling factor. However, in some cases transport does play a role and the fractional abundances $f_{S,i}$ and the cooling factor L_S are no longer only a function of the electron temperature only. The full ionization equilibrium becomes:

$$\frac{\partial n_i^{(Z)}}{\partial \mathrm{t}} + \vec{\nabla}\cdot\vec{\Gamma}_{Z,i} = -n_e n_i^{(Z)}\left(S_{(Z)}^{eff} + \alpha_{(Z+1)}^{eff}\right) + n_i^{(Z+1)} n_e \alpha_{(Z+1)}^{eff} + n_e n_i^{(Z-1)} S_{(Z-1)}^{eff} + s_{ext,Z,i} \qquad (6.9)$$

where, $S_{(Z)}^{eff}$ and $\alpha_{(Z+1)}^{eff}$ are referred to as effective collisional-radiative ionization and recombination coefficients. Both are functions of electron temperature T_e and weakly depend on density n_e. $s_{ext,Z,i}$ is the external source of i th ionization stage Z^i of a species with charge number Z and $\vec{\Gamma}_{Z,i}$ is the corresponding local particle flux, which is usually expressed as:

$$\vec{\nabla}\cdot\vec{\Gamma}_{Z,i} = -D_{Z,i}\vec{\nabla} n_i^{(Z)} + n_i^{(Z)}\vec{V}_{Z,i} \qquad (6.10)$$

Here, $D_{Z,i}$ and $\vec{V}_{Z,i}$ are diffusion and convection (or pinch) coefficients of the species Z^i.

Thanks to the efforts of [Jardin 2017], the tungsten fractional abundances in a WEST scenario (as shown in Figure 6.3) have been numerically obtained by using the Open-ADAS database. A set of profiles for diffusion coefficient D and pinch velocity V were assumed, shown in Figure 6.3. The profiles are compatible with the tungsten density profile in the scenario and homothetic to the electron density profile, with $n_W(0) \approx 8\cdot 10^{15}\ m^{-3}$, and account for higher collisionality at the plasma edge where T_e is lower. The expected order of magnitude of the tungsten diffusion and pinch coefficients is $D \sim 0.01 - 1\ \mathrm{m}^2/\mathrm{s}$ and $\mathrm{V} \sim 1 - 10\ \mathrm{m/s}$, respectively.

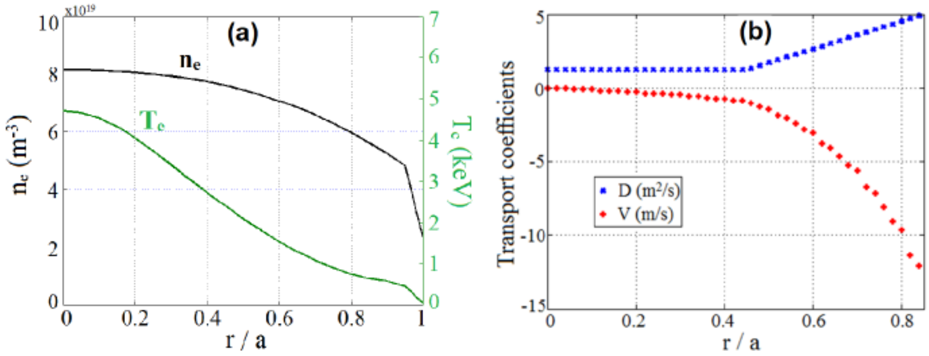

Figure 6.3. (a) Electron density and temperature profiles for the WEST scenario under consideration. (b) Corresponding profiles of the W diffusion and convection coefficients [Jardin 2017].

The numerically calculated profiles of the various W ionization stages assuming the influence of transport has been ignored, namely local ionization balance (LIB) are given in **Figure 6.4**. In addition, the profiles are shown that are obtained when taking into account the effect of transport according to the scenario described above. While the profiles of the individual species are seen to be significantly affected by transport, the mean ionization state ($\mathrm{Z_{mean}} = \sum_{Z=0}^{74} f_{W,i} \cdot Z$) is only weakly perturbed by transport.

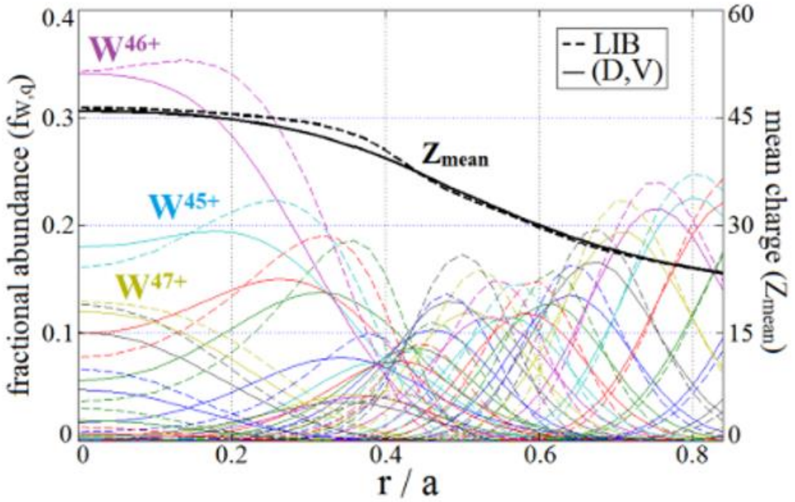

Figure 6.4. W ionization equilibrium for two transport cases: local ionization balanced (LIB) and WEST transport scenario [Jardin 2017].

From the above profiles, the tungsten cooling factor can be obtained by summation over the charge states, yielding the profiles with and without transport shown in **Figure 6.5**.

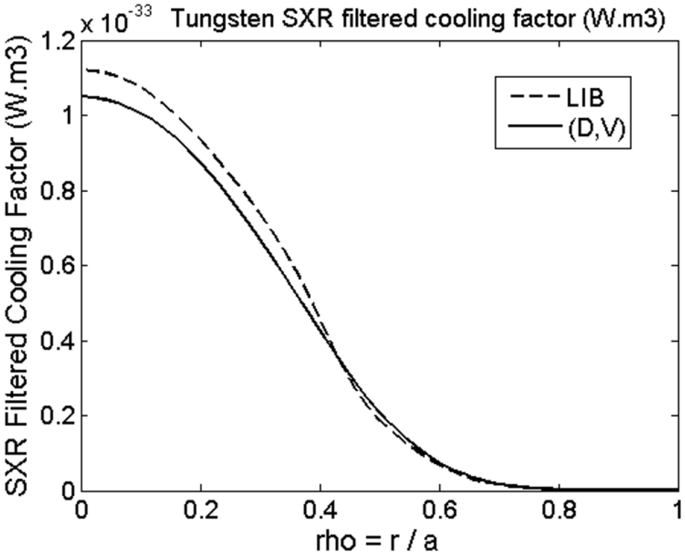

Figure 6.5. Radial profiles of the tungsten cooling factor in two cases: LIB and WEST transport scenario.

6.2. Direct tungsten density calculation from SXR tomographic reconstructions

Assuming for the moment local ionization balance and given the profiles of temperature, density and tungsten cooling factor from the WEST scenario, it is straightforward to calculate the tungsten density profile from the SXR emissivity profile, using Eq. (3.32). In doing so, we disregard the propagation of uncertainties, but it is instructive to do the calculation. Two tests were carried out, one with a poloidal tungsten distribution shown in **Figure 6.6** (d) and another one as shown in **Figure 6.7** (d). The maximum value of the tungsten concentration was fixed at 10^{-5}, corresponding to the typical tungsten tolerance introduced in **Figure 2.11**. In both tests, from the assumed tungsten poloidal distribution, together with the radial temperature, density and cooling factor profiles, an SXR poloidal distribution was calculated, as shown in **Figure 6.6** (a) and **Figure 6.7** (a). Then, synthetic SXR measurements were obtained by integrating the SXR profile according to the WEST SXR geometry. This is shown in **Figure 6.6** (f) and **Figure 6.7** (f) (blue curves). Finally, 5% Gaussian noise was added, resulting in the measurements given by the red dots in **Figure 6.7** (f) and **Figure 6.7** (f).

Next, using the synthetic SXR measurement, the SXR tomographic reconstruction was performed using the Equi-GPT algorithm. The results are presented in **Figure 6.6** (b) and **Figure 6.7** (b), and the reconstruction error maps in **Figure 6.6** (c) and **Figure 6.7** (c). Finally, the tungsten density was calculated in a poloidal cross-section directly from the reconstructed SXR emissivity distribution and the temperature, density and cooling factor profiles. These profiles are shown in **Figure 6.6** (e) and **Figure 6.7** (e).

In both tests, it appears that the calculated tungsten density profile is relatively accurate in a central region of the poloidal cross-section, but the error increases strongly outside that region. This is due to uncertainties of the various profiles, in combination with the low values reached by the electron density and tungsten cooling factor in the plasma edge region (both occurring in the denominator in $\mathrm{Eq.}\,(3.32)$). This leads to an amplification of the error on the calculated tungsten density in a large region outside the very plasma core.

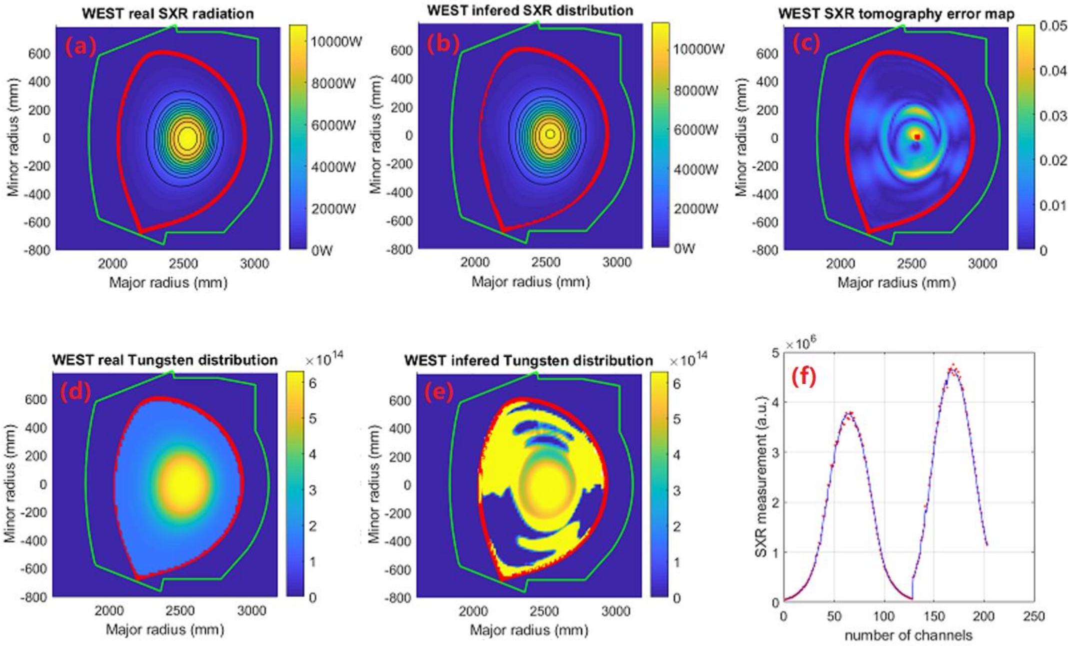

Figure 6.6. Illustration of the reconstruction of tungsten density profiles with a Gaussian shape from synthetic SXR measurements in a WEST scenario. (a) Modelled SXR radiation distribution based on the known tungsten distribution (d) and WEST scenario from Figure 6.3. (b) SXR tomography reconstruction using synthetic measurements from the phantom shown in (a). (c) SXR tomography error map. (d) The preset, known tungsten distribution. (e) Tungsten density distribution calculated directly from the SXR tomographic reconstruction (b). (f) Synthetic line-integrated SXR emissivity (blue curve) and synthetic measurements with 5% random noise added (red dots).

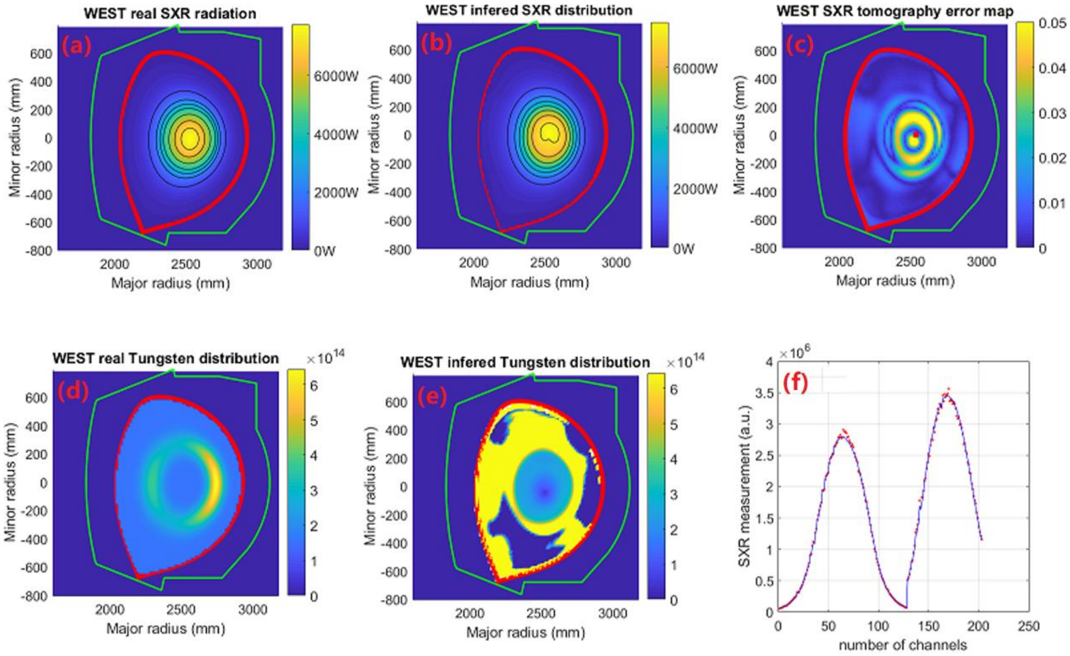

Figure 6.7. Similar to Figure 6.6, but starting from a hollow-shape tungsten density distribution.

6.3. Bayesian inference of tungsten density profiles

In this section, we proceed to Bayesian inference of tungsten density profiles, taking into account uncertainties on all input quantities. In particular, we outline a simple approach for inferring the density profile of a single dominant impurity, in our case tungsten, from measurements of soft X-ray (SXR) emissivity, electron cyclotron emission (ECE) and Thomson scattering (TS). For the SXR emissivity, as usual, a Gaussian process prior is assumed, and this is combined with the linear tomographic model. The rest of the forward model, used to derive the impurity concentration, is nonlinear in terms of the profiles of electron temperature (from ECE) and electron density (from TS). Within the scope of the PhD thesis, we therefore consider two very simple approaches: one where temperature and density profiles are assumed to be exactly known and one where Gaussian errors are assumed on the profiles. The possibility to estimate transport coefficients is proposed, but this would require a number of additional transport simulations.

6.3.1 Influence of transport neglected

Let us first assume that transport can be neglected, leading to local ionization balance. Let $\bar{d}_{SXR}$ represent the measurements of line-integrated soft X-ray emissivity. Assuming tungsten as the dominant impurity, the posterior distribution for the tungsten density profile (2D) is given as

$$p(\bar{n}_w|\bar{d}_{SXR}) \sim p(\bar{d}_{SXR}|\bar{n}_w) \cdot p(\bar{n}_w) \qquad (6.11)$$

Forward model:

$$\bar{d}_{SXR} = \bar{\bar{R}} \cdot \bar{\varepsilon}^{\eta} = \bar{\bar{R}} \cdot (\bar{\varepsilon}_w^{\eta} + \bar{\varepsilon}_H^{\eta})$$

$$= \bar{\bar{R}} \cdot \left(\bar{n}_e . \bar{n}_w . L_w^{\eta}(\bar{T}_e) + \bar{n}_e . \bar{n}_e . L_H^{\eta}(\bar{T}_e)\right) = \bar{R}(\bar{n}_e, \bar{n}_w, \bar{T}_e) \qquad (6.12)$$

Where $\bar{R}(\bar{n}_e, \bar{n}_w, \bar{T}_e)$ is the response function of forward model

Here, $\bar{\bar{R}}$ represents the response matrix of the lines-of-sight, while $\bar{\varepsilon}^{\eta}$, $\bar{\varepsilon}_w^{\eta}$ and $\bar{\varepsilon}_H^{\eta}$ represent the total SXR emissivity, as well as the contribution from tungsten and hydrogen in the GEM energy range, respectively. The temperature profile from ECE is a one-dimensional radial profile, but assuming exact knowledge of the magnetic equilibrium, it can easily be mapped to the two-dimensional poloidal cross-section.

The Gaussian process prior, SXR tomographic likelihood and Gaussian process posterior are given as:

Prior:

$$p(\bar{n}_w) = \frac{1}{(2\pi)^{\frac{n}{2}}\left|\bar{\bar{\Sigma}}_w\right|^{\frac{1}{2}}} exp\left[-\frac{1}{2}(\bar{n}_w - \bar{\mu}_w)^T\,\bar{\bar{\Sigma}}_w^{-1}\,(\bar{n}_w - \bar{\mu}_w)\right] \tag{6.13}$$

Likelihood:

$$p\left(\bar{d}_{SXR}\middle|\bar{n}_w\right) = \frac{1}{(2\pi)^{\frac{m}{2}}\left|\bar{\bar{\Sigma}}_{SXR}\right|^{\frac{1}{2}}} exp\left[-\frac{1}{2}\left(\bar{R}(\bar{n}_e,\bar{n}_w,\bar{T}_e)-\bar{d}_{SXR}\right)^T\,\bar{\bar{\Sigma}}_{SXR}^{-1}\,\left(\bar{R}(\bar{n}_e,\bar{n}_w,\bar{T}_e) - \bar{d}_{SXR}\right)\right] \tag{6.14}$$

$\mathrm{T_e}$ *and* $\mathrm{n_e}$ *profiles exactly known*

If we assume that the profiles of $\bar{T}_e$ and $\bar{n}_e$ are known exactly from their respective diagnostic measurements, without uncertainty, then the only remaining unknown in the tungsten density. In this case, the total forward model is still linear and the results are those already presented in *Section 6.2*.

Forward model:

$$\begin{gathered}\bar{d}_{SXR} = \bar{\bar{R}}\cdot\bar{\varepsilon}^{\eta} = \bar{\bar{R}}\cdot(\bar{\varepsilon}_w^{\eta} + \bar{\varepsilon}_H^{\eta}) \\ = \bar{\bar{R}}\cdot\left(\bar{n}_e.\bar{n}_w.L_w^{\eta}(\bar{T}_e) + \bar{n}_e.\bar{n}_e.L_H^{\eta}(\bar{T}_e)\right) \\ = \bar{\bar{R}}_w\cdot\bar{n}_w + \overline{C_H} \\ \bar{d}'_{SXR} = \bar{d}_{SXR} - \overline{C_H}\end{gathered} \tag{6.15}$$

Here, $\overline{C_H}$ is the contribution of hydrogen, which is a known constant when $\bar{T}_e$ and $\bar{n}_e$ are exactly known.

Prior: $$p(\bar{n}_w) = \frac{1}{(2\pi)^{\frac{n}{2}}\left|\bar{\bar{\Sigma}}_w\right|^{\frac{1}{2}}} exp\left[-\frac{1}{2}(\bar{n}_w - \bar{\mu}_w)^T\,\bar{\bar{\Sigma}}_w^{-1}\,(\bar{n}_w - \bar{\mu}_w)\right] \tag{6.16}$$

Likelihood: $$p\left(\bar{d}'_{SXR}\middle|\bar{n}_w\right) = \frac{1}{(2\pi)^{\frac{m}{2}}\left|\bar{\bar{\Sigma}}_{SXR}\right|^{\frac{1}{2}}} exp\left[-\frac{1}{2}\left(\bar{\bar{R}}_w\cdot\bar{n}_w - \bar{d}'_{SXR}\right)^T\,\bar{\bar{\Sigma}}_{SXR}^{-1}\,\left(\bar{\bar{R}}_w\cdot\bar{n}_w - \bar{d}'_{SXR}\right)\right] \tag{6.17}$$

Posterior: $$p\left(\bar{n}_w\middle|\bar{d}'_{SXR}\right) \sim \mathcal{N}\left(\bar{\mu}_w^{post},\bar{\bar{\Sigma}}_w^{post}\right)$$

$$\bar{\bar{\Sigma}}_w^{post} = \left(\bar{\bar{R}}_w^{\ T}\bar{\bar{\Sigma}}_{SXR}\bar{\bar{R}}_w + \bar{\bar{\Sigma}}_W^{\ -1}\right)^{-1} \tag{6.18}$$

$$\bar{\mu}_w{}^{post} = \bar{\mu}_w{}^{prior} + \left(\bar{\bar{R}}_w{}^T \bar{\bar{\Sigma}}_{SXR} \bar{\bar{R}}_w + \bar{\bar{\Sigma}}_w{}^{-1}\right)^{-1} \bar{\bar{R}}_w{}^T \, \bar{\bar{\Sigma}}_{SXR}{}^{-1} \left(\bar{d}'_{SXR} - \bar{\bar{R}}_w \cdot \bar{\mu}_w\right) \qquad (6.19)$$

T_e *and* n_e *profiles measured with Gaussian error*

In this case we assume that the measured profiles provided by ECE diagnostic ($\bar{d}_{ECE}$) and Thomson scattering diagnostic ($\bar{d}_{TS}$) are affected by uncorrelated Gaussian noise. The posterior distribution for the tungsten concentration, electron density and electron temperature is then written as

$$p\left(\bar{n}_w, \bar{n}_e, \bar{T}_e \middle| \bar{d}_{SXR}\, \bar{d}_{ECE}, \bar{d}_{TS}\right) \sim p\left(\bar{d}_{SXR}\, \bar{d}_{ECE}, \bar{d}_{TS} \middle| \bar{n}_w, \bar{n}_e, \bar{T}_e\right) \cdot p(\bar{n}_w, \bar{n}_e, \bar{T}_e) \qquad (6.20)$$

Since the measurement of soft X-ray, ECE and Thomson scattering are independent probability events, we factorize the likelihood and the prior:

$$\begin{gathered} p\left(\bar{n}_w, \bar{n}_e, \bar{T}_e \middle| \bar{d}_{SXR}, \bar{d}_{ECE}, \bar{d}_{TS}\right) \sim p\left(\bar{d}_{SXR} \middle| \bar{n}_w, \bar{n}_e, \bar{T}_e\right) p\left(\bar{d}_{ECE} \middle| \bar{n}_w, \bar{n}_e, \bar{T}_e\right) p\left(\bar{d}_{TS} \middle| \bar{n}_w, \bar{n}_e, \bar{T}_e\right) \\ p(\bar{n}_w)\, p(\bar{n}_e)\, p(\bar{T}_e) \end{gathered} \qquad (6.21)$$

Furthermore, the ECE measurement is assumed to depend only on electron temperature and the TS measurement on electron density. Then Eq. (6.21) becomes

$$\begin{gathered} p\left(\bar{n}_w, \bar{n}_e, \bar{T}_e \middle| \bar{d}_{SXR}, \bar{d}_{ECE}, \bar{d}_{TS}\right) \sim p\left(\bar{d}_{SXR} \middle| \bar{n}_w, \bar{n}_e, \bar{T}_e\right) p\left(\bar{d}_{ECE} \middle| \bar{T}_e\right) p\left(\bar{d}_{TS} \middle| \bar{n}_e\right) \\ p(\bar{n}_w)\, P(\bar{n}_e)\, P(\bar{T}_e) \end{gathered} \qquad (6.22)$$

We take Gaussian process priors for $\overline{n_w}$, $\overline{n_e}$ and $\bar{T}_e$:

Priors:

Tungsten density

$$p(\bar{n}_w) = \frac{1}{(2\pi)^{\frac{n}{2}} \left|\bar{\bar{\Sigma}}_w\right|^{\frac{1}{2}}} \, exp\left[-\frac{1}{2} (\bar{n}_w - \bar{\mu}_w)^T \, \bar{\bar{\Sigma}}_w^{-1} \, (\bar{n}_w - \bar{\mu}_w)\right] \qquad (6.23)$$

Electron density

$$p(\bar{n}_e) = \frac{1}{(2\pi)^{\frac{n}{2}} \left|\bar{\bar{\Sigma}}_e\right|^{\frac{1}{2}}} \, exp\left[-\frac{1}{2} (\bar{n}_e - \bar{\mu}_n)^T \, \bar{\bar{\Sigma}}_e^{-1} \, (\bar{n}_e - \bar{\mu}_n)\right] \qquad (6.24)$$

Electron temperature

$$p(\bar{T}_e) = \frac{1}{(2\pi)^{\frac{n}{2}} \left|\bar{\bar{\Sigma}}_T\right|^{\frac{1}{2}}} \, exp\left[-\frac{1}{2} (\bar{T}_e - \bar{\mu}_T)^T \, \bar{\bar{\Sigma}}_T^{-1} \, (\bar{T}_e - \bar{\mu}_T)\right] \qquad (6.25)$$

In this simple approach, the TS and ECE likelihoods express the Gaussian error on the measured profiles. Denoting the TS radial density profile by $\bar{d}_{TS}$ and the ECE radial temperature profile by $\bar{d}_{ECE}$, the mapping from the radial profiles to the 2D density profile $\bar{n}_e$ and temperature profile $\bar{T}_e$ can be written as a linear forward model using projection matrices $\bar{\bar{R}}_{ECE}$ and $\bar{\bar{R}}_{TS}$:

Likelihoods:

Thomson scattering

$$p(\bar{d}_{TS}|\bar{n}_e) = \frac{1}{(2\pi)^{\frac{m}{2}}|\bar{\bar{\Sigma}}_{TS}|^{\frac{1}{2}}} \, exp\left[-\frac{1}{2}(\bar{\bar{R}}_{TS} \cdot \bar{n}_e - \bar{d}_{TS})^T \, \bar{\bar{\Sigma}}_{TS}^{-1} \, (\bar{\bar{R}}_{TS} \cdot \bar{n}_e - \bar{d}_{TS})\right] \tag{6.26}$$

ECE

$$p(\,\bar{d}_{ECE}|\bar{T}_e) = \frac{1}{(2\pi)^{\frac{m}{2}}|\bar{\bar{\Sigma}}_{ECE}|^{\frac{1}{2}}} \, exp\left[-\frac{1}{2}(\bar{\bar{R}}_{ECE} \cdot \bar{T}_e - \bar{d}_{ECE})^T \, \bar{\bar{\Sigma}}_{ECE}^{-1} \, (\bar{\bar{R}}_{ECE} \cdot \bar{T}_e - \bar{d}_{ECE})\right] \tag{6.27}$$

The likelihood covariance matrices will assumed to be diagonal and corresponding to a noise level of 5%:

$$\bar{\bar{\Sigma}}_{TS} = \begin{pmatrix} (5\% \cdot d_{TS}^1)^2 & \cdots & 0 \\ \vdots & \ddots & \vdots \\ 0 & \cdots & (5\% \cdot d_{TS}^m)^2 \end{pmatrix} \tag{6.28}$$

$$\bar{\bar{\Sigma}}_{ECE} = \begin{pmatrix} (5\% \cdot d_{ECE}^1)^2 & \cdots & 0 \\ \vdots & \ddots & \vdots \\ 0 & \cdots & (5\% \cdot d_{ECE}^m)^2 \end{pmatrix} \tag{6.29}$$

SXR

$$\bar{d}_{SXR} = \bar{\bar{R}} \cdot \bar{\varepsilon}^{\eta} = \bar{\bar{R}} \cdot (\bar{\varepsilon}_w^{\eta} + \bar{\varepsilon}_H^{\eta}) = \bar{\bar{R}} \cdot \left(\bar{n}_e.\bar{n}_w.L_w^{\eta}(\bar{T}_e) + \bar{n}_e.\bar{n}_e.L_H^{\eta}(\bar{T}_e)\right) \tag{6.30}$$

$$\begin{aligned} p(\bar{d}_{SXR}|\bar{n}_e, \bar{n}_w, \bar{T}_e) \\ &= \frac{1}{(2\pi)^{\frac{m}{2}}|\bar{\bar{\Sigma}}_{SXR}|^{\frac{1}{2}}} \, exp\left[-\frac{1}{2}(\bar{\bar{R}} \cdot \left(\bar{n}_e.\bar{n}_w.L_w^{\eta}(\bar{T}_e) + \bar{n}_e.\bar{n}_e.L_H^{\eta}(\bar{T}_e)\right) - \bar{d}_{SXR}\right)^T \, \bar{\bar{\Sigma}}_{SXR}^{-1} \, \Big(\bar{\bar{R}} \\ &\cdot \left(\bar{n}_e.\bar{n}_w.L_w^{\eta}(\bar{T}_e) + \bar{n}_e.\bar{n}_e.L_H^{\eta}(\bar{T}_e)\right) - \bar{d}_{SXR}\Big)\Big] \end{aligned} \tag{6.31}$$

It is important to note that T_e and n_e also occur in the SXR forward model, and the uncertainty on the corresponding measurements propagates through this model. In any case, the model now becomes nonlinear and, in the most general situation, we will need to sample from the posterior using numerical methods, e.g. by means of MCMC. We have chosen a Hamiltonian Monte Carlo (HMC) sampler [Brooks 2011].

The results of the reconstructed profiles of tungsten density, electron density and electron temperature are shown in **Figure 6.8**. The comparison with the original phantoms is made and the error maps are shown as well. The results are relatively good, with errors on the $\bar{n}_w$ map below 8 %, 10 % for $\bar{n}_e$ and a somewhat higher level of 20% for $\bar{T}_e$. **Figure 6.9** also shows the SXR reconstruction. Future work could concentrate on constructing suitable approximations to the posterior, eliminating the need for full MCMC sampling.

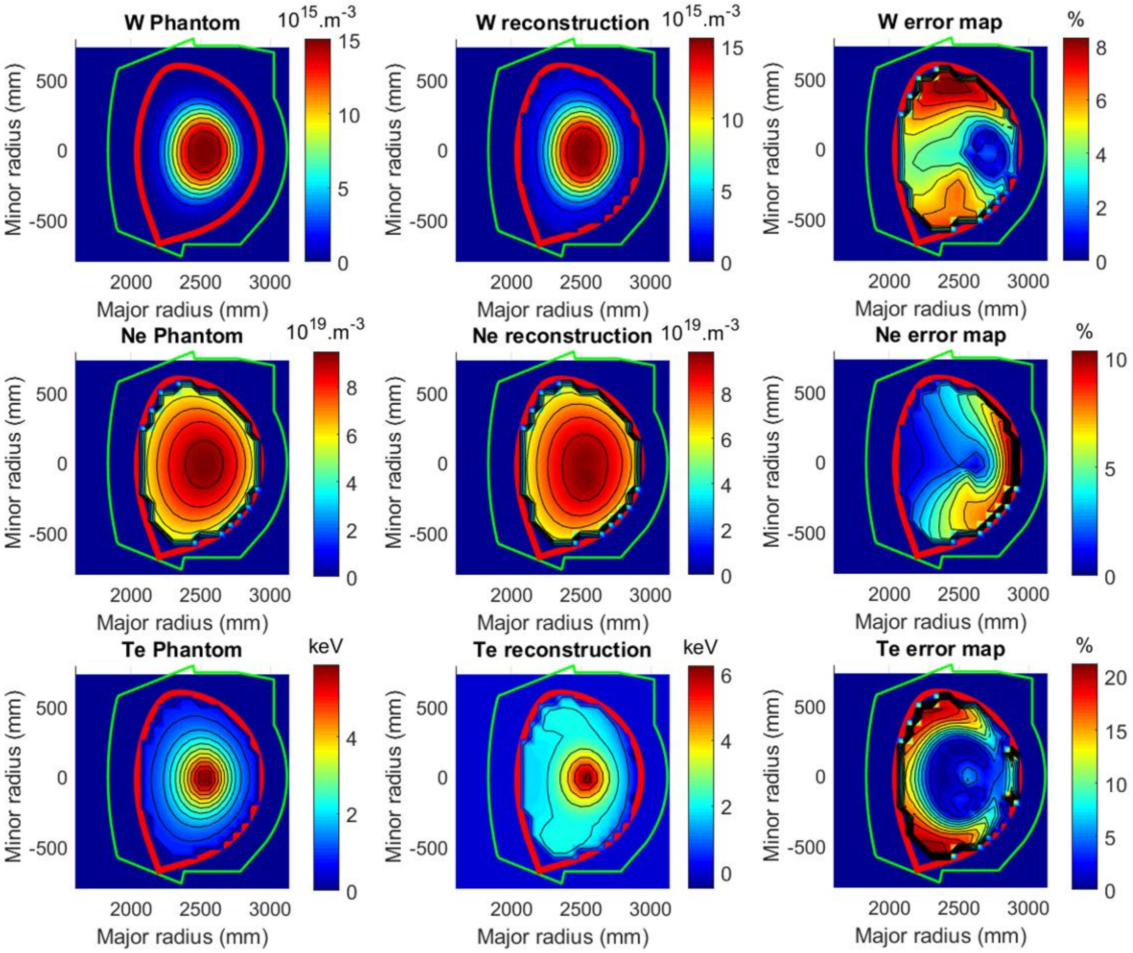

Figure 6.8. The integrated Bayesian inference results of tungsten density, electron temperature and electron density. Note that, to reduce the computation expense, the pixel grid has been reduced to (25×25) dimension.

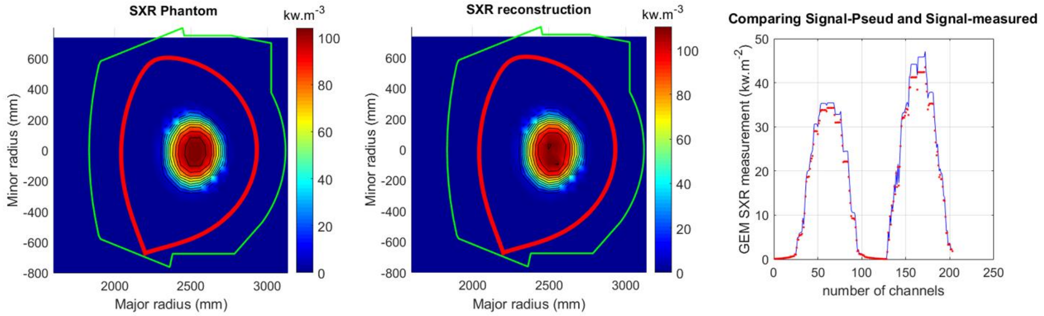

Figure 6.9. The resulting SXR emissivity from original phantoms n_e, T, n_{w} combination and reconstructed results. Note that, to reduce the computation expense, the pixel grid has been reduced to (25×25) dimension.

6.3.2. With the consideration of transport

We assume that transport is governed through a diffusion coefficient profile $\bar{D}$ and a convection coefficient profile $\bar{V}$, influencing the fractional abundances of tungsten as discussed before. In principle, this may provide an opportunity to infer the transport coefficients. Assuming measurement error on temperature and density, and proceeding as before, the full model becomes

$$p(\bar{D}, \bar{V}, \bar{n}_w, \bar{n}_e, \bar{T}_e | \bar{d}_{SXR}, \bar{d}_{ECE}, \bar{d}_{TS})$$

$$\sim p(\bar{d}_{SXR}, \bar{d}_{ECE}, \bar{d}_{TS} | \bar{D}, \bar{V}, \bar{n}_w, \bar{n}_e, \bar{T}_e) \cdot p(\bar{D}, \bar{V}, \bar{n}_w, \bar{n}_e, \bar{T}_e) \tag{6.32}$$

$$\begin{gathered} = p(\bar{d}_{SXR} | \bar{D}, \bar{V}, \bar{n}_w, \bar{n}_e, \bar{T}_e) \\ \cdot p(\bar{d}_{ECE} | \bar{D}, \bar{V}, \bar{n}_w, \bar{n}_e, \bar{T}_e) \\ \cdot p(\bar{d}_{TS} | \bar{D}, \bar{V}, \bar{n}_w, \bar{n}_e, \bar{T}_e) \\ \cdot p(\bar{D}) \cdot p(\bar{V}) \cdot p(\bar{n}_w) \cdot p(\bar{n}_e) \cdot p(\bar{T}_e) \end{gathered} \tag{6.33}$$

$$\begin{gathered} \left. = p(\bar{d}_{SXR} | \bar{D}, \bar{V}, \bar{n}_w, \bar{n}_e, \bar{T}_e) \right\} \boxed{\text{Cooling + tomography forward model}} \\ \left. \begin{matrix} \cdot p(\bar{d}_{ECE} | \bar{T}_e) \\ \cdot p(\bar{d}_{TS} | \bar{n}_e) \end{matrix} \right\} \boxed{\text{Other diagnostics' forward model}} \\ \cdot p(\bar{D}) \cdot p(\bar{V}) \cdot p(\bar{n}_w) \cdot p(\bar{n}_e) \cdot p(\bar{T}_e) \end{gathered} \tag{6.34}$$

There are now two additional priors:

Diffusion coefficient

$$p(\bar{D}) = \frac{1}{(2\pi)^{\frac{n}{2}}\left|\bar{\bar{\Sigma}}_D\right|^{\frac{1}{2}}}\, exp\left[-\frac{1}{2}(\bar{D}-\bar{\mu}_D)^T\, \bar{\bar{\Sigma}}_D^{-1}\,(\bar{D}-\bar{\mu}_D)\right] \tag{6.35}$$

Convection coefficient

$$p(\bar{V}) = \frac{1}{(2\pi)^{\frac{n}{2}}\left|\bar{\bar{\Sigma}}_V\right|^{\frac{1}{2}}}\, exp\left[-\frac{1}{2}(\bar{V}-\bar{\mu}_V)^T\, \bar{\bar{\Sigma}}_V^{-1}\,(\bar{V}-\bar{\mu}_V)\right] \tag{6.36}$$

The soft X-ray forward model now contains five independent variables:

$$\boxed{\begin{aligned} \bar{d}_{SXR} &= \bar{\bar{R}}\cdot\bar{\varepsilon}^{\eta} = \bar{\bar{R}}\cdot(\bar{\varepsilon}_w^{\eta}+\bar{\varepsilon}_H^{\eta}) \\ &= \bar{\bar{R}}\cdot\left(\bar{n}_e.\bar{n}_w.L_w^{\eta}(\bar{T}_e,\bar{D},\bar{V}\,)+\bar{n}_e.\bar{n}_e.L_H^{\eta}(\bar{T}_e)\right) \\ &= \bar{R}(\bar{n}_e,\bar{n}_w,\bar{T}_e,\bar{D},\bar{V}\,) \end{aligned}} \tag{6.37}$$

The likelihood is

$$p\left(\bar{d}_{SXR}\middle|\bar{D},\bar{V},\bar{n}_w,\bar{n}_e,\bar{T}_e\right) = \frac{1}{(2\pi)^{\frac{m}{2}}\left|\bar{\bar{\Sigma}}_{SXR}\right|^{\frac{1}{2}}}\, exp\Bigg[-\frac{1}{2}\left[\bar{\bar{R}}_{SXR}\cdot\left(\bar{n}_e.\bar{n}_w.L_w^{\eta}(\bar{T}_e,\bar{D},\bar{V}\,)+\bar{n}_e.\bar{n}_e.L_H^{\eta}(\bar{T}_e)\right)-\right.$$

$$\left.\bar{d}_{SXR}\right]^T\ \bar{\bar{\Sigma}}_{SXR}^{-1}\ \left[\bar{\bar{R}}_{SXR}\cdot\left(\bar{n}_e.\bar{n}_w.L_w^{\eta}(\bar{T}_e,\bar{D},\bar{V}\,)+\bar{n}_e.\bar{n}_e.L_H^{\eta}(\bar{T}_e)\right)-\bar{d}_{SXR}\right]\Bigg] \tag{6.38}$$

This forward model depends on the transport code, which means for each MCMC sampling, one entire transport epoch should be executed. The full cooling factor assumption proposed an expensive calculation where the implementation of HPC should be seriously considered, and the inference result is still absent so far in this thesis. However, given a number of representative outputs of the code for various representative profiles of temperature and transport coefficients, a surrogate model could be used in the forward model and the inference could still be done relatively fast.

$$\begin{aligned} &p\left(\bar{n}_w,\bar{n}_e,\bar{T}_e\middle|\bar{d}_{SXR}\ \bar{d}_{ECE},\bar{d}_{TS}\right) \\ &\sim p\left(\bar{d}_{SXR}\ \bar{d}_{ECE},\bar{d}_{TS}\middle|\bar{n}_w,\bar{n}_e,\bar{T}_e\right)\cdot p(\bar{n}_w,\bar{n}_e,\bar{T}_e) \\ &\sim p\left(\bar{d}_{SXR}\middle|\bar{n}_w,\bar{n}_e,\bar{T}_e\right)\ \cdot p\left(\ \bar{d}_{ECE}\middle|\bar{n}_w,\bar{n}_e,\bar{T}_e\right)\cdot p\left(\bar{d}_{TS}\middle|\bar{n}_w,\bar{n}_e,\bar{T}_e\right)\cdot p(\bar{n}_w)\cdot\ p(\bar{n}_e)\ \cdot p(\bar{T}_e) \\ &\sim p\left(\bar{d}_{SXR}\middle|\bar{n}_w,\bar{n}_e,\bar{T}_e\right)\ \cdot p\left(\ \bar{d}_{ECE}\middle|\bar{T}_e\right)\cdot p\left(\bar{d}_{TS}\middle|\bar{n}_e\right)\cdot p(\bar{n}_w)\cdot\ p(\bar{n}_e)\ \cdot p(\bar{T}_e) \end{aligned} \tag{6.39}$$

$$\sim \frac{1}{(2\pi)^{\frac{n}{2}}\left|\bar{\bar{\Sigma}}_w\right|^{\frac{1}{2}}}\ exp\left[-\frac{1}{2}(\bar{n}_w-\bar{\mu}_w)^T\,\bar{\bar{\Sigma}}_w^{-1}\,(\bar{n}_w-\bar{\mu}_w)\right]$$

$$\cdot\frac{1}{(2\pi)^{\frac{n}{2}}\left|\bar{\bar{\Sigma}}_e\right|^{\frac{1}{2}}}\ exp\left[-\frac{1}{2}(\bar{n}_e-\bar{\mu}_n)^T\,\bar{\bar{\Sigma}}_e^{-1}\,(\bar{n}_e-\bar{\mu}_n)\right]$$

$$\cdot\frac{1}{(2\pi)^{\frac{n}{2}}\left|\bar{\bar{\Sigma}}_T\right|^{\frac{1}{2}}}\ exp\left[-\frac{1}{2}(\bar{T}_e-\bar{\mu}_T)^T\,\bar{\bar{\Sigma}}_T^{-1}\,(\bar{T}_e-\bar{\mu}_T)\right]$$

$$\cdot\frac{1}{(2\pi)^{\frac{m}{2}}\left|\bar{\bar{\Sigma}}_{TS}\right|^{\frac{1}{2}}}\ exp\left[-\frac{1}{2}\left(\bar{\bar{R}}_{TS}\cdot\bar{n}_e-\bar{d}_{TS}\right)^T\,\bar{\bar{\Sigma}}_{TS}^{-1}\,\left(\bar{\bar{R}}_{TS}\cdot\bar{n}_e-\bar{d}_{TS}\right)\right]$$

$$\cdot\frac{1}{(2\pi)^{\frac{m}{2}}\left|\bar{\bar{\Sigma}}_{ECE}\right|^{\frac{1}{2}}}\ exp\left[-\frac{1}{2}\left(\bar{\bar{R}}_{ECE}\cdot\bar{T}_e-\bar{d}_{ECE}\right)^T\,\bar{\bar{\Sigma}}_{ECE}^{-1}\,\left(\bar{\bar{R}}_{ECE}\cdot\bar{T}_e-\bar{d}_{ECE}\right)\right]$$

$$\cdot\frac{1}{(2\pi)^{\frac{m}{2}}\left|\bar{\bar{\Sigma}}_{SXR}\right|^{\frac{1}{2}}}\ exp\Bigg[-\frac{1}{2}\left[\bar{\bar{R}}_{SXR}\cdot\left(\bar{n}_e.\bar{n}_w.L_w^{\eta}(\bar{T}_e,\bar{D},\bar{V})+\bar{n}_e.\bar{n}_e.L_H^{\eta}(\bar{T}_e)\right)-\bar{d}_{SXR}\right]^T\,\bar{\bar{\Sigma}}_{SXR}^{-1}\,\Big[\bar{\bar{R}}_{SXR}\cdot$$
$$\left(\bar{n}_e.\bar{n}_w.L_w^{\eta}(\bar{T}_e,\bar{D},\bar{V})+\bar{n}_e.\bar{n}_e.L_H^{\eta}(\bar{T}_e)\right)-\bar{d}_{SXR}\Big]\Bigg] \tag{6.40}$$

Log Posterior (up to a constant):

$$log\ p\left(\bar{n}_w,\bar{n}_e,\bar{T}_e\middle|\bar{d}_{SXR}\ \bar{d}_{ECE},\bar{d}_{TS}\right)$$
$$=\ log\ p\left(\bar{d}_{SXR}\middle|\bar{n}_w,\bar{n}_e,\bar{T}_e\right)+log\ p\left(\ \bar{d}_{ECE}\middle|\bar{T}_e\right)+log\ p\left(\bar{d}_{TS}\middle|\bar{n}_e\right)$$
$$+log\ p(\bar{n}_w)+log\ p(\bar{n}_e)+log\ p(\bar{T}_e)+ct. \tag{6.41}$$

$$=\ -\frac{n}{2}\log(2\pi)-log\left|\bar{\bar{\Sigma}}_w\right|-\frac{1}{2}(\bar{n}_w-\bar{\mu}_w)^T\,\bar{\bar{\Sigma}}_w^{-1}\,(\bar{n}_w-\bar{\mu}_w)$$

$$-\frac{n}{2}\log(2\pi)-log\left|\bar{\bar{\Sigma}}_e\right|-\frac{1}{2}(\bar{n}_e-\bar{\mu}_n)^T\,\bar{\bar{\Sigma}}_e^{-1}\,(\bar{n}_e-\bar{\mu}_n)$$

$$-\frac{n}{2}\log(2\pi)-log\left|\bar{\bar{\Sigma}}_T\right|-\frac{1}{2}(\bar{T}_e-\bar{\mu}_T)^T\,\bar{\bar{\Sigma}}_T^{-1}\,(\bar{T}_e-\bar{\mu}_T)$$

$$-\frac{m}{2}\log(2\pi)-log\left|\bar{\bar{\Sigma}}_{TS}\right|-\frac{1}{2}\left(\bar{\bar{R}}_{TS}\cdot\bar{n}_e-\bar{d}_{TS}\right)^T\,\bar{\bar{\Sigma}}_{TS}^{-1}\,\left(\bar{\bar{R}}_{TS}\cdot\bar{n}_e-\bar{d}_{TS}\right)$$

$$-\frac{m}{2}\log(2\pi)-log\left|\bar{\bar{\Sigma}}_{ECE}\right|-\frac{1}{2}\left(\bar{\bar{R}}_{ECE}\cdot\bar{T}_e-\bar{d}_{ECE}\right)^T\,\bar{\bar{\Sigma}}_{ECE}^{-1}\,\left(\bar{\bar{R}}_{ECE}\cdot\bar{T}_e-\bar{d}_{ECE}\right)$$

$$-\frac{m}{2}\log(2\pi) - log\left|\bar{\bar{\Sigma}}_{SXR}\right| - \frac{1}{2}\left[\bar{\bar{R}}_{SXR}\cdot\left(\bar{n}_e.\bar{n}_w.L_w^{\eta}(\bar{T}_e,\bar{D},\bar{V}\,) + \bar{n}_e.\bar{n}_e.L_H^{\eta}(\bar{T}_e)\right) - \bar{d}_{SXR}\right]^T \bar{\bar{\Sigma}}_{SXR}^{-1}\left[\bar{\bar{R}}_{SXR}\cdot\left(\bar{n}_e.\bar{n}_w.L_w^{\eta}(\bar{T}_e,\bar{D},\bar{V}\,) + \bar{n}_e.\bar{n}_e.L_H^{\eta}(\bar{T}_e)\right) - \bar{d}_{SXR}\right] + ct. \tag{6.42}$$

$$\sim\; - log\left|\bar{\bar{\Sigma}}_w\right| - \frac{1}{2}(\bar{n}_w - \bar{\mu}_w)^T\, \bar{\bar{\Sigma}}_w^{-1}\,(\bar{n}_w - \bar{\mu}_w)$$

$$-log\left|\bar{\bar{\Sigma}}_e\right| - \frac{1}{2}(\bar{n}_e - \bar{\mu}_n)^T\, \bar{\bar{\Sigma}}_e^{-1}\,(\bar{n}_e - \bar{\mu}_n)$$

$$-log\left|\bar{\bar{\Sigma}}_T\right| - \frac{1}{2}(\bar{T}_e - \bar{\mu}_T)^T\, \bar{\bar{\Sigma}}_T^{-1}\,(\bar{T}_e - \bar{\mu}_T)$$

$$-log\left|\bar{\bar{\Sigma}}_{TS}\right| - \frac{1}{2}\left(\bar{\bar{R}}_{TS}\cdot\bar{n}_e - \bar{d}_{TS}\right)^T\, \bar{\bar{\Sigma}}_{TS}^{-1}\,\left(\bar{\bar{R}}_{TS}\cdot\bar{n}_e - \bar{d}_{TS}\right)$$

$$-log\left|\bar{\bar{\Sigma}}_{ECE}\right| - \frac{1}{2}\left(\bar{\bar{R}}_{ECE}\cdot\bar{T}_e - \bar{d}_{ECE}\right)^T\, \bar{\bar{\Sigma}}_{ECE}^{-1}\,\left(\bar{\bar{R}}_{ECE}\cdot\bar{T}_e - \bar{d}_{ECE}\right)$$

$$-log\left|\bar{\bar{\Sigma}}_{SXR}\right| - \frac{1}{2}\left[\bar{\bar{R}}_{SXR}\cdot\left(\bar{n}_e.\bar{n}_w.L_w^{\eta}(\bar{T}_e,\bar{D},\bar{V}\,) + \bar{n}_e.\bar{n}_e.L_H^{\eta}(\bar{T}_e)\right) - \bar{d}_{SXR}\right]^T \bar{\bar{\Sigma}}_{SXR}^{-1}\left[\bar{\bar{R}}_{SXR}\cdot\left(\bar{n}_e.\bar{n}_w.L_W^{\eta}(\bar{T}_e,\bar{D},\bar{V}\,) + \bar{n}_e.\bar{n}_e.L_H^{\eta}(\bar{T}_e)\right) - \bar{d}_{SXR}\right] \tag{6.43}$$

6.4. Conclusion

In this chapter, the reconstruction of tungsten impurity distributions from SXR tomography has been investigated and tested on synthetic data in a WEST scenario. The impurity reconstruction method considers calculation of the cooling factor, which is affected by uncertainty on transport, electron temperature $\overline{T}_e$ and electron density $\overline{n}_e$. Three different stages of complexity have been proposed:

- without consideration of transport effects, $\overline{T}_e$ and $\overline{n}_e$ profiles exactly known;
- without consideration of transport effects, $\overline{T}_e$ and $\overline{n}_e$ profiles given by ECE and TS with Gaussian uncertainty;
- with consideration of transport effects, $\overline{T}_e$ and $\overline{n}_e$ profiles given by ECE and TS with Gaussian uncertainty.

In the first case, the impurity density can be calculated directly from the SXR profile, as demonstrated in *section 6.2*, and in principle the calculation can still be done in real time. However, outside the plasma core the model quickly gives erroneous results. On the other hand, this model still holds its value for avoiding core impurity accumulation in real time.

In the second case, the uncertainty on the radial profiles from ECE and TS is considered. However, this leads to a nonlinear forward model, necessitating posterior sampling using MCMC. As a result, the computational cost increases considerably.

In the last case, transport is taken into account, as well as uncertainties on the transport coefficients. This is the most complete model, but again its solution would require posterior sampling, increasing the computational cost. One way out of this would be to perform a large number of reconstructions and train a surrogate model to perform the mapping from the raw data to the reconstructed profiles. This possibility has been explored with a neural network model in the *Appendix*.

Chapter 7 Conclusion

The aim of this thesis was to develop a real-time tomography tool for a soft X-ray diagnostic at WEST, equipped with GEM detectors, with a view to real-time reconstruction of high-Z impurity concentration profiles, such as tungsten, and studies of MHD activity. The real-time monitoring of impurity distributions could be a first step in the direction of impurity control. In the following, we discuss the conclusions of our work, focusing on the aspects of Bayesian inference of SXR emissivity profiles using Gaussian processes, and the reconstruction of tungsten concentration profiles in a WEST scenario.

Real-time Gaussian process tomography

The most common successful tomography methods are based on iterative algorithms, and as a result they are not well suited for real-time applications. This includes real-time feedback control, which should be adapted to MHD and impurity transport time scales ($\leq 10\text{ms}$). This is because tomography is a challenging task, due to the limited number of detectors and the large number of parameters to be inferred to achieve sufficient resolution. It is an ill-posed inverse problem.

In this doctoral work, a new method has been adopted, validated and extended for reconstruction of SXR emissivity fields, based on the foundational work of [Svensson 2011]. The method, called Gaussian process tomography (GPT), is based on Gaussian process modeling of the emissivity field, providing a posterior distribution in the context of Bayesian inference. The regularization of the emissivity field is governed by the covariance matrix of the Gaussian process, with hyperparameters learned from the data. As the forward model is linear, the posterior is also a Gaussian process. As a result, the mean emissivity field and its covariance are available in closed form. Hence, the method has the advantage of being both non-iterative and nonparametric. The calculation is very fast, taking around 40 ms for a 100×100 pixels grid and 8 ms for 50×50 pixels grid on a recent PC with MATLAB. By comparison, the presently used algorithm (minimum Fisher information) easily reaches execution times up to seconds.

Moreover, the GPT method was extended so that it could account for the magnetic equilibrium information provided by EFIT or EQUINOX. This technique, called Equi-GPT, resulted in a significant improvement of the reconstructed SXR emissivity field. The equilibrium information was implemented by introducing anisotropy in the GP covariance matrix, through a length scale along the magnetic flux surfaces and another one in the perpendicular direction.

An additional advantage of GPT is that it offers uncertainties on the inferred profiles in terms of the posterior covariance. Not only does this give a measure of reconstruction accuracy, but it can also be exploited to improve the line-of-sight geometry of the diagnostic.

Finally, during this doctoral work, the GPT algorithm has been successfully implemented on four different line-of-sight type diagnostic systems: SXR on WEST with synthetic data, bolometry on HL-2A, SXR and XUV on EAST. Thus, the Equi-GPT method was validated on real data from experimental tokamak discharges and delivered a contribution to ongoing physics studies.

In summary, the first goal of the thesis has been achieved, to deliver and validate a reliable and fast tomographic inversion method, showing good potential for real-time application in the new GEM SXR diagnostic at WEST.

Reconstruction of impurity density profiles

Our work towards reconstruction of tungsten concentration profiles was based on previous efforts from [Jardin 2017, Vezinet 2013, Odstrcil 2017]. As a result, a forward model for determining tungsten concentrations could be established, using calculations of the tungsten cooling factor in the case of WEST scenario.

Hence, in the last part of this doctoral work, first steps were taken toward Bayesian inference of impurity density profiles from measurements of the line-integrated SXR emissivity, as well as temperature and density profiles. This was tested on synthetic data in the WEST scenario and it was shown that the Bayesian approach is far superior to a direct calculation from the SXR emissivity that does not consider the error propagation properly, due to uncertainty amplification. Nevertheless, in the core area of the plasma ($T_e \geq 2\mathrm{keV}$), a direct calculation from the SXR emissivity could still provide useful results in real time.

Moreover, in off-line approach, a full Bayesian analysis using Markov Chain Monte Carlo is feasible, providing a consistent estimate of the profiles of T_e, n_e and n_w, and also incorporating the magnetic equilibrium information as prior knowledge. Future work could concentrate on posterior approximations, which would allow inferring the tungsten concentration at a lower computational cost.

An additional perspective comes from the possibility of surrogate modeling of the entire inference process. This would include modeling of the cooling factor and the impurity transport. One of the most promising class of surrogate models in this respect are provided by neural networks, well known from the field of artificial intelligence and successfully applied in a host of different applications outside fusion. A preliminary test with neural networks has been given in the *Appendix*, indicating good potential for our purposes.

Appendix A: Learn deeper Neural Network Tomography

With a view to developing a real-time tomographic method that can be used as an ingredient for an impurity monitoring system, another very promising technique comes into reach, i.e. the convolutional neural network (CNN). Particularly for modeling the complex non-linear parts of the calculation, e.g. the cooling factor varying with transport coefficients, convolutional neural networks have attractive qualities for providing impurity concentrations in real time.

The inference chain of tungsten monitoring problem has been demonstrated in **Figure A.1**. In the forward model we start from the transport coefficients, the tungsten density, the electron density, the electron temperature. With the assumption of transport and ionization equilibrium, we can get the radiation contribution from each species in plasma, described by cooling factor. Then the sum over of individual contributions gives a global radiation distribution, and the diagnostic forward models gives the final diagnostic measurements in the end. The final purpose of this problem is to infer the original basic parameters, which is the inverse problem. However, due to its nonlinearity it cannot be solved in real time. Therefore we propose to use a surrogate model to approximate the inference, fast enough for real-time application. One of the most promising types of surrogate models are neural networks.

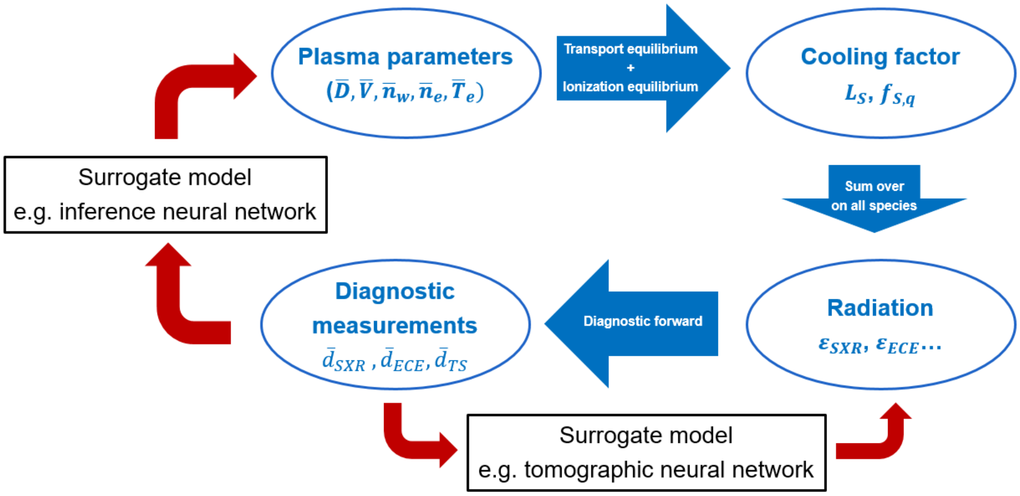
Plasma parameters
$(\bar{D}, \bar{V}, \bar{n}_w, \bar{n}_e, \bar{T}_e)$
Transport equilibrium + Ionization equilibrium
Cooling factor
$L_S, f_{S,q}$
Sum over on all species
Radiation
$\varepsilon_{SXR}, \varepsilon_{ECE} \cdots$
Diagnostic forward
Diagnostic measurements
$\bar{d}_{SXR}, \bar{d}_{ECE}, \bar{d}_{TS}$
Surrogate model e.g. inference neural network
Surrogate model e.g. tomographic neural network

Figure A.1. The inference chain of tungsten monitoring method.

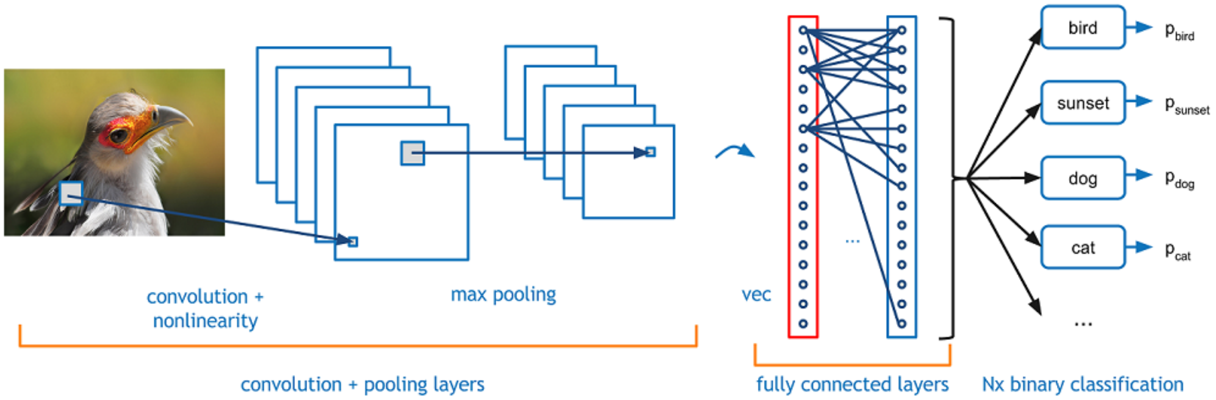

Figure A.2. A typical schematic layout of a convolutional neural network. [Deshpande 2019]

A CNN is a kind of artificial neural network (ANN), i.e. a computing system based on connectionist principles and vaguely inspired by the biological neural networks that constitute animal brains. The neural network itself is not an algorithm, but rather a framework for many different machine learning algorithms to work together and process complex data inputs. Such systems 'learn' to perform tasks by considering examples, generally without being programmed with any task-specific rules. An ANN is based on a collection of connected units or nodes called artificial neurons, which loosely model the neurons in a biological brain. Each connection, like the synapses in a biological brain, can transmit a signal from one artificial neuron to another. An artificial neuron that receives a signal can process it and then signal additional artificial neurons connected to it. In common ANN implementations, the signal at a connection between artificial neurons is a real number, and the output of each artificial neuron is computed by some nonlinear function of the sum of its inputs. The connections between artificial neurons are called 'edges'. Artificial neurons and edges typically have a weight that adjusts as learning proceeds. The weight increases or decreases the strength of the signal at a connection. Artificial neurons may have a threshold such that the signal is only sent if the aggregate signal crosses that threshold. Typically, artificial neurons are aggregated into layers. Different layers may perform different kinds of transformations on their inputs. Signals travel from the first layer (the input layer), to the last layer (the output layer), possibly after traversing the layers multiple times.

Back to our topic, we have worked on a preliminary approach to apply such a powerful technique to the SXR tomographic problem. The idea is that, since inference of SXR emissivity profiles using GPT can be done very fast, a database of inference results can be created with relatively limited computational resources. This database can then be used to train a CNN to learn the tomographic inference process. If this proves successful, the approach could be extended to a database of reconstruction results of impurity density profiles, which may pave the road to a real-time impurity monitor.

As a first test, a database has been established of GPT tomographic reconstruction of SXR emissivity profiles in the EAST geometry. In particular, 30,000 time-slices of SXR data in EAST discharge #70750 shot were selected, in the presence of the kink mode activity, see **Figure A.3**. Likewise, a test set for evaluating the performance of the network was selected from another discharge (#70754), also showing similar kink mode activity. This test set was used only in the last experiment described in this work. The SXR emissivity fields were inferred using Equi-GPT and then used as phantoms, line-integrated according to the EAST SXR geometry, leading to 30,000 sets of SXR synthetic measurements with 5% random noise added. This procedure is illustrated in Figure A.4.

Two complementary CNN approaches have been implemented to learn the tomographic reconstruction (standard and fully connected designs), each using a different architecture involving such details as the network depth, layer design, activation function.

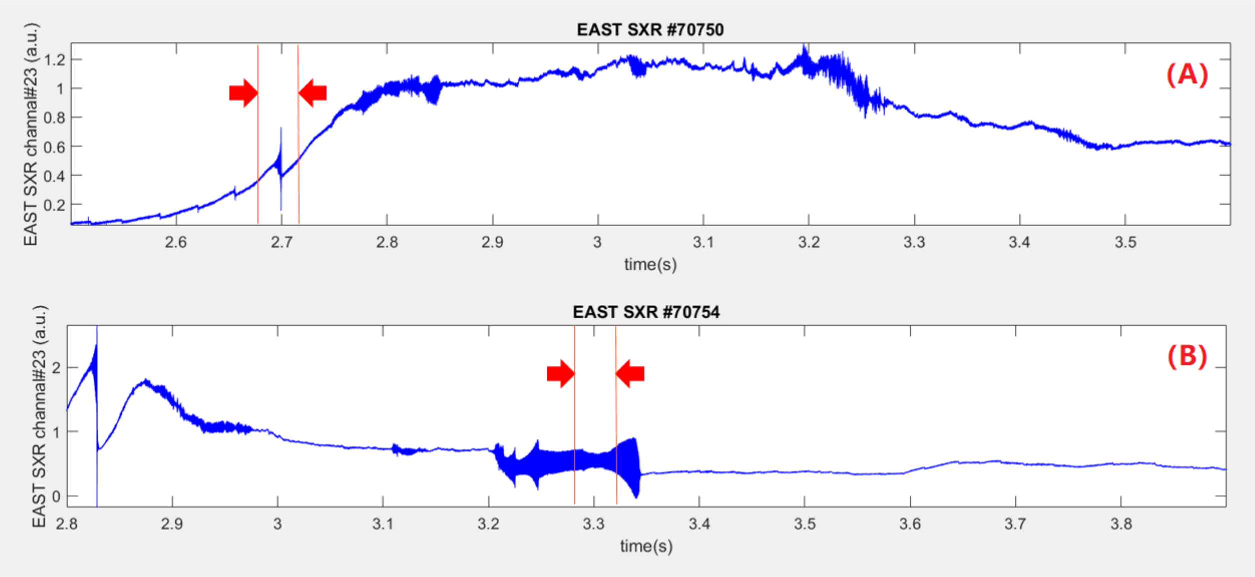

Figure A.3. (A) Time trace of one channel in the training data set obtained from SXR data in EAST discharge #70750. (B) Test data set from EAST discharge #70754. The red arrows indicate the selected range of data.

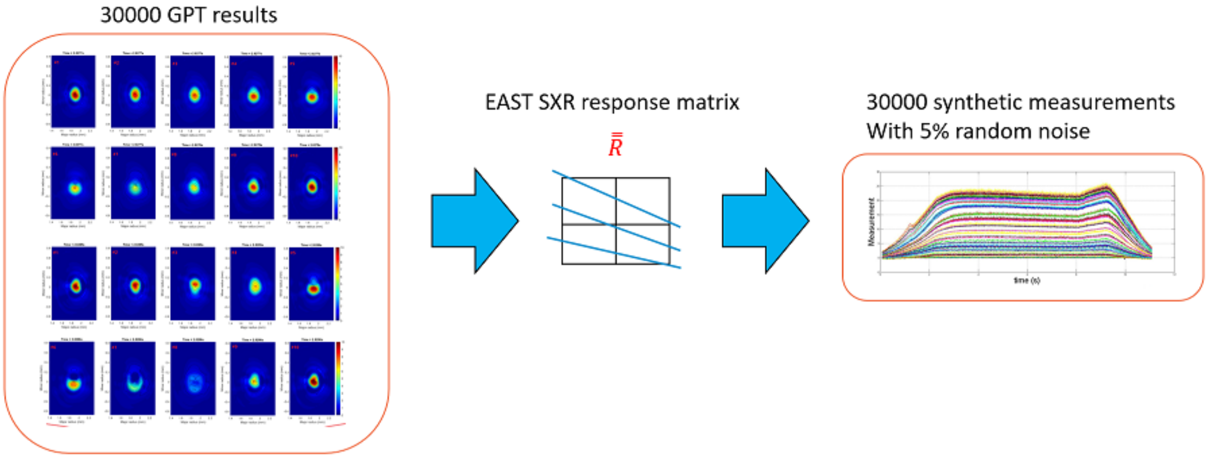
30000 GPT results
EAST SXR response matrix
$\bar{\bar{R}}$
30000 synthetic measurements
With 5% random noise
Measurement
time (s)

Figure A.4. Illustration of the procedure used to obtain the line-integrated SXR input data in the training set, originating from 30,000 time slices of GPT results in EAST discharge #70750.

Standard CNN

Here follows the standard CNN network structure designed for EAST SXR tomography. The network contains in total 6 layers, including 1 dimension expansion input layer, 4 convolutional hidden layers and 1 activation layer. The activation layer is equipped with the rectified linear unit function (ReLU).

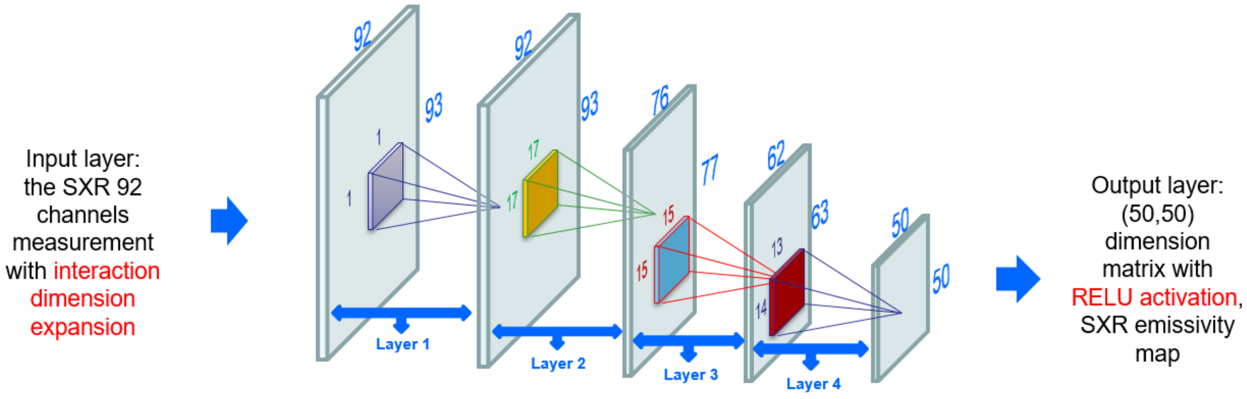
Input layer: the SXR 92 channels measurement with interaction dimension expansion
92
93
1
1
17
17
92
93
76
77
15
15
62
63
13
14
50
50
Layer 1
Layer 2
Layer 3
Layer 4
Output layer: (50,50) dimension matrix with RELU activation, SXR emissivity map

Figure A.5. Layout of the 6 layer standard CNN network.

The dimension expansion layer is given by

$$Input\ data = \{d_1, d_2, d_3, d_4 \dots, d_1 * d_1, d_1 * d_2, d_1 * d_3 \dots\} \qquad (A.1)$$

Thus the input data, which for the EAST SXR case originally contains 92 channels, becomes of dimension $92 + 92 \times 92$, as shown in the table above. The convolutional layer involves a dimensionality reduction process, so after the final layer the dimension of the data becomes 50×50, corresponding to the final dimension of the emissivity grid in this test.

Furthermore, the loss function during the training process is the mean squared deviation function, while the optimization was carried out by means of the ADAM technique [Diederik 2014]. The phantoms and reconstruction results using data from the training set are shown in Figure A.6 for three randomly selected time slices. The averaged maximum error reaches 6.7% and the average RMSD is 3.0×10^{-4}, which can be compared to the RSMD of 0.0034 using Equi-GPT (based on the original SXR line integrals). Furthermore, execution of a single time took only 3 ms on an NVidia GPU with Python.

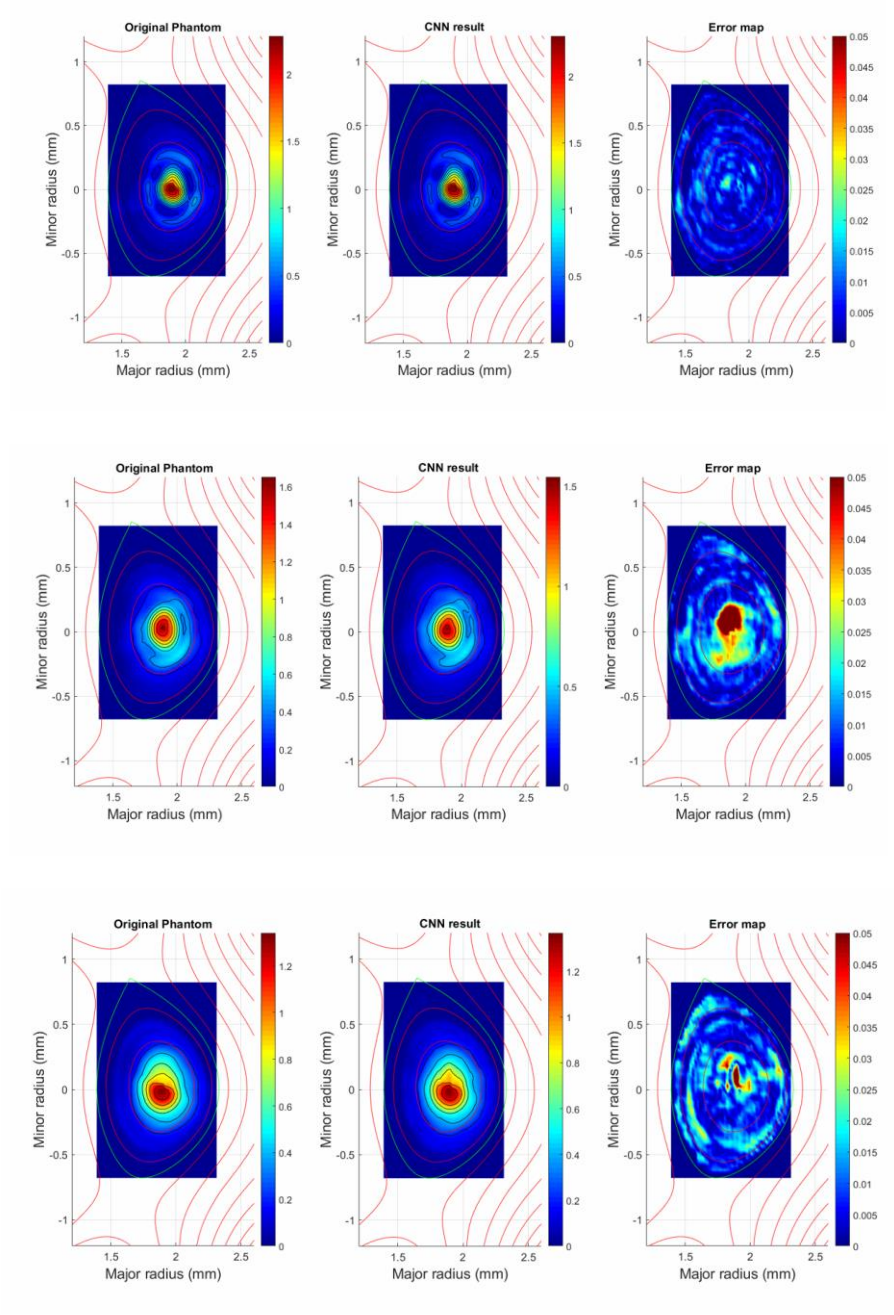

Figure A.6. From top to bottom, reconstruction results for three randomly selected time slices using a CNN, with the original phantoms in the first column, CNN results in the second column and reconstruction error maps in the third column. In the error map, the maximum error refers to 5%.

Fully connected CNN (FCNN)

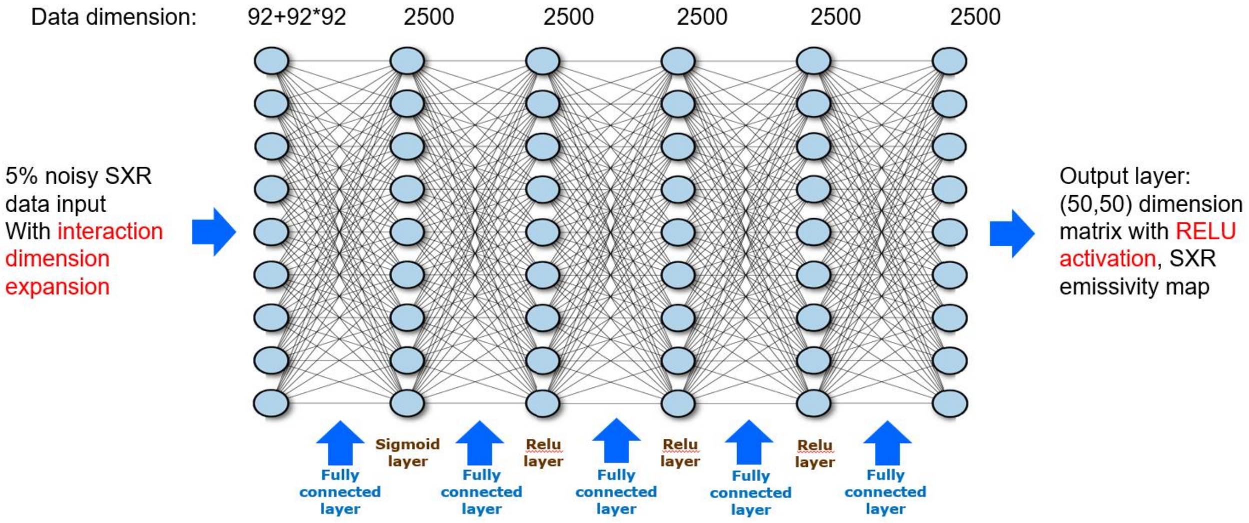
Data dimension:
92+92*92
2500
2500
2500
2500
2500
5% noisy SXR data input With interaction dimension expansion
Output layer: (50,50) dimension matrix with RELU activation, SXR emissivity map
Sigmoid layer
Relu layer
Relu layer
Relu layer
Fully connected layer
Fully connected layer
Fully connected layer
Fully connected layer
Fully connected layer

Figure A.7. Layout of the 11 layer FCNN network.

Apart from a standard CNN design, a fully connected CNN (FCNN) has also been implemented for SXR tomography using data from EAST. This network contains 11 layers in total, including 1 dimension expansion input layer with the same structure as described in Eq. (P.1), 1 ReLU activation output layer, and 9 hidden layers, as shown in **Figure A.7**. Again, the loss function during the training process was a mean squared deviation function, and the optimization function was ADAM. The phantoms and reconstruction results using data from the training set are shown in **Figure A.8**. The averaged maximum error reaches 2.4%, the average RMSD is 1.1×10^{-4} and one time slice executes in 1.6 ms on the NVidia GPU. Thus, the FCNN performs better than the standard CNN, which is probably caused by the higher number of layers.

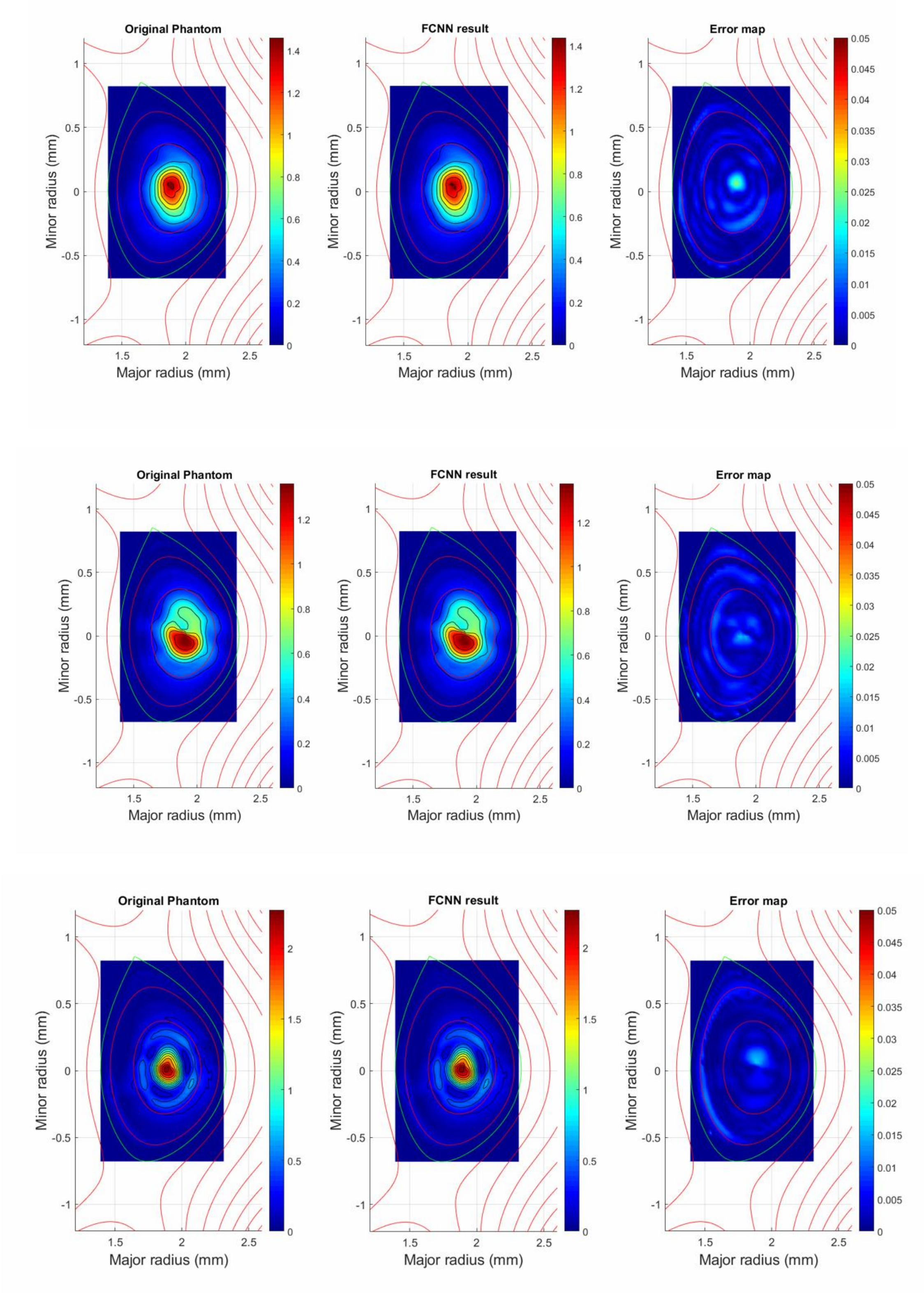

Figure A.8. From top to bottom, reconstruction results for three randomly selected time slices using an FCNN, with the original phantoms in the first column, FCNN results in the second column and reconstruction error maps in the third column. In the error map, the maximum error refers to 5%.

Test of FCNN on #70754 and benchmark with Equi-GPT

Due to the superior performance of the FCNN, it was selected for another experiment using test data from a different discharge than the one the network was trained on, i.e. EAST discharge #70754. A comparison was made with Equi-GPT.

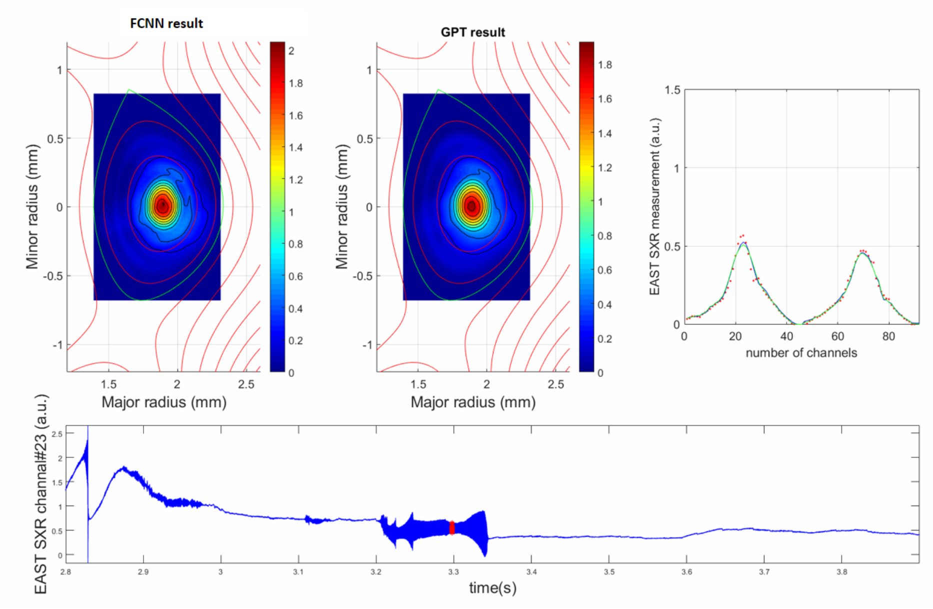

Figure A.9. Illustration for a single time slice of the validation of the FCNN reconstruction by using test SXR data from EAST discharge #70754. The recalculated line integrals are compared in the top right panel: FCNN (blue curve), Equi-GPT (green curve), and original data (red dots).

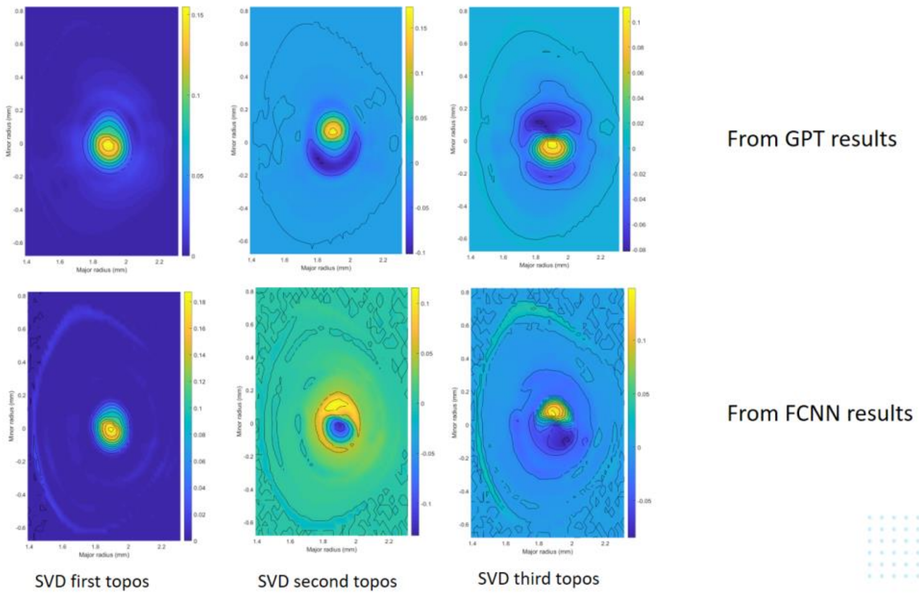

Figure A.10. SVD analysis results using the first three topos obtained by FCNN and Equi-GPT, showing the (1, 1) kink mode structure in both cases.

Conclusion

Based on a database of GPT tomography results, a complementary neural network approach has been implemented, using both fully connected and standard convolutional neural network architectures. This decreases the computational load significantly (order 1 ms GPU time with Python). This is a very first attempt to use a neural network technique to speed up tomography of SXR data, showing promising results both regarding reconstruction accuracy and computational speed. Nevertheless, the true value of a neural network technique would become clear in the context of a nonlinear forward model, e.g. for inferring impurity concentrations in real time. The approach might also be extended to multiple diagnostics and could also learn aspects of the control system in a tokamak. These will be very interesting topics for future research.

Bibliography

[Alper 1994] Alper B, Blackler K, Dillon S F, et al. The JET multi-camera soft X-ray diagnostic[R]. Europhysics Conference Abstracts: 21st Conf. Controlled Fusion and Plasma Physics, Montpellier, 1994, 18B, part III: 1304.

[Alper 1997] Alper B, Dillon S, Edwards A W, et al. The JET soft x-ray diagnostic systems[J]. Review of Scientific Instruments, 1997, 68(1): 778-781.

[Anton 1995] Anton M, Dutch M J, Weisen H. Relative calibration of photodiodes in the soft-x-ray spectral range[J]. Review of Scientific Instruments, 1995, 66(7): 3762-3769.

[Anton 1996] Anton M, Weisen H, Dutch M J, et al. X-ray tomography on the TCV tokamak[J]. Plasma Physics and Controlled Fusion, 1996, 38(11): 1849.

[Arnoux 2014] Arnoux G, Balboa I, Clever M, et al. Power handling of the JET ITER-like wall[J]. Physica Scripta 2014, 2014(T159): 014009.

[Autricque 2016] Autricque A, Hong S H, Fedorczak N, et al. Simulation of W dust transport in the KSTAR tokamak, comparison with fast camera data[J]. Nuclear Materials and Energy, 2017, 12: 599-604

[Bielecki 2015] Bielecki J, Giacomelli L, Kiptily V, et al. Phillips-Tikhonov regularization with a priori information for neutron emission tomographic reconstruction on Joint European Torus[J]. Review of Scientific Instruments, 2015, 86(9): 093505.

[Bockasten 1961] Bockasten K. Transformation of observed radiances into radial distribution of the emission of a plasma[J]. JOSA, 1961, 51(9): 943-947. [Krasheninnikov 2011] Krasheninnikov S I, Smirnov R D, Rudakov D L. Dust in magnetic fusion devices[J]. Plasma Physics and Controlled Fusion, 2011, 53(8): 083001.

[Boie 1982] Boie R A, Fischer J, Inagaki Y, et al. High resolution X-ray gas proportional detectors with delay line position sensing for high counting rates[J]. Nuclear Instruments and Methods in Physics Research, 1982, 201(1): 93-115.

[BP 2018] BP statistical review of world energy[R]. 2018. Available at: https://www.bp.com/content/dam/bp/business-sites/en/global/corporate/pdfs/energy-economics/statistical-review/bp-stats-review-2018-full-report.pdf. Last accessed: June 2019

[Brezinsek 2014] Brezinsek S, Stamp M F, Nishijima D, et al. Study of physical and chemical assisted physical sputtering of beryllium in the JET ITER-like wall[J]. Nuclear Fusion, 2014, 54(10): 103001.

[Brooks 2011] Brooks S, Gelman A, Jones J, et al. Handbook of markov chain monte carlo[M]. CRC press, 2011.

[Buttery 1999] Buttery R J, Hender T C, Huysmans G T A. Onset and control of neoclassical tearing modes on JET[C]//Proceedings of the 26th EPS Conference on Controlled Fusion and Plasma Physics (Maastricht). 1999, 121.

[Buttery 2000] Buttery R J, Günter S, Giruzzi G, et al. Neoclassical tearing modes[J]. Plasma Physics and Controlled Fusion, 2000, 42(12B): B61.

[Camacho 1986] Camacho J F, Granetz R S. Soft x-ray tomography diagnostic for the Alcator C tokamak[J]. Review of Scientific Instruments, 1986, 57(3): 417-425.

[Canfield 2000] Canfield L R, *Photodiode detectors* in Vacuum ultraviolet spectroscopy[M]. Academic Press, 2000: 117–138

[Casson 2014] Casson F J, Angioni C, Belli E A, et al. Theoretical description of heavy impurity transport and its application to the modelling of tungsten in JET and ASDEX upgrade[J]. Plasma Physics and Controlled Fusion, 2014, 57(1): 014031.

[Chang 1995] Chang Z, Callen J D, Fredrickson E D, et al. Observation of nonlinear neoclassical pressure-gradient–driven tearing modes in TFTR[J]. Physical Review Letters, 1995, 74(23): 4663.

[Chen 2016] Chen K, Xu L, Hu L, et al. 2-D soft x-ray arrays in the EAST[J]. Review of Scientific Instruments, 2016, 87(6): 063504.

[Chung 2005] Chung H K, Chen M H, Morgan W L, et al. FLYCHK: Generalized population kinetics and spectral model for rapid spectroscopic analysis for all elements[J]. High Energy Density Physics, 2005, 1(1): 3-12.

[Cox 1961] Cox R T. The algebra of probable inference. 1961[J]. Johns Hopkins University.

[da Cruz 1994] Da Cruz Jr D F, Donne A J H. Soft x-ray tomography diagnostic at the RTP tokamak[J]. Review of scientific instruments, 1994, 65(7): 2295-2305.

[Decoste 1985] Decoste R. X-ray tomography on plasmas with arbitrary cross sections and limited access[J]. Review of Scientific Instruments, 1985, 56(5): 806-808.

[Delgado 2015] Delgado-Aparicio L, Sugiyama L, Shiraiwa S, et al. Non-resonant destabilization of (1/1) internal kink mode by suprathermal electron pressure[J]. Physics of Plasmas, 2015, 22(5): 050701.

[Deshpande 2019] Deshpande A. A beginner's guide to understand convolutional neural network. Available at: https://adeshpande3.github.io/A-Beginner%27s-Guide-To-Understanding-Convolutional-Neural-Networks/. Last accessed: June 2019

[Diederik 2014] Diederik P K and Jimmy L B. Adam : A method for stochastic optimization[J]. arXiv preprint arXiv:1412.6980, 2014.

[Dudok 1994] Dudok de Wit T, Pecquet A L, Vallet J C, et al. The biorthogonal decomposition as a tool for investigating fluctuations in plasmas[J]. Physics of plasmas, 1994, 1(10): 3288-3300.

[Donné 2007] Donné A J H, Costley A E, Barnsley R, et al. Diagnostics[J]. Nuclear Fusion, 2007, 47(6): S337.

[Li 2013] Li D, Svensson J, Thomsen H, et al. Bayesian Tomography of Soft X-ray and Bolometer Systems Using Gaussian Processes[C]//40th EPS Conference on Plasma Physics. European Physical Society, 2013.

[Duan 2013] Duan Y, Hu L, Mao S, et al. Radiated power measurement with AXUV photodiodes in EAST tokamak[R]. 2013.

[Einstein 1905] Einstein A. On a heuristic point of view concerning the production and transformation of light[J]. Annalen der Physik, 1905, 17: 1-18.

[Engelhardt 1978] Engelhardt W, Feneberg W. Influence of an ergodic magnetic limiter on the impurity content in a tokamak[J]. Journal of Nuclear Materials, 1978, 76: 518-520.

[Feng 2019] Feng X, Liu A D, Zhou C, et al. I-mode investigation on the Experimental Advanced Superconducting Tokamak[J]. arXiv preprint arXiv:1902.04750, 2019.

[Fujimoto 1984] Fujimoto T, Kato T. Collisional-radiative model for heliumlike ions: Application to intermediate-density plasmas[J]. Physical Review A, 1984, 30(1): 379.

[Furno 2001] Furno I. Fast transient transport phenomena measured by soft x-ray emission in TCV tokamak plasmas[R]. 2001.

[Gao 2019] Gao J M, et al. Divertor heat load peak shift induced by ELMs[J]. Submitted for publication 2019.

[Garstka 2003] Garstka G D, Diem S J, Fonck R J, et al. Performance and stability of near-unity aspect ratio plasmas in the Pegasus Toroidal Experiment[J]. Physics of Plasmas, 2003, 10(5): 1705-1711.

[Gates 1997] Gates D A, Lloyd B, Morris A W, et al. Neoclassical islands on COMPASS-D[J]. Nuclear Fusion, 1997, 37(11): 1593.

[Gelman 2013] Gelman A, Stern H S, Carlin J B, et al. Bayesian data analysis[M]. Chapman and Hall/CRC, 2013.

[Gott 2005] Gott Y V, Stepanenko M M. Vacuum photodiode detectors for soft x-ray ITER plasma tomography[J]. Review of Scientific Instruments, 2005, 76(7): 073506.

[Gott 2009] Gott Y V, Stepanenko M M. A low-voltage ionization chamber for the ITER[J]. Instruments and Experimental Techniques, 2009, 52(2): 260-264.

[Granetz 1988] Granetz R S, Smeulders P. X-ray tomography on JET[J]. Nuclear Fusion, 1988, 28(3): 457.

[Gregory 2005] Gregory P. Bayesian Logical Data Analysis for the Physical Sciences: A Comparative Approach with Mathematica® Support[M]. Cambridge University Press, 2005.

[Guillemaut 2015] Guillemaut C, Jardin A, Horacek J, et al. Ion target impact energy during Type I edge localized modes in JET ITER-like wall[J]. Plasma Physics and Controlled Fusion, 2015, 57(8): 085006.

[Gullikson 1996] Gullikson E M, Korde R, Canfield L R, et al. Stable silicon photodiodes for absolute intensity measurements in the VUV and soft x-ray regions[J]. Journal of Electron Spectroscopy and Related Phenomena, 1996, 80: 313-316.

[Hansen 1992] Hansen P C. Analysis of discrete ill-posed problems by means of the L-curve[J]. SIAM review, 1992, 34(4): 561-580.

[Hirsch 2008] Hirsch M, Baldzuhn J, Beidler C, et al. Major results from the stellarator Wendelstein 7-AS[J]. Plasma Physics and Controlled Fusion, 2008, 50(5): 053001.

[Hutchinson 2002] Hutchinson I H. Principles of plasma diagnostics[J]. Plasma Physics and Controlled Fusion, 2002, 44(12): 2603.

[Huysmans 1999] JET Team. Observation of neoclassical tearing modes in JET[J]. Nuclear Fusion, 1999, 39(11Y): 1965.

[Igochine 2010] Igochine V, Gude A, Maraschek M, et al. Hotlink based soft x-ray diagnostic on ASDEX Upgrade[J]. 2010.

[Ingesson 2000] Ingesson L C, Maggi C F, Reichle R. Characterization of geometrical detection-system properties for two-dimensional tomography[J]. Review of Scientific Instruments, 2000, 71(3): 1370-1378.

[Jardin 2014] Jardin A. Technical Report: Analysis of divertor profiles for testing physics assumptions. JET Plasma Boundary Group, CCFE, UK, 2014.

[Jardin 2016] Jardin A, Mazon D, Bielecki J. Comparison of two regularization methods for soft x-ray tomography at Tore Supra[J]. Physica Scripta, 2016, 91(4): 044007.

[Jardin 2017] Jardin A. Soft X-ray measurements for impurity transport studies in tokamak plasmas[D]. Aix-Marseille, 2017.

[Jaynes 2004] Jaynes E T. Probability theory: The logic of science[M]. Cambridge University Press, 2004.

[Jensen 1977] Jensen R V, Post D E, Grasberger W H, et al. Calculations of impurity radiation and its effects on tokamak experiments[J]. Nuclear Fusion, 1977, 17(6): 1187.

[Kadomtsev 1987] Kadomtsev B B. Magnetic field line reconnection[J]. Reports on Progress in Physics, 1987, 50(2): 115.

[Kikuchi 2012] Kikuchi M, Lackner K, Tran M Q. Fusion physics[M]. International Atomic Energy Agency (IAEA), 2012.

[Kunze 2009] Kunze H J. Introduction to plasma spectroscopy[M]. Springer Science & Business Media, 2009.

[Lao 1985] Lao L L, John H S, Stambaugh R D, et al. Reconstruction of current profile parameters and plasma shapes in tokamaks[J]. Nuclear Fusion, 1985, 25(11): 1611.

[Lauret 2012] Lauret M, Felici F, Witvoet G, et al. Demonstration of sawtooth period locking with power modulation in TCV plasmas[J]. Nuclear Fusion, 2012, 52(6): 062002.

[Li 2014] Li D. Gaussian process tomography for the analysis of line-integrated measurements in fusion plasmas[D]. 2014.

[Ljepojevic 1984] Ljepojevoc N N, Hutcheon R J, McWhirter R W P. Spectral intensities from hydrogen-like ions[J]. Journal of Physics B: Atomic and Molecular Physics, 1984, 17(15): 3057.

[Mazon 2012a] Mazon D, Lotte P, Faugeras B, et al. Validation of the new real-time equilibrium code EQUINOX on JET and Tore Supra[C]//39th EPS Conference and 16th Int. Congress on Plasma Physics. 2012: 71.

[Mazon 2012b] Mazon D, Vezinet D, Pacella D, et al. Soft x-ray tomography for real-time applications: present status at Tore Supra and possible future developments[J]. Review of Scientific Instruments, 2012, 83(6): 063505.

[Mazon 2016] Mazon D, Jardin A, Coston C, et al. GEM detectors for WEST and potential application for heavy impurity transport studies[J]. Journal of Instrumentation, 2016, 11(08): C08006.

[Nardone 1992] Nardone C. Multichannel fluctuation data analysis by the singular value decomposition method. Application to MHD modes in JET[J]. Plasma Physics and Controlled Fusion, 1992, 34(9): 1447.

[Odstrcil 2017] Odstrcil T, Pütterich T, Angioni C, et al. The physics of W transport illuminated by recent progress in W density diagnostics at ASDEX Upgrade[J]. Plasma Physics and Controlled Fusion, 2017, 60(1): 014003.

[Ongena 2001] Ongena J and Van Oost G. Energy for Future Centuries– Will Fusion be an Inexhaustible, Safe and Clean Energy Source? EFDA–JET–RE(00)01, 2001. Available at: http://www.euro-fusionscipub.org/wp-content/uploads/2014/11/EFDR00001.pdf. Last accessed: June 2019.

[Open-ADAS 2017] Open-ADAS. The Open ADAS Project (Atomic Data and Analysis Structure). Available at: http://open.adas.ac.uk, 2017. Last accessed: June 2019

[Pan 2006] Pan YD, Yu GG et al. Fast bolometric measurement on the HL-2A tokamak[C]//33rd EPS Conference on Plasma Physics. Rome, 2006 30I(2):174

[Pfirsch 1962] Pfirsch D and Schluter A. Max Planck Institute, Rep. MPI/PA.7/62, 1962.

[Post 1955] Post D, Abdallah J, Clark R E H, et al. Calculations of energy losses due to atomic processes in tokamaks with applications to the International Thermonuclear Experimental Reactor divertor[J]. Physics of Plasmas, 1995, 2(6): 2328-2336.

[Putterich 2010] Pütterich T, Neu R, Dux R, et al. Calculation and experimental test of the cooling factor of tungsten[J]. Nuclear Fusion, 2010, 50(2): 025012.

[Ratynskaia 2011] Ratynskaia S, Castaldo C, Bergsåker H, et al. Diagnostics of mobile dust in scrape-off layer plasmas[J]. Plasma Physics and Controlled Fusion, 2011, 53(7): 074009.

[Reinke 2012] Reinke M L, Hutchinson I H, Rice J E, et al. Poloidal variation of high-Z impurity density due to hydrogen minority ion cyclotron resonance heating on Alcator C-Mod[J]. Plasma Physics and Controlled Fusion, 2012, 54(4): 045004.

[Rosmej 1997] Rosmej F B. Hot electron X-ray diagnostics[J]. Journal of Physics B: Atomic, Molecular and Optical Physics, 1997, 30(22): L819.

[Sauli 1997] Sauli F. GEM: A new concept for electron amplification in gas detectors[J]. Nuclear Instruments and Methods in Physics Research Section A: Accelerators, Spectrometers, Detectors and Associated Equipment, 1997, 386(2-3): 531-534.

[Sauter 1997] Sauter O, La Haye R J, Chang Z, et al. Beta limits in long-pulse tokamak discharges[J]. Physics of Plasmas, 1997, 4(5): 1654-1664.

[Shafranov 1962] Shafranov V D. Equilibrium of a toroidal plasma in a magnetic field[J]. Journal of Nuclear Energy. Part C, Plasma Physics, Accelerators, Thermonuclear Research, 1963, 5(4): 251.

[Sivia 2006] Sivia D, Skilling J. Data analysis: a Bayesian tutorial[M]. OUP Oxford, 2006.

[Smith 2006] Smith G C. Gas-based detectors for synchrotron radiation[J]. Journal of Synchrotron Radiation, 2006, 13(2): 172-179.

[Stangeby 2000] Stangeby P C. The plasma boundary of magnetic fusion devices[M]. CRC Press, 2000.

[Sugie 2003] Sugie T, Costley A, Malaquias A, et al. Spectroscopic Measurement System for ITER Divertor Plasma: Divertor Impurity Monitor[C]//Proc. 30th EPS Conference on Controlled Fusion and Plasma Physics St.-Petersburg. 2003: 7-11.

[Summers 2006] Summers H P, Dickson W J, O'mullane M G, et al. Ionization state, excited populations and emission of impurities in dynamic finite density plasmas: I. The generalized collisional–radiative model for light elements[J]. Plasma Physics and Controlled Fusion, 2006, 48(2): 263.

[Svensson 2011] Svensson J. Non-parametric tomography using Gaussian processes[M]. European Fusion Development Agreement, EFDA-ET-PR(11)24, 2011.

[Tikhonov 1977] Tikhonov A N, Arsenin V Y. Solutions of ill-posed problems: VH Winston & Sons. 1977. Translated from the Russian, Preface by translation editor Fritz John, Scripta Series in Mathematics.

[Udintsev 2005] Udintsev V S, Ottaviani M, Maget P, et al. Experimental observation of m/n= 1/1 mode behaviour during sawtooth activity and its manifestations in tokamak plasmas[J]. Plasma Physics and Controlled Fusion, 2005, 47(8): 1111.

[Verdoolaege 2010] Verdoolaege G, Fischer R, Van Oost G, et al. Potential of a Bayesian integrated determination of the ion effective charge via bremsstrahlung and charge exchange spectroscopy in tokamak plasmas[J]. IEEE Transactions on Plasma Science, 2010, 38(11): 3168-3196.

[Vezinet 2013] Vezinet D, Mazon D, Malard P. Absolute spectral characterization of silicon barrier diode: Application to soft X-ray fusion diagnostics at Tore Supra[J]. Journal of Applied Physics, 2013, 114(2): 023104.

[Vignitchouk 2014] Vignitchouk L, Tolias P, Ratynskaia S. Dust–wall and dust–plasma interaction in the MIGRAINe code[J]. Plasma Physics and Controlled Fusion, 2014, 56(9): 095005.

[von der Linden 2014] Von der Linden W, Dose V, Von Toussaint U. Bayesian probability theory: applications in the physical sciences[M]. Cambridge University Press, 2014.

[Wang 1991] Wang L, Granetz R S. A simplified expression for the Radon transform of Bessel basis functions in tomography[J]. Review of Scientific Instruments, 1991, 62(3): 842-843.

[WANG 2018a] Wang T, Mazon D, Svensson J, et al. Gaussian process tomography for soft x-ray spectroscopy at WEST without equilibrium information[J]. Review of Scientific Instruments, 2018, 89(6): 063505.

[WANG 2018b] Wang T, Mazon D, Svensson J, et al. Incorporating magnetic equilibrium information in Gaussian process tomography for soft X-ray spectroscopy at WEST[J]. Review of Scientific Instruments, 2018, 89(10): 10F103.

[Weinheimer 2001] Weinheimer J, Ahmad I, Herzog O, et al. High-resolution x-ray crystal spectrometer/polarimeter at torus experiment for technology oriented research-94[J]. Review of Scientific Instruments, 2001, 72(6): 2566-2574.

[Weinzettl 2010] Weinzettl V, Naydenkova D I, Sestak D, et al. Design of multi-range tomographic system for transport studies in tokamak plasmas[J]. Nuclear Instruments and Methods in Physics Research Section A: Accelerators, Spectrometers, Detectors and Associated Equipment, 2010, 623(2): 806-808.

[WEO 2017] WEO special Report: Energy Access Outlook, 2017. Available at https://webstore.iea.org/download/summary/274?fileName=English-Energy-Access-Outlook-2017-ES.pdf. Last accessed: June 2019.

[Wesson 1987] Wesson J, Campbell D J. Tokamaks[M]. Oxford University Press, 1987.

[Zohm 1995] Zohm H, Maraschek M, Pautasso G, et al. MHD stability and disruption physics in ASDEX Upgrade[J]. Plasma Physics and Controlled Fusion, 1995, 37(11A): A313.